

# A Total Hip Replacement Toolbox: From CT-Scan to Patient-Specific FE Analysis

Diogo Moreira Campos Ferreira de Almeida

Promotors: Prof B. Verheghe, PhD, Prof M. De Beule, PhD

Prof J. Folgado, PhD, Prof R. Ruben, PhD

Doctoral thesis submitted in order to obtain the academic degrees of  
Doctor of Biomedical Engineering (Ghent University) and  
Doutor em Engenharia Biomédica (Universidade de Lisboa)



Department of Electronics and Information Systems

Head of Department: Prof R. Van de Walle, PhD

Faculty of Engineering and Architecture



Department of Bioengineering

Head of Department: Prof J. P. Conde, PhD

Instituto Superior Técnico

Academic year 2016 - 2017

ISBN 978-90-8578-980-2  
NUR 954  
Wettelijk depot: D/2017/10.500/15

**Supervisors:**

Prof. dr. ir. Rui B. Ruben  
Prof. dr. ir. Benedict Verheghe  
Prof. dr. ir. João Folgado  
Prof. dr. ir. Matthieu de Beule

**Research institutions:**

Institute Biomedical Technology  
Biofluid, Tissue and Solid Mechanics for Medical Applications (bioMMeda)  
Ghent University  
De Pintelaan 185 - Blok B  
B-9000 Gent  
BELGIUM

Institute of Mechanical Engineering (IDMEC-IST)  
Associated Laboratory for Energy, Transports and Aeronautics (laeta)  
University of Lisbon  
Av. Rovisco Pais, 1  
1049-001 Lisbon  
PORTUGAL

**Members of the exam committee:***Chairman:*

Prof. dr. ir. Rik Van de Walle      Faculty of Engineering and Architecture,  
UGent, Belgium

*Secretaries:*

Prof. dr. ir. Jan Belis      Faculty of Engineering and Architecture,  
UGent, Belgium

Prof. dr. ir. Paulo Rui Fernandes      Instituto Superior Técnico,  
ULisbon, Portugal

*Other members:*

Dr. ir. Toon Huysmans      Department of Physics,  
Universiteit Antwerpen, Belgium  
Prof. dr. ir. Jef Vandemeulebroucke      Department of Electronics and Informatics,  
Vrije Universiteit Brussel, Belgium  
Prof. dr. ir. Rui B. Ruben      Center for Rapid and Sustainable Product Development,  
Polytechnic Institute of Leiria, Portugal  
Prof. dr. ir. Benedict Verheghe      Faculty of Engineering and Architecture,  
UGent, Belgium  
Prof. dr. ir. João Folgado      Instituto Superior Técnico,  
ULisbon, Portugal  
Prof. dr. ir. Matthieu de Beule      Faculty of Engineering and Architecture,  
UGent, Portugal



# Resumo

A artroplastia total da anca é uma intervenção cirúrgica que consiste em substituir a articulação da anca por uma articulação prótica. Ainda que seja considerada uma das intervenções cirúrgicas mais bem sucedidas, seguras e eficazes, complicações relacionadas com o seu design e posicionamento do implante ainda são frequentes. A ausência de pontos de referência que definam o alinhamento do fémur e da pélvis dificulta o posicionamento do implante na cirurgia. Todos os anos, cerca de um milhão de pacientes em todo o mundo são submetidos a uma artroplastia da anca, restaurando a funcionalidade da mesma. Devido ao envelhecimento da população, a quantidade de artroplastias tem tendência a aumentar, sendo que uma intervenção de revisão depende da quantidade de tecido ósseo ainda existente e por isso os seus riscos e custos são consideravelmente maiores.

Desta forma, o desenvolvimento de uma metodologia que automaticamente recria computacionalmente a articulação de um paciente específico com um conjunto de ferramentas que possibilitam o estudo e otimização do posicionamento dos diferentes implantes no fémur é o principal foco do trabalho aqui apresentado. Assim, um planeamento da intervenção cirúrgica baseado no processamento e modelação computacional de imagens médicas do paciente, usualmente TACs, permitirá ao cirurgião, numa fase pré-cirúrgica, obter informação quantitativa acerca do desempenho de diferentes implantes de uma forma rápida e simples e portanto melhorar o planeamento da intervenção, minimizando a influência da sua experiência e perícia e consequentemente reduzindo a duração e o risco de complicações na cirurgia.

De forma a criar um conjunto de ferramentas que possibilite a um utilizador inexperiente um planeamento de uma artroplastia da anca sem que lhe seja necessário ter um conhecimento profundo sobre os métodos utilizados para o efeito, tentou maximizar-se o nível de automatização das técnicas aqui apresentadas. Para tal, utilizou-se o pyFormex, um programa baseado na linguagem Python que permite transformações com modelos tridimensionais. As imagens médicas utilizadas são resultantes de TACs realizados a uma população heterogénea de pacientes, disponibilizadas pela clínica médica Quadrantes, em Lisboa, e pelo hospital universitário de Ghent, na Bélgica. As imagens diferem principalmente na sua resolução: enquanto que a distância entre as fatias das imagens provenientes do hospital de Ghent é de 0.625 mm, a resolução das provenientes da clínica Quadrantes é de 5 a 7 mm, isto é, cerca de dez vezes inferior. A metodologia será apresentada em duas fases distintas: a segmentação automática do osso do fémur a partir de imagens médicas e a extração automática de pontos de referência e eixos anatómicos que permite a otimização do posicionamento e orientação do implante.

A segmentação do fémur foi conseguida através de uma adaptação de métodos de análise estatística ao processamento de imagem médica denominada por Active Shape Models (ASM). A quantificação da variância de objectos é descrita por um modelo estatístico, conhecido por Statistical Shape Model (SSM). De forma a construir o SSM, uma malha de elementos de superfície paramétricos definidos por equações de Lagrange foi utilizada para descrever a geometria do fémur. De forma a remover todas as variações translacionais, rotacionais e de tamanho, foi utilizada uma análise de Procrustes. A modelação estatística e consequente redução de dimensão do problema foram conseguidas através de uma Análise de Componentes Principais (ACP).

Um ASM requer também uma forma de relacionar a geometria do fémur com a informação contida nas imagens médicas. Neste contexto, criou-se um modelo estatístico da aparência do fémur, conhecido por Local Appearance Model (LAM). O LAM é baseado no gradiente da imagem normalizado ao longo das normais à superfície do objecto em localizações específicas na geometria do mesmo. A sua construção baseia-se num conjunto de imagens previamente segmentadas, na qual se analisam os perfis do gradiente ao longo da fronteira do objecto e se identificam comportamentos que correspondem à fronteira da geometria do objecto. Uma ACP sobre cada um destes pontos resulta no LAM que é posteriormente usada para segmentar novas imagens.

O processo de treino do SSM e do LAM foi efectuado com 30 imagens médicas do hospital de Ghent. Cada uma dessas 30 imagens foi segmentada e adaptada a uma malha paramétrica, a partir da qual se construiu o ASM. A segmentação de uma nova imagem começa por estimar a localização do fémur no domínio dessa imagem através um método inovador baseado num algoritmo de Iterative Closest Point (ICP) com constrangimentos na forma das núvens de pontos. O algoritmo rapidamente estima a posição e a orientação do fémur para que o processo iterativo de segmentação comece. Neste, a cada iteração, o algoritmo compara o perfil do gradiente do modelo na imagem e do ASM e altera-se de forma a minimizar as diferenças entre ambos. Após, existe uma correcção de valores desenquadrados e possivelmente errados e a iteração termina com uma actualização da malha paramétrica.

A segmentação da cavidade medular é baseada na sua facilidade de identificação no domínio do fémur devido ao seu preenchimento com medula que difere do valor do osso cortical que rodeia a cavidade na escala de cinzentos da imagem.

Foi proposto um sistema de coordenadas que uniformizasse as operações com toda a população de fémures que possibilitou que se localizassem as coordenadas das proeminências ou eixos anatómicas mais relevantes do fémur. Com esta informação, desenvolveu-se um algoritmo em conjunto com cirurgiões ortopédicos que optimiza o posicionamento e o dimensionamento do implante para um fémur específico. Paralelamente, modelaram-se alguns implantes comercialmente disponíveis de forma a que se possam comparar os diferentes designs ou materiais constituintes dos mesmos.

Após o acoplamento do implante escolhido ao fémur segmentado, foi implementado um método de geração de uma malha de elementos finitos (EF) que combina duas técnicas de forma a conseguir uma malha de elementos hexaédricos homogénea e automática: existe uma primeira abordagem *grid-based* para o interior do domínio uma abordagem baseada na técnica *receding front* na zona mais externa que evita elementos distorcidos na superfície de

contacto.

O processo de treino do SSM provou ser preciso, compacto e generalizável. O processo de adaptação das nuvens de pontos da segmentação à malha paramétrica teve valores de erro médio de  $0.8895 \pm 0.0179$  mm, na ordem do tamanho do voxel que limita a precisão da segmentação inicial. Os primeiros quatro principais componentes da ACP à geometria do fémur representam mais de 95% da variação total, pelo que existiu uma grande redução de dimensionalidade. Por fim, a validação cruzada apresentou um erro médio de 1.42 mm quando usados apenas 5 componentes principais mas que diminuía à medida que estes aumentavam.

O método de inicialização do ASM tem resultados muito similares à inicialização manual em apenas 30 segundos, o que levou a que o processo iterativo de segmentação fosse mais eficiente. O método de segmentação foi validado por comparação com a segmentação manual de 10 fémures. De notar que por vezes a fronteira do fémur não se encontra bem visível na imagem pelo que a segmentação manual é também susceptível de erro. O método apresentou um erro médio de  $1.014 \pm 0.474$  mm e uma distância de Hausdorff média de  $4.336 \pm 0.861$  mm. O coeficiente de Dice médio foi de 94%. Comparativamente aos restantes métodos encontrados na literatura, o método provou ser eficiente em termos de tempo apresentando um bom compromisso com a precisão. A segmentação de um novo fémur é conseguida em menos de um minuto o que é apropriado num ambiente interactivo de preparação da artroplastia.

O método apresentado foi utilizado para segmentação de 148 fémures do grupo do Ghent (alta resolução) com uma taxa de sucesso de 98%. Devido à baixa resolução das imagens da clínica Quadrantes, não é por vezes possível diferenciar a cabeça do fémur da cúpula acetabular porque a distância entre as duas é menor que a resolução das imagens. Não obstante, o algoritmo convergiu e conseguiu segmentar os 10 fémures nelas presentes. O valor médio do erro foi de  $1.446 \pm 1.101$  mm e o valor da distância de Hausdorff foi de  $10.135 \pm 5.9478$  mm, o que é totalmente aceitável para a resolução destas imagens.

O conjunto de métodos implementados em pyFormex conseguiram que se localizasse de forma automática e robusta as mais importantes promínias e eixos anatómicos do fémur. Com isto, foi possível criar um algoritmo que automaticamente otimiza o posicionamento do implante na cavidade medular, dimensionando-o para que o contacto entre a superfície endosteal e a haste do implante seja maximizada e o suporte melhorado. A modelação dos diferentes implantes em conjunto com a geração da malha de EF permitiu que a performance dos diferentes designs e materiais dos implantes fosse comparada de forma a promover um melhor planeamento da artroplastia.

Em suma, nesta tese desenvolveu-se um conjunto de métodos que permite ir de uma imagem TAC a uma malha de EF de forma totalmente automática, robusta e eficiente. O processo de segmentação do fémur foi bem sucedido em 98% dos casos, obtendo bons resultados também em imagens de baixa resolução, frequentes em unidades de saúde pública. A geração da malha de EF e a modelação de diferentes implantes permite obter informações quantitativas sobre o seu desempenho tendo em conta a anatomia real do paciente.

**Palavras-chave:** Biomecânica, Artroplastia Total da Anca, Planeamento cirúrgico, Segmentação, Análise de Elementos Finitos.





# Samenvatting

Een totale heup arthroplastiek is een chirurgische ingreep waarbij het anatomische heupgewricht vervangen wordt door een prothese. Deze ingreep wordt algemeen aanvaard als één van de meest succesvolle, veilige en kost-efficiënte chirurgische procedures, maar toch komen nog steeds falingen van het implantaat voor die gerelateerd zijn aan het design en de plaatsing van de prothese. De afwezigheid van betrouwbare landmarks die de uitlijning van de femur en de pelvis definiëren en een beperkte toegankelijkheid maken het plaatsen van een heup implantaat geen sinecure. Elk jaar ondergaan wereldwijd één miljoen patiënten een totale heup arthroplastiek om de functionaliteit van de heup te herstellen. Wegens een verouderende populatie zal het aantal procedures stijgen in de komende jaren. Daarbij zullen ook revisies nodig zijn die afhankelijk zijn van de hoeveelheid overblijvend botweefsel waarbij de risico's en kostprijs van deze interventies zullen toenemen.

De focus van dit onderzoek lag op het ontwikkelen van een patiënt-specifiek computermodel van het heupgewricht in combinatie met een aantal tools om pre-operatief het effect van verschillende afmetingen en posities van heup implantaten te evalueren. Op deze manier zal functioneel gebruik gemaakt worden van de medische CT beelden van de patiënt en verkrijgt de arts specifieke kwantitatieve informatie omtrent het effect van verschillende protheses. Door deze verbeterde voorbereiding van de ingreep wordt de invloed van (het gebrek aan) ervaring van de arts geminimaliseerd en kunnen op termijn de complicaties dalen.

De ontwikkelde tool is geautomatiseerd om hem zo gebruiksvriendelijk mogelijk te maken voor een gebruiker zonder specifieke expertise in de onderliggende algoritmes. De tool is geïmplementeerd in pyFormex, een open-source programma onder ontwikkeling aan IBiTech-bioMMeda (Universiteit Gent) dat een hele reeks mogelijkheden biedt voor het genereren, transformeren en manipuleren van oppervlakte meshes. De medische beelden die gebruikt werden in deze studie vertegenwoordigen een heterogene populatie en zijn afkomstig van het Quadrantes ziekenhuis in Lissabon en het Universitair Ziekenhuis Gent. Beide populaties verschillen in resolutie: de afstand tussen 2 opeenvolgende slices was gemiddeld 0.625 mm voor Gent en 5 tot 7 mm voor Lissabon. De ontwikkelde methodologie bestaat uit 2 delen: het eerste deel focust op het automatisch segmenteren van de femur van de CT scans met zowel hoge als lage resolutie en in het tweede deel worden anatomische landmarks en assen bepaald die zullen gebruikt worden voor het positioneren van het implantaat.

De segmentatie is gebaseerd op Active Shape Models (ASM), een variant op gekende statistische methodes voor het verwerken van medische beelden. De hoeveelheid variatie binnen een populatie van een bepaalde vorm wordt

beschreven door een statistisch model, het Statistical Shape Model (SSM). Om een SSM te maken en te trainen werd een parametrische mesh van Lagrange elementen gecreëerd die de geometrie van de femur nauwkeurig beschrijft. De uitlijning en het verwijderen van alle translaties, rotaties en grootte variaties werd via een Procrustes analyses gerealiseerd. De statistische modellering en het reduceren van de dimensies werd gerealiseerd via een Principal Component Analysis (PCA).

Een ASM dient ook de geometrie van de femur te relateren aan de informatie uit de medische beelden. Hiervoor wordt een Local Appearance Model (LAM) gecreëerd en getraind van data te samplen, gelijkaardig aan de SSM. De LAM is een statistisch model van de genormaliseerde beeld gradiënt – gebaseerd op de intensiteitswaarden van de voxels – normaal op het oppervlak in specifieke landmarks. Dit wordt gerealiseerd door te samplen langs de normaal ten opzichte van de grens in de training set en dus een statistisch model te bouwen van de structuur van de grijswaarden – de LAM. Een PCA wordt berekend over elk van deze grenspunten om een gemiddeld profiel te bekomen en wordt dan gebruikt om nieuwe in-beeld femurs te segmenteren. De training sample van de SSM en de LAM bestond uit 30 at random geselecteerde medische beelden van de UZGent populatie. Elk van deze beelden werd gesegmenteerd en gefit aan de parametrische mesh. De workflow voor het segmenteren van een nieuwe dataset start bij het schatten van de locatie van de in-beeld femur via een nieuwe aanpak die gebaseerd is op een Iterative Closest Point (ICP) methode met vorm en buur beperkingen. Het algoritme maakt een vlugge schatting van de positie van de femur en bepaalt de initiële parameters van de mesh voor de ASM segmentatie. Vervolgens vergelijkt het algoritme bij iedere iteratie het profiel van de gradiënt van de nieuw geschatte in-beeld femur met het getrainde ASM gradiënt profiel en past dit aan om het verschil te minimaliseren. Bij elke iteratie word een eventuele error correctie toegepast en wordt de mesh geupdated.

De segmentatie van het medullair kanaal is gebaseerd op het verschil in trabeculair en corticaal bot op basis van de grijswaarden binnen in het domein van de femur.

Vervolgens werd een standaard coördinatensysteem voor de populatie van de femurs bepaald om anatomische landmarks te extraheren en metingen uit te voeren zonder interactie van de gebruiker. Op basis van dit coördinatensysteem werd een algoritme ontwikkeld samen met orthopedische chirurgen om de afmetingen en positie van heupimplantaten te optimaliseren voor een bepaalde patiënt. Terzelfdertijd werden commercieel beschikbare heupimplantaten gemodelleerd om hun performantie te vergelijken.

Een algoritme voor het creëren van de Finite Element (FE) mesh werd geïmplementeerd om de vergelijking van de verschillende heupprotheses zo objectief mogelijk te kwantificeren. Het algoritme maakt gebruik van verschillende technieken om volledig automatisch een hexahedrale mesh te genereren via een grid-gebaseerde aanpak waarbij eerst het binnenoppervlak van de femur gemesht wordt, gevolgd door een specifieke aanpak om sterk vervormde elementen te vermijden in de buurt van het contactoppervlak.

Het training proces van de SSM is nauwkeurig, compact en zeer generiek toepasbaar gebleken. Het fitten van de gesegmenteerde puntenwolk op de parametrische mesh had een RMS van  $0.8895 \pm 0.0179$  mm, dit is in dezelfde grootteorde van de afmetingen van de voxels die ook de nauwkeurigheid van

de manuele segmentaties bepalen.

De eerste vier principal components van de PCA van de femur geometrie bepalen 95% van zijn vormvariantie wat aangeeft dat dit een effectieve manier is om het aantal dimensies te reduceren. Tenslotte werd slechts een gemiddelde fout gevonden van 1.42 mm wanneer slechts 5 principal components van de PCA gebruikt werden, hoewel dit zoals verwacht het aantal componenten deed dalen.

De ASM initialisatie methode gaf gelijkaardige resultaten in vergelijking met manuele methodes en convergeerde in slechts 30 seconden. De nauwkeurigheid leidde tot een efficiënter iteratief segmentatie proces. De segmentatie methode werd gevalideerd door te vergelijken met de gouden standaard, i.e. manuele segmentatie van 10 verschillende femurs. Het is belangrijk om te vermelden dat ook bij de manuele segmentatie de femur niet altijd perfect afgelijnd is binnen de grijswaarden van de medische beelden en dat dus ook het manuele segmentatie proces onderhevig is aan fouten, zelfs voor een ervaren operator. De voorgestelde methode had een RMS van  $1.014 \pm 0.474$  mm en een Hausdorff afstand van  $4.336 \pm 0.861$  mm. De Dice coefficient was 94%. In vergelijking tot de state-of-the-art methodes voor femur segmentatie kan de voorgestelde methode als tijd efficiënt en nauwkeurig beschouwd worden. De segmentatie van een nieuwe femur duurt minder dan 1 minuut wat de bruikbaarheid bevestigt voor een real-time interactieve arthroplastiek planning tool.

De methode werd succesvol toegepast op 98% van de 148 femurs van UZ-Gent (hoge resolutie). Door de lage resolutie van de beelden uit Lissabon was het vaak onmogelijk om de femur te onderscheiden van de heup kom omdat de afstand kleiner was dan de resolutie van de beelden. Toch slaagde het algoritme erin om te convergeren voor 10 at-random geselecteerde femurs met een RMS van  $1.446 \pm 1.101$  mm en een Hausdorff afstand van  $10.135 \pm 5.9478$  mm, wat zeer aanvaardbare resultaten zijn gezien de resolutie van de beelden.

De in pyFormex geïmplementeerde tools bieden een nauwkeurige en robuuste methode om de belangrijkste anatomische karakteristieken en assen te bepalen. Dit maakt het mogelijk om een workflow te definiëren om de interactie tussen de femur en het implantaat te optimaliseren door het contactoppervlak tussen het implantaat en de heup te maximaliseren. Het modelleren van verschillende implantaten samen met de genereren van de mesh laat een kwantitatieve analyse toe van hun performantie in een specifieke femur wat een meer gedetailleerde arthroplastiek planning toelaat.

Het doel van de thesis was om een toolbox te creëren om op basis van de CT scan van een patiënt een patiënt-specifiek computermodel op te bouwen op een automatische, robuuste en efficiënte manier. De methode werd succesvol toegepast in 98% van de gevallen, zowel in hoge als lage resolutie beelden die vaak gebruikt worden in de algemene gezondheidszorg wegens beschikbaarheid en lagere kost. Het genereren van de mesh en het modelleren van de implantaten laat toe om pre-operatieve planning te doen op een patiënt-specifieke schaal.

**Trefwoorden:** Biomechanica, Een Totale Heupprothese, Chirurgie Planning, Segmentatie, Finite Element Analyse.



# Abstract

The total hip arthroplasty is a surgical intervention that replaces the anatomical hip joint for a prosthetic joint. Even though it is considered to be among the most successful, safe and cost-effective surgical procedures, implant failures related to the prosthesis' design and placement still occur in a considerable number. The absence of reliable landmarks defining the alignment of the femur and pelvis and restricted accessibility makes the placement of the hip implant even more difficult during surgery. Every year, around one million individuals around the world undergo a total hip replacement, therefore restoring its functionality. Due to an ageing population, the amount of primary THA interventions tends to increase in the near future. In addition, revision arthroplasties depend on the amount of bone tissue remaining and therefore the risks and cost of this intervention are increased.

Hence, the development of a methodology that computationally recreates the patient-specific hip joint combined with a set of tools that enable the pre-surgical study and optimization of the different hip prosthesis sizing and positioning is the main focus of the work here presented. This way, a surgical planning based on the processing and computational modeling of medical images, usually CT-Scans, will provide the physician, at an early pre-surgical stage, quantitative information about the performance of the different implant designs and materials in a straightforward, time-effective way, and therefore enhance the surgery planning minimizing the influence of the surgeon's expertise and clinical practice and ultimately reducing the incidence of related complications.

In a way to create a set of tools directed for an inexperienced user without technical knowledge on the implemented algorithms, the methodologies here presented are mostly automatic and straightforward. The framework was implemented in pyFormex, which is an open source program under development at IBiTech-bioMMeda that provides a wide range of operations for generating, transforming and manipulating surface meshes. The medical images used in this study were acquired from a heterogeneous population of patients by computerized tomography and were made available to us by the medical clinic Quadrantes, in Lisbon, and by the Universitair Ziekenhuis, in Ghent. Both image groups differ in resolution: while the slice thickness in the Ghent images is 0.625 mm on average, the slice thickness of the Lisbon image group is between 5 and 7 mm, which is around 10 times higher. The presented methodology will have two different stages: the first is the automatic segmentation of the femur bone from CT-Scans with high and low resolution and the second is the anatomical landmark and axis extraction that will allow the guidance and positioning of the implant.

The segmentation was based on Active Shape Models (ASM), which are an adaptation of known statistical methods to medical image processing. The amount of variance of a certain population of a shape is described by a statistical model, known by Statistical Shape Model (SSM). In order to create and train the SSM, a piece-wise parametric mesh based on Lagrange elements was used to describe the geometry of the femur. The alignment and removal of all translational, rotational and size variations, a Procrustes Analysis was performed. Lastly, the statistical modeling and consequent dimensionality reduction was achieved through a Principal Component Analysis (PCA).

An ASM also needs to relate the geometry of the femur with the information provided in the medical image datasets. Within this context, a Local Appearance Model (LAM) was created and trained from sampling data, in a similar way to the SSM. The LAM is a statistical model of the normalized image gradient – based on the voxel intensity values – normal to the object surface at specific landmarks. This is achieved by sampling along the profile normal to the boundary in the training set and building a statistical model of the gray-level structure - the LAM. A PCA is computed over each of these boundary points producing a mean profile and is then used to segment new in-image femurs.

The training sample of the SSM and the LAM was 30 randomly selected medical datasets from the Ghent group. Each of those images was segmented and fitted to a piece-wise parametric mesh. The segmentation pipeline of a new dataset starts by estimating the location of the in-image femur in the dataset domain through an novel approach based on an Iterative Closest Point (ICP) method with shape and neighbor constraints. The algorithm rapidly estimates the femur’s pose and location and sets the basis parameters of the mesh for the ASM segmentation to begin. Then, at each iteration, the algorithm compares the gradient profile of the newly estimated in-image femur with the trained ASM gradient profile and adapts in order to minimize the differences between both. Still at each iteration, an element-wise error correction of possibly erroneously estimated points is performed and the mesh is updated.

The threshold segmentation of the medullary cavity is based on its obvious difference of cancellous bone and cortical bone inside the femoral domain in the grayscale image.

Secondly, a standardized coordinate system for the population of femurs was defined so that the key anatomical landmarks could be extracted and its common measurements estimated without any user interaction. Based on such coordinate system, an algorithm was developed together with orthopedic surgeons that optimizes the sizing and positioning of hip implants in a patient-specific segmented femoral volume. Simultaneously, several of the most significant commercially available implants were modeled so that the performance of its material properties and geometries could be compared.

A Finite Element (FE) mesh generation algorithm was implemented so that the comparative performance of the implants could be objectively quantified. The mesh generation combines different techniques that favor the femoral geometry to develop a fully automatic homogeneous hexahedral mesh: firstly, a grid-based approach meshes the interior of the femur and then a receding front approach of the outer area avoids distorted elements near the contact surface.

The training process of the SSM proved to be accurate, compact and have a high generalisability. The fitting of segmented point clouds to the parametric

mesh had a Root Mean Square (RMS) of  $0.8895 \pm 0.0179$  mm, which is of the same order of the image voxel size and limits the precision of the initial manual segmentation. The first four principal components of the PCA to the femur geometry account for more than 95% of its total shape variance, which proves the advantages of the use of such method for dimensionality reduction. Lastly, the leave-one-out cross validation presented an average error of 1.42 mm when used merely 5 principal components of the PCA, although it tended to decrease as the number of components increased, as expected.

The ASM initialization method presented results similar to manual initialization, converging in only 30 seconds. Its accuracy ultimately led to a more efficient iterative segmentation process. The segmentation method was validated by comparison to the gold standard, chosen to be the manual segmentation, of 10 different femurs. It is important to mention that the femoral volume boundary is often not precisely defined in the image dataset and hence manual segmentation is also prone to errors, even for an experienced user. The method presented a RMS of  $1.014 \pm 0.474$  mm and Hausdorff distance of  $4.336 \pm 0.861$  mm. The Dice coefficient was 94%. In comparison to the literature state-of-the-art methods for femur segmentation, the method proved to be time-efficient and at the same time presenting a good compromise with accuracy. The segmentation of a new in-image femur is achieved in less than one minute which is suitable for a real time interactive arthroplasty planning software.

The method was used for the segmentation of 148 femurs of the Ghent group (high resolution) with a success rate of convergence of 98%. Due to the low resolution of the Lisbon dataset group, the head of the femur was often not distinguishable from the surrounding acetabular cup because the distance between both was less than the image resolution. Regardless, the algorithm managed to converge and present a segmentation for the 10 randomly selected femurs with an RMS of  $1.446 \pm 1.101$  mm and an Hausdorff distance of  $10.135 \pm 5.9478$  mm, which are considered to be reasonably remarkable results when taking in account the image resolution.

The pyFormex implemented set of methods achieved an accurate and robust extraction of the most important femoral prominences and anatomical axis. Hence, it was possible to develop a pipeline that optimizes the femur-implant coupling, taking in account its size, position and the medullary cavity shape such that contact between the endosteal surface and implant stem is maximized. The modeling of the different prosthesis altogether with the FE mesh generation allowed a quantitative analysis their performance on a patient-specific femur regarding a richer and more accurate arthroplasty planning.

In sum, the main scope of the thesis is the development and integration of a set of methods that allows the femoral FE element mesh generation from a CT-Scan dataset in an automatic, robust and efficient manner. The success rate of such methods was 98%, presenting outstanding performances even in very low resolution images which are often used in public health services due to its immediacy and low cost. The FE mesh generation and implant modeling allows pre-surgical studies of their performance in real patient-specific anatomies.

**Keywords:** Biomechanics, Total Hip Arthroplasty, Surgery Planning, Segmentation, Finite Element Analysis.





# Acknowledgements

First and above all, I would like to acknowledge my supervisors Prof. Rui Miguel Barreiros Ruben and Prof. João Orlando Marques Gameiro Folgado at Instituto Superior Técnico, in Lisbon, as well as Prof. Benedict Verheghe and Prof. Matthieu de Beule at the University of Ghent, in Belgium, not only for the granted privilege of working together with them during the development of my doctoral work but also for all their support, companionship and guidance. Without them, the success of this work would have been impossible to reach.

I would also like to thank Dr. João Gamelas and Dr. Emmanuele Audenaert for the clinical guidance, for providing the CT scans that served as basis for the methodology here presented and for the opportunity to attend hip arthroplasty surgeries. Prof. Paulo Fernandes who, even though isn't credit as a supervisor, has always showed support and guidance as one, so I'd like to acknowledge him for that and for the strength to apply to a doctoral program. I would also like to thank Ju Zhang for the precious help with the parametric mesh design and its adaptation to statistical modeling. A special acknowledgment note to Saskia for her help and patience with the bureaucratic paperwork that made my stay in Ghent possible and unforgettable.

Throughout the development of this thesis I was lucky enough to have been surrounded by colleagues whose eagerness for science has often driven my research in a better direction. For that reason, I would like to thank my colleagues at IDMEC, in Lisbon, and at bioMMeda, in Ghent, without whom I would still be struggling my way into pyFormex.

Last but not least, on a personal level, I would like to thank my parents Carlos and Ana Teresa, my brother Guilherme and Maria Inês for the unconditional love, support and belief in me. I would also like to thank my friends who have been on my side during these last few years, giving me the motivation to succeed on this goal. The list seems never-ending in moments like this but they know who they are.

The work developed on this thesis has been supported by Fundação para a Ciência e Tecnologia under the project PTDC/SAU-BEB/103408/2008 and the scholarship SFRH/BD/71822/2010 and by IDMEC, under LAETA, through the project UID/EMS/50022/2013. This work has also been supported by the University of Ghent, under the Special Research Fund (BOF) 01SF2613.



# Contents

<b>Resumo</b>	<b>i</b>
<b>Samenvatting</b>	<b>v</b>
<b>Abstract</b>	<b>ix</b>
<b>Acknowledgements</b>	<b>xiii</b>
<b>Contents</b>	<b>xv</b>
<b>List of Figures</b>	<b>xix</b>
<b>List of Tables</b>	<b>xxxi</b>
<b>Acronyms</b>	<b>xxxiii</b>
<b>1 Introduction</b>	<b>1</b>
1.1 Motivation . . . . .	1
1.2 Problem definition . . . . .	2
1.3 Novel Contributions . . . . .	3
1.4 Thesis overview . . . . .	4
1.5 Publications . . . . .	5
1.5.1 Papers in peer-reviewed journals . . . . .	5
1.5.2 Conference Proceedings . . . . .	6
<b>2 Acetabulofemoral Joint Morphology</b>	<b>9</b>
2.1 Terminology . . . . .	9
2.2 Hip Joint Anatomy . . . . .	9
2.3 Hip Bone Anatomy . . . . .	14
2.4 Femur Anatomy . . . . .	15
2.4.1 External Features . . . . .	15
2.4.2 Cortical and Cancellous Bone . . . . .	17
2.4.3 Endosteum and Periosteum . . . . .	18
2.4.4 Traditional Measurements . . . . .	18
2.5 Hip Joint Kinematics . . . . .	21
2.5.1 Coordinate System . . . . .	21
2.5.2 Range of Movements . . . . .	23
2.5.3 Gait Cycle . . . . .	23
2.6 Pathologies . . . . .	24
2.6.1 Osteoporosis . . . . .	24

2.6.2	Osteoarthritis . . . . .	25
2.6.3	Rheumatoid Arthritis . . . . .	26
2.6.4	Avascular Necrosis . . . . .	26
2.6.5	Acetabular Dysplasia and Protrusion . . . . .	27
2.6.6	Femoroacetabular Impingement . . . . .	27
2.6.7	Other Pathologies . . . . .	29
2.7	Proximal Femur Fractures . . . . .	29
2.8	Total Hip Arthroplasty . . . . .	30
2.8.1	The History of the Total Hip Arthroplasty . . . . .	31
2.8.2	Incidence of Total Hip Arthroplasty . . . . .	34
2.8.3	The Surgical Procedure . . . . .	35
2.9	Materials and Design of the Hip Implant . . . . .	41
2.9.1	Material Properties . . . . .	42
2.9.1.1	Metals . . . . .	42
2.9.1.2	Polymers . . . . .	43
2.9.1.3	Ceramics . . . . .	43
2.9.2	Components of Modular Hip Prosthesis . . . . .	43
2.9.2.1	The femoral stem . . . . .	44
2.9.2.2	The femoral head . . . . .	45
2.9.2.3	The acetabular liner . . . . .	45
2.9.2.4	The acetabular shell . . . . .	45
2.9.3	Design Criteria . . . . .	46
2.9.3.1	Fixation methods: cemented vs. uncemented prosthesis . . . . .	46
2.9.3.2	Fatigue resistance and stiffness of the stem . . . . .	47
2.9.3.3	Femoral head diameter and range of motion . . . . .	47
2.9.3.4	Wear, wear processes and lubrication conditions . . . . .	48
2.10	Hip Implant Failures . . . . .	49
2.10.1	Aseptic Loosening . . . . .	51
2.10.2	Pseudotumors . . . . .	51
2.10.3	Dislocation . . . . .	52
2.10.4	Fracture . . . . .	52
<b>3</b>	<b>Femur Segmentation</b> . . . . .	<b>55</b>
3.1	Computed Tomography scan . . . . .	55
3.2	Digital Imaging Communications in Medicine . . . . .	58
3.3	Medical Image Segmentation . . . . .	59
3.3.1	Threshold Segmentation . . . . .	63
3.3.2	Active Contours Segmentation . . . . .	63
3.3.3	Shape Models . . . . .	66
3.3.3.1	Shape representation . . . . .	66
3.3.3.2	Alignment . . . . .	70
3.3.3.3	Dimensionality Reduction . . . . .	71
3.3.3.4	Enlarging variations . . . . .	73
3.3.3.5	Shape correspondence . . . . .	74
3.3.3.6	Local Appearance Models . . . . .	79
3.3.3.7	Search Algorithms . . . . .	80
3.3.4	Graph cuts . . . . .	84
3.3.5	Clustering techniques . . . . .	85
3.3.6	Summary . . . . .	87

<b>4</b>	<b>CT Images</b>	<b>89</b>
4.1	The 'Quadrantes' Images . . . . .	89
4.2	The 'UZ Gent' Images . . . . .	91
4.2.1	Data Demographics . . . . .	93
4.2.2	Image Artifacts . . . . .	93
4.3	Cadaveric Femurs . . . . .	95
4.4	The Crop Algorithm . . . . .	97
4.4.1	The Generalized Hough Transform . . . . .	98
4.4.2	The Circle Hough Transform . . . . .	99
4.4.3	3D Extension of the Hough Transform . . . . .	100
4.4.4	The developed method . . . . .	100
<b>5</b>	<b>Femur Active Shape Model: Training</b>	<b>105</b>
5.1	Segmentation . . . . .	107
5.2	Statistical Shape Model . . . . .	110
5.2.1	Shape Descriptor . . . . .	111
5.2.1.1	Quartic Lagrange Basis Function . . . . .	112
5.2.2	Mesh Fitting . . . . .	115
5.2.2.1	Data Error . . . . .	115
5.2.2.2	Smoothing Errors . . . . .	117
5.2.2.3	Fitting Methods . . . . .	118
5.3	Alignment and Dimensionality Reduction . . . . .	120
5.3.1	Computation . . . . .	122
5.4	Active Shape Modeling . . . . .	123
5.4.1	Training . . . . .	123
5.5	Femur Mesh Design . . . . .	125
5.6	Femur Shape Model Training . . . . .	128
5.6.1	Fitting Meshes . . . . .	129
5.6.2	Mesh Training . . . . .	132
5.7	Conclusions . . . . .	136
<b>6</b>	<b>Femur Active Shape Model: Segmentation</b>	<b>139</b>
6.1	Initialization . . . . .	140
6.2	Segmentation . . . . .	144
6.2.1	Surface Prediction . . . . .	145
6.2.2	Element-wise Error Correction . . . . .	146
6.2.3	Mesh Update . . . . .	146
6.3	Segmentation of the medullary canal . . . . .	147
6.4	Results . . . . .	148
6.4.1	Initialization results . . . . .	149
6.4.2	'UZ Gent' datasets results . . . . .	150
6.4.3	'Quadrantes' datasets results . . . . .	157
6.5	Conclusions . . . . .	160
<b>7</b>	<b>Total Hip Arthroplasty planning</b>	<b>163</b>
7.1	Introduction . . . . .	163
7.2	Automatic extraction of femoral landmarks . . . . .	165
7.2.1	Standardized coordinate system . . . . .	165
7.2.2	Femoral middle diaphysis axis and prosthesis insertion axis	166
7.2.3	Femoral neck axis and head center extraction . . . . .	168

7.2.4	Greater and lesser trochanters . . . . .	168
7.2.5	Neck saddle point . . . . .	170
7.2.6	Femoral neck-shaft angle and anteversion angle . . . . .	171
7.3	Osteotomy . . . . .	171
7.4	Prosthesis modeling . . . . .	173
7.5	Prosthesis placement . . . . .	175
7.6	Automatic finite element mesh generation . . . . .	177
7.7	Results . . . . .	179
7.8	Discussion . . . . .	184
7.9	Conclusions . . . . .	185
<b>8</b>	<b>Conclusions and Future Work</b>	<b>187</b>
8.1	Conclusions and Key Achievements . . . . .	187
8.2	Limitations and Future Work . . . . .	188
8.2.1	ASM: Training and Segmentation . . . . .	188
8.2.2	THA Planning . . . . .	189
	<b>Bibliography</b>	<b>191</b>

# List of Figures

1.1	Main steps of the automatic femur segmentation pipeline and their corresponding chapters. . . . .	4
1.2	Main steps of the THA planning framework and its corresponding chapter. . . . .	5
2.1	Anatomical planes and terms of motion. . . . .	10
2.2	Location of the human hip joint relatively to other bones of the human skeleton, anterior and posterior views respectively. Adapted from innerbody.com . . . . .	11
2.3	Schematic representation of the coronal view of the hip joint [2]. . . . .	11
2.4	Ventral view of the right side of a partial opening of the hip joint [2]. . . . .	12
2.5	Schematic representation of the coronal view of the hip joint [2]. . . . .	12
2.6	Schematic representations of the anterior and posterior views of the hip joint [2]. . . . .	13
2.7	Schematic representation of the antero-lateral views of the pelvic bone [4]. . . . .	14
2.8	Schematic representation of the femur and its location in the human body. Courtesy of innerbody.com . . . . .	16
2.9	Major external anatomic features of the femur. Anterior and posterior views, respectively. Courtesy of innerbody.com . . . . .	17
2.10	Coronal cross section of the proximal femur. Dense cortical bone forms the outer shell to the spongy cancellous bone within. Cancellous bone displays distinctive anisotropic patterns coinciding with the directions of principal stress [8]. . . . .	18
2.11	Schematic representation of the femoral endosteum and periosteum. Image of public domain. . . . .	19
2.12	Definitions of femoral lengths: (a) shows the long femoral length, (b) shows the short femoral length and (c) the sub-throcanteric, mid-femoral and epi-condilar lengths. . . . .	19
2.13	Femoral axes and angles. On (a) the neck-shaft angle is plotted on the CT-Scan and (b) shows the femoral neck width and the femoral head diameter. . . . .	20
2.14	Schematic representation of the femoral neck anteversion (FNA) angle in a right femur, which is the angle between the femoral neck axis and the line that connects both condyles. (a) represents the normal femoral case, while (b) and (c) correspond to the anatomically abnormal femurs, respectively increased femoral anteversion and retroversion. Adapted from apta.org. . . . .	21

2.15	Illustration of the pelvic coordinate system (XYZ) and femoral coordinate system (xyz), and the JCS for the right hip joint [13]. . .	22
2.16	Range of motion in the hip joint [2]. The figure shows the maximum ranges of motion for the extension-flexion (a), abduction-adduction (b) and lateral-medial rotation (c) and (d) movements. . . . .	23
2.17	X-ray image of the pelvis showing early changes in bone density in the affected hip. Courtesy of orthoinfo.aaos.org. . . . .	25
2.18	On the left there is a X-Ray image of a healthy femur with normal space in the ball and socket joint. On the right, an X-Ray image of an arthritic hip that shows severe bone loss and cartilage degeneration which led to a narrowed joint space and the formation of bone spurs. Courtesy of orthoinfo.aaos.org. . . . .	25
2.19	Radiography of avascular necrosis of left femoral head. Man of 45 years old with AIDS. Image of public domain. . . . .	26
2.20	X-ray showing a patient with a posterior dislocation of the left (right on image) hip. Courtesy of orthoinfo.aaos.org. . . . .	27
2.21	X-ray showing a patient with an acetabular protrusion. It is noticeable the migration of the head of the femur into the pelvis ring. Image of public domain. . . . .	28
2.22	Different types of femoroacetabular impingement (FAI). On the left, the pincer impingement is shown while on the right a cam impingement is illustrated. Courtesy of orthoinfo.aaos.org. . . . .	28
2.23	Most common fracture types. Combinations of these can occur [19].	30
2.24	X-Ray of the pelvic area, showing a replaced right (left on image) hip joint. Image of public domain. . . . .	31
2.25	ULTRAMET <sup>®</sup> Metal-On-Metal Hip System, based on the Austin Moore model. Courtesy of Depuy Orthopaedics. . . . .	32
2.26	Hip resurfacing THA covers the reshaped femoral head with a new metallic articulating surface. Image of public domain. . . . .	33
2.27	Hip replacement surgery, per 100,000 population in 2012 [36]. . . .	34
2.28	Trend in hip replacement surgery in selected countries, 2000-2012 [36]. . . . .	35
2.29	Lateral approach (a) and posterior approach (b) to a Total Hip Arthroplasty, respectively. Courtesy of aofoundation.org. . . . .	36
2.30	Radiographic planning of the THA: manual (a) [49] and with the help of a software (b) [48]. . . . .	37
2.31	Comparison of a hemiarthroplasty and a total hip arthroplasty, where an acetabular component is also inserted in the pelvis. Courtesy of aofoundation.org. . . . .	37
2.32	Reaming (a) and anchorage holes drilling (b) for the fixation of the acetabular cup. Courtesy of aofoundation.org. . . . .	38
2.33	The normal acetabulum of a right femur rotated anteriorly $\alpha = 15^\circ$ (a) and with an abduction of $A = 45^\circ$ (b). Courtesy of aofoundation.org. . . . .	39
2.34	(a) shows the removal of the femoral head with the use of a threaded handle and (b) shows the measuring of the removed head diameter in order to properly choose the prosthetic head. Courtesy of aofoundation.org. . . . .	39



2.35	Preparation of the stem insertion in the femur. (a) shows the correct osteotomy planning and (b) schematically represents the correct alignment of the prosthesis. Courtesy of aofoundation.org. . . . .	40
2.36	Preparation of the stem insertion in the femur. Broaching is exemplified in (a) and (b) illustrates how the medullary cavity should be shaped in case of cemented or uncemented implants. Courtesy of aofoundation.org. . . . .	41
2.37	Proper placement of the femoral component. (a) shows the correct insertion for the stem and (b) shows the ideal head configuration. Courtesy of aofoundation.org. . . . .	41
2.38	Illustration of a successfully replaced hip joint. Courtesy of aofoundation.org. . . . .	42
2.39	Components of modular hip prosthesis [25]. . . . .	44
2.40	Schematic representation of the lubrication regimes between two contact surfaces, as for example the femoral head and the acetabular liner. (a) exemplifies boundary lubrication, (b) mixed lubrication and (c) the ideal fluid-film lubrication [1]. . . . .	49
2.41	Radiography of an example of aseptic loosening of the femoral stem in a THA. Image of public domain. . . . .	52
2.42	Radiography of an example of implant dislocation in a THA. Image of public domain. . . . .	53
2.43	Radiography of an example a broken femoral stem in a THA. Image of public domain. . . . .	53
3.1	Example of a modern CT scanner. Image of public domain. . . . .	58
3.2	Volume reconstruction from CT scan. (a) shows the acquired images from the CT scan; (b) shows the conversion to HU with Equation 3.3; (c) shows the reconstruction of the same volume with HU of fat tissue, i.e., 200. [79]. . . . .	59
3.3	Common challenges in automatic femur segmentation from CT-scan volumes. In red, we can observe weak and diffuse bone boundaries; in blue, the same boundaries are nonexistent mainly due to osteoporotic bone tissue; in green, there is very little or no space in between the femur and the pelvis; finally, in yellow, we can observe the different intensity distributions for both cortical and cancellous bone, depending on their location in the femur. . . . .	62
3.4	In the upper-left corner shows a bounded region and below it it the graph of a level set function $\phi$ (in red) determining its shape. The plane in blue represents the xy-plane. The boundary of the shape is then the zero level set of $\phi$ , while the shape itself is the set of points in the plane for which $\phi$ is positive (interior of the shape) or zero (at the boundary). The columns in the center and the left show how advantageous is to work with a shape through its level set function rather than with the shape directly, where it's necessary to consider all the possible deformations the shape might undergo. Image of public domain. . . . .	65
3.5	From left to right, placement, evolution and final convergence of the Chan-Vese algorithm on a sample CT scan of the distal part of the human femur. . . . .	66

3.6	An example of a 2D point distribution model. The shape is described by the coordinates of the landmarks around the object boundary [100]. . . . .	67
3.7	An example of a 2D medial shape description. The shape is described by the skeleton (black dotted lines) and vectors, radiating from the skeleton to the object boundary [100]. . . . .	68
3.8	An example of a 2D piece-wise parametric shape description. The shape is described by piece-wise parametric functions (outlined in red) controlled by parameters at nodes (black points) [100]. . . . .	68
3.9	An example of a 2D oscillatory modes of a global shape description. The shape is described by the coefficients of the oscillatory function used to approximate the shape [100]. . . . .	69
3.10	A femur aligned according to its anatomic coordinate system (a) and to its center of mass and its principal axes of inertia (b). . . . .	71
3.11	PCA of a multivariate Gaussian distribution centered at (1,3) with a standard deviation of 3 in roughly the (0.878, 0.478) direction and of 1 in the orthogonal direction. The vectors shown are the eigenvectors of the covariance matrix scaled by the square root of the corresponding eigenvalue, and shifted so their tails are at the mean. Image of public domain. . . . .	72
3.12	A simple example of finding point correspondence for PDMs. The reference (in black) and data boundaries (in blue) are aligned and then the closest data point to each reference point is found as its corresponding point (red arrows). Local curvature or other information can be used to support the distance measure and improve the robustness [100]. . . . .	75
3.13	An example of parameterization correspondence. Both the data and the reference PPMs have the same shape, but their domain is differently mapped (or parameterized) by the elements [100]. . . . .	76
3.14	An example of the main steps of population-based correspondence [139], In each iteration, a shape model is trained from the population, a related metric is calculated and then optimized by adjusting the parameterization of each training shape [100]. . . . .	77
3.15	The Hough Transform accumulator space. This method is based on a radial voting: for each point on the edge, the normal is drawn and points along that normal, within a radius range, are selected for sphere parameters (center and radius estimation). The vote of each edge point is accumulated into the Hough accumulator space (a). (b) figures the Gaussian sphere accumulator space for the detection of the cylinder direction [150]. . . . .	81
3.16	One iteration of an ASM search: at the beginning, the model (contour with landmarks) is located at the lower left of the true position (solid gray object). LAMs for all landmarks are evaluated at different positions normal to its surface. The best positions are highlighted with small circles in the center image. Finally, model parameters were updated to minimize the squared distances to the found best positions, bringing the model closer to its true position [86]. . . . .	82

3.17	One iteration of an AAM search: initially, the model (contour with landmarks) is located at the lower left of the true position (solid gray object). The texture beneath the model is sampled and compared to the region based appearance model. The corresponding residuals are shown in the center image and suggest a move of the model up and rightwards - suggested during the training and encoded in matrix $R$ . The resulting parameter update does indeed bring the model closer to the correct solution [86]. . . . .	83
3.18	The graph-cut algorithm applied for segmentation of bones from a 3D CT volume. In (a) there is the manual initialization, where the user marks the object in red and background in blue seeds. (b) shows the segmented 3D object [161]. . . . .	85
3.19	Feature representation for clustering. Image measurements and positions are transformed to features. Clusters in feature space correspond to image segments [163]. . . . .	86
4.1	An example of an image of the group 'Quadrantes'. It shows the maximum intensity projection in the coronal plane, showing the full extent of the image in the superior-inferior direction. The image was interpolated in the superior-inferior direction in order to have a continuous domain. . . . .	90
4.2	An example of an image of the group 'UZ Gent'. It shows the maximum intensity projection in the coronal plane, showing the full extent of the image in the superior-inferior direction. The image was interpolated in the superior-inferior direction in order to have a continuous domain. . . . .	92
4.3	Age distribution of the examined individuals data by gender. . . . .	93
4.4	Example of a cropped femur due to body misalignment at the image acquisition. (a) shows a maximum intensity projection of the femur region and (b) is an axial image taken from the region of the neck of the femur. . . . .	94
4.5	Example of a abnormal bone formations in two different patients. In (a) the patient has developed a tip-like structure at the level of the inferior trochanter of the right femur. (b) shows a misformed right condyle on the left femur. . . . .	95
4.6	Examples of metallic objects in the datasets that excluded them from this study. On the left, two maximum intensity projections of the area of interest, where it is clearly observable the much higher radiation attenuation coefficient of the metals compared to the bone tissue. On the right, two axial images of the radiation scattering and artifacts produced. In (a) the image is taken from the sub-trochanteric region and in (b) the image is taken from the distal epiphysis of the femur, just superior to the epicondyles. . . . .	96
4.7	Preliminary results of manual segmentation. Different femurs are represented in different colors. . . . .	98
4.8	Generalized Hough Transform example. . . . .	99
4.9	Circle Hough Transform (CHT). . . . .	99

4.10	Two axial slices of the accumulator image. The color-scale represents the amount of votes for every candidate (pixel) according to the side scale. (a) is a slice on the maximum peak found and corresponds to the location of the femoral head. (b) shows two nearby peaks who stand for stand for the pixels that represent the center of the spherical femoral condyles. This proved to be enough to accurately locate the femoral bounding box and crop the original image in a way that transformations become more time efficient. . . . .	101
4.11	Anterior and posterior views of the superior-inferior plane of the original dataset image domain, containing information from the superior torso to just inferior of the ankle. Femoral heads and condyles are identified in green and red, respectively for the right and left femur.	102
4.12	Maximum intensity projections of the left and right femur image domains, respectively. The algorithm crops the original dataset image in a way that ideally only the axial slices corresponding to the femur bone are selected. . . . .	103
5.1	Overview of the femur shape model training pipeline. The starting point are the CT Scan datasets (a) from where a semiautomatic segmentation process generates the triangulated meshes of the femoral volume (b). In (c), the fitting of the triangular mesh to the piecewise parametric mesh is shown, enabling correspondence between the mesh nodes across the femur population. A Procrustes Analysis is performed to remove all translational, rotational and scaling variations from the femur population, as illustrated in (d). The creation of the statistical shape model and local appearance model based on a Principal Component Analysis of the available data is shown in the last two figures: in (e) the mean shape is illustrated, along with a couple of variations of the first principal component and (f) shows a plot of the mesh normals along which the image gradient profiles are acquired. . . . .	106
5.2	Screen-shot of 3DSlicer. On the left there is the Module panel, where the segmentation functions are visible; on the center, the 3D viewer where an example dataset is shown; and on the right the axial (red), sagittal (yellow) and coronal (green) views of the dataset.	107
5.3	3D view of the full image domain in (a) and cropped image limits in blue. (b) shows the 3D reconstruction of the initial thresholded region, expected to be bone tissue. . . . .	108
5.4	3D reconstruction of the largest pixel island in the cropped image domain. The patella, the tibia and the fibula no longer figure on the image as they were not connected to the femoral island in the binary map. . . . .	109
5.5	An axial slice of the region where the blood vessel attaches to the bone is shown in (a). After manual island separation, the resulting volume reconstruction is shown in (b). Only the acetabulum and the femoral volumes are shown at this point. . . . .	109

5.6	(a) shows an axial slice where the femoral head and acetabular cup border definition problem is present. Due to low bone mass density and proximity of both surfaces, the femoral segmentation problem is often complex to approach with conventional segmentation methods. For the shape model training, it was done manually and the resulting volume is shown in (b). . . . .	110
5.7	Final smoothed and decimated 3D reconstruction of the segmented femoral volume. . . . .	111
5.8	A quartic four-element Lagrange piece-wise parametric mesh. The element boundaries are marked in gray and the mesh nodes are marked in red. . . . .	112
5.9	1D Quartic Lagrange line element. . . . .	113
5.10	2D Quartic Lagrange quadrilateral (a) and triangular (b) elements. Node numbers correspond to basis functions in equations 5.5 and 5.6, respectively. . . . .	114
5.11	Flexibility of quartic Lagrange elements. (a) shows the inflection points on a 1D line element and (b) illustrates a 2D element that efficiently models protrusions and ridges, present on the femoral surface. . . . .	114
5.12	Fitting error defined as the distance between each data point and its orthogonal projection on the mesh, i.e., the minimum distance between both. . . . .	116
5.13	Fitting error defined as the distance between each data point and its closest material point sampled on the mesh. . . . .	116
5.14	Fitting error defined as the distance between each sampled material point and its closest data point. . . . .	117
5.15	Mesh defects resulting from a lack of smoothing penalties. In (a) a sharp crease was formed at the element boundary and in (b) the crease was formed within an element. Different penalty functions are used to suppress both defects. . . . .	117
5.16	Tangent smoothing for 1D line elements (a) and normal smoothing for 2D surface elements (b). . . . .	119
5.17	Free-Form Deformation of a rectus femoris muscle. The mesh of the muscle is embedded as a slave mesh in a simple host mesh. Material points on the slave mesh are fitted to data points by deforming the host mesh, which deforms the embedded slave mesh [178]. . . . .	120
5.18	PCA on 2D data. The longest of the principal components (in red) is the first and the orthogonal is the second. This length depends on the standard deviation in each direction. . . . .	121
5.19	Reconstruction of the PCA on 2D data using just the first principal component. . . . .	123
5.20	Anterior and posterior views of the active shape model with its normals to material points (in red), along which the image gradient profiles are sampled. . . . .	124

5.21	Image profiles sampled normal to material points (a) and (b). On the left, the model with the corresponding normal is shown and on the right the average normalized gradient profiles. (a) corresponds to a point in the femoral head and (b) to the femoral shaft. Error bars show one standard deviation from the mean at each sample point. For the femoral head, the rise in value past the half-way point of the profile is due to the pelvis. The shaft shows a much cleaner profile with only soft-tissue on the side of the cortex. . . .	126
5.22	Partitioning regions on the femoral surface. (a) shows the Gaussian curvature of estimation at vertices, where hot colors (red) represent regions of high curvature and contrarily regions of low curvature are represented by cold colors (blue), and (b) shows the vertices classified by Gaussian curvature sign, where red and blue regions represent negative and positive curvatures, respectively. In both cases, left figure corresponds to posterior view and right figure to anterior view. . . . .	128
5.23	The ensemble femur mesh, composed by six region meshes. Region boundaries are shown in black and element boundaries in gray. Anterior view on the left and posterior view on the right [100]. . .	129
5.24	From left to right, anterior and posterior views of the template mesh of the femur. The 634 nodes are shown in red. . . . .	130
5.25	Posterior and anterior views of the data point cloud originated by the segmentation (in red) and the reference mesh. . . . .	130
5.26	Posterior and anterior views of the rigid scale aligned data point cloud (in red) and the reference mesh. . . . .	131
5.27	A segment of the boundary curve between the greater trochanter and the proximal shaft regions in blue, with the boundary nodes in red. One to one correspondence between both meshes and the curve nodes ensures continuity when assembled. . . . .	132
5.28	Posterior and anterior views of the coarsely fitted reference mesh to the data point cloud (in red). . . . .	133
5.29	Posterior and anterior views of the final result of the fitting of the aligned data point cloud (in red) and the reference mesh. . . . .	133
5.30	Aligned ensemble meshes fitted to the segmented data. These were the 30 femurs that were used to build the statistical shape model. . . . .	135
5.31	RMS distance between points sampled on the mesh and their closest data point, averaged across the training set, of the iterative fitting pipeline. Values are presented connected through the line in red with standard deviations of each step in black. Step 1 corresponds to the mean RMS error after the rigid-scale alignment. Step 2 shows the RMS error after the free-form deformation described above. Iterations 3 to 10 are part of the nodal fit. The errors gradually decrease with the step number. . . . .	136
5.32	Principal components of the femur shape model. (a) to (d) show shape variations along the first four principal components at $-2$ and $+2$ standard deviations. . . . .	137
6.1	Schematic overview of the ASM segmentation pipeline. . . . .	140

6.2	Manual initialization of the ASM segmentation. In (a), the manually extracted landmarks (in green), which correspond to easily identifiable anatomic prominences, are shown. (b) also features the landmarks together with shape reconstruction based on the SSM (in red). . . . .	141
6.3	ASM initialization pipeline. (a) shows the data cloud that represents the bone tissue region. The mean model (in red) is then translated and scaled to the image coordinate space (b) and the initial $k$ -D tree correspondence is shown in (c). The final result of the iterative fitting is shown in (d). . . . .	143
6.4	Surface prediction along a sampled profile in the ASM segmentation. A 1D profile of length $2(l + l')$ is sampled from the image and portions of length $2l$ are used to calculate the Mahalanobis distances against the LAM to quantify its likelihood of being from the object surface. . . . .	145
6.5	Error correction for the ASM segmentation. (a) shows femoral head with erroneous predictions (in red) that are corrected in (b). . . .	146
6.6	Achieved ASM segmentation example, initiated by the proposed method. . . . .	147
6.7	Examples of the contours generated by thresholding the dataset at the suggested values. (a) is located at mid-shaft, where the linea aspera is visible, and (b) is located in the distal shaft, hence the higher section area. . . . .	148
6.8	Anterior and posterior views of a segmented femur, in beige with 50% opacity, and its correspondent medullary canal in red. . . . .	149
6.9	ASM initialization comparison: manually extracted landmarks (red) and the proposed method (green). (c) shows a superimposition of both shapes. . . . .	151
6.10	Multiple views of an example of a femur ASM segmentation. In (a) the whole femur geometry is represented and in (b) the femoral epiphysis are represented. . . . .	152
6.11	Anterior and posterior views of a ASM segmentation example initiated by the proposed method of a 'UZ Gent' image. Manual segmentation is represented in beige and the obtained result is represented in red. . . . .	153
6.12	RMS error in mm. (a) is the distance mapping between the result of the proposed method and the manually segmented femur and (b) is the opposite. . . . .	154
6.13	RMS error plotting of four segmented femurs (a-d) by the proposed method to the corresponding manually segmented femur, assumed to be the ground truth. Scale goes from cold to hot colors and maximum Hausdorff distance (HD) value is again 4.336 mm. . . .	155
6.14	Two examples of mesh defects in the proximal (a) and distal (b) femur. . . . .	156
6.15	Low resolution femur segmentation. (a) shows an axial slice of the dataset 'Patient 1' in the 'Quadrantes' image group. (b) and (c) illustrate the manual and automatic prediction of the femoral head boundaries, respectively. The whole femur is shown next to a detailed view of the head surface. . . . .	157

6.16	Anterior and posterior views of two ASM segmentation examples initiated by the proposed method on the 'Quadrantes' image. Manual segmentation is represented in beige and the obtained result is represented in red. . . . .	158
6.17	RMS error distances measured on patient 4 in mm. (a) is the distance mapping between the result of the proposed method and the manually segmented femur and (b) is the opposite. Hausdorff distance was 7.43 mm. . . . .	159
6.18	RMS error of the automatically segmented femurs of patient 2, where slice spacing was 7 mm. From left to right, the figure shows the anterior and posterior view of the RMS error plotted over the whole femur surface and femoral head and the condyle region in detail, where the RMS error is the highest. Scale goes from cold to hot colors and maximum value is 10 mm, slightly over slice thickness.	160
7.1	Principal axes of inertia of a femur model, respectively frontal, lateral and bottom views. For labeling simplifications, the RL, AP and DP axes will be respectively referred to as $x$ , $y$ and $z$ . . . . .	166
7.2	Anterior and posterior views of the femoral diaphysis medial axis. The axis (in blue) is the principal mode of variation of the medial points (in red) of the centroids obtained by cross-sectioning the femoral shaft along the inferior-superior direction. . . . .	167
7.3	Anterior and posterior views of the prosthesis insertion axis and the cavity isthmus. The axis (in blue) is the principal mode of variation of the medial points (in red) of the medullary canal (in green). The isthmus (in yellow) is defined as the minimum cross-section area of the cutting planes along the prosthesis insertion axis. . . . .	167
7.4	Posterior view of the proximal femur. In (a) the smallest cross section of the femoral neck is shown in blue. The red line shows the normal vector of the slicing plane, positioned at the center of the cross-section. In (b) the sphere fitted to the femoral head is shown in green. The red lines show the normal of the vertices considered for the fitting and the yellow mark at the center of the femoral head represents the geometrical center of the fitted sphere, also assumed the center of the femoral head. . . . .	169
7.5	Posterior view of the femur and the femoral neck axis (FNA) shown in red. . . . .	169
7.6	Lesser (left) and greater (right) femoral trochanters shown in yellow. The extraction algorithm starts in a automatically predicted point and segments the surface mesh perpendicularly to a given normal as shown in red. The normals are $\mathbf{n} = (0, 0, -1)$ for the lesser trochanter (left) and $\mathbf{n} = (1, 0, 1)$ for the greater trochanter (right).	170
7.7	Extraction of the femoral neck saddle point. The minimal femoral neck cross-section perimeter is shown in blue and the neck saddle point, shown in red, is considered to be the point with the highest value in the $z$ axis. . . . .	171



7.8	The femoral neck-shaft angle $\alpha$ is represented in (a). It is the angle around the yellow intersection point of the FNA (in red) and the FMDA (in blue). This measure is clinically relevant as it diagnosis coxa vara and coxa valga abnormalities. Similarly, the anteversion angle $\beta$ is shown in (b). It is the angle around the intersection (in orange) of the condylar axis (in blue, a parallel axis is shown for better visual understanding) and the FNA (in red). For visualization purposes, the proximal femur is represented in green and the femoral shaft and distal femur in yellow. . . . .	172
7.9	Posterior views of the proximal femur. The femoral offset (in yellow) is defined as the distance along the femoral neck axis (in red) between the anatomical center of the femoral head and its intersection with the FMDA (in blue). The limits of the femoral offset are also shown in yellow. . . . .	173
7.10	Posterior views of the proximal femur. Three planned osteotomy cutting planes are visible. As a reference, the saddle point of the femoral neck (in red) and the cutting plane perpendicular to the femoral neck axis (in white). The cutting planes shown in yellow are 2 cm deviated from the saddle point in both senses of the left-right direction and their normal is 6 degrees deviated from the reference cutting plane, respectively. . . . .	174
7.11	From left to right, DePuy Synthes TRI-LOCK <sup>®</sup> Bone Preservation Stem, the Zimmer <sup>®</sup> VerSys Epoch <sup>®</sup> FullCoat Hip System, the Zimmer <sup>®</sup> MS-30 <sup>TM</sup> stem and the the Zimmer <sup>®</sup> Mayo <sup>®</sup> Conservative Hip Prosthesis. The first row shows the computational models of the prosthesis and the second row shows their corresponding real aspect. . . . .	175
7.12	Meshing of an oval implant cross-section. The exterior part is meshed using receding front method and the interior part is using a grid-based algorithm. This way, distorted elements such as the one highlighted in red are avoided in the contact surface which is the external boundary in this case. . . . .	178
7.13	Meshing of the DePuy Synthes TRI-LOCK <sup>®</sup> Bone Preservation Stem, increasing its discretization from left to right. . . . .	178
7.14	Meshing of the DePuy Synthes TRI-LOCK <sup>®</sup> Bone Preservation Stem and the femur. . . . .	179
7.15	Cross-section of the femur-implant coupling in the femoral shaft. The meshing of implant stem was done combining the receding front method around a grid-based center. The femur was meshed using a receding method approach. The medullary cavity is represented with an higher intensity in the gray-scale. Elements have material properties according to the domain they belong to: implant, medullary cavity or cortical bone. . . . .	179
7.16	From left to right: posterior, left, anterior and right views of an example of a DePuy Synthes TRI-LOCK <sup>®</sup> implant fitting to a patient-specific femur. The femur is represented in translucent black with the center of the femoral head in black. The implant and the medullary cavity are shown in blue and green, respectively. In red, the prosthesis neck axis is visible. . . . .	180

7.17	From left to right: posterior, left, anterior and right views of an example of a VerSys Epoch <sup>®</sup> FullCoat Hip System fitting to a patient-specific femur. The femur is represented in translucent black with the center of the femoral head in black. The implant and the medullary cavity are shown in blue and green, respectively. In red, the prosthesis neck axis is visible. . . . .	181
7.18	From left to right: posterior, left, anterior and right views of an example of a Zimmer <sup>®</sup> MS-30 <sup>™</sup> implant fitting to a patient-specific femur. The femur is represented in translucent black with the center of the femoral head in black. The implant and the medullary cavity are shown in blue and green, respectively. In red, the prosthesis neck axis is visible. . . . .	181
7.19	From left to right: posterior, left, anterior and right views of an example of a Zimmer <sup>®</sup> Mayo <sup>®</sup> implant fitting to a patient-specific femur. The femur is represented in translucent black with the center of the femoral head in black. The implant and the medullary cavity are shown in blue and green, respectively. In red, the prosthesis neck axis is visible. . . . .	182
7.20	Examples of hexahedral meshes of two different patient's femurs, (a) and (b), coupled with the DePuy Synthes TRI-LOCK <sup>®</sup> Bone Preservation Stem. . . . .	182
7.21	Examples of contact pressure (in MPa) on the interface of the implant resulting from the FE analysis of two different implant sizes. Implant 1, shown in (a), accounts for size 12.5 and implant 2, respectively shown in (b), stands for size 12. . . . .	183
7.22	Examples of the tangential displacement (in mm) on the interface of the implant resulting from the FE analysis of two different implant sizes. Implant 1, shown in (a), accounts for size 12.5 and implant 2, respectively shown in (b), stands for size 12. . . . .	183

# List of Tables

2.1	Range of movement in the hip joint [2]. . . . .	23
2.2	Summary of material selection for THA components. . . . .	46
2.3	Summary of the most important advantages and disadvantages of tribological couplings in THA [1]. . . . .	50
3.1	Intervals in the Hounsfield scale for the most common tissues in the human body [77]. . . . .	57
3.2	Comparison of shape descriptors available in the literature. . . . .	70
3.3	Brief description of the advantages and disadvantages of the segmentation techniques here reviewed. . . . .	88
4.1	'Quadrantes' CT scans parameters. Distances are shown in millimeters. . . . .	91
4.2	'UZ Gent' CT scanner parameters. . . . .	93
4.3	CT scanner parameters for the cadaveric femurs acquisition. . . . .	97
5.1	Averaged fitted RMS errors for each of the steps in the fitting pipeline.	134
5.2	Percentage significance of the first four principal components of the femur shape model. . . . .	134
6.1	Averaged fitted RMS errors for the the proposed initialization method and the manual initialization, in mm. . . . .	150
6.2	Processing times for femur segmentation of the proposed method and others found in the literature. . . . .	151
6.3	Averaged RMS error, Hausdorff Distance (HD) and Mean Dice Coefficient of the proposed method against three other found in the literature. . . . .	154
6.4	Classification of the segmentation results together with the number of occurrences verified for each category. . . . .	156



# Acronyms

**1D** One Dimensional.

**2D** Two Dimensional.

**3D** Three Dimensional.

**AAM** Active Appearance Model.

**ASM** Active Shape Model.

**CHT** Circle Hough Transform.

**CoC** Ceramic-on-Ceramic.

**CoCrMo** cobalt-chromium-molybdenum.

**CT** Computerized Axial Tomography.

**CTCS** Computed Tomography Imaging Coordinate System.

**DICOM** Digital Imaging and Communications in Medicine.

**FAI** Femoroacetabular Impingement.

**FE** Finite Element.

**FFD** Free-Form Deformation.

**FMDA** Femoral Middle Diaphysis Axis.

**FNA** Femoral Neck Axis.

**GHT** Generalized Hough Transform.

**GPA** Generalized Procrustes Analysis.

**HD** Hausdorff Distance.

**HRS** Hip Resurfacing Surgery.

**HT** Hough Transform.

**HU** Hounsfield Unit.

**ICA** Independent Component Analysis.

**ICP** Iterative Closest Point.

**ISB** International Society of Biomechanics.

**ITK** Insight Segmentation and Registration Toolkit.

**JCS** Joint Coordinate System.

**LAM** Local Appearance Model.

**MDL** Minimum Description Length.

**MoM** Metal-on-Metal.

**MoP** Metal-on-Polyethylene.

**MRI** Magnetic Resonance Imaging.

**NURBS** Non-Uniform Rational Splines.

**OA** Osteoarthritis.

**OECD** Organisation for Economic Co-operation and Development.

**OP** Osteoporosis.

**PCA** Principal Component Analysis.

**PDM** Point Distribution Model.

**PMMA** Polymethyl Methacrylate.

**PPM** Piece-wise Parametric Mesh.

**RCS** Reference Coordinate System.

**RMS** Root Mean Square.

**SDF** Signed Distance Function.

**SPHARMs** Spherical Harmonics.

**SSA** Statistical Shape Analysis.

**SSM** Statistical Shape Model.

**SVD** Singular Value Decomposition.

**THA** Total Hip Arthroplasty.

**UHMWPE** Ultra High Molecular Weight Polyethylene.

# Chapter 1

## Introduction

This doctoral thesis presents a fully automated pipeline for the planning of the Total Hip Arthroplasty (THA), i.e., the surgical replacement of the hip joint with a prosthetic joint, in a reconstructive procedure that allows the restoration of the patients' anatomical gait cycle. The presented pipeline starts by automatically segmenting the femur morphology based on an Active Shape Model (ASM) from a x-ray Computerized Axial Tomography (CT) scan of the patient. The statistical shape modeling contemplates a population of 91 CT datasets of high resolution from the University Hospital of Ghent as well as 5 other datasets of lower resolution from the Quadrantes medical clinic in Lisbon. The ASM segmentation converged automatically in 98% of the cases. Moreover, a toolbox to optimize the sizing and alignment of the implants to the patient-specific femur is presented.

This chapter will present the motivations for this work, address its aims and scope, enumerate its contributions and present a review of the structure of this thesis.

### 1.1 Motivation

Every year, around one million patients worldwide undergo a THA surgery [1]. This surgery consists in the replacement of the anatomical hip joint with a prosthetic joint. With so, the often severely injured hip joint's functionality is restored and the patient regains pain-free mobility. Due to an ageing population, the amount of primary THA interventions tends to increase in the near future. Moreover, the decreasing average age of the first intervention combined with the limited lifespan of hip prostheses, leads to an increase of a second intervention that takes place whenever the prosthetic joint needs repairing or substitution. This second intervention depends on the amount of bone tissue remaining after the removal of the first implant which is often very reduced. Therefore the risks and cost of the surgical intervention are increased.

Even if it is among the safest and most cost-effective medical interventions, there is still a part of its success that is inherently attached to the surgeon's expertise and practice. The surgery is significantly invasive and the recovery process is slow. Furthermore, the guidelines for implant insertion described in its brochure are often based on anatomical landmarks which are sometimes hard to locate intraoperatively. This gives way to an often empiric approach to

the intervention and frequent unnecessary trial-and-error cavity reaming, for example.

Recent developments in medical imaging allow the three dimensional reconstruction of the patient-specific anatomy. The proliferation of CT imaging in the last 20 years provides a cost and time effective insight into the patients' bone structures. Understanding the hip joint morphology is of significant interest in subjects such as anthropology, forensics and clinical medicine. More specifically, it can provide the basis for a computational framework for THA planning. Parameters such as femur length or the medullary cavity size can be used to presurgically estimate the size of the implant. The surgical prosthesis placement can be done according to the previously neck-shaft or anteversion angles of the femur and in this way compensate such deviations in order to maintain leg length and the hip center of rotation.

However, both three dimensional computational recreation of the patient-specific hip joint, also known as segmentation, and the location of key landmarks for prosthesis placement are time consuming and non repeatable, besides requiring an extensive anatomical and mathematical knowledge. Statistical shape analysis has been using computer graphics and machine learning methods to interpret imaging data for some time now. These can be used to classify, characterize or even predict geometries and thus be essential for the automation of the segmentation process and extraction of anatomical landmarks for prosthesis insertion and orientation guidance.

The clinical long-term outcome of the THA also depends on factors related to the applied type of prosthesis. There are several complications inherent to the fabrication, the design and the materials of hip implants. The history of the THA and the constant evolution of the implants design and fabrication have led to a considerable amount of commercially available alternatives. The implant is the most determining factor on the final cost of the intervention. The computational modeling of the implants and its placement on the patient-specific anatomy can provide important information on the performance of the different commercially available implants and therefore be of considerable value in a THA planning.

The development of a pipeline that automatically recreates the patient-specific anatomy computationally along with a set of tools that allow previously modeled implant placement and their performance comparison can be determining in the outcome of the THA. The surgeon would be provided with *a priori* quantitative information about the risks attached to each of the implants and therefore better prepared to choose which implant to use and ultimately reduce the cost and risk of the intervention.

## 1.2 Problem definition

The development of a computational framework for real-time THA planning to be used by medical doctors has a series of issues attached to it that needs further discussion. Firstly, the user interface should be simple and intuitive, so that the user does not need to understand the methodology behind the femur segmentation or landmark extraction. It is also important that the tasks performed are time and cost effective, in order for the user to experience a real-time experience on a regular processing unit, such as a laptop. Automation of



the pipeline is a demanding task due to the great variability of the input data, but also essential in order to achieve a toolbox with good usability.

The first problem is to define a three dimensional model of the femur of the patient from medical imaging data, such as CT scan image stacks. This task should be fully automated and unsupervised. A statistical shape analysis approach can be used to surpass these challenges and can be used to characterize a population of femurs. The segmentation of the femoral bone should take in account the definition of the medullary cavity of the femur as it is where the implant stem is fixated and hence where the majority of the load of the gait cycle is concentrated.

Secondly, a standardized coordinate system for the population of femurs should be defined so that the key anatomical landmarks are extracted without any user interaction. Methods should be developed in order to estimate the common femoral measurements, namely the shaft or neck axis or the neck-shaft or anteversion angles. These can provide the basis for the diagnostic of excessively anteverted or retroverted femurs.

Lastly, a review of the commercially available prosthesis should be done in order to understand and model the most significant implants used in THA. The problem of femur-implant coupling should be addressed and an automated pipeline based on the experience of the orthopedic surgeons and the implants brochure should be implemented. The finite element mesh generation of the coupling of the sized and oriented implant and the patient-specific femur should also be looked into in order to perform a quantitative analysis of the performance of such coupling.

The thesis will focus on these three tasks and provide the necessary tools to the surgeon in order to help a THA planning in an effective way. The developed methodology should be robust and precise as it is ultimately intended to be used in clinical practice.

### 1.3 Novel Contributions

The pipeline presented in this thesis intends to solve the problems defined in previous section 1.2. Within this section, the achievements of this doctoral work and its novel contributions will be listed.

- Fully automatic, unsupervised and time-effective femur segmentation from CT-scan images based on ASM, in a way that makes it possible to integrate in an interactive surgery planning software.
- Medullary cavity and endosteal definition, so that the optimization of the size and design of the femoral stem of the implant is possible.
- Statistical modeling of a large population (218) of femur models which allowed the characterization of the size and shape of the femoral anatomy of the population with the identification of its main modes of variance.
- A novel computationally effective shape and pose estimation of the femur in the CT image domain is presented, which is used for the placement of the ASM template femur and ultimately optimizes the iterative segmentation process.
- A standardized coordinate system is presented for the femoral anatomy which allows the automatic landmark extraction on femoral surface meshes.

- The modeling of commercially available hip joint implant systems was conducted, establishing a database of computational representations of such which will allow their shape and design comparison.
- An algorithm based on the orthopedic surgeons pipeline for prosthesis placement was virtually recreated and allows the automatic prosthesis sizing and placement, including orientation, optimization based on the patient-specific proximal femur anatomy.
- Fully automatic finite element mesh generation of the femur-implant coupling with hexahedral elements so that a quantitative analysis of the performance of the different implants can be compared for the same proximal femur anatomy. This will provide guidance and reduce the time of the THA, consequently reducing the cost and risk of the surgical intervention.

## 1.4 Thesis overview

The remainder of this thesis extends over seven more chapters that will be briefly described within this section. The three dimensional model generation from CT-scan images is composed of two phases: training and segmentation, as seen in Figure 1.1.

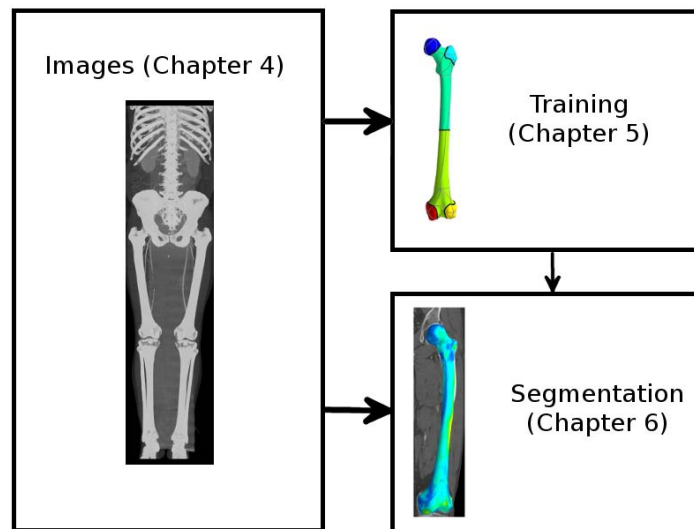


Figure 1.1: Main steps of the automatic femur segmentation pipeline and their corresponding chapters.

The training phase involves designing a femur mesh and training a femur statistical shape model. The segmentation phase is the application of the statistical model to medical imaging in order to define the in-image femur using a three dimensional shape descriptor.

The prosthesis modeling and standardized coordinate system definition is addressed in the following chapter and illustrated in Figure 1.2.

The THA planning addresses the problem of prosthesis sizing and placement taking in account several measured femoral axis and angles.

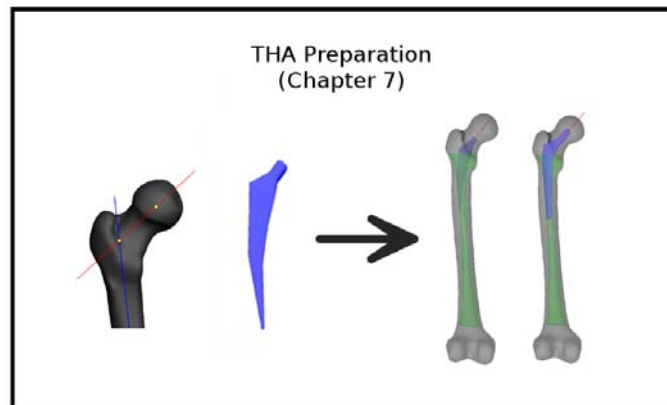


Figure 1.2: Main steps of the THA planning framework and its corresponding chapter.

In sum, the remainder of thesis is organized as follows: chapter 2 presents an introduction to the anatomy, kinematics and complications of the hip joint, as well as a detailed look into the THA: its history, incidence, the surgical procedure, the state of the art of its planning and the types of implants used; chapter 3 will thoroughly address the problem of femur segmentation, presenting the basis of medical image acquisition, an extensive literature review and a detailed insight on the proposed methods; in chapter 4 the images that served as basis for the development of the pipeline are analyzed, and the background of the demographics of the population is looked into; chapter 5 will focus on the definition of a shape descriptor and shape correspondence for the population of femurs, in order to statistically train a model capable of automatically segment new femurs; chapter 6 describes the testing and validation the segmentation pipeline proposed in this thesis; the description of the THA planning here proposed is looked into in chapter 7, where the problems of implants modeling, optimized fitting in the patient-specific femur and finite element mesh generation are addressed; lastly, chapter 8 concludes the thesis by summarizing the design and implementations of the pipeline and discussing the directions of future work.

## 1.5 Publications

Throughout the development of the doctoral work presented in this thesis, the following papers have been published. The list of scientific conferences attended is also present in this section.

### 1.5.1 Papers in peer-reviewed journals

1. Diogo F. Almeida, Rui. B. Ruben, João Folgado, Paulo R. Fernandes, Emmanuel Audenaert, Benedict Verhegghe, Matthieu de Beule. “Fully Automatic segmentation of femurs with medullary canal definition in high and in low resolution CT scans”, *Medical Engineering and Physics* 38.12 (2016): 1474-1480.

2. Diogo F. Almeida, Rui. B. Ruben, João Folgado, Paulo R. Fernandes, João Gamelas, Benedict Verhegghe, Matthieu de Beule. “Automated femoral landmark extraction for optimal prosthesis placement in total hip arthroplasty”, *International Journal For Numerical Methods In Biomedical Engineering*. Accepted on the 14<sup>th</sup> September 2016, available online.
3. Diogo F. Almeida, Rui. B. Ruben, João Folgado, Paulo R. Fernandes, Matthieu de Beule, Benedict Verhegghe, “Automatic Hexahedral Finite Element Mesh Generation for Total Hip Arthroplasty”, *International Journal For Numerical Methods In Biomedical Engineering*. Elsevier. In preparation.
4. Diogo F. Almeida, Rui. B. Ruben, João Folgado, Matthieu de Beule, Benedict Verhegghe, “Orthosoft: A Total Hip Replacement Toolbox”, *International Journal of Computer Assisted Radiology and Surgery*. In preparation.

### 1.5.2 Conference Proceedings

#### International Conference Proceedings

1. Diogo F. Almeida, João Folgado, Paulo R. Fernandes, Rui B. Ruben, “Development of an Automated Procedure for a Patient Specific Segmentation of the Human Femur Body from CT Scan Images”, III ECCOMAS Thematic Conference on Computational Vision and Medical Image Processing – VIP IMAGE 2011, pp. 355-359, Olhão, Portugal, 12-14 October, 2011.
2. Diogo F. Almeida, Rui B. Ruben, João Folgado, Paulo R. Fernandes, “Development of an Automated Procedure for a Patient Specific Segmentation of the Femur Body”, *Journal of Biomechanics* Vol. 45 Supplement 1, Page S458, 18th Congress of the European Society of Biomechanics, Lisbon, Portugal, 1-4 July, 2012.
3. Diogo F. Almeida, Rui B. Ruben, João Folgado, Paulo R. Fernandes, “Histogram Based Threshold Segmentation of the Human Femur Body for Patient Specific Acquired CT Scan Images”, *CompIMAGE 2012 Computational Modelling of Objects Presented in Images: Fundamentals, Methods and Applications*, pp. 281-284, Rome, Italy, 5-7 September, 2012.
4. Diogo F. Almeida, Rui B. Ruben, João Folgado, Paulo R. Fernandes, “A Patient-Specific Automatic Segmentation Of The Femur Bone Based In 3D Active Contours.”, *Proceedings of the 19th Congress of The European Society of Biomechanics*, Patras, Greece, 25-28 July, 2013.
5. Diogo F. Almeida, João Folgado, Paulo R. Fernandes, Rui B. Ruben, “3D Shape Prior Active Contours for an automatic segmentation of a patient specific femur from a CT Scan”, *Proceedings of the III ECCOMAS Thematic Conference on Computational Vision and Medical Image Processing: VipIMAGE 2013*, ISBN: 9781138000810, pp: 271-275, Taylors and Francis.

6. Diogo F. Almeida, Rui B. Ruben, João Folgado, Paulo R. Fernandes, Matthieu de Beule, Benedict Verhegghe, “Hip Arthroplasty preparation: From CT-Scan to Patient-Specific FE Analysis”, Proceedings of the 7th World Congress of Biomechanics, Boston (USA), July 6-11, 2014.
7. Diogo F. Almeida, Rui B. Ruben, João Folgado, Paulo R. Fernandes, Matthieu de Beule, Benedict Verhegghe, “A Total Hip Replacement Toolbox: From CT-Scan to Patient-Specific FE Analysis”, Proceedings of the 21st Congress of The European Society of Biomechanics, Prague, Czech Republic, 5-8 July, 2015.

### **Portuguese Conference Proceedings**

1. Diogo F. Almeida, Rui B. Ruben, João Folgado, Paulo R. Fernandes, “Segmentação da Diáfise do Fémur por Threshold Segmentation para Apoio à Artroplastia Total da Anca”, 4º Congresso Nacional de Biomecânica, pp. 445-448, Coimbra, 4-5 February, 2011.
2. Diogo F. Almeida, João Folgado, Paulo R. Fernandes, Rui B. Ruben, “Segmentação da Diáfise do Fémur por Threshold Segmentation para Apoio à Artroplastia Total da Anca”, Congresso de Métodos Numéricos em Engenharia – CMNE 2011, p. 419, Coimbra, Portugal, 14-17 June, 2011.
3. Diogo F. Almeida, Rui B. Ruben, João Folgado, Paulo R. Fernandes, “Segmentação do Fémur com Recurso a Contornos Activos para Apoio à Artroplastia Total da Anca”, 5º Congresso Nacional de Biomecânica – Livro de Resumos, pp. 343-344, Espinho, 8-9 February, 2013.
4. Diogo F. Almeida, Rui B. Ruben, João Folgado, Paulo R. Fernandes, Matthieu de Beule, Benedict Verhegghe, “Total Hip Replacement Preparation: A Framework For Femur And Prosthesis Coupling”, 6º Congresso Nacional de Biomecânica – Livro de Resumos, pp. 297-298, Monte Real, 6-7 February, 2015.



## Chapter 2

# Acetabulofemoral Joint Morphology

Acetabulofemoral joint morphology is the study of the joint form, its constituting anatomical entities and their shape and internal structure. The hip joint is supported by stable ligaments that ensure steadiness while standing and relieve the muscle groups on the buttocks. The replacement of this joint is the main focus of this thesis, so an understanding of its biomechanics, kinematics and physiology is helpful for the comprehension of the arthroplasty procedure. This chapter presents the conventional understanding of the pelvic bone and the femur, as well as their interaction, and the pathological complications that may occur.

### 2.1 Terminology

It is important at this point to familiarize the reader with the anatomical terminology. Hence, Figure 2.1 is important to illustrate the anatomical terms of motion and planes of reference that are used throughout the thesis to locate the anatomical structures and landmarks.

### 2.2 Hip Joint Anatomy

More commonly known as hip joint, it is the joint that connects the femur to the acetabulum of the pelvis. The hip region is located lateral and anterior to the gluteal region, inferior to the iliac crest, and overlying the greater trochanter of the femur, as seen on detail in Figure 2.2.

It is considered to be a synovial joint, which is distinguishable from cartilaginous and fibrous joints by the existence of capsules surrounding the articulating surfaces and the presence of the fluid within these capsules, as observable in Figure 2.3. This is the type of joint that allows the widest range of movements to the connecting bones. Moreover, it is also considered a spheroidal joint, also known as ball and socket joint, due to the morphology of the bone regions that define this joint: the cup-like cavity on the acetabulum of the pelvis and the ball-shaped head of the femur. This allows the distal bone motion around an indefinite number of axis around a common center and thus allowing the bone to move in almost every direction. Along with the shoulder joint, they're

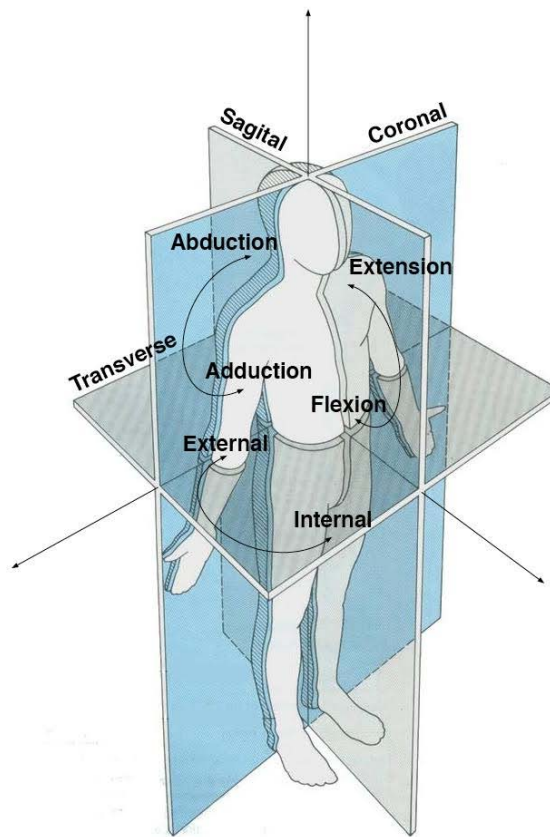


Figure 2.1: Anatomical planes and terms of motion.

considered enarthrosis due to the fact that the socket covers the sphere beyond its equator clearly as one can see in Figure 2.3.

The articular surfaces are the femoral head, and the concave surface of the pelvic bone, commonly known as acetabulum or cotyloid cavity, augmented by the labrum. The head of the femur represents two thirds of a sphere and has a small depression under its center, known as the fovea of the head of the femur, where the ligament of head of femur attaches (Fig. 2.4). The acetabulum is the result of the junction of three distinct bones of the *coxae*: the ischium, the ilium and the pubis. It is bounded by a prominent uneven rim, thick and strong above, that serves as attachment to the acetabular labrum. The labrum presents a non-articular quadrilateral portion at the end of the cavity named *fossa acetabuli* and an articular peripheral portion, the *facies lunata*. These structures can be identified in Figure 2.5.

The head of the femur presents an hyaline cartilage coating with maximum thickness at the center of the head and decreasing as we go further from the center (Fig. 2.4). On the other hand, the acetabulum cartilage coating varies contrary to the femoral head. These cartilages are soft and resistant allowing very low friction between the two surfaces which consequently minimizes the wear of the joint. The cartilage's functionality extends to load bearing and



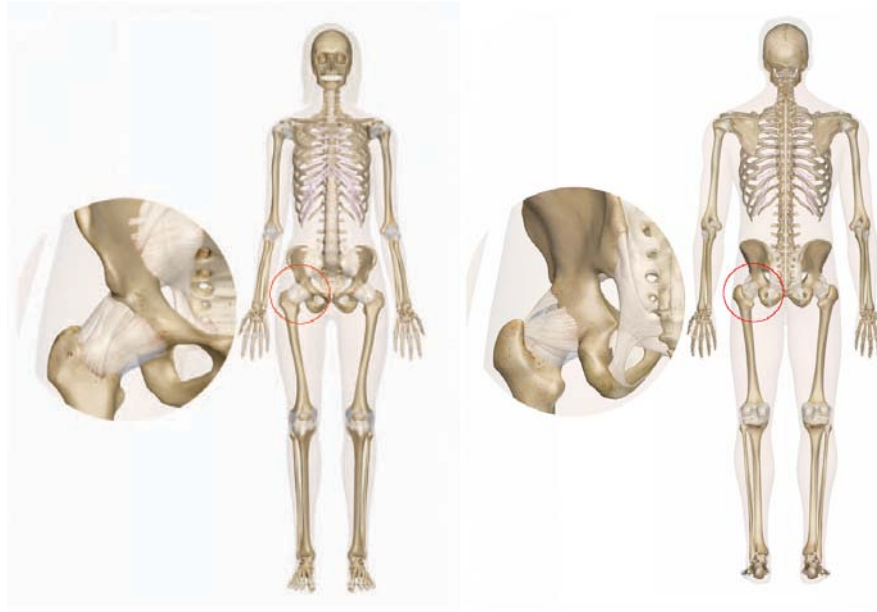


Figure 2.2: Location of the human hip joint relatively to other bones of the human skeleton, anterior and posterior views respectively. Adapted from innerbody.com

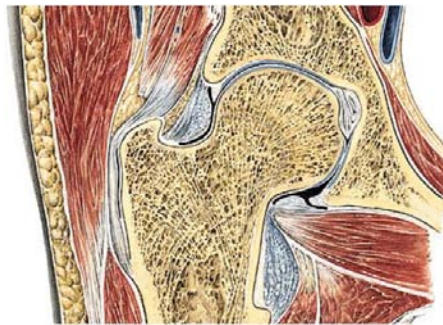


Figure 2.3: Schematic representation of the coronal view of the hip joint [2].

shock absorption due to its material properties. They result from a combination of three principal phases: a solid phase, mainly formed by type 2 collagen fibers; a fluid phase, of which 80% is water and interstitial fluid; an ion phase of dissolved electrolytes. The solid matrix and the interstitial fluid are incompressible and because they are encapsulated by the labrum, they carry a good portion of the load.

The labrum is a fibrocartilaginous rim that circumscribes the cotyloid cavity. It resembles a C-shaped structure with an opening antero-inferiorly at the site of the acetabular notch, where it is bridged by the transverse ligament. Elsewhere it is attached to the margins of the acetabulum. The labrum is thickest postero-superiorly and widest antero-superiorly and has a triangular cross-section. Its biomechanical role is yet to be fully determined but it is

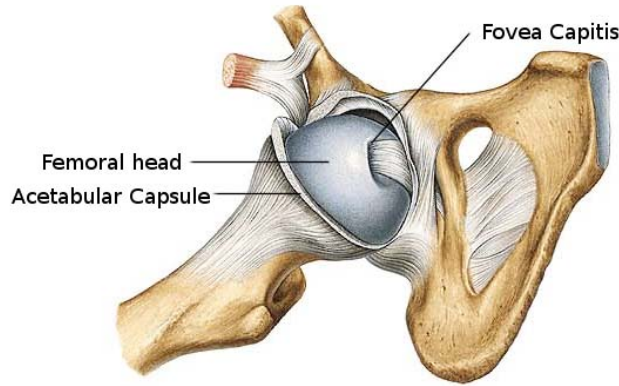


Figure 2.4: Ventral view of the right side of a partial opening of the hip joint [2].

known that it deepens the acetabulum for increased stability and force dissipation. In addition, it functions as a sealing rim. With compression, fluid is exuded from the cartilage increasing hydrostatic pressure between the two contact surfaces. This fact increases the synovial lubrication and provides added resistance to the joint distraction. Figure 2.5 shows a schematic representation of the opening of the acetabular capsule with complete exarticulation of the femoral head.

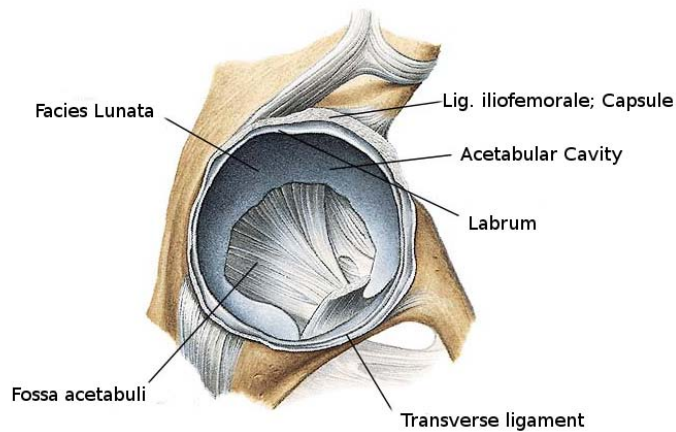


Figure 2.5: Schematic representation of the coronal view of the hip joint [2].

The hip joint stability is assured by the capsule with the help of a series of ligaments: the iliofemorale, the pubofemorale and the ischiofemorale are the external ligaments and are also attached to the ilium, pubis and ischium

respectively. All three strengthen the capsule and prevent an excessive range of movement in the joint. The intracapsular ligament, also known as ligamentum teres, is attached to a depression in the acetabulum (the acetabular notch) and a depression on the femoral head (the fovea of the head, visible on Figure 2.4) but lacks mechanical function in the joint. Instead, its function is to connect the head of the femur to the ischiopubic ramus and a small artery to the head of the femur, the foveal artery. The ligament transversum acetabuli inferiorly closes the acetabulum and together with the labrum serve to guide the femoral head.

The capsule of the hip joint is limited by the cotyloid cavity and the femur. It is fixed to the acetabular labrum in its major part but also to the transverse ligament on the pelvic side and around the neck of the femur on the femoral side. More extensively, it surrounds the neck of the femur, and is attached: in front, to the intertrochanteric line; above, to the base of the neck; behind, to the neck about 1.25 cm above the intertrochanteric crest; below, to the lower part of the neck, close to the lesser trochanter. The resistance of the articular capsule is not even, being softer and looser on the inferior and posterior part and stronger at the upper and forepart of the joint, where the longitudinal fibers are much thicker. Some of the fibers are circular, as seen on the annular ligament of Figure 2.6. These fibers are named zona orbicularis and form a collar around the neck of the femur.

The ligaments are displayed as follows: the iliofemorale attaches superiorly on the anterior inferior iliac spine and inhibits the extension and adduction of the lower limb; the pubofemorale ligament is located on the anterior inferior part of the joint and serves to inhibit extension, abduction and lateral rotation, the ischiofemorale ligament inhibits extension, medial rotation and adduction and is located on the posterior inferior part of the joint. Figure 2.6 shows a schematic representation of the ligaments of the hip joint. A more detailed explanation of the movements is part of section 2.5.2.

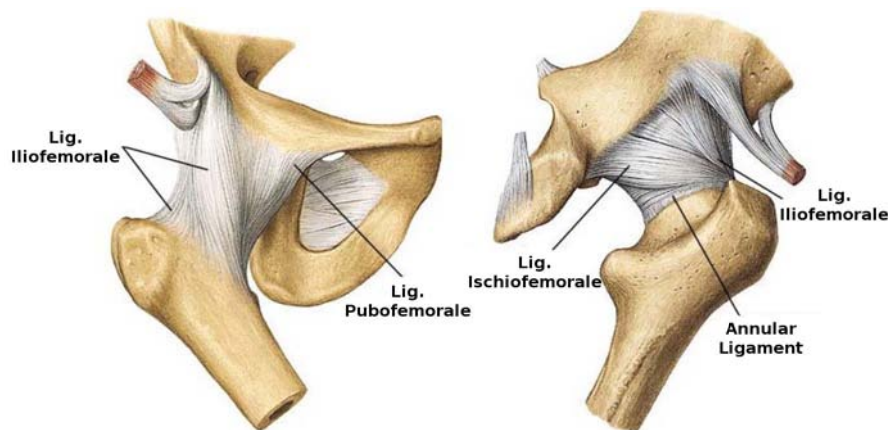


Figure 2.6: Schematic representations of the anterior and posterior views of the hip joint [2].

The synovial membrane is the soft tissue that is found between the articular capsule (joint capsule) and the joint cavity of synovial joints. The hip synovial

membrane is formed by the capsule and the lining of the round ligament of the femur and consist in vascularized connective tissue and are responsible for the secretion of the synovial fluid. This viscous and incompressible liquid lubricates the opposing and connecting bone surfaces of the joint. It is a combination of a low-level filtering of the plasma by the synovial membrane and the secretion of a mucopolysaccharide along with a small amount of proteins of high molecular weight by the cells of the membrane. This grants the fluid its characteristic viscosity and its yolk-like consistency. It acts as a lubricant of the joint, allowing the flattening of the articular surfaces and consequently the reduction of the friction coefficient. It is responsible for the smooth and painless hip joint motion of the individual. Such low friction coefficient remains unrivaled by any combination of materials of which hip prosthesis can be made of up to the present date [3].

### 2.3 Hip Bone Anatomy

The pelvic bone consists of three single bones which are connected by synostoses once human growth is completed: the ilium, the ischium and the pubis. It is connected dorsally to the sacrum and the coccyx, which are part of the spine, and inferiorly to the corresponding femur at the hip joint. The ring formed by the sacrum and both pelvic bones has differences between the genders: it resembles a heart in men and has a transverse oval shape in women [2]. Figure 2.7 shows the parts originated by the respective merged bone as well as the significant anatomical features.

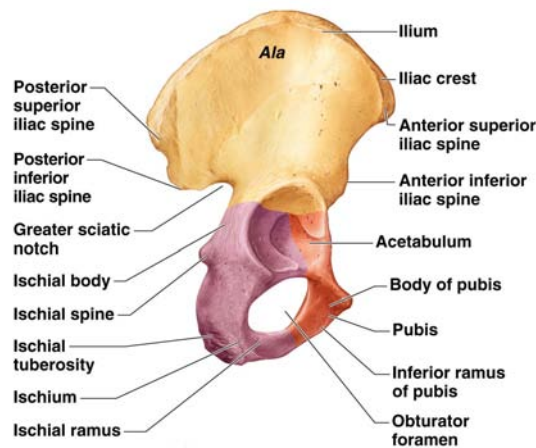


Figure 2.7: Schematic representation of the antero-lateral views of the pelvic bone [4].

The ilium is the uppermost and largest bone comprised in the hip bone. It makes up two fifths of the acetabulum, where the femoral head connects, and can be divided in two parts: the body and the ala. The body of the ilium forms the sacroiliac joint with the sacrum and the ala forms the S-shaped iliac crest easily tangible through the skin. The ischium forms the lower and posterior

part of the pelvic bone and is located below the ilium and behind the pubis. It's the most resistant of the three bones. It forms a large swelling, commonly known as ischial tuberosity, that supports most of the weight in a sitting stance as the gluteus maximus leaves it free. The pubis is the ventral and anterior part of the hip bone. It can be divided into two ramus, superior and inferior, and a body. The body is part of the acetabular cavity where the femoral head connects. The superior ramus forms a large opening through which nerves and blood vessels make way, called the obturator foramen, and the inferior ramus is thin and flat, located below the superior ramus and becomes narrower as it descends and joins the ischium.

## 2.4 Femur Anatomy

Also known as thigh bone, the femur is the most proximal bone of the leg in the human skeleton, which means it is the closest to the center of the body. It is also the longest and most stiff bone. Its shape is usually divided in three distinct parts, as shown in Figure 2.8: both extremities (proximal and distal femur) and the femoral shaft (diaphysis). It plays a substantial role in the lower limb locomotion and bears the weight of the upper body at rest. It enables prolonged standing without much effort and the ability to take larger steps, resulting in accelerated locomotion. Its outer limits are made of dense and stiff cortical bone and its interior is mainly filled with rod-like, spongy cancellous bone. Proximal and distal regions are part of the hip and knee joint and are partially covered in cartilage, as shown in Figure 2.8 magnified representation.

### 2.4.1 External Features

The following paragraphs present a more extensive description of the relevant anatomical features of each of the femur parts. These include articular joint surfaces, muscles and ligament insertion sites. Figure 2.9 shows a schematic representation of the femoral bone and its labeling.

The proximal femur covers the head, neck, both trochanters and adjacent less relevant structures. The head (epiphysis) is shaped as the greater part (2/3) of a sphere and articulates with the acetabulum of the pelvic bone. It is covered with flat and smooth cartilage to ease the friction on the hip joint. It features a small depression, the fovea capitis, where the round ligament connects the femur to the acetabular notch. The neck is roughly 4 to 5 cm long and extends from the femoral head, increasing in diameter, to the intertrochanteric line in an anterior part and to the intertrochanteric crest in the posterior part. The transition area between the head and the neck is where the hip joint capsule attaches. Simultaneously, the greater and lesser trochanter are found in this area. The great trochanter is the most lateral prominent feature of the femur and is where several muscles and tendons attach. The lesser trochanter is a cone-shaped extension of the lower part of the femur neck. The muscles responsible for the flexion and external rotation of the hip joint attach to its tip.

The body of femur (diaphysis) begins distal to the lesser trochanter and extends to the condyles at the distal femur. It has a cylindrical shape, slightly broader on its anterior side. It narrows as it descends and broadens again as it reaches the distal end. Some are moderately arched with the concavity facing

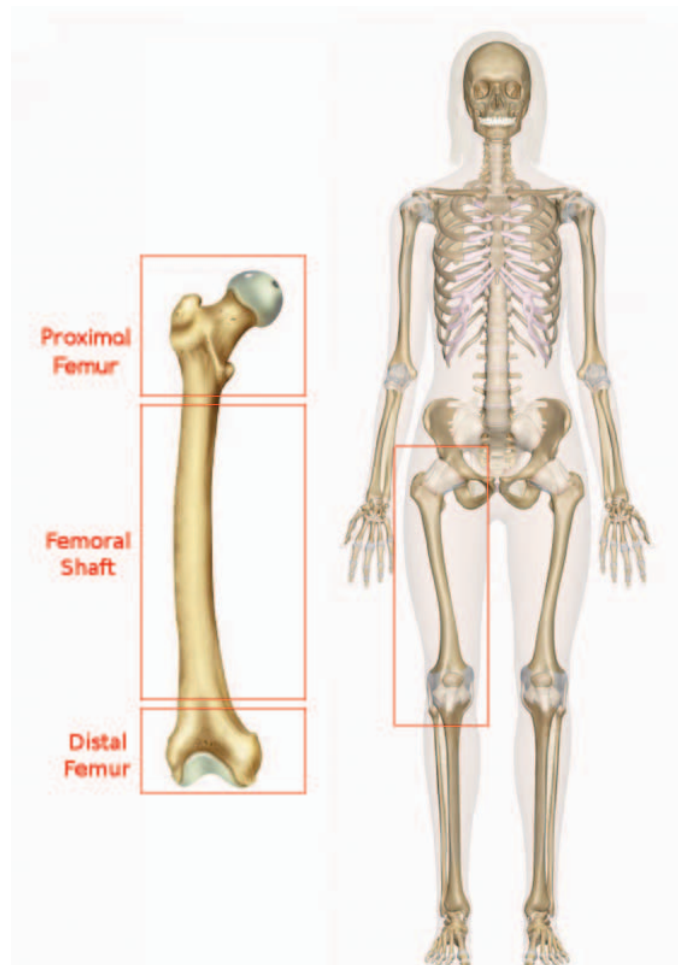


Figure 2.8: Schematic representation of the femur and its location in the human body. Courtesy of innerbody.com

the posterior side. The main feature of the shaft is a rough, prominent ridge along the posterior side of the shaft named *linea aspera*. It diverges proximally as the medial and lateral ridge: the lateral ridge becomes the gluteal tuberosity while the medial ridge continues as the pectilineal line. Distally, it diverges again into lateral and medial ridges which continue to the epicondyles. These ridged structures are mainly where the muscles attach the femur.

The distal femur encompasses the lateral and medial condyles and the distal metaphysis which, in its turn, consists in the epicondyles and the adductor tubercle. Due to the fact that it's part of the knee joint, the anterior, inferior and posterior sides of the condyles are covered in smooth cartilage. Anteriorly, the condyles are prominent features separated by a smooth shallow articular depression named patellar groove. On the other hand, the condyles present a much more considerable prominence and consequently a deeper notch in between called the intercondylar fossa, where both posterior and anterior cruciate ligaments attach. The lateral condyle is broader while the medial is longer. In

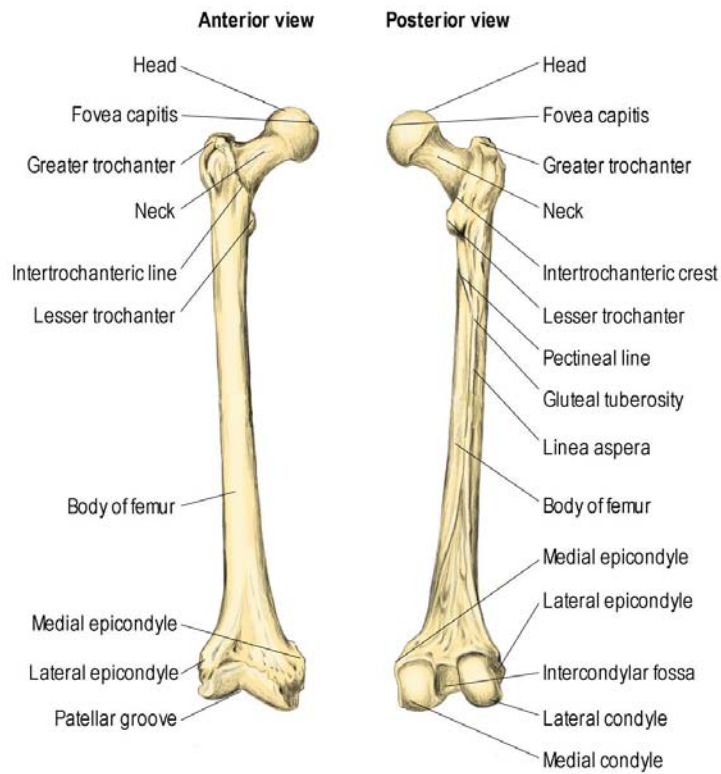


Figure 2.9: Major external anatomic features of the femur. Anterior and posterior views, respectively. Courtesy of innerbody.com

their natural oblique position, the lower surfaces of the two condyles lie practically in the same horizontal plane. The medial and lateral epicondyles are positioned on the sides of the respective condyles and serve mainly as attachments for muscles and ligaments.

### 2.4.2 Cortical and Cancellous Bone

Bone tissue usually refers to the matrix that forms the rigid sections of the bone and not to the organs, as they are made of marrow, blood vessels, epithelium and nerves as well. Structurally, it is divided in two types: cortical bone and cancellous bone. Cortical bone is more dense and compact while cancellous bone refers to a trabecular and spongy bone. Usually, the cortical bone forms the hard outer layer of the organ and cancellous fills the interior. These tissues are biologically similar but differ in the way their micro-structure is organized and their ratio may be altered as a response to mechanical stimulus [5].

The femur presents a dense cortical bone layer, also named cortex, forming the shell of the femur. Its thickness ranges from about 7 mm in the femoral shaft [6] to under 0.1 mm in the femoral head [7]. This is a very rough estimate as age and gender have a significant influence on the bone remodeling phenomena. These cortical and cancellous bone arrangement is what grants the femur its

resistance to bending and torsion. The cortex is the thickest around the shaft, specially at the *linea aspera* due to the attachment of the major thigh muscles and the bending moment in the coronal plane created by the femoral head under standing posture. Medial-side thickening extends to the inferior femoral neck where high compressive stresses occur. Cancellous bone is mainly found in the proximal and distal femur and basically it consists in an anisotropic lattice of trabecular bone elements in the shape of plates, rods and struts. The preferred direction for the arrangement of these plates coincides with the directions of principal stress, granting the bone an added stiffness in that direction [8]. This phenomena is noticeable in Figure 2.10.



Figure 2.10: Coronal cross section of the proximal femur. Dense cortical bone forms the outer shell to the spongy cancellous bone within. Cancellous bone displays distinctive anisotropic patterns coinciding with the directions of principal stress [8].

### 2.4.3 Endosteum and Periosteum

The femoral endosteum is a thin vascular membrane of connective tissue that lines the surface of the bony tissue that forms the medullary cavity of the femur. This endosteal surface is usually resorbed during long periods of malnutrition, resulting in less cortical thickness.

Similarly, the outer surface of a bone is lined by a thin layer of connective tissue that is very similar in morphology and function to endosteum. It is called the periosteum, or the periosteal surface. During bone growth, the width of the bone increases as osteoblasts lay new bone tissue at the periosteum. To prevent the bone from becoming unnecessarily thick, osteoclasts resorb the bone from the endosteal side. Figure 2.11 shows a schematic representation of the endosteum and the periosteum.

### 2.4.4 Traditional Measurements

Anatomists and morphophysiologicals have always been keen on the femoral shape, size, position, structure, blood supply and innervation of an organ such as the femur or the pelvic bone. Such knowledge provides a better understanding of its associated pathologies and what caused them. General measurements are usually calliper-like measurements or angles between anatomical axes. Conventionally, the measurements are taken on a femur on its anterior or posterior



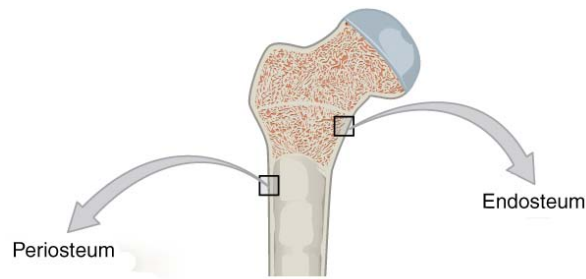


Figure 2.11: Schematic representation of the femoral endosteum and periosteum. Image of public domain.

side placed on a flat surface, with its shaft aligned horizontally. This section intends to present a guide to the terminology of the femoral measurements and considered axes. The following Figure 2.12 shows the traditional measured lengths and widths of the femoral bone. The long femur length measures the tip of the femoral head to the inferior side of the medial condyle (Fig. 2.12a) and the short femur length measures the superior tip of the greater trochanter to the inferior side of the lateral condyle (Fig. 2.12b) [9]. Widths are measured just below the lesser trochanter, at the saddle point of the shaft and between the condyles (Fig. 2.12c).

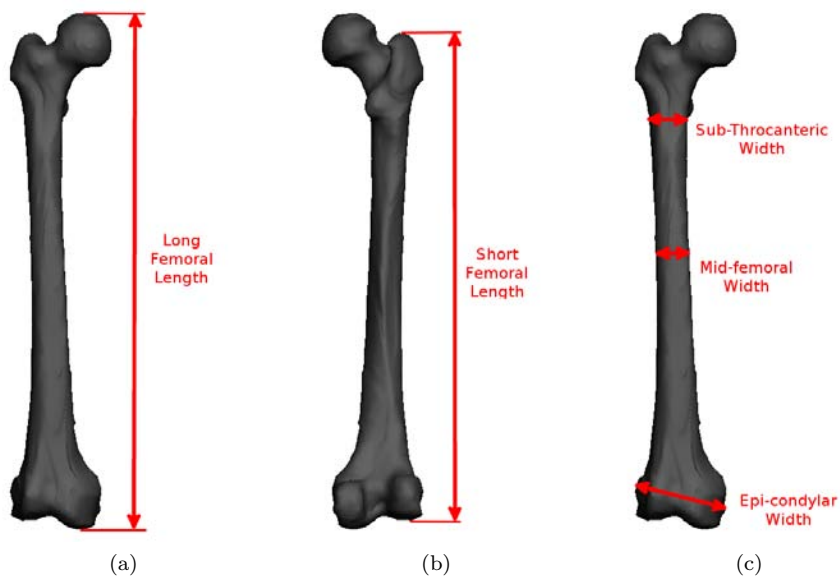


Figure 2.12: Definitions of femoral lengths: (a) shows the long femoral length, (b) shows the short femoral length and (c) the sub-throcanteric, mid-femoral and epi-condylar lengths.

Another important measure is the femoral neck width which corresponds to the narrowest part of the neck and can be used to determine the femur strength [10]. The femur head diameter can be used to determine the gender

of the patient [11]. The femoral neck width and the femoral head diameter are schematically represented in Figure 2.13a.

The angle formed between the femoral neck axis and the femoral shaft axis (Fig. 2.13b) can be estimated and are important to determine the hip fracture risk. A decreased neck-shaft angle is called coxa vara or varus alignment. An increased neck-shaft angle is called coxa valga or valgus alignment. These anomalies may also cause hip pain and degeneration.

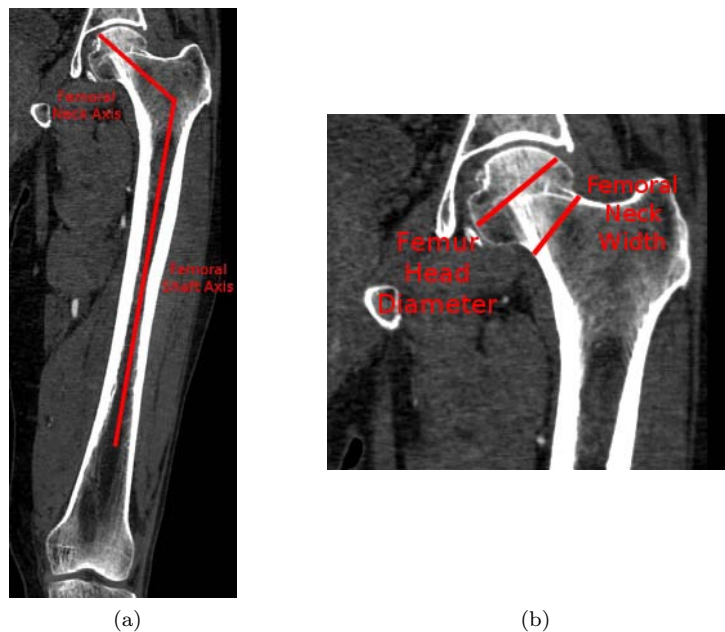


Figure 2.13: Femoral axes and angles. On (a) the neck-shaft angle is plotted on the CT-Scan and (b) shows the femoral neck width and the femoral head diameter.

The anteversion angle describes the twisting of the femur along its shaft, e.g., the angle between the femoral neck axis and the knee axis in a plane perpendicular to the femoral shaft axis as shown in Figure 2.14 [12]. A person with excessive hip anteversion (Fig. 2.14b), in order to maintain a more stable hip joint position, will instinctively tend to walk with the toes pointed in toward the middle of the body ("in-toeing"). This may cause discomfort in the hip, but also an added risk of damaging the labrum and consequently arthritis, as the cartilage that lines the joint is damaged. People with retroverted femurs (Fig. 2.14c) tend to walk with their feet turned out ("out-toeing"). As a result of abnormal alignment of the femoral head in the acetabulum there is increased impingement at the margins of the joint during hip movement. When this condition occurs due to a ridge of excess bone on the femoral neck, it is known as cam impingement; if the ridge of bone develops along the rim of the socket or acetabulum, the condition is called pincer impingement.

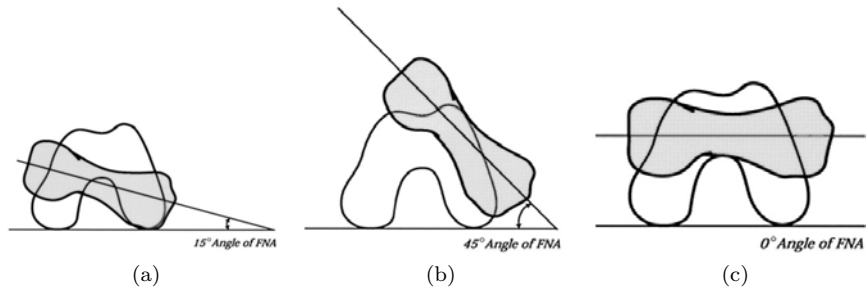


Figure 2.14: Schematic representation of the femoral neck anteversion (FNA) angle in a right femur, which is the angle between the femoral neck axis and the line that connects both condyles. (a) represents the normal femoral case, while (b) and (c) correspond to the anatomically abnormal femurs, respectively increased femoral anteversion and retroversion. Adapted from apta.org.

## 2.5 Hip Joint Kinematics

In this section, the hip joint biomechanics will be briefly reviewed. Firstly, the pelvic and femoral body segment coordinate frames will be introduced and then how these body segments are aligned in a hip joint coordinate frame to express joint articulation.

### 2.5.1 Coordinate System

The International Society of Biomechanics (ISB) recommends the following definition for the hip joint coordinate system with the purpose of reporting human joint motion based on the Joint Coordinate System (JCS) first proposed by Grood and Suntay in 1983 [13]. The JCS can reproduce joint motion in a clinically relevant way and its standardization allows a straightforward data crossing among studies.

The JCS is based on easy to identify anatomical landmarks: the ASIS (anterior superior iliac spine), the PSIS (posterior superior iliac spine) and the FE (femoral epicondyle). The normal human hip joint is treated as a ball and socket joint, with the center of rotation defined as the center of hip joint. Figure 2.15 shows the pelvic and femoral coordinate systems.

#### Pelvic Coordinate System (XYZ)

- $O$  : The origin coincident with the right (or left) hip center of rotation.
- $Z$  : The line parallel to a line connecting the right and left ASISs, and pointing to the right.
- $X$  : The line parallel to a line lying in the plane defined by the two ASISs and the midpoint of the two PSISs, orthogonal to the  $Z$ -axis, and pointing anteriorly.
- $Y$  : The line perpendicular to both  $X$  and  $Z$ , pointing cranially.

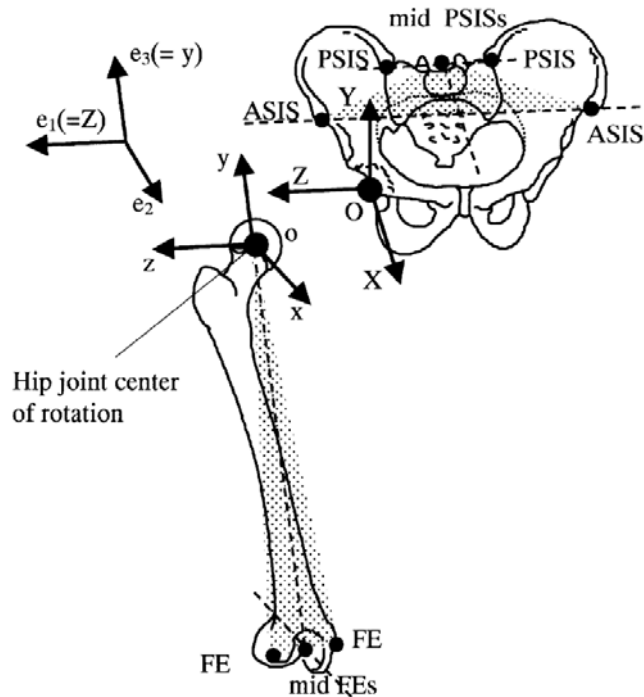


Figure 2.15: Illustration of the pelvic coordinate system (XYZ) and femoral coordinate system (xyz), and the JCS for the right hip joint [13].

### Femoral Coordinate System (XYZ)

- $o$  : The origin coincident with the right (or left) hip center of rotation, coincident with that of the pelvic coordinate system ( $O$ ) in the neutral configuration.
- $y$  : The line joining the midpoint between the medial and lateral FEs and the origin, and pointing cranially.
- $z$  : The line perpendicular to the  $y$ -axis, lying in the plane defined by the origin and the two FEs, pointing to the right.
- $x$  : The line perpendicular to both  $y$ - and  $z$ -axis, pointing anteriorly.

### JCS and motion for the right (or left) hip joint

- $e_1$  : The axis fixed to the pelvis and coincident with the  $Z$ -axis of the pelvic coordinate system.  
Rotation ( $\alpha$ ): flexion or extension.  
Displacement ( $q_1$ ): medio-lateral translation.
- $e_3$  : The axis fixed to the femur and coincident with the  $y$ -axis of the right (or left) femur coordinate system.  
Rotation ( $\gamma$ ): internal and external rotation.  
Displacement ( $q_3$ ): proximo-distal translation.
- $e_2$  : The floating axis, the common axis perpendicular to  $e_1$  and  $e_3$ .  
Rotation ( $\beta$ ): adduction or abduction.

Displacement ( $q_2$ ): antero-posterior translation.

### 2.5.2 Range of Movements

Due to its ball and socket nature, described in section 2.2, it allows movement along the three axes passing through the center of the head of the femur. The range of motion is limited by the inflexible guidance of the acetabulum and its ligaments. All of these together restrict extension (retroversion) by enclosing the femoral head like a spiral ligamentous screw, thus enabling a stable upright position supporting forces up to eight times the body weight. The flexion (anteversion) of the femur is possible due to a much higher degree and exclusively limited by soft tissues. Moreover, medial and lateral rotation as well as adduction and abduction are limited by ligaments. Figure 2.16 features a schematic representation of the movements here described and Table 2.1 the range of these movements.

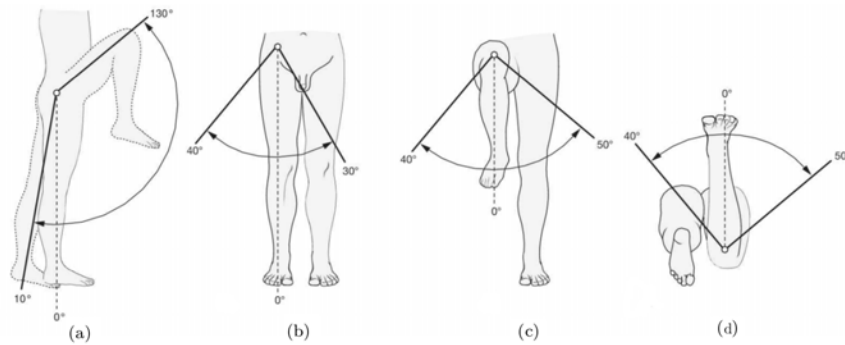


Figure 2.16: Range of motion in the hip joint [2]. The figure shows the maximum ranges of motion for the extension-flexion (a), abduction-adduction (b) and lateral-medial rotation (c) and (d) movements.

Movement	Range (in degrees)
(a) Extension - Flexion	10° - 0° - 130°
(b) Abduction - Adduction	40° - 0° - 30°
(c) and (d) lateral - medial rotation	50° - 0° - 40°

Table 2.1: Range of movement in the hip joint [2].

### 2.5.3 Gait Cycle

Support and locomotion are the primary functions of the hip joint. Bipedal animals' gait cycle considers the time period or sequence of events during locomotion in which one foot contacts the ground to when that same foot again touches the ground. It involves forward propulsion of the center of gravity. It may be divided in two phases: the stance phase and the swing phase. The stance phase is defined as the part of the cycle where the foot remains in contact with the ground and constitutes 60% of the total cycle. It starts out with

the heel strike followed by the loading response, where the weight is transferred onto the other leg and finishes with the toe off movement, where the tip of the foot rises to swing in the air. The swing phase corresponds to the 40% of the total gait cycle where the foot is not in contact with the ground and swings in the air. Minimal influences on the hip joint kinematics have major repercussions in the gait cycle, sometimes leading to the necessity of crutches or cane to compensate the deficient cycle.

## 2.6 Pathologies

This section will focus on the diversity of complications that may occur and lead to the replacement of the hip joint. As any contact surface between bones, it is expected that any diseases that have a direct impact on the cells and bony structures also affect the functionality of the joint. Avascular necrosis and osteoporosis are examples of such. In addition, there are complications directly related to the joint itself, as osteoarthritis or rheumatoid arthritis. If any of these pathologies can not be fixed with medication or physiotherapy, even if at the cost of a cane or crutches, then a THA will be the adopted solution. The following subsections will provide a more detailed view on some relevant complications of the hip joint. Less frequent complications will be looked into in section 2.6.7.

### 2.6.1 Osteoporosis

Osteoporosis (OP) is a disease that alters bone remodeling parameters leading to decreased bone strength, therefore increasing the risk of fracture. It tends to affect majorly the cancellous bone structure because it has more surface area than cortical bone, on which over-active bone reabsorbing takes place. The breakage and loss of trabecular struts and rods are among its symptoms consequently decreasing trabecular connectivity and bone strength. Hence, osteoporotic fractures tend to occur in regions that depend on cancellous bone for strength, such as the femur or the spine.

According to the Portuguese Ministry of Health<sup>1</sup>, OP is an issue that affects more than half a million people. Moreover, the number of fractures of the neck of the femur ascends to about 10000 per year, which reflects in over 52 million euros in health care. It also states that it occurs three times more in women than in men. These fractures are a significant cause of death or serious incapacity. The World Health Organization<sup>2</sup> goes further and states that it affects 75 million people in Europe, United States and Japan alone.

The disease doesn't present any kind of specific symptoms. Age and gender are the major risk factors, but also previous fractures and inheritance factors may affect the bone mass which can be detected with the help of an X-Ray image, for example (Fig. 2.17). If there is an osteoporotic fracture of the neck of the femur, the replacement of the hip joint is the most common proposed solution, in order to compensate for the reduced bone mass density in nearby areas.

---

<sup>1</sup><http://www.portugal.gov.pt/>

<sup>2</sup><http://www.who.int/en/>



Figure 2.17: X-ray image of the pelvis showing early changes in bone density in the affected hip. Courtesy of orthoinfo.aaos.org.

Regular physical exercise or the moderate consumption of calcium and vitamin D can help prevent osteoporotic fractures [14].

### 2.6.2 Osteoarthritis

Osteoarthritis (OA) also known as degenerative arthritis or degenerative joint disease, is a type of joint disease that results from breakdown of joint cartilage and underlying bone which results in joint pain and stiffness but also joint swelling and consequently decreased range of motion [7]. It is considered the most common musculoskeletal disorder worldwide and affects in Portugal alone 6% of the total population in 2013 [15]. The cartilage damaging is usually associated with reduction on the production of the synovial fluid, resulting in a narrowed joint space. The hip is among the most frequent joints affected by this complication. Figure 2.18 shows an X-Ray image of a healthy hip joint and joint space against an arthritic hip joint.

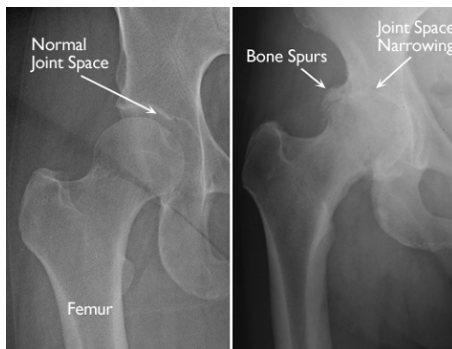


Figure 2.18: On the left there is a X-Ray image of a healthy femur with normal space in the ball and socket joint. On the right, an X-Ray image of an arthritic hip that shows severe bone loss and cartilage degeneration which led to a narrowed joint space and the formation of bone spurs. Courtesy of orthoinfo.aaos.org.

The causes often include inherited factors but also previous joint injuries or abnormal limb development. The risk is increased in overweight individuals or different sized lower limbs.

Pain relief might happen in a temporary initial stage due to the use of analgesic or anti-inflammatory drugs. Understanding of the femur morphology could help on the diagnosis and prevention of OA and in cases where joint replacement is necessary, medical imaging can be used to better plan the surgical procedure.

### 2.6.3 Rheumatoid Arthritis

Rheumatoid Arthritis is an autoimmune condition characterized by the swelling of the synovial lining, invading its surrounding tissues and producing chemical substances that attack and destroy the joint surface. Unlike OA, in rheumatoid arthritis, which is primarily an inflammatory condition, the joints typically become hot or red. It is extremely painful for the patient and may have an influence on the range of motion of the hip joint. In an initial stage, anti-inflammatory drugs may relieve the pain, as well as steroids, but in long term the joint will be completely deteriorated.

The disease focuses more on individuals aged between 35 and 55 years and in women more than men.

### 2.6.4 Avascular Necrosis

Avascular necrosis, as its name suggests, is a result of the shortage of bone irrigation, either temporarily or permanent. With the lack of blood supply, bone tissue dies and loses its properties. While it can affect any bone, about half of cases show multiple sites of damage, avascular necrosis primarily affects the joints at the shoulder, knee, and hip. Consequently, the bone strength diminishes and the neck of the femur becomes more susceptible to fracture. The causes for this complication are countless and diversified but alcoholism, steroid abuse and blood-clotting bodies are among the most common [16]. However, it's most common in people between the ages of 30 and 60. An example of a X-Ray image picturing a femur affected by avascular necrosis may be seen in Figure 2.19. Because of this relatively young age range, avascular necrosis can have significant long-term consequences.



Figure 2.19: Radiography of avascular necrosis of left femoral head. Man of 45 years old with AIDS. Image of public domain.



Even though a new, more promising treatment based on bisphosphonates is being used [17], the most common treatment is still a replacement of the hip joint.

### 2.6.5 Acetabular Dysplasia and Protrusion

Hip dysplasia can be a congenital or developmental deformation but also a result of a traumatic hip dislocation that occurs when the head of the femur is forced out of its socket. On the congenital case, it is usually caused by a defective acetabulum. On the other case, it typically takes a major trauma to tear the ligaments and dislocate the hip such as car collisions and falls from significant heights. As a result, other injuries like broken bones often occur with the dislocation. An acetabular dysplasia dislocation is a serious medical emergency, so immediate treatment is mandatory.

Symptomatically, an acetabular dysplasia is very painful for the patient and prevents any movement of the leg. In some cases, the nerves are damaged and the patient can may lose any feeling in the foot or ankle area. Figure 2.20 shows a radiography of a femoral head out of his socket.



Figure 2.20: X-ray showing a patient with a posterior dislocation of the left (right on image) hip. Courtesy of orthoinfo.aaos.org.

The hip protrusion, more rarely seen, is medial displacement of the femoral head in that the medial aspect of the femoral cortex is medial to the ilioischial line [18]. The gradual deepening of the acetabular cavity is caused by primary idiopathic and secondary neoplastic, infectious, metabolic, inflammatory, traumatic, and genetic disorders. There is an immediate reduction of the range of motion of the joint and a very severe pain. An open-joint surgery, which is a surgery to repair, re-position, replace, or remove parts in a joint, sometimes solves the complication. However, in the more severe cases a total hip arthroplasty is required.

### 2.6.6 Femoroacetabular Impingement

Femoroacetabular Impingement (FAI) is a condition where the bones of the hip are abnormally shaped. Because of the ball and socket nature of the hip joint, they might not fit perfectly together and the hip bones rub against each other, due to the development of bone spurs around the femoral head or along



Figure 2.21: X-ray showing a patient with an acetabular protrusion. It is noticeable the migration of the head of the femur into the pelvis ring. Image of public domain.

the acetabulum. This can result in a tearing of the labrum and breakdown of the cartilages.

There are three types of FAI, illustrated on Figure 2.22: the pincer, where the impingement occurs because extra bone extends out over the normal rim of the acetabulum; the cam, where the femoral head is not round and can't rotate inside the acetabulum, damaging the cartilage on the acetabulum; lastly, a combined of the two previous one is also sometimes seen.

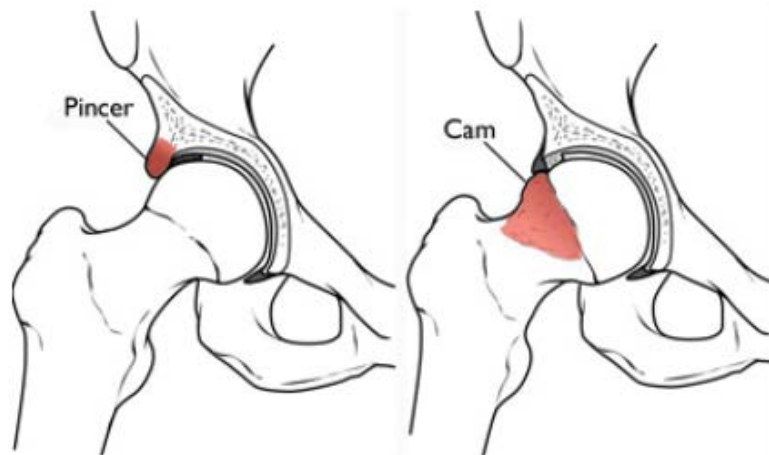


Figure 2.22: Different types of femoroacetabular impingement (FAI). On the left, the pincer impingement is shown while on the right a cam impingement is illustrated. Courtesy of orthoinfo.aaos.org.

The FAI are normally caused by malformation of the hip bone during the growing years and very little can be done to prevent so.

### 2.6.7 Other Pathologies

Nevertheless, other less frequent complications may occur in the hip joint and lead to its replacements. Bone tumors may promote the unbridled growth of bone mass and change the properties of the bone tissue and the contact surfaces of the bones. Another example is Paget's disease, of unknown cause, where there is an abnormal breakdown of bone tissue followed by abnormal bone formation, usually less strong.

## 2.7 Proximal Femur Fractures

In addition to the pathologies that affect the hip joint (Sec. 2.6), the number of hip fractures associated with falls that might be as minor as from the standing position is considerable. Hip fractures in this age group are associated with a substantial mortality, as many as 12-36% within the following year. Osteoporosis, as seen on section 2.6.1, contributes to a decrease of the bone mineral density which increases the susceptibility to fracture. Postmenopausal women are especially at risk because of estrogen deficiency. Women can lose as much as 35% of their cortical bone and 50% of their trabecular bone in the 30 to 40 years after menopause. Radiography is the first choice for diagnosis, although magnetic resonance or nuclear imaging are often used.

Traumatic proximal femur fractures can be divided into four types based on their location: neck (sub-capital and trans-cervical), intertrochanteric and sub-trochanteric [9]. They occur when the femur is loaded beyond its fracture stress which depends on the magnitude of the loading. The direction and the location of the loading are critical as the bone material properties spatially vary. They can also be classified according to their stability - a stable fracture exhibits no displacement or deformity while an unstable does - and according to its surrounding media - intracapsular if inside the articular capsule or extra-capsular. Intracapsular fractures are prone to complications due to the disruption of blood supply and to the head fragment of the fracture that contains fragile cancellous bone and provides poor anchorage for a fixation device [19]. Figure 2.23 illustrates the basic fracture types.

The femoral neck is the most common location for a hip fracture, accounting for 45% to 53% of all hip fractures. Per 100,000 person-years, approximately 27.7% femoral neck fractures occur in men and 63.3% occur in women. In the United States alone, each year more than 250,000 fractures occur, with associated health care costs of 8.7 billion dollars [20]. Treatment of stable neck fractures is done by operative pinning with three parallel cannulated screws placed adjacent to the femoral neck cortex. Unstable fractures, i.e., where the femoral head is displaced in a varus or valgus position, can also be fixed with pinning for younger patients in order to reduce the risks of arthroplasty, including prosthetic wear and loosening. However, treatment by pinning carries a higher risk of more surgery in the future as the fracture is intracapsular. As implied, arthroplasty results in more acute postoperative morbidity, but it offers fewer re-operations for nonunion, hardware failure, and osteonecrosis.

Intertrochanteric fractures account for approximately 38% to 50% of all hip fractures. Stable fractures are those in which the femur is broken into two or three parts. Unstable fractures are those in which the femur is broken into four parts or the fracture is of the reverse oblique pattern. Reverse oblique fractures

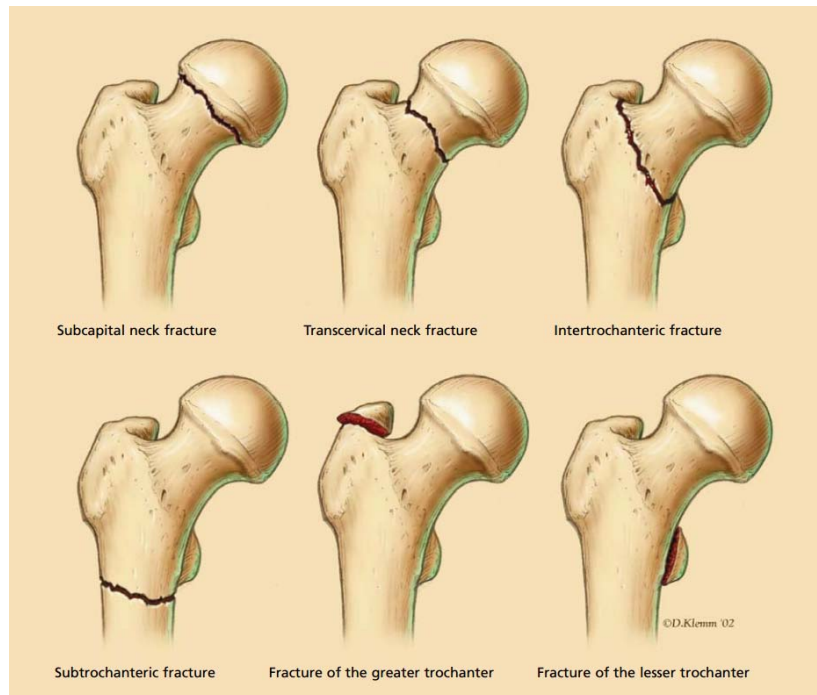


Figure 2.23: Most common fracture types. Combinations of these can occur [19].

are unstable because of the femur’s tendency to displace medially. Suggested treatment includes the fixation sliding hip screw across the neck and coupled to a side plate that is screwed onto the femoral shaft.

Sub-trochanteric fractures are located between the lesser trochanter and the femoral isthmus that is, in the proximal part of the femoral shaft accounting for approximately 5% to 15% of hip fractures. They are treated with an intramedullary hip screw.

Isolated fractures of the greater or the lesser trochanters can occur, mostly in osteoporotic females and as the result of a fall. They can be effectively treated with open reduction, internal fixation with wire, and allogeneic bone-grafting [21].

## 2.8 Total Hip Arthroplasty

The THA appears as a solution to the several issues regarding either the pelvis or the femur, enumerated in previous section 2.6, which lead to the malfunction of the hip joint. It consists in a surgical replacement of the hip joint by a prosthetic implant. Every year, about one million patients worldwide undergo such surgery, considered to be one of most successful, cost-effective and safe medical interventions. This number is expected to increase due to an ageing population, decreasing average age at the first operation and the limited lifespan of the implants.

In this section it will be reviewed: firstly, a glimpse on the history and evolution of the prosthesis; then, an overview of modern approaches to the

replacement; and lastly, the broad specter of hip implants will be reviewed, with focus on the difference in design and properties but also on their fixation methods with the corresponding failure risks. Figure 2.24 shows a X-Ray of a replaced right hip (left of image) with the ball of this ball-and-socket joint replaced by a metal head that is set in the femur and the socket replaced by a white polymeric cup.



Figure 2.24: X-Ray of the pelvic area, showing a replaced right (left on image) hip joint. Image of public domain.

### 2.8.1 The History of the Total Hip Arthroplasty

The Total Hip Arthroplasty was considered to be the most important development in orthopedic research of the twentieth century [22] not only due to its direct impact on the treatment of degenerative hip diseases but also as an incentive to the development of implants on other joints. The earliest recorded attempts were led by Themistocles Glück in Germany, who used ivory to replace the femoral head and a socket joint that he fixated to the bone with nickel-plated screws [23]. However, it was not until 1923 that surgeon Smith-Peterson provided synthetic inter-positional arthroplasty with a mold prosthesis. He developed a glass mold to be placed between the femoral head and the acetabulum that he thought would guide natural repair of the joint but most ended up breaking and led him to give up using this material. He then started using Vitallium<sup>®</sup>, a metal alloy of chromium, cobalt and molybdenum that was being used in dentistry and obtained satisfying results - only 50% of his patients showed joint pain after the surgery [22] and 500 ensured ten years of good clinical results [23].

At a time where very little was known about the bio-compatibility of the materials, the Judet brothers in Paris started using acrylic in 1948 with success but it turned out to be exceptionally susceptible to wear. It was Austin Moore together with Harold R. Böhlman that first inserted metal prosthesis replacing the first twelve inches of the femur with custom made Vitallium<sup>®</sup> prosthesis. In 1952 Böhlman and Moore refined their implant and in 1952 described a model that featured a fenestrated stem to allow bone ingrowth. This femoral implant featured a distinctive flared collar below the head and a vertical intramedullary stem [24] and was the first to be widely distributed, becoming a reference in the hip prosthesis world. Although rarely, the so called

Austin Moore implant is still in use today. Contrary to a modern prosthesis (Fig. 2.25), the Austin Moore prosthesis featured only one component, i.e., the femoral stem component acted directly on the acetabular cavity.



Figure 2.25: ULTRAMET<sup>®</sup> Metal-On-Metal Hip System, based on the Austin Moore model. Courtesy of Depuy Orthopaedics.

The first hip prosthesis that consisted in two different components - acetabular and femoral - was proposed by Gilberty and Bateman. This allowed different combinations of stem, neck length, and head with distinct properties and therefore gave way to several studies that aimed to improve the stability and longevity of the implant. These provide a better-fitting prosthesis for most patients, so that leg length may be equalized, and hip muscle tension can be adjusted for better function and reduced risk of dislocation. Firstly, it was proved that the acrylic and polyethylene (PE) femoral heads had a good damping coefficient but a rather considerable wear rate. The heads of steel and chromium-cobalt-molybdenum alloy ensured much better wear rates [25].

The use of bone cement was introduced by John Charnley whose work in the field of tribology resulted in a design that almost completely replaced the other designs by the 1970s. His prosthesis design consisted of a stainless steel femoral stem and head and a polyethylene acetabular cup - Metal-on-Polyethylene (MoP) - that were fixated to the bone using Polymethyl Methacrylate (PMMA) bone cement. The replacement joint became famous under the name Low Friction Arthroplasty due to the reduction of the surface area by the use of a smaller femoral head diameter [26]. However, the success of Charnley's prosthesis in recovering joint friction and achieving pain relief was afflicted over time by a surprisingly high number of loose stems and/or acetabular cups. This phenomenon is known as aseptic loosening and consists in a loss of fixation of the stem or the acetabular cup and is the main reason of revision surgery up to date [27]. Other reasons are infection, dislocation of the hip joint, fracture of the stem or the acetabular component or unexplained pain.

Aseptic loosening is a consequence of polyethylene wear. Advanced wear-induced dimensional changes may impair the mechanical function of the implant and wear debris may induce adverse tissue reactions leading to periprosthetic osteolysis [28]. This led to the development of Ultra High Molecular Weight Polyethylene (UHMWPE) and cross-linked UHMWPE. It also led to

the resurgence of Metal-on-Metal (MoM) prosthesis due to their lower rate of osteolysis. A second generation of MoM implants was developed in the late 1980s which in spite of the good results, no study could demonstrate that the expected reduced wear could outperform the MoP prosthesis.

The THA was becoming a well established and successful procedure for elderly patients, but also young age patients saw their expectations raised [29]. However, in order to provide no restrictions on the physical activities of the patients, hip prosthesis were required to withstand higher load for extended time periods. This led to the development of the Ceramic-on-Ceramic (CoC) prosthesis that exhibit excellent wear performance but also increase the risk of fragile fracture of the ceramic components [30]. This has been improved over time and nowadays CoC implants are considered a reasonable alternative to MoM and MoP prosthesis.

Simultaneously and intended for younger patients, hip resurfacing has lately been advocated because it preserves the femoral bone as seen on Figure 2.26.



Figure 2.26: Hip resurfacing THA covers the reshaped femoral head with a new metallic articulating surface. Image of public domain.

This means that the revision surgery, nearly inevitable for patients below the age of 50 at the time of the primary THA, will intervene for the first time in the main femur mass [31]. It was also expected to achieve lower failure rates because stem loosening be less likely to occur. This kind of surgery mainly uses MoM bearings. However, the surgical procedure for the implantation of prosthesis is more demanding and complications may occur due to the interruption of the blood supply on the proximal femur (avascular necrosis) and the increased incidence of femur neck fractures [31, 32]. Furthermore, patients who underwent a hip resurfacing have developed inflammatory lesions in periprosthetic tissues and exhibit elevated concentrations of cobalt and chromium ions in the blood flow, subsequently requiring revision surgery [33].

More recently, advances on the THA have been made in an attempt to minimize the invasive surgery damage on the patient. The use of a single incision, less than 10 cm long, provides soft tissue sparing and bone conservation

options. These techniques also give way to reduced intra-operative blood loss, faster rehabilitation and improved cosmetic result while not compromising the feasibility of the surgery or the physical function on the post-op [34, 35]. The automation of the process is also part of the state-of-the-art research topics on hip replacement. The increased precision on implant placement by minimally invasive procedures is a motivation for researchers even though it has not yet been shown to have a clinical benefit. They are also not cost effective and often lead to increased surgical time [34].

### 2.8.2 Incidence of Total Hip Arthroplasty

Data retrieved from the Organisation for Economic Co-operation and Development (OECD) shows that in 2012, Germany, Austria, Sweden, Finland and Belgium had the highest rates of hip replacement among the European Union countries. Hip replacement rates were also very high in Switzerland (Fig. 2.27). Differences in population structure may explain part of these variations across countries, and age-standardization reduces to some extent the variations across countries. But still, large differences remain and the country ranking does not change significantly after age standardization [36].

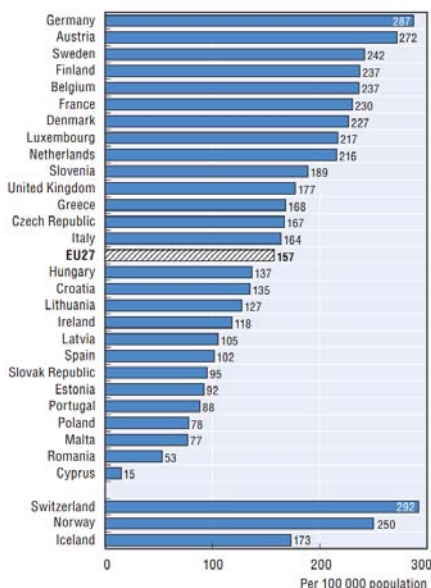


Figure 2.27: Hip replacement surgery, per 100,000 population in 2012 [36].

The number of hip replacements has increased in recent years in most European countries, as seen on Figure 2.28, also made available by the OECD. In Denmark, for example, the number of hip replacement per 100,000 population increased by 40% between 2000 and 2012 although the rates have been stable or declined slightly in recent years. The growth rate for total hip arthroplasty was lower in France, but still increased by more than 10% in the past years. The growing volume of hip replacement is contributing to health expenditure growth since these are expensive interventions. In 2011, the estimated price



of a primary hip replacement on average across European countries was about 6,800 euros [37], while their revision is even more expensive.

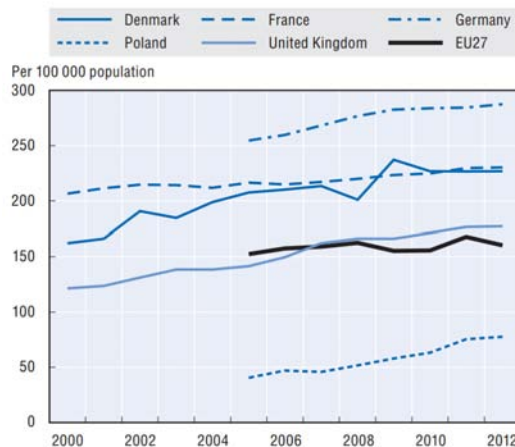


Figure 2.28: Trend in hip replacement surgery in selected countries, 2000-2012 [36].

Furthermore, a study shows that the increase in the number of knee and hip arthroplasties due to OA in the Netherlands will probably continue in the coming 20 years. More specifically, the trend projection suggests that the numbers may increase to 51,680 for the hip (+149%) and to 57,893 for the knee (+297%) [38]. In the United States, Kurtz [39] states that by 2030, the demand for primary total hip arthroplasties is estimated to grow by 174% to 572,000.

### 2.8.3 The Surgical Procedure

There are several approaches to it: the posterior (Moore [24]), lateral (Hardinge or Liverpool [40]), antero-lateral (Watson-Jones [41]), anterior (Smith-Petersen, [42]) and, more recently the minimally invasive approach [34]. There is no compelling evidence in the literature for any particular approach, but consensus of professional opinion favors either modified antero-lateral or posterior approach. Therefore, both are schematically represented in Figure 2.29. Figure 2.29a shows the patient positioned laterally or supine and the approach to the joint requires elevation of the hip abductors which has been reported to be an issue as sometimes they do not heal back on. However, it preserves the posterior capsule and reduces the risk of prosthetic dislocation. On the other hand, Figure 2.29b examples the posterior approach, where the patient positioned on his side and the surgeon accesses the joint and capsule through the back. This approach gives excellent access to the acetabulum and femur and preserves the hip abductors and thus minimizes the risk of abductor dysfunction post operatively at the cost of a higher dislocation rate. Moreover, the surgeons contacted during the development of this doctoral work have different opinions on the matter and most of the reasons so are empirical and therefore it is hard to infer which of the techniques is the most reliable.

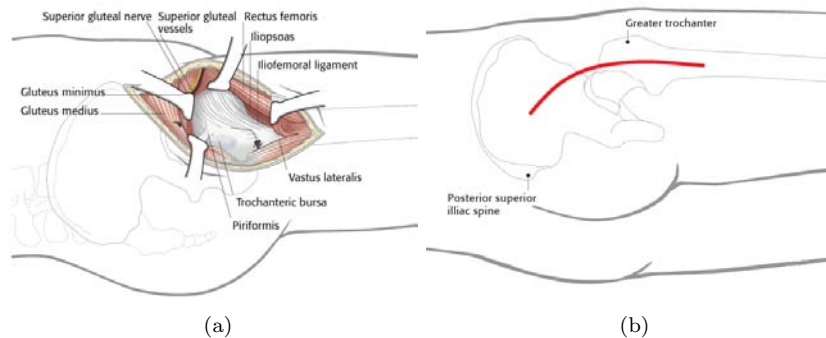


Figure 2.29: Lateral approach (a) and posterior approach (b) to a Total Hip Arthroplasty, respectively. Courtesy of aofoundation.org.

### Preoperative Planning

Firstly and above all, there should be a pre-operative planning. Whatever arthroplasty approach is chosen, the procedure should be carefully planned with sufficient detail. Its value and accuracy has been extensively reported [43, 44, 45].

A common form of planning is the selection of the prosthesis with the aid of radiographic templates and appropriate X-rays of the normal and injured hip [46, 47]. A standardized radiography of the antero-posterior view of the pelvis with a known magnification is used for templating the optimal size and orientation of the prosthesis. Figure 2.30a shows an example of two dimensional radiographic planning. This conventional technique is however outdated in a digitized world as today's. Hence, this manual and meticulous process has been digitized and a more straightforward computational approach has been achieved [48], as shown in 2.30b. It is as reliable as conventional templating techniques [49]. It is also considerably more cost effective over time as the use of film is disposed, even though the initial cost of technology development might be substantial.

More recently, Three Dimensional (3D) approaches to pre-operative planning [50, 51] have been suggested and will be discussed further along the thesis as it is within the scope of the presented work. Contrary to Two Dimensional (2D) approaches, these are able to determine the 3D position and orientation of the implants. The optimization of this process can be more or less automatic at the cost of interactive surgical planning.

Regardless on how accurate the planning can be, alternatives should be taken to the operative room as complications occasionally occur and an immediate change of plans is due. Recently, the presence of a technician with expertise and knowledge of the available implants who will aid the surgeon on the choice of an implant that is thought to boost the performance of the patient specific femur-implant coupling.

However, it is the type and location of the injury that will ultimately determine the pipeline for surgical intervention. Although less frequently performed nowadays, a hemiarthroplasty is a surgery that is used to treat a fractured hip. The operation is similar to a THA, but it involves only the insertion of

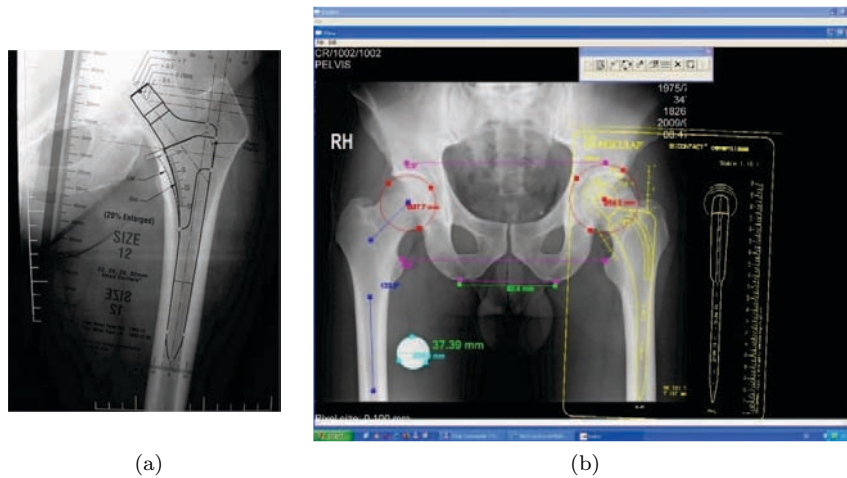


Figure 2.30: Radiographic planning of the THA: manual (a) [49] and with the help of a software (b) [48].

the femoral component of the implant, i.e., it replaces only the ball portion of the hip joint, not the socket portion. A hemiarthroplasty and a total hip arthroplasty can be compared in Figure 2.31.

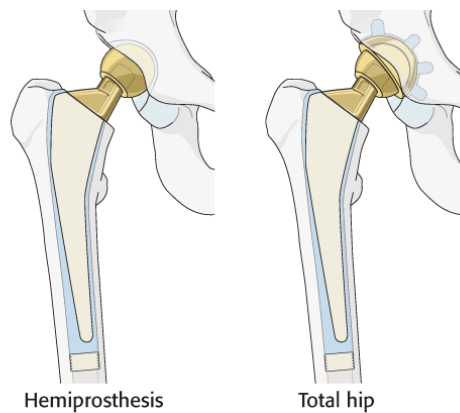


Figure 2.31: Comparison of a hemiarthroplasty and a total hip arthroplasty, where an acetabular component is also inserted in the pelvis. Courtesy of aofoundation.org.

### Acetabular Component

The acetabular component is chosen based upon the patients anatomy, with the aid of pre-operative X-rays and intraoperative trials. While the external diameter of the acetabular component is definitively selected intraoperatively, its internal diameter, the same as that of the matching femoral head component, is a feature of the chosen prosthetic system. The fixation of the acetabular component to the pelvis can be either done with bone ingrowth or with cement.

Implants may show a porous surface or a coating of hydroxyapatite which promote osseointegration [52] on the external surface of the cup. In addition, the hydroxyapatite coating can be used for local drug delivery in bone [53, 54]. Alternatively, metallic scaffolds [55] are also used to obtain biological fixation and improve longevity of orthopedic implants. Early weight bearing may be safer with cement and is usually preferable in the elderly as the probability of a revision is much lower when compared to young patients. Cement fixation might require excessive bone removal if an implant revision is due.

In the first stage of the surgery, the acetabular cartilage is removed with a reamer (Fig. 2.32a) oriented perpendicularly to the plane of the bony acetabulum. Reaming is done until cancellous bone is exposed and the desired fit is reached. Optionally, fixation of the cup might be improved with the drilling of holes in the pelvic cavity (Fig. 2.32b). The cup should fill as much of the available space in the acetabulum as possible, extending only a little beyond the bone.

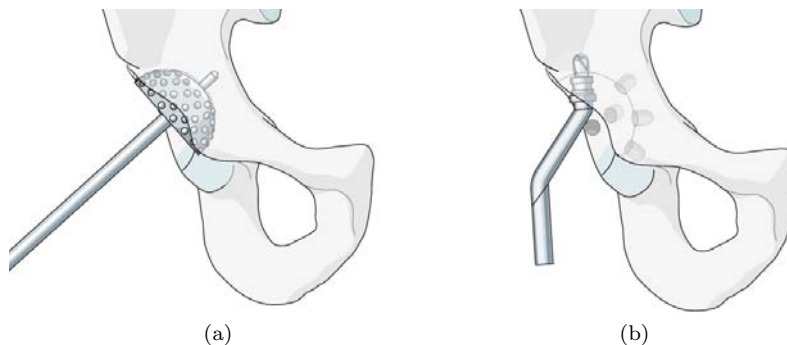


Figure 2.32: Reaming (a) and anchorage holes drilling (b) for the fixation of the acetabular cup. Courtesy of aofoundation.org.

Ideal placement of the acetabular cup matches the patient's own acetabulum. It should not be directed posteriorly (retroverted) nor too anteriorly (excessive anteversion). For optimal hip joint stability and prosthetic wear, approximately 45 degrees abduction (Fig. 2.33b) and 15 degrees anteversion (Fig. 2.33a) are commonly advised. Both anteversion and abduction must be set correctly during placement of the acetabular prosthesis.

### Femoral Component

The removal of the femoral head in case of a total neck fracture is done with the help of a threaded handle, according to Figure 2.34a, retracting the distal femur and tearing the ligaments if necessary. An additional osteotomy of the neck might be required in order to obtain correct neck length and to fit the flange of the prosthesis. The remaining femoral neck should be long enough to maintain equal leg lengths, as well as proper soft-tissue tension. The orientation of the osteotomy depends on the chosen prosthesis. It usually begins in the fossa below the greater trochanter. The osteotomy should also be perpendicular to the axis of the femoral neck, so the prosthetic anteversion is correct. After the osteotomy, it is important to check the acetabulum and its cartilages for

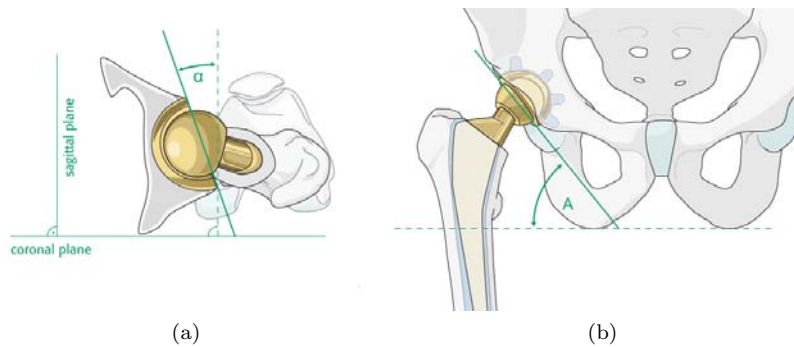


Figure 2.33: The normal acetabulum of a right femur rotated anteriorly  $\alpha = 15^\circ$  (a) and with an abduction of  $A = 45^\circ$  (b). Courtesy of aofoundation.org.

arthrosis. The prosthetic head size may be inferred by the removed head size (Fig. 2.34b), although ultimately it's the surgeon's choice.

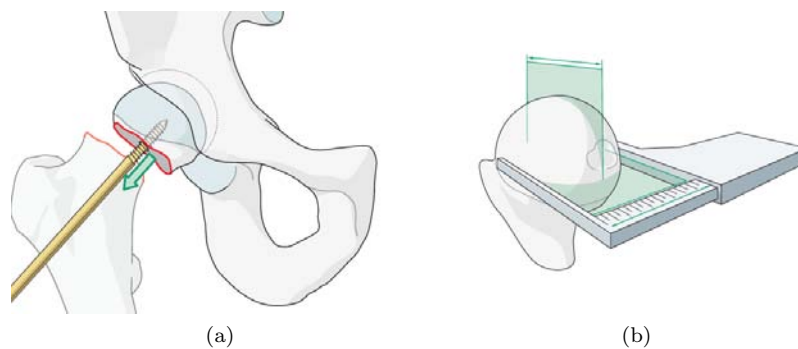


Figure 2.34: (a) shows the removal of the femoral head with the use of a threaded handle and (b) shows the measuring of the removed head diameter in order to properly choose the prosthetic head. Courtesy of aofoundation.org.

A common pitfall at this point is if the femoral neck is too short, which can result in insufficient muscle tension and consequently increase the risk of a post-operative dislocation of the prosthesis. Usually, at least a centimeter or two of neck should remain proximal to the lesser trochanter - Figure 2.35a. The prosthesis must be correctly aligned in the femoral transverse plane - Figure 2.35b. The neck of the femoral component should usually be co-axial with the femoral neck.  $\beta$  indicates the angle of anteversion of the femoral neck and later of the prosthesis. Correct rotational alignment is achieved by cutting the femoral neck perpendicularly to its axis and maintaining the desired anteversion while preparing the femoral medullary canal with rasps and broaches.

The proximal femoral prosthesis is inserted into the femur after cutting the femoral neck to fit, and preparing the medullary canal. The canal can be shaped so that the prosthetic stem fits tightly (press-fit), but without great stability. Stability can be increased by using a smaller stem than the canal and anchoring it with PMMA cement. It typically includes use of a femoral

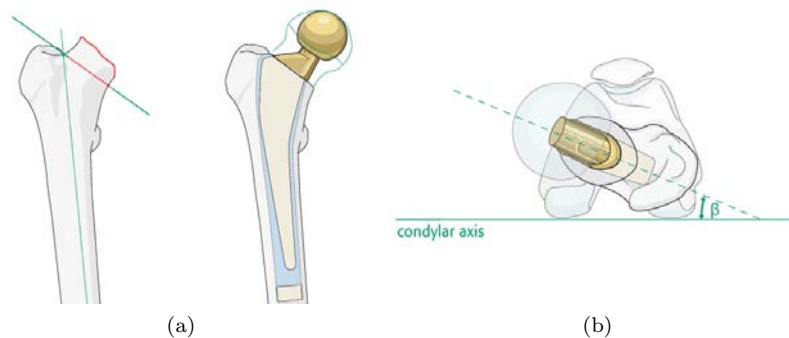


Figure 2.35: Preparation of the stem insertion in the femur. (a) shows the correct osteotomy planning and (b) schematically represents the correct alignment of the prosthesis. Courtesy of aofoundation.org.

plug and pressurized injection of a more fluid cement which reduces the risk of cement failure. Another alternative for a stable fixation is to use a stem that fits the bone snugly and has a surface coated with hydroxyapatite which promotes osseointegration [52]. However, it requires a more expensive prosthesis and protection from early weight bearing, thus it is less appropriate for the elderly. The advancements and drawbacks of cement use against press-fitting will be more extensively reviewed on section 2.9.2.

The femoral awl is inserted, initially laterally, in the femoral neck, and rotated to match the femoral neck anteversion (approximately 15 degrees). This helps avoid varus malposition. Intramedullary cancellous bone is progressively removed, usually with a series of rasps as seen in Figure 2.36a, until the prosthesis fits appropriately within the medullary canal. This process is known as broaching. If an uncemented implant is used, the stem of the prosthesis should snugly fill the prepared medullary cavity. If, on the contrary, a cemented implant is to be used, the stem size should be slightly smaller than the medullary cavity in order to make room for the layer of cement. Figure 2.36b shows precisely this.

Ensuring a properly broached cavity, the prosthesis insertion is done with a valgus orientation with the proximal stem laterally, and its distal tip close to the medial femoral cortex, as represented in Figure 2.37a, so that it can bear the eccentric bending forces acting on the prosthetic head. A similar trial prosthesis should be used to check length and offset. Head size, however, is determined by the pre-operatively selected acetabular component. Figure 2.37b shows proper head placement in order to maximize the implant stability.

### Final Considerations

Once the prosthetic components are in place and stable, the hip is gently reduced. After reduction, stability and soft-tissue tension is checked. A more appropriate neck length may improve stability. Equalizing leg length is a valid goal, but avoiding dislocation is probably more important. Figure 2.38 shows a successfully replaced hip joint, where both interacting parts of the joint are now prosthetic.

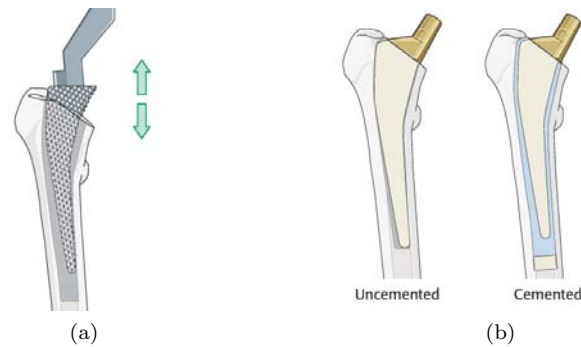


Figure 2.36: Preparation of the stem insertion in the femur. Broaching is exemplified in (a) and (b) illustrates how the medullary cavity should be shaped in case of cemented or uncemented implants. Courtesy of aofoundation.org.

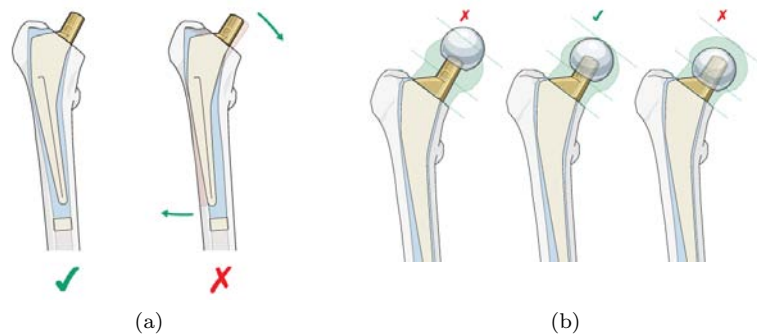


Figure 2.37: Proper placement of the femoral component. (a) shows the correct insertion for the stem and (b) shows the ideal head configuration. Courtesy of aofoundation.org.

## 2.9 Materials and Design of the Hip Implant

As mentioned in the previous section 2.8.1, hip prosthesis are categorized according to the material combination of the femoral head and the acetabular cup. The most common combinations are MoP, MoM and CoC. These fit within the range of bio-compatible materials, i.e., materials used to replace a part or a function in the human body in a safe, reliable, economic and physiologically acceptable manner [56]. Their interaction with the human body can range from bio-inert to bio-active or bio-resorbable materials. Bio-inert materials, such as stainless steel, titanium, alumina or UHMWPE, have minimal interaction with the surrounding tissues and consequently minimal inflammatory response. Bio-active materials interact with the surrounding tissues and modify their surface along time. Hydroxyapatite used as coating on metals to promote osseointegration is an example of a bio-active material. Finally, bio-resorbable materials dissolve after implantation and are slowly replaced

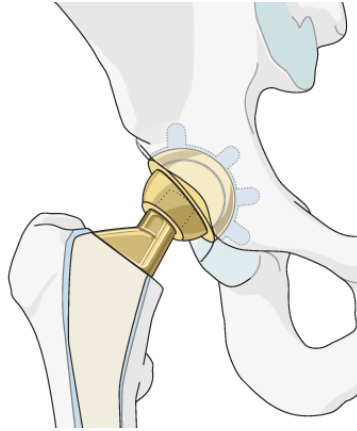


Figure 2.38: Illustration of a successfully replaced hip joint. Courtesy of aofoundation.org.

by tissue. Examples of such material behavior include coronary scaffolds and stents.

### 2.9.1 Material Properties

The material couplings chosen to replace the anatomical hip joint must feature different compatibility requirements: structural, tribological and biological. The first relate to the weight-bearing of the joint, i.e., the materials must exhibit adequate mechanical strength and fatigue strength in order to bear the body weight and resist the millions of mechanical load cycles, respectively. Tribological requirements ensure that the relative range of motion of the musculoskeletal system remains uncompromised by wear, which is one of the major post surgical concerns of the THA. Finally, the materials should provide good osseointegration, resist to the highly corrosive surrounding environment and the released wear particles. Thus, the structural and load bearing components should be bio-inert whereas in case of cementless fixation the stem and shell of the acetabular cup should exhibit good bio-active surfaces in order to promote a good fixation. Surfaces should be hard to resist wear while stem and shell should be as elastic as possible to better match the properties of the surrounding bone, as stiff as possible to avoid aseptic loosening. These conditions require a modular design of the hip prosthesis.

#### 2.9.1.1 Metals

Metals exhibit elevated mechanical strength and fracture toughness, i.e., are able to contain a crack and still resist to fracture. Nowadays, there are three groups of metals still widely used for joint replacements [57]:

- Stainless steel contains as main alloying materials chromium (Cr), nickel (Ni), molybdenum (Mo) and nitrogen (N) and overall exhibit good corrosion resistance. They are relatively inexpensive and allow the manufacturer to take advantage of the relative proportions of its alloying mate-



rials, improving its mechanical properties at the cost of a more complex and higher cost manufacturing, for example.

- Cobalt-chromium-molybdenum (CoCrMo) can be considered as cast or wrought alloys. Cast alloys exhibit elevated mechanical properties and optimal corrosion resistance under friction conditions at the cost of poor fatigue resistance and high cost. Wrought CoCrMo is even more expensive but its fatigue resistance is enhanced. However, its tribological are too poor for bearing surfaces.
- Titanium (Ti) alone is considered to be one of the most bio-compatible materials. Its mechanical properties (smaller Young's elastic modulus and low fracture stress) have limited application in joint replacement, so titanium alloyed with aluminum (Al) is best suited for femoral stems. Its bio-compatibility is however reduced in this way due to the presence of toxic elements.

### 2.9.1.2 Polymers

UHMWPE is a subset of semi-crystalline thermoplastic polyethylene materials and exhibits a considerable toughness with a very high impact strength. It's highly resistant to corrosive chemicals, exhibits a low friction coefficient, is self-lubricating and highly resistant to abrasion. The bulk material can be considered as inert even though its wear particles are not [28]. The viscoelasticity of UHMWPE is able to compensate for slight component misalignments and poor working tolerances without causing excessive stresses on the bearing [58, 59]. However, the wear properties of UHMWPE are still limiting the lifespan of MoP hip implants, due to the adverse reaction of bone tissue triggered by the release of the wear debris in vivo.

### 2.9.1.3 Ceramics

Used in THA since the 1970s, the hardness and the wettability of ceramic surfaces results in excellent abrasion and wear resistance [60]. Three types of ceramics are used in hip implants:

- Alumina is the short for aluminum oxide and represents the gold standard in THA due to its high compression strength, high hardness and its resistance to abrasion and chemical attack. Its hydrophilicity plays an important role on the lubrication efficiency under friction. However, this is a brittle material and cannot stand elevated tensile and impulsive stresses.
- Zirconia is the short for zirconium oxide exhibits lower hardness than alumina but higher fracture toughness.
- Alumina-Zirconia Composite Ceramics have been developed in order to take advantage from both types of ceramics, improving the ageing behavior of zirconia and to reducing the brittleness of alumina.

## 2.9.2 Components of Modular Hip Prosthesis

Developments in the field gave way to material combination in order to combine advantages of more than one of the materials above described. Figure 2.39 shows a generic modular hip prosthesis, which is constituted by two main

components: the acetabular component, which includes the liner and the shell, and the femoral component, which comprises the stem and the head. At the end of this subsection, the information is summarized in Table 2.2, crossing information on the different materials enumerated in subsection 2.9.1 and the components below presented.

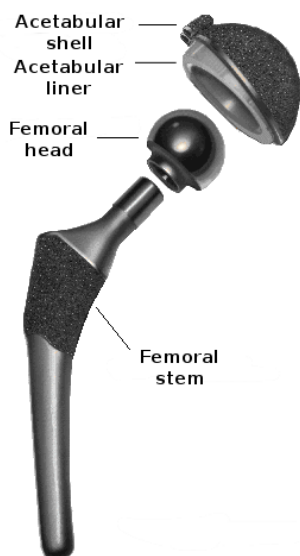


Figure 2.39: Components of modular hip prosthesis [25].

### 2.9.2.1 The femoral stem

After the femoral neck osteotomy and the drilling and broaching of the medullary canal, the femoral stem is inserted (see section 2.8.3). The femoral stem firmly fixes to the femoral bone ensuring an uniform load transfer from the prosthesis to the lower limb. The fixation strategy (press-fit or cemented) influences its design, the material choice and the surface finishing. Among all, it is the component that bears the highest mechanical stresses and therefore must feature high mechanical strength and fatigue resistance. Hence, metals are the gold standard for stem manufacturing.

Stem length directly relates to the device stability: a longer stem would improve stability at the cost of a higher bone mass removal. It would require more reaming and in the case of cemented prosthesis, more distally cement deployment which consequently results in less bone availability in case of a revision surgery.

The cross-section is designed to ensure rotational stability and to reduce stress concentration around the device [25]. Some stems feature a collar in correspondence of the calcar bone on the medial side, just below the neck. The function of such is to ensure primary fixation of stems, to transfer loads to calcar bone and to avoid prosthesis subsidence [61].

The neck angle is another important parameter that influences the load transfer of the whole stem and therefore its long-term resistance. Generally, the stem and the neck are part of the same metal component, although rarely

they are independent and coupled by means of a taper junction. This is said to increase the degree of customization of the implant and more closely meet the patient specific anatomy in terms of neck length and orientation [62].

#### **2.9.2.2 The femoral head**

Tapered to the femoral stem, it is one of the contact surfaces of the prosthetic hip joint. Its diameter plays an important role in determining the range of motion of the artificial joint as well as its stability against dislocation. Critical parameters for the manufacturing of femoral heads are: minimal surface roughness, which influences friction and wear rate; maximum outer diameter; mechanical resistance of the material to the tensile stresses generated along the taper junction. The femoral head diameter and range of motion will be more carefully looked into in section 2.9.3.3.

Ceramic heads are the smoothest, resulting in the lowest friction coefficients, but their maximum diameter is limited by manufacturing techniques to about 38-40 mm [63]. Increasing femoral head diameters improves the stability [64] and increases the range of motion of the artificial hip joints at the cost of their toughness, i.e., the risk of fragile fracture.

#### **2.9.2.3 The acetabular liner**

Also named insert, the socket is the counterpart of the femoral head. It usually features a half-spherical cavity that represents the tribological surface worn by the action of the femoral head. In a hard-soft material coupling (MoP, for example), it is the cup that corresponds to the soft component and is consequently the component that wears out more quickly. This choice can be seen as a precaution because, in a spherical head-socket configuration, it ensures a geometrical alteration on the shape of the components does not interfere too much with the relative motion kinematics.

The liner is mechanically locked into the shell. Its choice is dependent on the thickness of the shell, which ensures the mechanical stability of the acetabular cup. In addition, its maximum diameter is dependent on the iliac cavity size so if a relatively high femoral head size is required, a CoCrMo liner has to be used in order to provide mechanical stability with the remaining low thickness.

#### **2.9.2.4 The acetabular shell**

The shell attaches to the iliac bone, either with the use of PMMA cement or by press-fitting. Its fixation can be strengthened by the use of screws inserted into the massive pelvis bone. The design of the external surface is once again conditioned by the fixation method. Uncemented shells present a porous surface finishing, for example Ti beads, or hydroxyapatite coatings to foster improved bone integration. Comparing the stress level of the shells to the stems, it can be concluded that it is lower and therefore allows the fabrication of pure titanium shells.

MoM shell and liner couplings may be fabricated from the same material and the acetabular cup may consist in only a single component. The problem related to this is that in a revision surgery the shell may still present good bone

integration and its removal should be avoided. Thus, a two-module acetabular cup allows the preservation of a well fixed shell, replacing only the worn out liner. When a UHMWPE or ceramic liner is used, the shell ensures the mechanical strength of the acetabular component.

Component	Material Class	Most used material
Femoral stem	Metal	CoCrMo-wrought, Ti-alloys, stainless steel
Femoral head	Metal	CoCrMo-cast, stainless steel
	Ceramic	Alumina, Zirconia
Acetabular cup liner	Polymer	UHMWPE, Cross-linked UHMWPE
	Metal	CoCrMo-cast
	Ceramic	Alumina, Zirconia
Acetabular cup shell	Metal	Commercially pure Ti, stainless steel

Table 2.2: Summary of material selection for THA components.

### 2.9.3 Design Criteria

Due to the materials properties and forces that the components are subjected to during the patients' everyday physical activities, some criteria has to be taken in account in prosthesis planning. Although some of this has been mentioned in previous sections 2.9.1 and 2.9.2, it is important to extensively look into the fixation method of the prosthesis, the fatigue resistance and stiffness of the shell and the femoral head diameter and range of motion.

#### 2.9.3.1 Fixation methods: cemented vs. uncemented prosthesis

As seen in section 2.8.3, the fixation of both the acetabular cup and the femoral stem components can be achieved by pressing against the bone or by using acrylic bone cement (PMMA is the gold standard material).

In cemented THAs, the cement does not bond the prosthesis to the bone but rather acts as a filler occupying the space between prosthesis and surrounding bone. Hence, it fixes the prosthesis in its position and creates a stable interface allowing uniform load transfer between the bone and the implant, preventing high local stresses that can lead to periprosthetic fractures or implant loosening. Disadvantages attached to the use of cement are mainly related to its dense polymerized structure that does not allow osseointegration for improved bone fixation or to its exothermic reaction, which may cause necrosis of the surrounding bone tissue, leading to implant loosening. In addition, it requires high surgical skills for its preparation, which is done in a short time window during the surgical intervention. A slightly too low monomer content may reduce both toxicity and polymerization peak temperature and a slightly too high monomer content makes the cement too liquid, distributing inhomogenously around the implant due to its tendency to flow [31].

On the other hand, uncemented THA relies on the close surface contact of the implant and the prosthesis that enables bone integration. In order to promote long-term osseointegration, components might exhibit a porous

surface finish [55] or coatings [52]. These pores are intended to be filled by newly formed trabecular bone tissue. The shape of uncemented stems exhibits edges and grooves, which are meant to mechanically enhance primary fixation. However, the long-term fixation also depends on the patient's health status and age, which influence the capability of bone growth in the femur-prosthesis interface and therefore the stability of press-fit implants. Younger patients have biologically more active bone tissue, hence they are more suited for an uncemented prosthesis. In addition, this group will likely undergo revision surgery which is complicated by the presence of cement and cement debris. The more sophisticated surface requirements for uncemented devices makes their fabrication more expensive when compared to cemented prosthesis [65].

### **2.9.3.2 Fatigue resistance and stiffness of the stem**

Mechanical fatigue describes failure of a material that has been subjected to oscillating mechanical loads, even if these are of an inferior magnitude than the static load material can support. This is a consequence of accumulating micro-structural damage that nucleates microscopically small cracks which then propagate until fracture. Shape and surface finish significantly affect the fatigue life. The loading conditions of the stem are so demanding that femoral stem fatigue fracture can be a concern.

The stiffness or rigidity determines the extent to which a component resists to deformation in response to an applied force. It is determined by geometrical parameters, such as cross-sectional area, shape and length of the stem and by the elastic modulus of the material [25]. It influences the interaction with the surrounding bone tissue which exhibits very different and varying mechanical properties, due to bone remodeling. Therefore, the implantation of a hip prosthesis is drastically changing the normal physiological load transfer leading to bone response [66].

The elasticity of bone is significantly lower than most of the major prosthesis materials. This mechanical mismatch may cause stress shielding where the prosthesis do not transfer load to the surrounding bone. Insufficiently loaded bone responds with bone resorption which will compromise the long-term clinical performance of the prosthesis [66].

The combination of these concepts and the two previously fixation strategies (see 2.9.3.1) leads to different stiffness requirements for cemented and uncemented prosthesis. Cemented prosthesis should feature a higher stiffness to reduce the amount of stress transmitted to the bone cement in order to avoid cement fracture while cementless prosthesis should present a lower stiffness so that it better matches the properties of the surrounding bone [1]. Hence, frequently cemented stems are made of CoCrMo or stainless steel while uncemented stems are made from Ti alloys, which have a significantly inferior elastic modulus.

### **2.9.3.3 Femoral head diameter and range of motion**

Recent trends point to larger femoral head diameter, which best reproduce the anatomy of a healthy hip joint, enhancing stability against dislocation and a wider range of motion [64]. Both factors influence the level of post surgical physical activity accomplished by the patient. For metal or ceramic

on UHMWPE joints an increased head size yields results in a larger sliding distance and higher sliding velocity on the articulating surfaces and thus on increased polymer wear. Hence, the usage of UHMWPE on large femoral heads is limited. In addition, the inner and outer diameter of the acetabular liner would consequently have to become larger too which is not feasible due to the anatomical size of the pelvis cavity. On the other hand, a thinner shell couldn't provide sufficient mechanical stability to support a soft or brittle material for the liner. Thus larger femoral head sizes require metallic liners or monoblock acetabular cups to provide enough mechanical strength [63].

MoM couplings are currently the only material choice for prosthesis with large diameters for the femoral head and this is the reason why all hip resurfacing systems, which include 58-60 mm femoral head diameters, are MoM devices.

#### 2.9.3.4 Wear, wear processes and lubrication conditions

Wear is considered to be the most important limitation in long term stability of hip implants [67]. Very succinctly, it quantifies the erosion or the sideways displacement of material from its original shape and position on a solid surface performed by the action of another surface. Wear depends on three factors:

- the load compressing the two surfaces and determining their contact stress;
- the relative motion that continuously modifies the location and extent of the contact area;
- the lubricant interrupting the direct contact of the two surface.

The study of the processes of wear is part of the discipline of tribology. The complex nature of wear has delayed its investigations and resulted in isolated studies towards specific wear mechanisms or processes. Some commonly referred to wear mechanisms (or processes) include:

- Adhesive wear quantifies the plastic deformation in very small areas of the surface layers resulting in increasing surface roughness and the creation of protrusions above the original surfaces. In THA this condition is observable in UHMWPE surfaces.
- Abrasive wear occurs when a hard rough surface slides across a softer surface (e.g. MoP) and the softer material is abraded by the microscopic asperities on the harder surface.
- Third body wear is a particular case of the abrasive wear caused by the hard particles of a third material entrapped in between the surfaces. Its presence can cause damage even on the harder surface. Such situation can be created after a revision of a fractured CoC implant, when residual ceramic fracture debris may cause massive wear on the replacement implant [68].
- Surface fatigue occurs when the surface is weakened by cyclic loading producing wear particles that are detached by cyclic micro-crack growth.
- Corrosion related wear is a material degradation process due to the combined effect of corrosion and wear. It mainly occurs when friction destroys an oxide passivation layer and exposes fresh material to corrosion thereby creating new oxide on the surface [69].

The manufacturing technology plays a key role in surface finishing, namely in achieving a low residual surface roughness and hence controlling the distance between the surfaces, also known as clearance. Ideally, fluid-film lubrication is due, where there is a complete separation of the surfaces (Fig. 2.40c) and consequently producing the lowest wear amounts. It can be achieved with a CoC pairing due to the extreme hardness of ceramics. However, softer materials such as UHMWPE or even the metal alloys limit the regime of lubrication to the boundary condition (Fig. 2.40b) due to achievable imperfect surface finish.

In summary, CoC is the best choice for minimizing wear due to its highest hardness, scratch resistance, wettability and good lubrication. A combination of ceramics with metal alloys or UHMWPE represents a good trade-off between low wear, articulation size or fracture resistance. Table 2.3 synthesizes the tribological couplings used in THA, as well as in Hip Resurfacing Surgery (HRS).

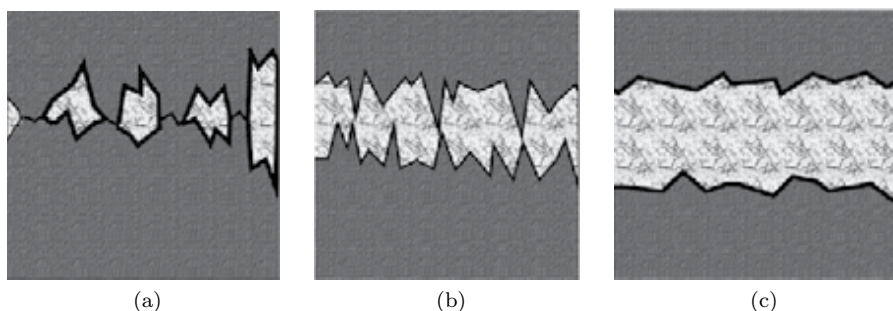


Figure 2.40: Schematic representation of the lubrication regimes between two contact surfaces, as for example the femoral head and the acetabular liner. (a) exemplifies boundary lubrication, (b) mixed lubrication and (c) the ideal fluid-film lubrication [1].

## 2.10 Hip Implant Failures

As seen on section 2.8.1, hip arthroplasty and more specifically hip implants have evolved due to advancements in implant design, materials, surgical technique and anesthesia [70]. This is reflected in an increased durability of the arthroplasty and decreased prevalence of complications. The surgery now reports success rates of greater than 95% in many series with a longer than 10-year follow-up [71]. Even though artificial hip joints are designed to last at least 20 years, their lifespan is often limited by wear. The clinical long-term outcome of THA depends on the factors related to the applied type of prosthesis, the health status of the patient and his post-operative physical activities, but also depends critically on the expertise and practice of the surgeon.

Revision surgery comes when a failed hip implant can only be repaired by another surgery. These second procedures are considered complex and significantly invasive: revisions require more planning, more time to complete and more experience on the part of the surgeon. The risk of complications is also greater than for a primary hip replacement.

Comb.	Advantages	Disadvantages	Remarks
<b>MoP</b> (UHMWPE)	<ul style="list-style-type: none"> <li>- Most commonly used, longest experience and follow-up.</li> <li>- Most economic device.</li> </ul>	<ul style="list-style-type: none"> <li>- High PE wear volumes.</li> <li>- Late aseptic loosening.</li> <li>- Insufficient longevity for patients younger than 65 years old.</li> </ul>	<ul style="list-style-type: none"> <li>- Wear rate <math>\approx</math> 0.1 mm/year.</li> </ul>
<b>MoP</b> (cross-linked UHMWPE)	<ul style="list-style-type: none"> <li>- Reduced wear rate and risk of aseptic loosening.</li> </ul>	<ul style="list-style-type: none"> <li>- Very recent, limited follow-up studies.</li> </ul>	<ul style="list-style-type: none"> <li>- Wear rate <math>\approx</math> 0.01-0.02 mm/year.</li> </ul>
<b>MoM</b>	<ul style="list-style-type: none"> <li>- Low volumetric wear rate.</li> <li>- Improved joint stability due to larger femoral heads.</li> <li>- Low rate of aseptic loosening.</li> </ul>	<ul style="list-style-type: none"> <li>- Risk of metallosis, metal allergy or hypersensitivity.</li> <li>- Unknown long-term effect of exposure to metal ions.</li> </ul>	<ul style="list-style-type: none"> <li>- Wear rate <math>\approx</math> 0.005 mm/year.</li> <li>- Represent 1/3 of all THAs in the US.</li> </ul>
<b>MoM</b> <b>HRS</b>	<ul style="list-style-type: none"> <li>- Femoral bone conserved; eases revision surgery.</li> <li>- Improved joint stability and range of motion due to larger head.</li> <li>- Low volumetric wear rate.</li> </ul>	<ul style="list-style-type: none"> <li>- Surgically more complex.</li> <li>- Increased risk of neck fracture.</li> <li>- Risk of excessive wear.</li> <li>- Pseudotumors observed.</li> <li>- Increased metal ion concentration in the blood flow.</li> <li>- Possible toxicity of the wear debris.</li> </ul>	<ul style="list-style-type: none"> <li>- Wear rate <math>\approx</math> 0.005 mm/year.</li> <li>- Not suitable for people with renal insufficiency and pregnant women.</li> </ul>
<b>CoP</b>	<ul style="list-style-type: none"> <li>- Wear rate reduced compared to MoP.</li> <li>- Elasticity of UHMWPE mitigates fracture risk of ceramic head.</li> </ul>	<ul style="list-style-type: none"> <li>- Residual PE wear with risk of aseptic loosening.</li> </ul>	<ul style="list-style-type: none"> <li>- Wear rate <math>\approx</math> 0.03-0.1 mm/year.</li> <li>- Wear rate <math>\approx</math> 0.01 mm/year when using cross-linked UHMWPE.</li> </ul>
<b>CoM</b>	<ul style="list-style-type: none"> <li>- Improved joint stability and range of motion with larger heads.</li> <li>- Low volumetric wear rates.</li> </ul>	<ul style="list-style-type: none"> <li>- Catastrophic fragile fracture of the ceramic components.</li> <li>- Wear debris even smaller than MoM.</li> </ul>	<ul style="list-style-type: none"> <li>- Reduced in vitro wear rates.</li> <li>- CoCrMo cup give way to larger ceramic heads.</li> </ul>
<b>CoC</b>	<ul style="list-style-type: none"> <li>- Lowest wear rate.</li> <li>- Weak tissue interaction with ceramic wear debris.</li> <li>- High scratch resistance.</li> <li>- Very low surface roughness.</li> <li>- Good lubrication conditions.</li> <li>- High wettability.</li> </ul>	<ul style="list-style-type: none"> <li>- Catastrophic fragile fracture of the ceramic components.</li> <li>- Squeaking affects 1-20% of the patients.</li> <li>- Most expensive device.</li> </ul>	<ul style="list-style-type: none"> <li>- Wear rate <math>&lt;</math> 0.003 mm/year.</li> <li>- Head diameter up to 40 mm.</li> <li>- Head failure rates below 0.02-0.004%.</li> </ul>

Table 2.3: Summary of the most important advantages and disadvantages of tribological couplings in THA [1].



Mechanical failure is often multi-factorial and depends on materials, design [72], surface finish [73], position, bone quality or disproportionate biological response to wear debris [74]. Ulrich [71] extensively compiled available information on implant failure and the main reason for implant failure is aseptic loosening, which accounts for more than half (51.9%) of the 237 revised implants revised implants. Other reasons that lead to a secondary hip replacement, by order of significance, are instability (16.9%), infection (15.6%), pain (8%), and periprosthetic failure (7.6%). In the same paper crossed his data with other studies and corroborated this trend in hip implant failures. Hence, in this section some of these failure mechanisms will be looked into with more detail, because the THA marks the beginning and not the end of the treatment [27].

In conclusion, although total hip arthroplasty has become an extremely successful operation, a proportion of failures are inevitable. As the procedure evolved, significant resources have been deployed to reduce the rate of failure attributable to implant design or manufacturing techniques. Other factors related to the insertion procedure are under the control of the surgeon and are therefore optimizable.

### **2.10.1 Aseptic Loosening**

The most common reason for revision surgery is the loosening of the femoral stem and/or the acetabular cup. This means that the components lost contact with the bone or cement and are allowed some dislocations in the directions of the arrows in figure 2.41, for example that influence the normal function of the prosthetic joint.

There are several reasons that might lead to a situation like this such as misalignment of the cup that may increase to hip loads and promote femoral loosening or an insufficient contact between the bone and implant that may cause stress shielding and influence negatively bone remodeling in the areas where it no longer carries load. Aseptic loosening has been traced back in MoP prosthesis to an inflammatory response to polyethylene wear debris. Due to the relatively high polyethylene wear rates (Table 2.3), exposure to the wear debris occurs during the whole lifespan of the component. Wear particles larger than a certain threshold size (0.2 - 0.8  $\mu\text{m}$ ) are phagocytised by macrophages which activates the osteoclasts leading to periprosthetic osteolysis [75].

Aseptic loosening can affect patients even decades after the surgery following a period of subtle progression of periprosthetic tissue destruction in response to exposure to wear debris. Although it has not been reported as an important failure mechanism in MoM implants, metallurgical improvements of CoCrMo alloys and reduced fabrication tolerances for prosthetic devices motivated the resurgence of MoM implants nowadays. However, MoM wear debris ions have been associated with the abnormal soft tissue reactions (section 2.10.2).

### **2.10.2 Pseudotumors**

Recently, in patients who underwent a hip resurfacing have been observed sterile inflammatory lesions found in the soft tissues surrounding the MoM implant with still unclear pathogenesis. Since the biopsy of these lesions is difficult to

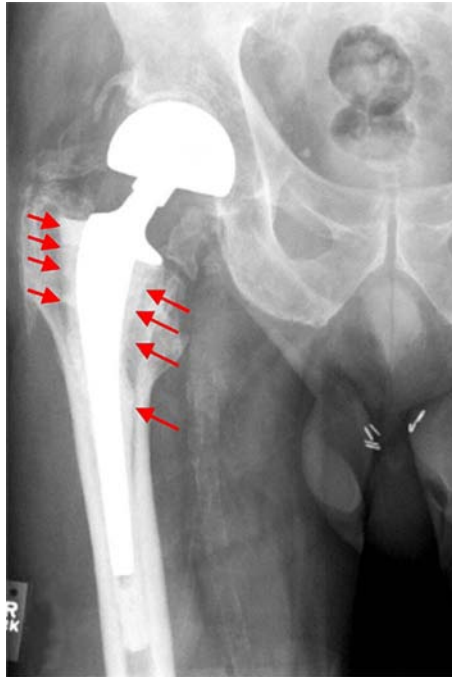


Figure 2.41: Radiography of an example of aseptic loosening of the femoral stem in a THA. Image of public domain.

distinguish from necrotic tumor tissue, they were labeled pseudotumors [33]. It has not been proved in the literature that the early failure of conventional MoM prosthesis with a large femoral head is related with the formation of pseudotumors, although it is thought to be related to tiny metal debris particles. Their incidence is accompanied by increased metal ion concentrations in blood serum which points to excessive wear as a possible reason [33, 76].

### 2.10.3 Dislocation

Dislocation is described as the physical disconnection between the femoral head and the acetabular cup and is a common complication in the first few weeks after the surgery (Fig. 2.42), when tissue has not yet been recovered with a particular incidence for low diameter femoral heads. This condition strongly depends on the amount of damaged tissue and therefore on the approach and experience of the surgeon (section 2.8.3).

### 2.10.4 Fracture

Bones with internal fixation devices *in situ* are at risk of periprosthetic fractures at the end of the implant, an area of relative mechanical stress. Moreover, the breakage of stem has also been observed, even though more frequently in the past and with cemented prosthesis. Oscillating gait loads may lead to fatigue failure, when the distal part was well fixed with cement, whereas the proximal part was loose. An example of a stem breakage is shown in Figure



Figure 2.42: Radiography of an example of implant dislocation in a THA. Image of public domain.

2.43. Improved implant design and cementing techniques have significantly decreased the rate of incidence of this issue.



Figure 2.43: Radiography of an example a broken femoral stem in a THA. Image of public domain.



## Chapter 3

# Femur Segmentation

In this chapter, an overview of the problem of the segmentation of the femur is presented, enumerating some of the different approaches to the development of three dimensional computational models from medical images. Hard tissue segmentation, such as bone tissue, is enhanced by CT images. Therefore, this chapter starts by presenting its basis and fundamentals, followed by a brief explanation of how the acquired images are encoded - the Digital Imaging and Communications in Medicine (DICOM).

Lastly, there will be a section focused on medical image segmentation itself. It starts by enumerating the main issues of medical image analysis. Then, the principles of the most well-known techniques of image segmentation are presented: threshold, active contours, shape models, graph-cuts and clustering segmentations. Shape model based segmentation is reviewed thoroughly as it was the author's choice over the remaining. A table featuring the advantages and disadvantages of the presented methods is shown at the end of the chapter, for comparative purposes.

In sum, the development of an algorithm that automatizes the process of femur segmentation is complex and time consuming, although it can be achieved with relative accuracy as shown in this chapter. Hence, it is the author's intention in the present thesis to understand the advantages of the different approaches and develop an approach that outperforms the documented approaches by its accuracy and time consumption. This way, its inclusion in a software for the planning of the hip joint replacement is possible.

### 3.1 Computed Tomography scan

X-Ray, for example, allows the *in vivo* acquisition of femoral images, as its intensity is attenuated differently when projected through a body to a detector, according to the media it travels through. Projections taken in several angles around the area of interest can be reconstructed into a 2D image, or slice, in the axial plane, using tomographic techniques. The intensity of each reconstructed pixel is measured in Hounsfield Units (HUs) and computationally represents the density of the tissue. A volumetric image can be constructed from a series of slice images. CT and Magnetic Resonance Imaging (MRI) allow the combination of 2D images to create a 3D image domain. While CT imaging is based on X-Rays, MRI uses a magnetic field and pulses of radio wave energy

to make images of the human body. CT, when compared to MRI, presents a similar spatial resolution but much higher temporal resolution and is more cost effective. Because our volume of interest is bone tissue, CT is more suitable to acquire it due to the mineral composition of the bone which gives it exceptional contrast in X-ray images.

CT scan as we know it today was first introduced by Sir Godfrey Hounsfield in 1972 and granted him a Nobel prize for such accomplishment. It was considered to be a turnover point in medical imaging as it allowed a look inside the human body without the superimposition of organs intrinsic to two dimension imaging. This way, occluded tumors and other organs' anatomical pathologies could be diagnosed for the first time without the need of invasive surgery.

### X-Ray Imaging Theory

Given a tissue between the X-rays source and the detector, the beam is attenuated by two main phenomena: Compton scattering and the photoelectric effect. Compton scattering is the inelastic scattering of a photon by a charged particle, the X-ray in this case, with an atomic electron, resulting in a decrease in energy due to the energy transfer to the electron. In photoelectric effect interaction the energy of the photon is completely absorbed by the electron, causing it to be ejected from the atom. In both cases, scattering and absorption, the beam is attenuated, due to the decrease in the number of photons that reaches the detector and also their energy. This attenuation can be quantified according to Beer's law:

$$I_{out} = I_{in}e^{-\int \mu(x)dx} \quad (3.1)$$

where  $I_{out}$  and  $I_{in}$  are the incident and detected X-ray beams intensity and  $\mu$  is the attenuation coefficients in the direction  $x$ . Godfrey Hounsfield normalized these attenuation coefficients with water as reference and used in equation 3.2 to quantify the different tissue coefficients. Considering  $\mu_{tissue}$ ,  $\mu_{water}$  and  $\mu_{air}$  as the attenuation coefficient of the tissue, water and air, respectively, Hounsfield Unit (HU) is given by

$$HU_{tissue} = \frac{\mu_{tissue} - \mu_{water}}{\mu_{water} - \mu_{air}} \times 1000 \quad (3.2)$$

In X-ray CT, scanning parameters are calibrated so that water has a HU of 0 and air of -1000. This way, it is possible to establish a correspondence between the human body tissue and its value on the HU scale. However, this correspondence is not exclusive as some tissue or substances share the same values. Table 3.1 shows the average HU values intervals for the corresponding tissue. About the inaccuracy of these intervals, one has to take in account that the values are dependent on the incident beam, as well as on the scanner calibration and the patients' age and gender.

The ground limits for the HU scale are  $[-1000, 3000]$  and therefore a 12 bit value voxel, ranging from -1024 to 3071, is commonly used to represent the scale. However, CT scanners' output might be different and therefore a conversion is needed. The manufacturers usually append two additional tag constants called *RescaleSlope* and *RescaleIntersect* that allow the conversion according to equation 3.3.

$$HU = VoxelValue \times RescaleSlope + RescaleIntersect \quad (3.3)$$

Tissue	HU interval
Air	$[-1005, -995]$
Lung	$[-900, -500]$
Fat	$[-200, 50]$
Mamma	$[-100, -50]$
Water	$[-5, 5]$
Intestine	$[5, 35]$
Kidney	$[20, 40]$
Heart	$[20, 50]$
Tumor	$[20, 50]$
Pancreas	$[30, 50]$
Spleen	$[40, 50]$
Muscle	$[40, 50]$
Blood	$[50, 60]$
Cancellous Bone	$[50, 250]$
Liver	$[60, 70]$
Thyroid	$[60, 80]$
Bone	$[250, 3000]$

Table 3.1: Intervals in the Hounsfield scale for the most common tissues in the human body [77].

Even though they allow an initial straightforward approach to an identification and segmentation problem, they can't be determinant. If we look at the diverse organs listed in table 3.1, they all present a very similar interval, characteristic of soft tissues. This allows us to conclude that X-ray might not be the best modality to acquire such anatomical structures. On the other hand, bone tissue is immediately identifiable and simply segmented, with exception for cancellous bone tissue.

### Tomography

Tomography is the process by which projections through an object from multiple angles are reconstructed into a planar or volumetric image. It was pioneered by Johann Radon [78] in 1917. On a planar image, the Radon transform is the integral of any line through the image. In conventional X-ray CT, these lines are obtained by projection of a fan-shaped beam that rotates synchronously around an object. Applying the inverse Radon transform on the obtained multiple lines at known angles gives a gray-scale image composed by the different densities of the objects' internal materials. The modern X-ray CT uses a cone-shaped beam instead of a fan-shaped, because of the incorporation of multiple detector rows, and every projection is a 2D section through a 2D volume instead of a One Dimensional (1D) section through a 2D slice.

As mentioned above, the 3D reconstruction is based on the projections that are acquired. Overall, the more projections and therefore angles, the more accurate the reconstruction. This is the reason why manufacturers designed the X-ray source and detectors at opposite ends of a ring centered around the long axis of the target, as seen in Figure 3.1.

As the ring spins, a large number of projections can be quickly taken and reconstructed into a 3D image. Then, the ring incrementally moves along



Figure 3.1: Example of a modern CT scanner. Image of public domain.

the center axis of the target continuously taking new projections in order to reconstruct the next slice.

Although at first glimpse the process seems relatively simple, it's not time effective and requires the patient to lie still for long periods of time. Patient movements reflect in image artifacts that difficult and sometimes even makes impossible the process of segmentation of the volume of interest. This will be more extensively looked into further along the thesis.

### 3.2 Digital Imaging Communications in Medicine

As seen in previous section 3.1, a CT scan generates a finite set of cross-sectional images taken along the patient. Each of these slices is then saved in the DICOM format. This is the standardized format for handling, storing, printing and transmitting information in medical imaging. The name appeared in 1993 in an attempt to standardize the images that CT and MRI devices generate. Attached to the image itself, it comes with useful information for the doctor, such as the patient name, gender and age, the patients position in relation to the medical system, the pixel resolution, the slice spacing and the time and place of acquisition, among others. The variables needed for equation 3.3 are also part of this attached information.

The Computed Tomography Imaging Coordinate System (CTCS) is a standard for all manufacturers and is defined as follows: the  $z$ -axis coincides with the path of the center of the acquisition ring, i.e., along the superior-inferior axis of the patient in supine position, i.e., lying face upwards; the  $y$ -axis is defined as from sky to earth (antero-posterior axis of the patient in supine); and the  $x$ -axis is the floating axis, the common perpendicular to the two previous ones (transverse axis in the patient in supine). In case the acquisition is made with the patient in other position than supine, the DICOM usually provides information about the transformation between the CTCS and the image Reference Coordinate System (RCS) so that it's possible to map objects orientation computationally.



Volume reconstruction starts with the storage of the position of every slice when acquired along the  $z$ -axis, resulting in a 3D grid when stacked together. The resulting volume of the region of interest is then transformed if necessary to reach coordinate systems compliance. Figure 3.2a shows the stack of images from the CT scanner. Figure 3.2b shows the image after conversion to the HU scale according to Equation 3.3 and Figure 3.2c shows the same volume reconstruction with different HU values that enhance soft tissues and make fat and bones distinguishable. All three images were transformed in order to resemble the standing up position, although the patient was lying down in the CT scanner.

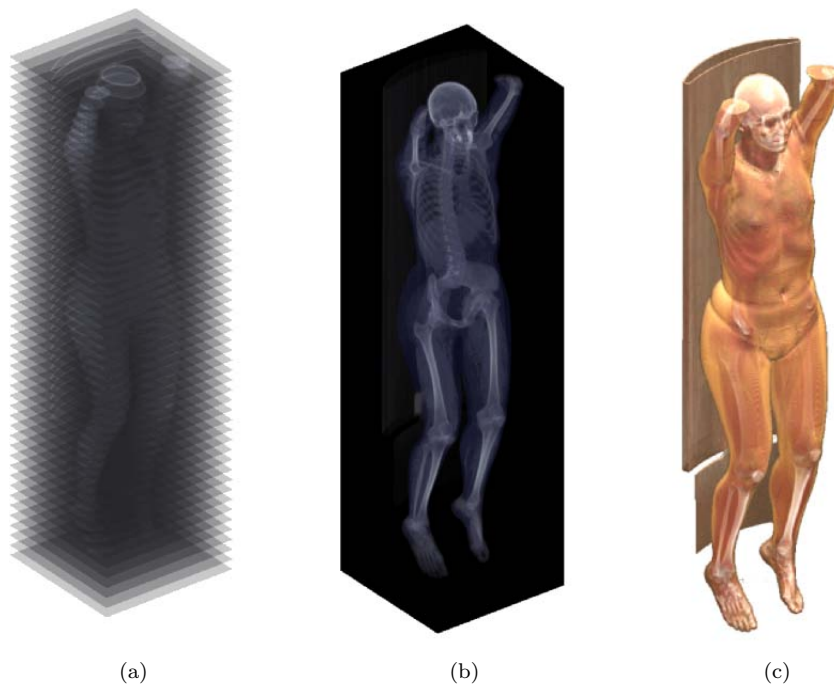


Figure 3.2: Volume reconstruction from CT scan. (a) shows the acquired images from the CT scan; (b) shows the conversion to HU with Equation 3.3; (c) shows the reconstruction of the same volume with HU of fat tissue, i.e., 200. [79].

### 3.3 Medical Image Segmentation

In image processing and computer vision, the process of image segmentation is defined as the partitioning of a digital image into multiple regions with the specific purpose of isolating the set of pixels corresponding to some object of interest from the remaining pixels. Therewith, it is possible to obtain a more or less precise definition of the border between these regions and proceed to represent it in a more meaningful way, generally easier to analyze. In other words, it's the process of finding the boundaries of our object of interest in the image and labeling the pixels according to a set of characteristics they share. Among these characteristics, the most common are color, intensity or texture.

Results are normally presented under the form of contours, which are curves in 2D and surfaces in 3D, that allow a reconstruction of the region or volume of interest. These can be done with the help of interpolation algorithms, such as the Marching Cubes [80].

In medical imagiology, the sprout and standardization of CT and MRI scanners allowed the exploration of the human body interior in a non invasive way, or nearly invasive if we consider the small effect of radiation. Human soft tissue organs as the liver or the heart or rigid structures as bones can be computationally represented with considerable levels of accuracy. This enormous breakthrough allows a patient-specific computational representation of the human body. It made possible the diagnosis and tracking of tumors in the most diverse body parts, as the brain [81, 82], otherwise inaccessible without major repercussions to the patient, or the skin [83], among others. It also allowed surgery planning or even real time guidance for computer assisted orthopedic surgery in the skull [84] or the knee joint [85]. In addition and more commonly, it gave way to computational representation of anatomical entities such as the liver [86], the pancreas [87] or the vertebrae [88]. These representations provide information about its properties and morphology and enhance possible abnormalities in shape that might be a pathological symptom. These segmented structures may also be used in statistical analysis which are used in morphometric studies to characterize a certain population of individuals. A more detailed insight on shape models will be featured in section 3.3.3.

With the increase in image resolution, to manually label the pixels of the object of interest in the image is very time demanding and requires a considerable expertise from the user. A common approach are semiautomatic methods in which the user has some interaction (input and supervision, usually) with the algorithm in order to achieve a more robust segmentation. Hence, the fully automation of the segmentation problems will be very time effective while providing a more straightforward doctor's approach to the diagnosis problem. However, due to the variance of anatomical organs or image artifacts, among others, a full automatic 3D segmentation from a CT or MRI scan is complex and usually computationally very demanding.

A glimpse on the state of the art of this matter makes clear that, among the several different segmentation techniques developed, it is not obvious to state which one provides the best results for a generic use. Khan [89] recently reviewed the different segmentation techniques and concluded that there is no perfect method for a generic image segmentation because the result depends on many factors, such as pixel color, texture, intensity, similarity of images, image content, and problem domain. Therefore, it is not possible to consider a single method for all type of images nor all methods can perform well for a particular type of image. Hence, it is good to use hybrid solution, i.e., that consists of multiple methods for image segmentation problem.

Generally, the binary segmentation of an image can be formulated as follows: assuming that  $I : \Omega \rightarrow \mathfrak{R}$  is an image on a grid of domain  $\Omega$ . Segmenting an object means finding a labeling function

$$A : \Omega \rightarrow \{obj, bkg\} \tag{3.4}$$

which classifies all the pixels as belonging to the object of interest (*obj*) or background (*bkg*). Then, the image can be considered as a union of two disjoint sections  $S_{obj}, S_{bkg} \subset I$ , where  $S_{obj}$  and  $S_{bkg}$  are the object and background

parts of the image, respectively. The image  $I$  is represented as a matrix of real numbers where its entries are values expressed in the Hounsfield scale (Sec. 3.1). However, due to the variability of the bone mass density along the body of the femur, it is not feasible to reach a band of values that exclusively represent bone tissue in the Hounsfield scale. Moreover, on the one hand, the diaphysis of the femur consists of rigid, strongly attenuating and dense cortical tissue, which exhibits high HU values in CT scans. On the other hand, the bone structure is significantly different in the epiphysis where more flexibility has to be provided due to pressure and body movement and therefore the interior bone consists almost exclusively of low-attenuating and vascular cancellous tissue, represented by low HU values.

Hence, the femur segmentation faces the following issues, also exemplified on Figure 3.3:

**Low-contrast and weak bone boundaries** Thickness of the cortical shell decreases rapidly towards the epiphysis area which results in low-contrast bone boundaries (in red and blue in Fig. 3.3). In elderly patients with chronically decreased bone density this problem is increased. Furthermore, the bone boundary often appears to be heavily diffused or is not visible at all, due to the presence of a cartilage or a vessel nourishing the bone interior.

**Varying density of cancellous tissues** Cancellous bone tissue is vascular and spongy which causes the bone to appear textured and inhomogeneous. Therefore, the density properties of bone tissues cannot be standardized. From the density perspective, the epiphysis interior partially resembles low-attenuating fat and soft-tissues (in yellow in Fig. 3.3); partially high-attenuating cortical tissue. This is the main reason why rudimentary segmentation techniques like thresholding or region growing inevitably yield insufficient results.

**Narrow inter-bone spacing** Articular space between adjacent bones is extremely narrow (in green in Fig. 3.3). Due to partial volumetric effect, inherently present in CT modality, the inter-bone regions are diffused and brighter and the bones appear as being in direct contact.

**Low quality of CT-scans** Seldom, the overall quality of CT scans is generally rather low. Volumes suffer from noise and low-resolution. Voxels are usually anisotropic with dimensions ranging from 0.5mm to 2mm. The resolution of a CT scan is often insufficient for the image processing purposes. Conversely, memory requirements coupled with software processing are very high with respect to the current computer capacities. Consider a CT volume of a resolution 512x512x1024. If four bytes per voxel are used for the HU, the volume size reaches 1GB.

In the following sections, the main segmentation techniques will be briefly reviewed with particular incidence to the ones on which this thesis has its foundations upon.

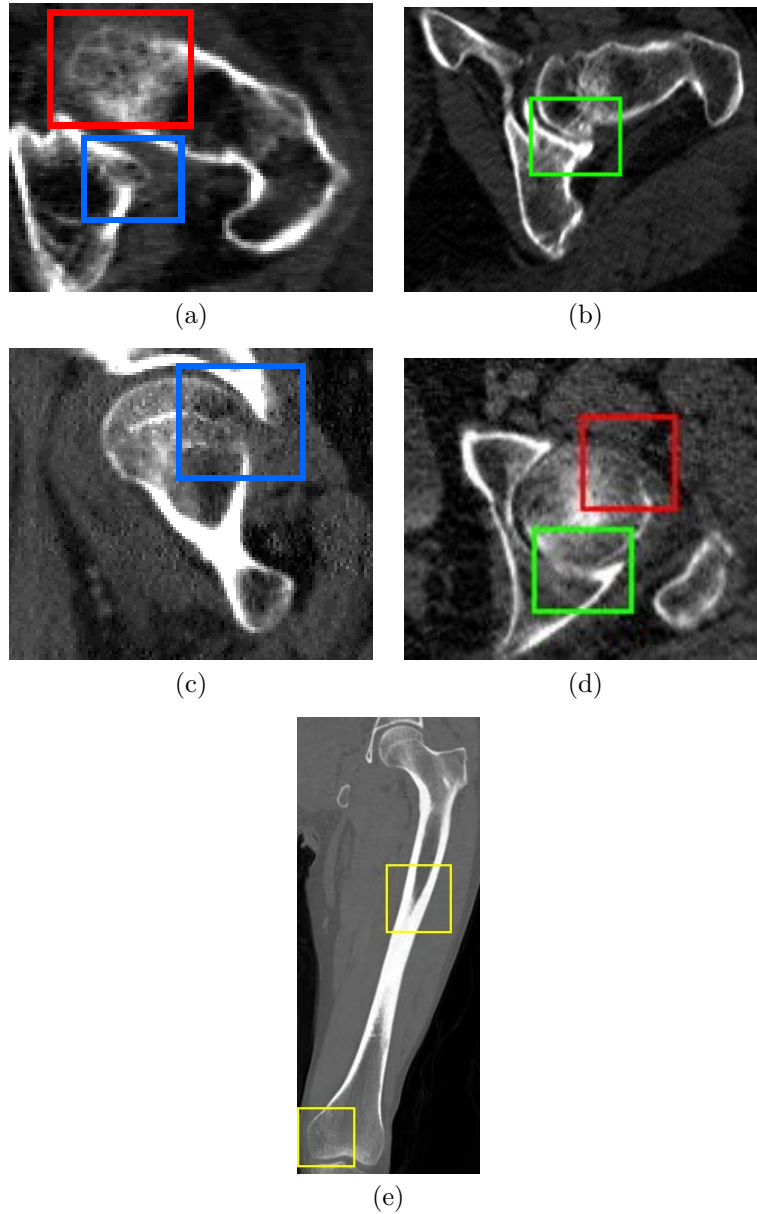


Figure 3.3: Common challenges in automatic femur segmentation from CT-scan volumes. In red, we can observe weak and diffuse bone boundaries; in blue, the same boundaries are nonexistent mainly due to osteoporotic bone tissue; in green, there is very little or no space in between the femur and the pelvis; finally, in yellow, we can observe the different intensity distributions for both cortical and cancellous bone, depending on their location in the femur.

### 3.3.1 Threshold Segmentation

The simplest form of image segmentation is called thresholding. Images with high contrast where the object of interest clearly differentiates from the background in the intensity spectrum. What the algorithm does is to define as background all the pixels above (or below) the user defined threshold, labeling them as 0 as opposed to 1 for the object of interest. Variations to this approach include bandwidth thresholding or automatic ways to estimate the threshold, as is Otsu's method [90].

However, when the object of interest presents variability in its intensity and its edges blend in with the background this approach becomes obsolete. As this is a problem often seen in medical imaging, many approaches have been developed to address this problem and will be reviewed in the following sections.

### 3.3.2 Active Contours Segmentation

#### Freely deformable models

Kass et al. [91] started the use of deformable models for image segmentation in their seminal snakes paper. The main idea behind them is the evolution of a curve to fit the boundaries of the object of interest in the image in an elastic way. It is the balance of two energies that drive the contour progression: an internal energy that stabilizes its shape based on general smoothness constraints, often based on the curvature, and an external energy that adapts the model to the image data. The energy functional controls the energy balance and its minimization leads to the optimal image segmentation. Terzopoulos, who was working with Kass, rapidly extended the snakes to three dimensions [92]. These became known as explicit active contours and the curve is represented by a parametric function such as  $C(s) = [x(s), y(s)]$  in 2D, where  $s$  is the parametric variable and usually lies within the interval  $[0, 1]$ . Equation 3.5 describes the energy functional for these contours:

$$E_{snake} = \underbrace{\alpha_{sn1} \int_0^1 |C'(s)|^2 ds + \alpha_{sn2} \int_0^1 |C''(s)|^2 ds}_{\text{Internal energy}} - \underbrace{\gamma_{sn} \int_0^1 |\nabla I(C(s))|^2 ds}_{\text{External energy}} \quad (3.5)$$

where  $I$  is the image to be segmented and  $\alpha_{sn1}$ ,  $\alpha_{sn2}$  and  $\gamma_{sn}$  are weighting constant terms. The internal energy of the curve depends on the first and second derivatives of the curve in respect to  $s$ , i.e., corresponds to the stretch elastic energy and the bending elastic energy of the snake respectively. They are responsible for the smoothness of the curve as they avoid unexpected sharp edges. The external energy term is based on the gradient of the image at the contour,  $\nabla I(C(s))$ . Regions where the intensity of the pixels varies abruptly which usually correspond to the edges of the object attract the contour towards them with the functional minimization. The algorithm is able to segment organs with well defined boundaries but depends on the initial placement of the snake in order to avoid the convergence to a local minima. The initialization is often user input. In addition, freely deformable models are topologically

inflexible, i.e., during the curve evolution it may not change its shape, split or merge.

In order to battle against objects with poorly defined boundaries, Delingette et al. [93] introduced the deformable simplex mesh, which features a stable internal energy that can easily be customized to deform towards a specific shape template. He based his approach on the fact that the shape of the object to segment is known *a priori* and added a term to the internal energy of the functional that took precisely that into account. However, the underlying deformation algorithm does not incorporate constraints of shape variability. Although freely-deformable models can be customized to represent specific shapes (and often are), the stabilizing forces or energies are based on general smoothness properties and are not driven by statistical information.

### Level-sets deformable models

Implicit active contours, also known as level-sets, were introduced by Osher and Sethian [94] and were made popular in computer vision and image processing by Malladi et al. [95]. They feature an implicit shape representation and can be employed with regional or edge-based features. They differ from freely deformable models because the curve is defined implicitly, i.e., the curve is defined as the zero level set of a high-order function  $\phi(\underline{x}, t)$ , where for 2D  $\underline{x} = (x, y)$ . An example of an implicit curve can be a circle  $\phi(x, y) = x^2 + y^2 - r^2$ , where  $r$  is the radius. Points outside the circle will have positive function values, whereas points inside the circle will have negative function values. At the boundary of the circle, points will have zero function values. These value mapping of the functional values is defined by its pixel distance to the zero level-set and constitutes the Signed Distance Function (SDF). The main advantages of such representation are its support for topological changes as split and merge, the possibility of representations in any dimension and its easiness of computational implementation. However, the level-sets are still not robust enough for objects with poorly defined edges. Figure 3.4 shows an example of the topological changes made possible by the level set method.

Chan and Vese [96] proposed an algorithm where the implicit active contour  $C$ , which evolves through time  $t$ , is defined as  $C = \{(\underline{x}) \in \Omega : \phi(\underline{x}, t) = 0\}$ , where  $\Omega$  is the image domain and  $\phi$  is the implicit contour function. However, this function is driven by region forces instead of the local image gradient. The exterior and interior intensity averages are calculated and its difference is maximized at each iteration. This way, gradient artifacts and noisy edges are often surpassed. The energy functional that controls the Chan-Vese algorithm is:

$$\begin{aligned}
 E_{CV}(c_1, c_2, \phi) = & \underbrace{\alpha_{cv} \int_{\Omega} |\nabla H(\phi(\underline{x}, t))| d\Omega + \beta_{cv} \int_{\Omega} H(\phi(\underline{x}, t)) d\Omega}_{\text{Internal energy}} + \\
 & \underbrace{\gamma_{cv1} \int_{\Omega} |I(\underline{x}) - c_1|^2 H(\phi(\underline{x}, t)) d\Omega + \gamma_{cv2} \int_{\Omega} |I(\underline{x}) - c_2|^2 (1 - H(\phi(\underline{x}, t))) d\Omega}_{\text{External energy}}
 \end{aligned}
 \tag{3.6}$$

where  $\alpha_{cv}$ ,  $\beta_{cv}$ ,  $\gamma_{cv1}$ , and  $\gamma_{cv2}$  are weighting constants,  $H$  is the Heaviside

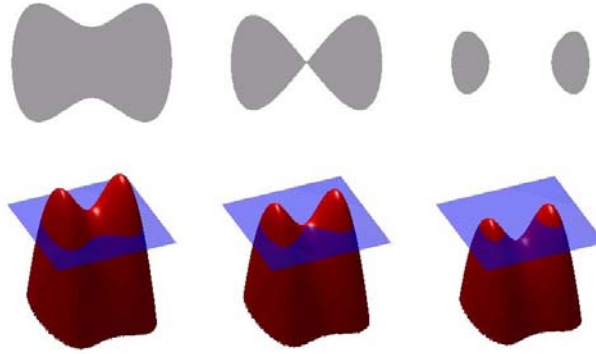


Figure 3.4: In the upper-left corner shows a bounded region and below it it the graph of a level set function  $\phi$  (in red) determining its shape. The plane in blue represents the xy-plane. The boundary of the shape is then the zero level set of  $\phi$ , while the shape itself is the set of points in the plane for which  $\phi$  is positive (interior of the shape) or zero (at the boundary). The columns in the center and the left show how advantageous is to work with a shape through its level set function rather than with the shape directly, where it's necessary to consider all the possible deformations the shape might undergo. Image of public domain.

function,  $c_1$  and  $c_2$  are the average intensities respectively inside and outside the contour, defined as:

$$c_1 = \frac{\int_{\Omega} I(\underline{x})H(\phi(\underline{x}, t))d\Omega}{\int_{\Omega} H(\phi(\underline{x}, t))} \quad (3.7)$$

$$c_2 = \frac{\int_{\Omega} I(\underline{x})(1 - H(\phi(\underline{x}, t)))d\Omega}{\int_{\Omega} (1 - H(\phi(\underline{x}, t)))} \quad (3.8)$$

The first two terms on Equation 3.6 corresponding to the internal energy take in account the length of the contour and its area, respectively. They are again smoothing terms and avoid interlacing of the contour, for example. The other two terms, corresponding to the external energy, are the energy terms accounting for the internal and external average intensities, respectively. They are responsible for the pulling and pushing of the contour. The balance is achieved when both are minimum. Figure 3.5, from left to right, shows the placement, the evolution and the final convergence for the Chan-Vese algorithm on a sample CT scan of the distal part of the human femur.

Simultaneously to Chan and Vese, and also in way to improve the poor results of the previous attempts, Leventon et al. [97] extended the original energy functional formulation by adding a term which deforms the contour towards a previously learned shape model. The inclusion of a shape prior term influences the contour evolution to the desired form, making the algorithm sensitive enough to find the true object boundaries but at the same time robust to image noise and even occluded parts of the object. However, a frequent criticism is that the SDF which the shape model is based on, does not form a linear space, which can lead to invalid shapes if training samples vary too much. Nevertheless and despite the considerable computational load of these

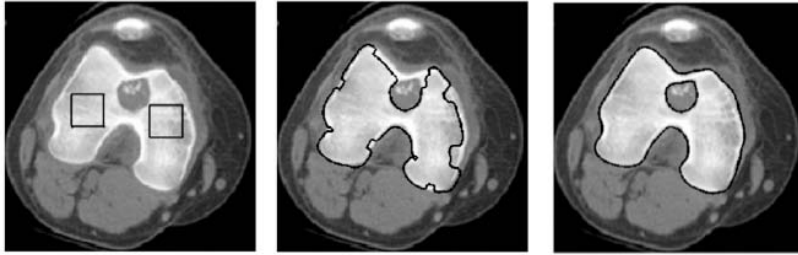


Figure 3.5: From left to right, placement, evolution and final convergence of the Chan-Vese algorithm on a sample CT scan of the distal part of the human femur.

models, the approach quickly gained popularity and was extended in several directions reviewed by Cremers et al [98].

### 3.3.3 Shape Models

Statistical Shape Analysis (SSA) is defined as the use of statistical methods to model the variations in shape of a determined object. It is able to locate and quantify shape differences, generate representative shapes or correlate shape to other measurements. Shape, in its turn, is defined as the geometric information invariant to translation, rotation and scaling. Nevertheless, when some SSA methods are applied to data, they contain more general information such as size and appearance.

The seminal work of Cootes et al. [99] in 1995 made SSA famous with medical imaging as it allowed not only the means to quantify shape variations of objects in images but also the tools to robustly segment the objects themselves. In this section, the theory and fundamentals of shape models will be reviewed.

Hence, the key steps in SSA are [100]:

- Describing each object in a training set using a shape descriptor;
- Aligning the descriptions to remove translational, rotational and size variations;
- Statistical analysis and modeling of the variations in the aligned shape descriptions.

#### 3.3.3.1 Shape representation

The shape descriptor is a way to mathematically describe the shape information and its choice is the first fundamental decision when designing Statistical Shape Models (SSMs). In medical imaging, it will most likely represent segmented volumetric images. Depending on the segmentation method used, the initial representation might be binary voxel, fuzzy voxel data (e.g. from probabilistic methods) or surface meshes. Most of the subsequent steps depend on this initial decision, and many methods are technically limited to certain representations. Flexibility and capturing the morphology are the determinant factors that should be looked into to ensure correspondent descriptions. In any case, all shape representations can be converted into each other at relative effort.



### Point Distribution Models (PDMs)

Point Distribution Models (PDMs) are probably the simplest and the most widely used method to represent shapes as a set of points distributed across a surface - Fig. 3.6. Coordinates from all  $k$  points are concatenated to one vector  $\mathbf{x}$  that will describe the shape.

$$\mathbf{x} = (x_1, y_1, z_1, \dots, x_k, y_k, z_k)^T \quad (3.9)$$

The coordinates are known in SSM literature as landmarks. They do not need to be located in external salient anatomical features of the volume of interest most commonly known as anatomical landmarks. When the number of landmarks increases, the level of detail that describes the shape is higher, although manual placement becomes unfeasible. Shape descriptions based on a dense distribution of points are named PDMs [99].

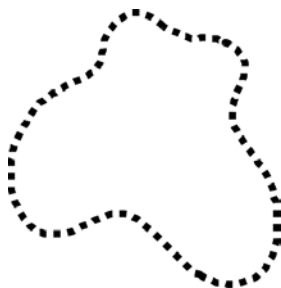


Figure 3.6: An example of a 2D point distribution model. The shape is described by the coordinates of the landmarks around the object boundary [100].

Often, additional connectivity information between the points is stored to allow reconstruction of the surface and calculation of the normal vectors, resulting in a mesh or point-cloud surface. However, the number of points in a PDM is usually in the thousands or tens of thousands. Consequently, the correspondence between the points is a challenging problem and is still an area of research for many research groups.

### Medial Models

Medial models (or skeletons) have been introduced by Blum [101] to describe biological shapes and are still used in image analysis. They represent objects by their centerline and the corresponding radii along their length - Fig. 3.7. It is often a more compact description when compared to PDMs. However, these parameters do not vary linearly and may be a limiting factor for common statistical analysis methods.

The concept of medial atoms was introduced with deformable shape loci by Fritsch et al. [102] and later by his colleague Pizer et al. [103], who presented a similar approach with a coarse-to-fine representation for 2D. This consisted in a collection of points on their centerlines and vectors pointing from there towards the boundary and was later extended to 3D [104] and termed *m rep*. These represent a 3D slab-like volume by arranging medial atoms in a 2D manifold interpolated by Bezier splines. More recently, Yushkevich et al. [105] generalized *m reps* to a continuous representation and added image

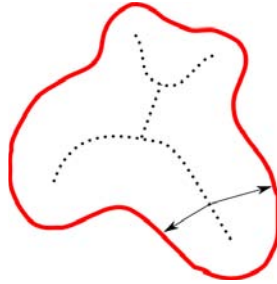


Figure 3.7: An example of a 2D medial shape description. The shape is described by the skeleton (black dotted lines) and vectors, radiating from the skeleton to the object boundary [100].

appearance to the description, allowing a number of medial image processing tasks, including segmentation, registration and shape discrimination.

### Piece-wise Parametric Meshes (PPMs)

A Piece-wise Parametric Mesh (PPM) is based in piece-wise parametric functions that can be used to represent continuous curves, surfaces or volumes. They map their properties as a mesh of smooth patches or elements controlled by parameters such as the coordinates of the control points within each element - Fig. 3.8. These control points, also known as mesh nodes, can be used in statistical analysis and are frequently in smaller number than PDMs, which translates in more efficient modeling of the object's shape, especially for smooth objects.

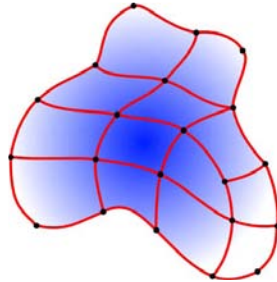


Figure 3.8: An example of a 2D piece-wise parametric shape description. The shape is described by piece-wise parametric functions (outlined in red) controlled by parameters at nodes (black points) [100].

They were first introduced in SSA in 1994 [106, 107] as curves for 2D shapes. For surfaces, B-spline patches were used to model the proximal tibia [108] and the heart [109]. Non-Uniform Rational Splines (NURBS) were used to model and segment kidneys [110] where principal curvatures at correspondent points on the mesh were used as the shape parameters. Principal curvatures are invariant to translation, rotation and scaling, so no alignment is needed for the surfaces. More recently, Zhang [111] extended this approach to Lagrange-element meshes.

## Global Descriptors

Global descriptors parameterize the object's shape according to its spatial frequency components. Both 2D and 3D shapes can be decomposed into oscillatory modes of various basis functions with corresponding dimensions. The coefficients for these modes are the parameters for statistical analysis - Fig. 3.9.



Figure 3.9: An example of a 2D oscillatory modes of a global shape description. The shape is described by the coefficients of the oscillatory function used to approximate the shape [100].

Staib and Duncan [112] employ an extension of the classical 1D and 2D Fourier transforms, named Fourier surfaces, to describe shapes of several different topologies. Closely related is the technique of Spherical Harmonics (SPHARMs), a set of basis functions that can be used to describe closed surfaces of spherical topology, where points must be mapped to spherical coordinates in a corresponding method. This method was later extended and adapted for generic deformable models in image segmentation. Surface harmonics [113] extended SPHARMs to non-spherical topologies by mapping the points to a generic coordinate system. Wavelet-based methods were later introduced [114] and accommodate surfaces of arbitrary topology by partitioning the surface into patches, similarly to PDMs.

These global descriptors allow a good representation of smooth shapes, usually in a compact description, making them efficient for soft tissue structures. However, a large number of terms is required to accurately describe high-frequency features, such as sharp ridges. In addition, their parameters do not describe local geometry, so local shape change modeling can be influenced negatively.

## Summary

This section reviews the literature for shape model descriptors for shape statistical analysis up-to-date and classifies them according to their mathematical formulation. All of them offer advantages depending on the type of structure to model and analyze. When designing a statistical shape model, the first fundamental is the choice of a representation method as most of the subsequent steps depend on it. Table 3.2 tries to summarize the advantages and drawbacks of the different shape representation methods above mentioned in order to properly choose a method over the others.

It is expected that landmarks remain the dominant representation of SSMs in the time to come. However, this doesn't mean that they are the optimal choice for all applications [86]. From the sake of computational efficiency they

Descriptor	Advantages	Disadvantages
<b>PDMs</b>	<ul style="list-style-type: none"> <li>- Most widely used</li> <li>- Simple and intuitive</li> <li>- Straightforward implementation</li> </ul>	<ul style="list-style-type: none"> <li>- Point correspondence</li> <li>- Computational cost is too high to describe surfaces with high level of detail</li> </ul>
<b>Medial</b>	<ul style="list-style-type: none"> <li>- Compact</li> <li>- Straightforward modeling of tube-like structures</li> <li>- Intuitive for diameters and bending angles</li> </ul>	<ul style="list-style-type: none"> <li>- Non-linear</li> <li>- Common statistical analysis methods are non-compatible</li> </ul>
<b>PPMs</b>	<ul style="list-style-type: none"> <li>- Compact but flexible</li> <li>- Suitable for the modeling of an arbitrary topology</li> <li>- Straightforward implementation</li> </ul>	<ul style="list-style-type: none"> <li>- Ensuring smooth boundaries between patches can be problematic</li> </ul>
<b>Global</b>	<ul style="list-style-type: none"> <li>- Compact</li> <li>- Popular for modeling the brain structure</li> </ul>	<ul style="list-style-type: none"> <li>- Very complex implementation</li> <li>- Complex parameterization for shape correspondence in spherical structures</li> </ul>

Table 3.2: Comparison of shape descriptors available in the literature.

should be avoided when dealing with shapes with a high level of detail and therefore represented by a enormous data point cloud.

### 3.3.3.2 Alignment

Building a SSM basically consists of extracting the mean shape and a number of modes of variation from a collection of training samples. Based on the chosen shape representation, a method to correctly align the training shapes has to be implemented. Shape is defined as a property which does not change under similarity transformations, i.e., it's invariant to translation, rotation and scaling. The alignment process corresponds to the removal of these transformations to a common coordinate system. Some anatomical structures have a standard coordinate system defined based on anatomical landmarks, as seen for the femur on the coordinates section of chapter 2. Hence, Figure 3.10a shows a femur aligned according to this coordinate system. On the other hand, Figure 3.10b shows a femur aligned according to its principal axes of inertia. The center of this coordinate system is chosen to be the center of mass of the femur.

The Procrustes analysis was first introduced by Gower [115] in 1975 and later applied to SSA by Goodall [116]. In order to remove all similarity-transform variations, it minimizes the mean squared distance between two shapes and can be calculated analytically. However, it can be only performed if there is correspondence among the landmarks. As seen in previous section 3.3.3.1, not all shape descriptors have this advantage, so in that case variations of the method of the Iterative Closest Point (ICP) [117] can be applied in order to perform non-correspondent three dimensional shape alignment.

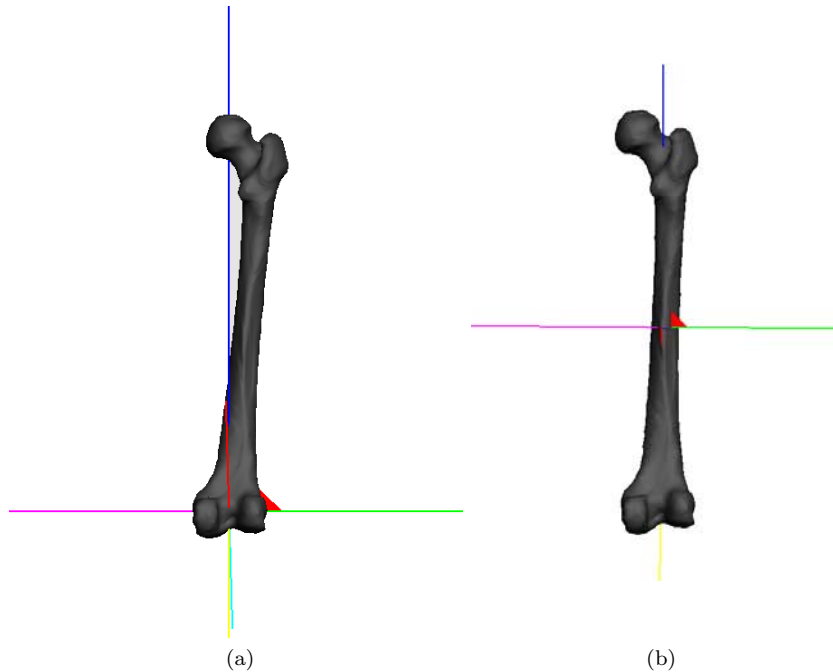


Figure 3.10: A femur aligned according to its anatomic coordinate system (a) and to its center of mass and its principal axes of inertia (b).

A Generalized Procrustes Analysis (GPA) is performed by transforming a group of geometries in order to align with a target geometry, possibly already aligned according to one of the referentials in Figure 3.10, for the sake of standardization. If the target is unknown, Gower proposes to start from an initial Procrustes analysis and iteratively define the mean geometry as the target for the next iteration until the mean shape converges. Regarding the alignment of training shapes, the GPA is the current method of choice [86] as it is reasonably simple to implement and backed by well-elaborated theory.

### 3.3.3.3 Dimensionality Reduction

After the alignment, the next step is to reduce the dimensionality of the training set, i.e., to find a smaller set of modes that approximates the observed variations. The number of parameters in shape descriptions is often too high for efficient or meaningful statistical analysis, so usually the dimensionality reduction is mandatory. The most common method is using the Principal Component Analysis (PCA) [118]. The number of modes of underlying variation are therefore significantly fewer than the number of shape description parameters due to covariance between parameters. Consequently, dimension reduction usually precedes statistical shape models construction.

Following equation 3.9, every aligned training shape is described by  $3k$  point coordinates in the vector  $\mathbf{x}_i$ . The mean shape can be formed by simply averaging over all  $s$  shapes:

$$\bar{\mathbf{x}} = \frac{1}{s} \sum_{i=1}^s \mathbf{x}_i \quad (3.10)$$

The corresponding covariance matrix  $S$  is given by:

$$S = \frac{1}{s-1} \sum_{i=1}^s (\mathbf{x}_i - \bar{\mathbf{x}})(\mathbf{x}_i - \bar{\mathbf{x}})^T \quad (3.11)$$

An eigendecomposition on  $S$  delivers the  $\max((s-1), 3k)$  principal modes of variation  $\phi_m$ , named eigenvectors, and their respective variances  $\lambda_m$  (eigenvalues). Figure 3.11 shows the two largest modes for an example multivariate Gaussian distribution centered at  $(1,3)$  with a standard deviation of 3 in roughly the  $(0.878, 0.478)$  direction and of 1 in the orthogonal direction.

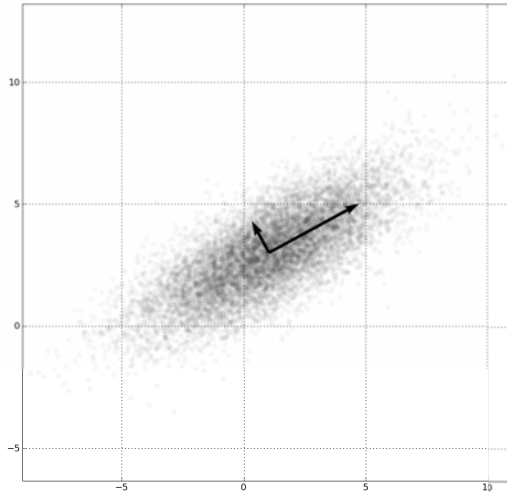


Figure 3.11: PCA of a multivariate Gaussian distribution centered at  $(1,3)$  with a standard deviation of 3 in roughly the  $(0.878, 0.478)$  direction and of 1 in the orthogonal direction. The vectors shown are the eigenvectors of the covariance matrix scaled by the square root of the corresponding eigenvalue, and shifted so their tails are at the mean. Image of public domain.

Intuitively, the principal components are found by rotating orthogonal axes so that the first axis aligns with the direction of maximum variance, the second axis with the second greatest variance, perpendicular to the first, and so on. Assuming meaningful variations in the training set, the first few modes will capture most of the variation. This means also that shapes can be approximately reconstructed by linear combinations of just the few first modes, leading to a reduction in the dimensionality of the data. In the scope of the present thesis this is of major interest as it is possible to recreate synthetic femoral shapes that approximate femurs represented in merely two dimensions, as in a radiography.

Another way to calculate  $\phi_m$  and  $\lambda_m$  without using the eigenanalysis, is also possible by a Singular Value Decomposition (SVD) on the aligned landmark matrix  $L = ((x_1 - \bar{x}) \dots (x_s - \bar{x}))$ . From a computational point of view, this method offers a higher numerical stability. However, both methods are susceptible to outliers as they set up their principal modes according to least-squares estimation - sometimes an entire sample might be outside the expected distribution or some other times only a small number of landmarks for a given example. De la Torre and Black [119] and Skocaj et al. [120] proposed the robust PCA and the weighted PCA, respectively, in order to handle both types of previously described outliers.

In any case, the resulting modes of variation are ordered by significance variance, so that  $\lambda_1 \geq \lambda_2 \geq \dots \lambda_{s-1}$ . The synthetic shape generation that approximates every valid shape by a linear combination of the first  $c$  modes is given by:

$$X = \bar{x} + \sum_{m=1}^c b_m \phi_m \quad (3.12)$$

The choice of the number of representative modes  $c$  is so that the accumulated variance  $\sum_{m=1}^c \lambda_m$  reaches a certain threshold  $r$  of the value of the total variance  $\sum_{m=1}^{s-1} \lambda_m$ . Vector  $b$  holds the shape parameters. To constrain allowed variation to plausible shapes,  $b$  has to be limited to a certain interval. The most common method is to treat all modes as independent distributions and constrain each  $b_m$  to lie inside  $[-3\lambda_m, 3\lambda_m]$ . If the shape does not follow a Gaussian distribution, the presented constraints for  $b$  will result in invalid shapes. The Independent Component Analysis (ICA) [121] does not assume a Gaussian data distribution and delivers statistically independent projections.

Overall, PCA results in global modes which influence all variables simultaneously, i.e., varying one mode will affect all landmarks of the shape model. For models where local variations are the main interest, it is usually better to have more isolated effects, which are therefore easier to interpret. With this, each mode would only affect a limited, clustered number of landmarks. Orthomax rotation [122] and sparse PCA [123] rotate the PCA modes to increase sparsity.

Unlike the method for alignment, the choice between methods of dimensionality reduction is not consensual. On the one side, the PCA approach is the most commonly employed, has a straightforward implementation and is very robust although a small amount of shapes will not feature a Gaussian distribution and the linear approximation model fails to model the variances. On the other side, the ICA seems like a reasonable alternative but its implementation is complex and might not be worth the effort. In 3D SSMS problems as over-fitting and lacking robustness of non-linear methods are thus more present and, depending on the complexity of the shape variances to model, the PCA suits the majority of the demands.

### 3.3.3.4 Enlarging variations

The potential of a statistical model is intrinsically related to the quantity of available training data. In the particular case of three dimensional models, the images are hard to obtain and their manual segmentation is time-demanding

and cumbersome. In addition, even if data exists, it might not be fully used due to a poor estimate of the required sample size. This will result in over-constrained models, i.e., the restrictions imposed on the deformations do not allow them to adapt accurately to new data. As Lamecker [124] reports in his statistical model for liver segmentation, if adding training shapes to the model results in a better segmentation accuracy then the model contained insufficient training data.

Cootes and Taylor [125] use finite element methods to calculate vibrational modes for each training shape and generate a number of modified training shapes from it. All these variants are subsequently included in the construction of the SSM, which leads to a model featuring original and synthetic data. Depending on the amount of initial training data, it is possible to adapt the number of generated synthetic shapes conferring more flexibility to the model.

Another approach to increase the flexibility of the model is to divide the SSM into several independently modeled parts. This is based on the fact that smaller parts exhibit less variation which can be captured with fewer training samples when compared to the variation of the full shape [114, 126].

In sum, enhancing the flexibility during training cannot by itself guarantee that the applications of the SSM will have an higher accuracy on fitting the new data, as the allowed variation is still limited by hard constraints [86]. Hence, additional flexibility should better be incorporated in the application, such as the search algorithms in image segmentation.

### 3.3.3.5 Shape correspondence

The last step in the construction of a SSM is the establishment of a set of correspondences among the training shapes. Depending on the chosen representation (section 3.3.3.1), the methods here described that best fit them vary. Nevertheless, the definition of the correspondence is the most challenging part of 3D model construction and at the same time one of the major factors influencing the model quality. Manual landmarking a 2D shape is time consuming and is becoming old fashioned. In 3D, the problem is of even bigger proportions. In addition, the reproductibility of such method is reduced as the anatomical edges where the landmarks are to be placed are of ambiguous definition.

The automatic computation of the correspondences is actually no more than a registration between the involved shapes. In this section, the different proposed methods have been categorized according to the type of registration process and a brief description of each is presented. In the end, there is a summary and a comparison of their performance. This will ultimately support the optimal choice for the SSM developed in this thesis.

#### Point-to-point Registration

Mesh-to-mesh registration try to identify corresponding points (landmarks) between two dense, unstructured clouds of surfaces. They can also be vertices on a mesh. This is the most commonly used method for shape correspondence when PDMs are chosen as shape representatives (see 3.3.3.1). These methods consider two surfaces with potentially different number of vertices as input and deliver the optimal similarity transformation from one surface (reference) to the other (data) as a result. Several established algorithms exist for surface



matching. Besl and McKay [117] proposed the famous ICP and Rangarajan et al. [127] proposed the softassign Procrustes matching algorithm. These algorithms stand as foundations for most of the algorithms for SSMs registration.

The idea behind the algorithm is for each reference point to assign its closest data point as its corresponding point, as illustrated in Figure 3.12. The corresponding data points later become the landmarks of the data surface. An improvement that was made to this class of correspondence detection is the modification of the similarity metric if the point matching algorithm is to include additional features, rather than solely based on the distance. These features may include crest lines [128], normal vectors [129], surface curvature [130] or local shape and pattern information [131].

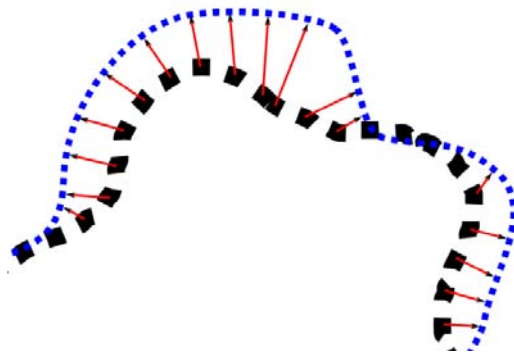


Figure 3.12: A simple example of finding point correspondence for PDMs. The reference (in black) and data boundaries (in blue) are aligned and then the closest data point to each reference point is found as its corresponding point (red arrows). Local curvature or other information can be used to support the distance measure and improve the robustness [100].

The largest drawback of such algorithms for landmark creation is the restriction to similarity transformations, i.e., in a population of shapes with large variations the determination of corresponding points by proximity alone can not only lead to wrong correspondences but also to non-homeomorphic mappings and this to flipping triangles in the mesh. Therefore, for such cases a non-rigid registration is necessary [128]. An alternative to point correspondence proposed by Wang et al. [130] is to create a correspondence by matching a small number of landmarks by local surface geometry and determine the other points by geodesic interpolation.

Due to the fact that 3D SSMs derive from medical imaging, the training of the shapes is done not on a mesh but on a volume. Hence, a different approach to landmark generation is adapting a deformable surface model to these volumes. Mesh-to-volume correspondence is then defined by the vertex locations on the deformable template after the surface evolution has converged to the segmented binary volumes. This has the advantage that training images do not need to be segmented manually beforehand while it is obviously limited to structures that can be segmented reliably using templates, which are very few [132]. The key to a successful landmark generation using mesh-to-volume registration is the robustness of the deformable template algorithm.

Instead of adapting a template mesh to the training data, it is also possible to register a volumetric atlas - volume-to-volume registration. Using the resulting deformation field, landmarks placed on the atlas can propagate to the training data to define the correspondences for the SSM [133].

Similarly to mesh-to-volume registration, there has also been work on registering a volumetric atlas to the original gray-scale images, i.e., avoiding the precedent manual segmentations. This, however, faces the same problems as the previously described.

### Parameterization

Domain parameterization is a bijective mapping between boundaries, surfaces or volumes to an appropriate base domain. In 2D, the common base domain for closed contours is a circle, and registering two contours by their parameterization is the equivalent of determining correspondences by their relative arc-length. In 3D, the problem of parameterization of surfaces is far more complex and usually depends on the topology of the shape. In other words, if two surfaces have corresponding parameterization, then a point defined in their common parametric space will map the corresponding points on each surface. There are two approaches to obtain correspondent parameterizations between the reference and the data surfaces. The first is to smoothly deform the reference to fit the data, so that the deformed reference parameterizes the data. The second is to adjust the parameterization of the data surface to match that of the reference (Fig. 3.13).

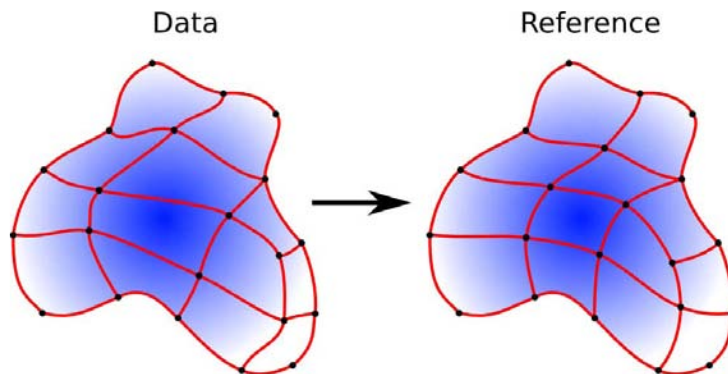


Figure 3.13: An example of parameterization correspondence. Both the data and the reference PPMs have the same shape, but their domain is differently mapped (or parameterized) by the elements [100].

SPHARMs [134] or 3D topological disks [135] were chosen for the mapping of the surfaces. These were then aligned by their first ellipsoid or by optimizing the disk rotation, respectively, so that the correspondence between the population can be established. While these methods guarantee a diffeomorphism between all the shapes, the obtained correspondences are mostly arbitrary and the quality of the resulting SSM will strongly depend on the input shapes. Moreover, problems arise when surfaces are not topologically spherical. Another approach to parametric surfaces was to fit reference triangle meshes of

the human body [136] and femur [137] to data surfaces, using a coarse to fine procedure and mesh smoothness constraints.

An alternative is to map 3D surfaces to 2D parametric space with the use of parametric surfaces [138] (see Sec. 3.3.3.1), i.e., surfaces of arbitrary topology can be parameterized by partitioning them into patches, which are parameterized individually. The assumption is that if surfaces are partitioned into correspondent patches, then the parameterization of each patch will also be correspondent across surfaces, due to the similar patch geometry.

### Population-based

This method was first introduced by Korcheff and Taylor [139] and is rather based on the desired properties of the resulting SSM. This means that in order to achieve a model as compact as possible, i.e., featuring low eigenvalues concentrated in only a few modes, they minimized the determinant of the shape model's covariance matrix. Each iteration of the optimization involved parameterizing the shapes (mapping landmarks to a unit circle), training the statistical model to calculate the covariance matrix determinant and updating the parameterization to minimize the determinant (Fig. 3.14). This iterative framework still serves as foundations for most population-based approaches.

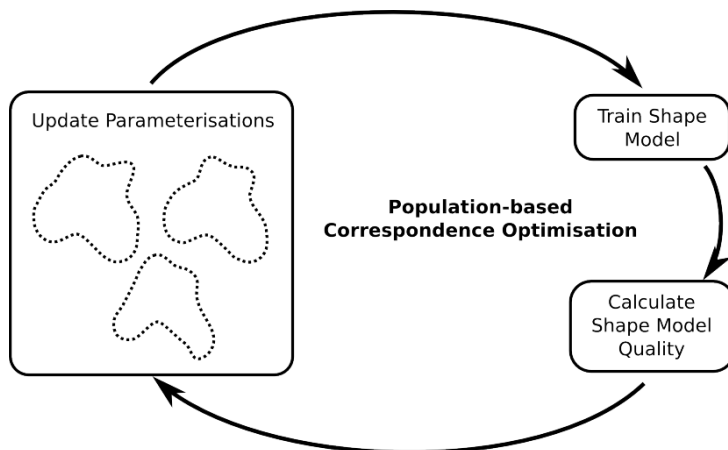


Figure 3.14: An example of the main steps of population-based correspondence [139], In each iteration, a shape model is trained from the population, a related metric is calculated and then optimized by adjusting the parameterization of each training shape [100].

This way, correspondence can be optimized by considering the entire training set instead of aiming for correspondence to a particular reference. The determinant of the covariance matrix is a good indicator of the quality of training set-wide correspondence. Although in some cases better results than manually placed landmarks were achieved, the method didn't converge in all cases and there was no sound theoretical foundation of the objective function [86].

Years later, Davies et al. [140] proposed a new objective function based on the Minimum Description Length (MDL) of the statistical model. The MDL

postulates that the best description of a set of data leads to the best compression of data, i.e., the best parameterization produces a model which describes each shape using the minimum number of principal components and additional error terms. The model was extended to 3D surfaces by parameterizing landmarks using spherical coordinates. Its significant computational complexity and cost were significantly bettered by Thodberg and Olafsdottir [141].

MDL has become a benchmark method for optimizing correspondence across training sets, although a number of alternative population-based methods co-exist [142, 143].

## Summary

The comparison of shape descriptors and correspondence methods has been given very limited attention. The numerous methods mostly rely on their application and the assumption of the existence of a general approach would mostly lead to fallacious interpretations. This evaluation is hampered by the fact that the true correspondence of the biological shapes are generally not known. Davies [140] introduced three measures to evaluate the overall quality of a SSM: generalization ability, specificity and compactness. Generalization ability quantifies the capability of the model to represent new shapes. It can be estimated by performing a series of leave-one-out tests on the training set, measuring the distance of the omitted training shape to the closest of the reduced model. Specificity validates the shapes produced by the model, i.e., generates random parameter values from a normal distribution and the respective standard deviation from the PCA and averages the distance of the shapes over a large number of runs. Lastly, compactness simply measures the accumulative variance of the model as a function of the number of modes or parameters used by the model.

Styner et al. [144] states that the MDL is superior to SPHARMs parameterization and manually initialized subdivision surfaces based on the three measures described in the last paragraph. In a latter study [145], it was shown that the choice of the shape description and correspondence method significantly influences the ability of resulting shape models to identify shape differences in brain structures. In addition, in a test with synthetic shapes, Ericsson and Karlsson [146] found that models with optimal correspondences score worse results for specificity than those with slightly altered correspondences. Hence, the main problem in the area is the lack of reliable measures to quantify model quality. Zhang [100] states that these three parameters are not enough to accurately compare the approaches: the number of shape description parameters should also be considered. An overly complex description can introduce more noise to the resulting shape model (over-fitting).

In sum, while most methods for correspondence deal with PDM descriptions, the development of new, more sophisticated shape descriptors has caused the correspondence methods to evolve. For example, the SPHARMs provided more straightforward correspondent parameterizations on a spherical topology. In its turn, these methods served as the basis for the MDL postulation. As shown by the success of the MDL, the correspondence across all the training set led to an increased quality in the shape model, rather than old one-to-one correspondence methods. Ultimately, quantitative comparison of the methods here described demands further investigation.

### 3.3.3.6 Local Appearance Models

The biggest share of SSMs are developed with the purpose of automatic image segmentation, which in other words, means that the model is fitted to new, previously unseen data. This requires a Local Appearance Model (LAM) besides the statistical model of the object shape [99]. Similarly, the LAM is also trained from sampling data and models the appearance of the shape. There are a number of different appearance models based on boundary and region features, in a roughly similar approach as the active contours presented in subsection 3.3.2.

#### Boundary-based features

The main idea behind boundary based features is to sample profiles perpendicularly to the object surface in all training images and extract the mean profile and principal modes of variation for each landmark, in a similar way to the shape model construction. During search, the fit of a profile model at a certain position is evaluated by measuring the Mahalanobis distance between the sample profile and the model. This measures the distance between a point of the fit to the model, i.e., how many standard deviations away the point is from the mean model. Typically, the used profiles contain the plain pixel intensity values, their corresponding derivatives or the normalized versions thereof.

#### Region-based features

Within this approach, the entire inner region of the shape model is used to build a feature vector  $\mathbf{g}$ , the simplest case being storing the plain intensity values of all pixels in the region also known as image texture. In order to build this vector  $\mathbf{g}$  for different shapes, the respective region has to be transformed into a standard shape first, usually the mean shape of the SSM. The LAM is then created by performing a PCA on the covariance matrix of textures. Similarly to profile models, normalization of the intensities is generally useful and can be accomplished by adding an offset and by scaling to transform all gray values to zero-mean and unit-variance. As an alternative to pixel intensities, gradient direction and strength can also be mapped [147].

However, memory requirements have to be taken in account when using data from the entire image region. Even in 2D, the involved matrices can get considerably large. Alternatives to this have been proposed but efficiency results haven't yet rivaled boundary-based feature extraction.

#### Clustering techniques

Intuitively, clustering would benefit both above proposed approaches as several landmarks with similar boundary appearance are combined to train a shared appearance model. This would result in more training samples and thus offer improved generalization ability. Beijl and Sonka [148] described the first use of clustering for appearance models, employing the c-means algorithm to generate a user-specified number of  $n$  clusters from all landmarks in training images. During search, they compare the sampled features with all  $n$  models and select the boundary fitting costs of the most similar one.

## Summary

Up to present date, the majority of studies has employed standard profile sampling techniques and estimates the goodness of fit using the Mahalanobis distance. It is relatively accurate and has a straightforward implementation. However, this might be the technical part with the highest potential to improve SSM-based image segmentation [86]. This is partly due to the fact that segmentation is intrinsically linked to initial feature detection and improvements in the local appearance model will have a direct impact on the final accuracy of the method.

### 3.3.3.7 Search Algorithms

This section starts with a review on the initialization methods. Furthermore, the often large 3D image domain of medical imaging requires an initial placement of the statistical model. Then, a state of the art overview in Active Shape models and Active Appearance models will follow, as well as an introduction to the concepts and techniques used in these. A more detailed description of the methodology for their application to image segmentation is the main focus of chapters 5 and 6 as it is one of the novel contributions of presented work.

## Initialization

The easiest solution to initializing an SSM is its manual placement [134, 138, 104]. However, this requires user interaction for the rough alignment of the position and the rotation of the mean shape to the 3D image, which requires the development of a framework to do so and expertise from the user. Generally, the time spent in this task decreases as the user gets familiarized with the user interface and the computational pipeline. Some of the most common alternatives to manual placement are based on image processing techniques. Soler et al. [149] based his approach on an automatic Gaussian fitting on the imaging histogram to estimate the position of the liver. Brejl and Sonka [148] extended the Generalized Hough Transform (GHT) to incorporate shape variability. Both of these methods were used to successfully segment objects in 2D images. However, their extension to 3D is not feasible without a significant increase of the processing time as the image data to process is significantly larger. Younes [150] recently combined the 3D generalized Hough Transform with Random Sample Consensus to identify spherical and cylindrical entities in the search space (Fig. 3.15), corresponding to the femoral head and shaft, respectively. However, the method is not extensively described and is not time-effective.

Another possibility of conducting a global search on the entire image is the use of evolutionary algorithms, more specifically genetic algorithms. A large population of solutions (each one encoded as a binary chromosome) is initially spread across the entire search space and evaluated simultaneously. The best set of chromosomes is selected for reproduction to produce the next generation of solutions. Similarly to biological evolution, there are mutations (random bit changes) and cross-over operators which influence the process. Iteratively, the method will converge to a best-rated chromosome in the population. This was first applied to SSM initialization by Hill and Taylor [151] and various authors have implemented variants to the technique that best match their SSM

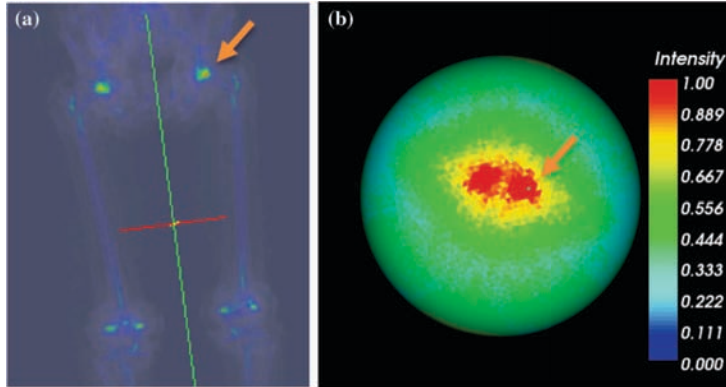


Figure 3.15: The Hough Transform accumulator space. This method is based on a radial voting: for each point on the edge, the normal is drawn and points along that normal, within a radius range, are selected for sphere parameters (center and radius estimation). The vote of each edge point is accumulated into the Hough accumulator space (a). (b) figures the Gaussian sphere accumulator space for the detection of the cylinder direction [150].

demands. Similarly, particle filtering or condensation [152] has been applied to SSM initialization.

### Active Shape model search

First introduced by Cootes et al. [99], ASMs are considered to be the application of SSMs to image segmentation and are one of the most popular techniques among medical image segmentation. ASM is a local search algorithm based on a point distribution model, although it has been adapted to fit other shape descriptors, as the present thesis shows. An instance of the model  $\mathbf{y}$  in the image domain is defined by a similarity transformation  $T$  and shape parameters  $\mathbf{b}$  according to:

$$\mathbf{y} = T(\bar{\mathbf{x}} + \Phi\mathbf{b}) \quad (3.13)$$

where  $\Phi = (\phi_1, \dots, \phi_c)$  is the matrix of eigenvectors. From an initial state, adjustments are calculated individually for each landmark by evaluating the fit of the appearance model at different positions along the normal vector to the surface. This leads to a vector of optimal displacements  $\mathbf{d}\mathbf{y}_p$ . In an initial step, the pose  $T$  of the model is adjusted by a Procrustes match of the model to  $\mathbf{y} + \mathbf{d}\mathbf{y}_p$ , leading to a new transformation  $T$  and new residual displacements  $\mathbf{d}\mathbf{y}_s$ . Following,  $\mathbf{d}\mathbf{y}_s$  is transformed into model space and then projected into parameter space to give the optimal parameter updates:

$$\mathbf{d}\mathbf{b} = P^T \tilde{T}^{-1}(\mathbf{d}\mathbf{y}_s) \quad (3.14)$$

where  $\tilde{T}$  is the same as  $T$  but without the translational part. After updating  $\mathbf{b}$  and applying appropriate parameter limits (Sec. 3.3.3.3), an updated valid instance of the model is obtained. These two steps are conducted iteratively until a specified convergence criterion is achieved, e.g., the maximum or average

landmark movement is under a certain threshold. Figure 3.16 shows a simple 2D example of the update procedure.

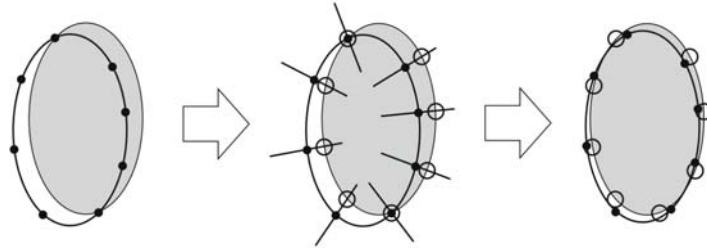


Figure 3.16: One iteration of an ASM search: at the beginning, the model (contour with landmarks) is located at the lower left of the true position (solid gray object). LAMs for all landmarks are evaluated at different positions normal to its surface. The best positions are highlighted with small circles in the center image. Finally, model parameters were updated to minimize the squared distances to the found best positions, bringing the model closer to its true position [86].

Among the several variants published, the coarse-to-fine approach achieved some relevance. The image data is organized as a multi-resolution pyramid and the SSM has separate appearance models for each level. The search starts at the coarsest level and switches to the next resolution when a predefined criterion is met until it converges in the finest resolution. This procedure leads to a considerable increase in speed, robustness and quality of fit. However, it requires to train as many LAMs as the number of levels of resolution.

Most of the proposed modifications to the original ASM algorithm try to improve stability against outliers, either by identifying and correcting them [153, 154] or by decreasing their influence using the weighting residuals  $\mathbf{d}\mathbf{y}$  [155, 156].

### Active appearance model search

Active Appearance Models (AAMs) were also introduced by Cootes et al. [157] and belong to the class of generative models, i.e., they can synthesize realistic images of the modeled data. This is made possible by storing the complete appearance (or texture) of the object, including its variations, in addition to the expected shape. However, AAMs are more than shape models with region-based features as they also feature a proprietary search method which completely differs from ASMs. Shape and appearance variations are combined into one linear system, allowing for shape  $\mathbf{x}$  and appearance  $\mathbf{g}$  to be described by a common parameter vector  $\mathbf{c}$ :

$$\begin{aligned}\mathbf{x} &= \tilde{\mathbf{x}} + \Phi_s W_s Q_s \mathbf{c} \\ \mathbf{g} &= \tilde{\mathbf{g}} + \Phi_g Q_g \mathbf{c}\end{aligned}\tag{3.15}$$

In this formulation,  $\Phi_s$  and  $\Phi_g$  are the independent eigenvector matrices of shape and gray-value model, respectively, and  $W_s$  is a diagonal weight matrix for the shape parameters.  $Q = \begin{pmatrix} Q_s \\ Q_g \end{pmatrix}$  is the eigenvector matrix of the combined



shape and gray-value parameters and obtained by a PCA on the independent parameters  $\mathbf{b} = \begin{pmatrix} W_s \mathbf{b}_s \\ \mathbf{b}_g \end{pmatrix}$ . An instance of an AAM in an image is thus defined by a similarity transformation  $T$  and the combined shape-appearance parameters  $\mathbf{c}$ , below denoted together as  $\mathbf{p}$ . To evaluate how good a fit is, the image texture is warped to the mean shape and normalized, resulting in  $\mathbf{g}_s$ . Using the modeled gray-value appearance  $\mathbf{g}_m = \mathbf{g}$  from equation 3.15, the residuals are then given by  $\mathbf{r}(\mathbf{p}) = \mathbf{g}_s - \mathbf{g}_m$ , and the error by  $E = \mathbf{r}^2$ .

The idea of AAM search is to assume a constant relationship between texture residuals  $\mathbf{r}(\mathbf{p})$  and parameter updates  $d\mathbf{p}$  over the entire search:

$$d\mathbf{p} = -R\mathbf{r}(\mathbf{p}) \quad (3.16)$$

The derivative matrix  $R$  highly influences the optimization scheme and is computed using multivariate linear regression on a large number of simulated disturbances on the training images. Figure 3.17 shows an example of simple 2D update procedure.

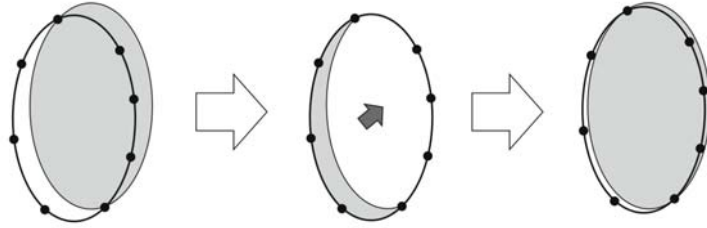


Figure 3.17: One iteration of an AAM search: initially, the model (contour with landmarks) is located at the lower left of the true position (solid gray object). The texture beneath the model is sampled and compared to the region based appearance model. The corresponding residuals are shown in the center image and suggest a move of the model up and rightwards - suggested during the training and encoded in matrix  $R$ . The resulting parameter update does indeed bring the model closer to the correct solution [86].

AAMs quickly gained popularity and similarly to the ASMs, various modifications were proposed throughout the years. However, they are mainly described for 2D and their main application field is face recognition.

### Summary

The search algorithm is, together with the correspondence issue and the AAMs, part of the most important components in an ASM segmentation pipeline. Although other methods with strict shape constraints or with relaxed shape constraints are present in the literature, it's the ASM and the AAM search methods that assume major relevance.

Currently, the ASM is the most popular method for searching 3D SSMs in volumetric images. The algorithm has proved to have a straightforward implementation, to be reasonably robust and time-effective. A wide range of variants has been presented, mostly addressing the presence of outliers.

The AAM, on its hand, is very successful for tasks like face recognition and video tracking, but has rarely been employed to medical image segmentation.

The main problem of this approach is the excessive memory usage of the 3D texture model. In addition, it appears that the mostly homogeneous texture encountered in typical biological shapes does not deliver the same quality of features as in, for example, face recognition.

The problem with all local search algorithms is that they always detect a minimum of the cost function, not the global optimum. If the search is initialized reasonably well and the data similar to that used for training, the found local minimum will be close enough to the optimal solution and the segmentation successful. However, for initializations far from the true shape or for largely different data (e.g. pathological organs or different acquisition methods) the segmentation can be drastically influenced and fail. In sum and similarly to the situation for the correspondence methods, there is not enough information about the performance of the algorithms, therefore it is difficult to recommend any specific variant of the methods for a given segmentation problem.

### 3.3.4 Graph cuts

Graph cuts have been successfully applied to medical image segmentation, namely the forearm [158] or the femur [159]. Pioneered by Greig et al. [160] in the late 1980s it was quickly adapted to the several different areas of computer vision. The graph cut framework is an energy minimizing segmentation method based on combinatorial mathematics. For the graph-cut, an image of dimension  $n$  is represented as a set of pixels  $\mathcal{P}$  within a neighborhood system  $\mathcal{N}(\binom{\mathcal{P}}{2})$ . Generally, the method requires the definition of the two components of the cost function:

$$R_p : \mathcal{P} \times \{obj, bkg\} \rightarrow R_0^+ \quad (3.17)$$

$$B(\{p, q\}) \propto e^{-\frac{(I_p - I_q)^2}{2\sigma^2}} \frac{1}{dist(p, q)}$$

The per-pixel term  $R_p$  specifies for each label  $L \in \{obj, bkg\}$  and each pixel  $p \in \mathcal{P}$  an individual penalty for assigning the label  $L$  to the pixel  $p$ , usually based on the pixel intensity. The boundary term  $B(\{p, q\}) : \mathcal{N} \rightarrow R_0^+$  defines a penalty for classifying adjacent pixels  $p$  and  $q$  with different labels. It therefore penalizes discontinuities and encourages spatial coherence between intensities  $I_p$  and  $I_q$  within both the object and the background at the control of a threshold  $\sigma$ . The graph cut then computes a binary labeling  $A$  as the global minimum of the energy function:

$$E(A) = \sum_{p \in \Omega} R_p(A_p) + \lambda \sum_{\{p, q\} \in \mathcal{N}} \delta(A_p, A_q) B(\{p, q\}) \quad (3.18)$$

where  $A_p \in \{obj, bkg\}$  is a label assigned to the pixel  $p$  in the segmentation  $A$ , the function  $\delta$  is the Kronecker delta and  $\lambda$  is a weighting parameter to balance the per-pixel and the boundary term. The purpose of  $\delta(A_p, A_q)$  is to restrict discontinuity penalties for cases where  $p$  and  $q$  are assigned different labels.

However, in most objects of interest, their regional boundaries are not enough to segment them from the background and therefore there is the need to constrain the search space of possible solutions before computing the optimal

one [161]. The graph-cut framework provides flexible support for incorporating prior topological information to segmentations. Figure 3.18 shows an example of a constrained graph cut framework applied to bone tissue segmentation.

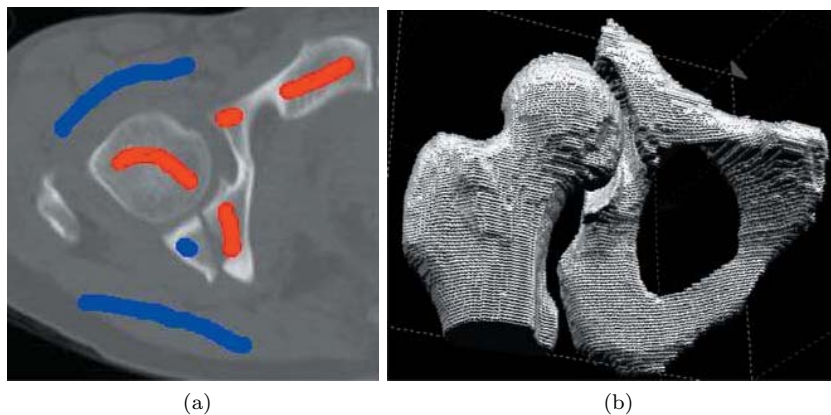


Figure 3.18: The graph-cut algorithm applied for segmentation of bones from a 3D CT volume. In (a) there is the manual initialization, where the user marks the object in red and background in blue seeds. (b) shows the segmented 3D object [161].

Graph cut methods have become popular alternatives to the level set-based approaches for optimizing the location of a contour, even outperforming them in terms of speed, robustness to initialization and robustness to parameter settings [162]. However, there are limitations to this approach such as: metrication artifacts caused by a 4-connected lattice image representation, where graph cuts methods can exhibit unwanted "blockiness" artifacts; shrinking bias, i.e., when graph cuts finds a minimum cut, the algorithm can be biased toward producing a small contour.

### 3.3.5 Clustering techniques

Also known as cluster analysis, it is the task of grouping a set of objects in such a way that objects placed in the same group (named a cluster) are more similar according to a predefined characteristic or property to each other than to those in other clusters. It is a well explored technique in the areas of data mining, machine learning, pattern recognition but has also been applied to medical image segmentation. Its applicability problem was recognized over four decades ago and the paradigms underlying the initial pioneering efforts are still in use today. A recurring theme is to define feature vectors at every image location (pixel) composed of both functions of the image intensity and functions of the pixel location itself. The basic idea, depicted in Figure 3.19, has been successfully used for medical images.

The first mention of local feature clustering to segment gray-scale images [164] emphasized the appropriate selection of features at each pixel rather than the clustering methodology, and proposed the use of spatial coordinates as additional features to be employed in clustering-based segmentation. Many other features were later discussed and applied to clustering segmentation, mostly regarding unsupervised cluster classification.

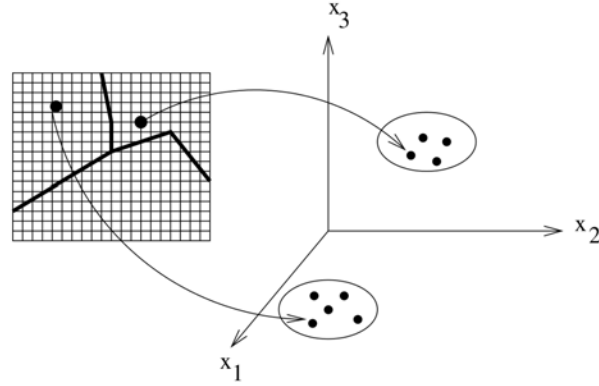


Figure 3.19: Feature representation for clustering. Image measurements and positions are transformed to features. Clusters in feature space correspond to image segments [163].

There are several algorithms proposed to solve this task. They differ on their notion of what defines a cluster, how efficiently it classifies them or even on the notion of distance among the clusters. The appropriate clustering algorithm and parameter settings depend on the individual data set and intended use of the results.

The fuzzy  $c$ -means clustering algorithm [165] became the most widely studied and used algorithm in image segmentation due to its simplicity and the ability to obtain more information from images. In fuzzy clustering, every point has a degree of belonging to clusters, as in fuzzy logic, rather than belonging completely to just one cluster. Thus, points on the edge of a cluster, may be in the cluster to a lesser degree than points in the center of cluster. It attempts to partition a finite collection of  $n$  pixels  $X = \{x_1, \dots, x_n\}$  into a collection of  $c$  fuzzy clusters with respect to some given criterion, e.g., pixel intensity. Given a set of finite data, the algorithm returns a list of  $c$  cluster centers  $C = \{c_1, \dots, c_c\}$  and a partition matrix  $W = w_{i,j} \in [0, 1], i = 1, \dots, n; j = 1, \dots, c$ , where each element  $w_{i,j}$  tells the degree to which element  $x_i$  belongs to the cluster  $c_j$ . The fuzzy  $c$ -mean clustering algorithm aims to minimize the objective function

$$\operatorname{argmin}_C \sum_{i=1}^n \sum_{j=1}^c w_{ij}^m \|x_i - c_j\|^2 \quad (3.19)$$

where

$$w_{ij} = \frac{1}{\sum_{k=1}^c \left( \frac{\|x_i - c_j\|}{\|x_i - c_k\|} \right)^{\frac{2}{m-1}}} \quad (3.20)$$

This adds the membership values (or degree of belonging)  $w_{ij}$  and the fuzzifier  $m \in \mathcal{R}$  with  $m > 1$  to the classic  $k$ -means objective function. The fuzzifier  $m$  determines the level of cluster fuzziness: a larger  $m$  results in smaller memberships and hence fuzzier clusters. Other than that, the algorithm is very similar to the  $k$ -means.

The iterative algorithm starts by choosing the number of clusters. Besides manual input, there are several approaches to automatize the process. Then,

it randomly assigns to each point coefficients for being in the clusters and repeats the process until the cluster labels do not change anymore, i.e., the coefficients' change between two iterations is no more than a given threshold. Finally, the points are clustered based on the distance of their intensities from the corresponding centroid according to the objective function (Eq. 3.19) and the centroids are recalculated according to:

$$c_k = \frac{\sum_x w_k(x)^m x}{\sum_x w_k^m} \quad (3.21)$$

Even though its potential on image segmentation is considerable, it shares the same limitations as the k-means clustering: the minimum found can be local minimum and the results depend on the initial choice of weights.

### 3.3.6 Summary

In this section, the most common approaches for medical image segmentation were briefly introduced. As already mentioned, there is no method that stands out as the gold standard in bone tissue segmentation. Moreover, to the author's knowledge, there was no documented pipeline that accurately segments the femoral bone in a computationally effective way, hence allowing the integration of the method in an image-guided surgery software. The problem is rather complex and strongly depends on the bone to segment and the quality of the image itself. Table 3.3 features a comparison between all the methods here described, focusing their advantages and disadvantages. This literature revision extensively enumerates and briefly describes the state of the art techniques for bone tissue segmentation. This portrayal proved to be crucial for the development of the present thesis as it allowed the author to accurately identify the advantages of the various methods and make use of them to develop a novel robust, time effective and automatic algorithm for femur segmentation.

<b>Methodology</b>	<b>Advantages</b>	<b>Disadvantages</b>
<b>Thresholding</b>	<ul style="list-style-type: none"> <li>- Easy to implement and efficient in simple problems</li> <li>- Simple and intuitive</li> </ul>	<ul style="list-style-type: none"> <li>- Noisy and blurred edges</li> <li>- Not suitable for segmenting tissues with varying intensity in the HU scale (e.g. bone).</li> </ul>
<b>Active Contours</b>	<ul style="list-style-type: none"> <li>- Widely used</li> <li>- Versatile (e.g. edge or region driven)</li> <li>- Possibility to include prior knowledge</li> <li>- Robust to noise</li> </ul>	<ul style="list-style-type: none"> <li>- Highly sensitive to initialization</li> <li>- Computationally not efficient</li> <li>- Edge detection assumes a clear background</li> </ul>
<b>ASMs</b>	<ul style="list-style-type: none"> <li>- Ensures model specificity</li> <li>- Highly robust to noise and clutter</li> </ul>	<ul style="list-style-type: none"> <li>- Its training is complex and time demanding</li> <li>- Due to the shape constraints, small variations may be missegmented</li> </ul>
<b>Graph-cuts</b>	<ul style="list-style-type: none"> <li>- Robust to initialization</li> <li>- Robust to parameter settings</li> <li>- More efficient than active contours</li> </ul>	<ul style="list-style-type: none"> <li>- Metrication artifacts</li> <li>- Shrinking bias</li> <li>- Multiple labels</li> <li>- Requires a large amount of memory</li> </ul>
<b>Clustering</b>	<ul style="list-style-type: none"> <li>- Simple and generates reliable outputs</li> <li>- Straightforward implementation</li> <li>- Recent variations are more time-efficient</li> </ul>	<ul style="list-style-type: none"> <li>- Sensitive to initialization and noisy data</li> <li>- Possibility of convergence to a local minimum</li> </ul>

Table 3.3: Brief description of the advantages and disadvantages of the segmentation techniques here reviewed.

## Chapter 4

# CT Images

In this chapter, the CT scan images used for the development of the work presented in this thesis will be extensively detailed. There are two groups of datasets, one large group made available by the Universitair Ziekenhuis Gent (UZ Gent) of the University of Ghent and a smaller group made available by the Quadrantes – Clínica Médica e de Diagnóstico (Quadrantes). Section 4.1 reviews the 'Quadrantes' image group, which consists of only 5 low resolution scans of the lower limbs of the patients. Section 4.2 will feature the 'UZ Gent' group which consists of 91 high resolution scans of both lower limbs of the patients. Each dataset on both groups was complemented with information about the patient and the parameters of the data acquisition. This allowed a demographic study of the population of the datasets and therefore try to establish a relation between the poor bone quality sometimes observed and the average age of the patients. In addition, 60 cadaver femur specimens were also made available for CT scanning at the Pathological anatomy Department of the UZ Gent and will be reviewed in section 4.3. Even though they can't be used to build an appearance model, they were considered for the statistical shape modeling.

Lastly, section 4.4 describes a computational tweak that enhances the processing time of operations with large image datasets. Due to the high resolution of some of the datasets, mostly the 'UZ Gent' group, they require considerably large amounts of both physical and virtual memory in their operations. Therefore, an algorithm that locates the femur in the image domain was developed, so that its bounding box can be roughly estimated and extracted as a new image dataset. This new dataset, reasonably smaller and yet with the same resolution, proved to be more suitable for the segmentation approach presented in this thesis.

### 4.1 The 'Quadrantes' Images

The first set of images was kindly made available by Doctor João Gamelas. They were acquired at the private clinic Quadrantes, in Lisbon. The clinic was established in May 1998 and is nowadays considered a reference in terms of medical diagnosis, due to the equipment they have but also to the medical team. The images were acquired from living patients who presented symptoms of an injured hip joint. Each dataset contains axial slices from just superior of

the pelvis to just inferior to the knee, as pictured in Figure 4.1.



Figure 4.1: An example of an image of the group 'Quadrantes'. It shows the maximum intensity projection in the coronal plane, showing the full extent of the image in the superior-inferior direction. The image was interpolated in the superior-inferior direction in order to have a continuous domain.

Five different scans were made available. In all of them, the pelvis, both femurs, both patella and the superior epiphysis of the tibia and the fibula are visible, as well as the soft tissues surrounding them. They were acquired using a Siemens Sensation Cardiac 64<sup>1</sup> CT scanner. The patients' position was feet first-prone in every case. Other conditions of the imaging procedure, e.g. exact positioning of the body, are unknown to this thesis author and therefore a wide range of limb positions and orientations were observed. As there are only five exams and some variables are not common to all of them, Table 4.1 features the most important parameters of the image datasets.

---

<sup>1</sup><http://www.healthcare.siemens.com/>



	Patient 1	Patient 2	Patient 3	Patient 4	Patient 5
Gender	F	F	M	F	M
Age	47	49	55	76	62
Slice Thickness	5	7	5	5	5
Rows x Columns	512x512	512x512	512x512	512x512	512x512
Pixel Spacing	0.781x0.781	0.678x0.678	0.775x0.775	0.742x0.742	0.742x0.742

Table 4.1: ‘Quadrantes’ CT scans parameters. Distances are shown in millimeters.

The number of slices in the axial plane that define the image domain varies from 90 to 128. The reason for such a high variance is because one of the exams (Patient 2) has a 7 mm slice thickness compared to the 5 mm in the rest of the exams. In fact, all the other four exams have nearly the same number of slices defining the image domain, ranging from 113 to 128 slices. This might be due to different patient’s height. Moreover, intuitively we can infer that a 5 mm distance between axial slices will reflect in a low quality reconstruction. It is nearly ten times superior to the pixel spacing in the sagittal and the coronal planes. This fact will limit the quality of the obtained segmentation. Nevertheless, it can also be useful to validate the behavior of the proposed method in low quality images.

## 4.2 The ‘UZ Gent’ Images

Contrary to the ‘Quadrantes’ set of images, the ‘UZ Gent’ is considerably larger with 91 different exams. These were acquired in the University Hospital of the University of Ghent, in Belgium and kindly made available by Doctor Emmanuel Audenaert. As part of the University of Ghent, it is of high scientific value to acquire clinical images and make them available for research. Similarly, the images were taken from living patients who had symptoms of an injured hip joint. However, the datasets now contain full axial slices from the superior torso to just inferior to the ankle. An example of an exam of this group of images is shown in Figure 4.2.

This is a group of 91 different images, where in all cases the lower part of rib cage, the vertebral column, the pelvis, both femurs, both patella, both tibias and fibulas and the ankle joint are present. In addition, the surrounding tissues are also visible, including both kidneys well visible in Figure 4.2. They were acquired with a GE Health care LightSpeed VCT<sup>2</sup> scanner. The patient’s position was also feet first-prone in every case. Again, the conditions of the acquisition pipeline were unknown and therefore a wide range of limb positions and orientations were observed. Table 4.2 features the parameters of the scanning common to all exams in the group.

The image domain is defined over roughly 2000 axial slices, on average. That is a groundbreaking improvement in image resolution when compared to the other group of images. Pixel spacing is  $0.666 \pm 0.069$  mm, on average, which means images have sub-millimeter resolution. This also happens in the superior-inferior direction, where the slice thickness is 0.625 mm. Hence, images in this group present a voxel size of 0.666 mm x 0.666 mm x 0.625 mm, on average. Computationally, transformations with these images are very hard to handle as they require a huge amount of virtual memory. However, they allow

<sup>2</sup><http://www.gehealthcare.com/>

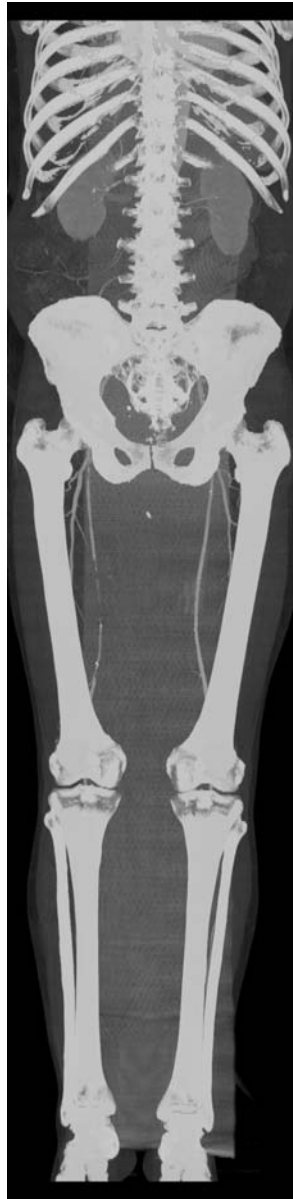


Figure 4.2: An example of an image of the group 'UZ Gent'. It shows the maximum intensity projection in the coronal plane, showing the full extent of the image in the superior-inferior direction. The image was interpolated in the superior-inferior direction in order to have a continuous domain.

a re-sampling in a way that computational cost can be improved at the cost of image resolution without compromising the level of detail of the object of interest.

Scan Type	helical
Slice Thickness	0.625 mm
Slice Spacing	0.6 mm
Slice Overlap	0.25 mm
Pixel Spacing	$0.666 \pm 0.069$ mm x $0.666 \pm 0.069$ mm
Rows x Columns	512x512
Typical Resolution (Avg.)	1.5 pixels per mm

Table 4.2: 'UZ Gent' CT scanner parameters.

### 4.2.1 Data Demographics

The complete group consisted of 91 individuals, mostly Belgian, that were examined due to suspicions of issues with the hip joint. Among them, 54 were men and 37 were women. Figure 4.3 shows the age distribution of examined individuals, both male (Fig. 4.3a) and female (Fig. 4.3b).

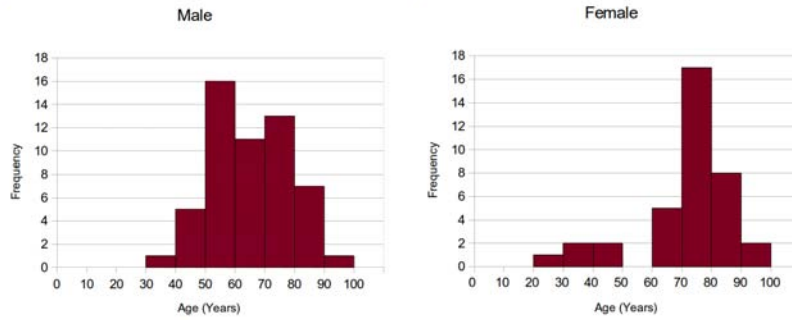


Figure 4.3: Age distribution of the examined individuals data by gender.

The average age of the male individuals was  $64.66 \pm 13.63$  years old while for the female individuals this was  $71.70 \pm 14.40$  years old. The combined average age was  $67.66 \pm 14.32$  years old. This data comes in concordance with the expected in a European country, due to the ageing population and consequent bone mass quality decrease (see Section 2.6.1), making the hip joint more susceptible to anatomical complications. Even though female age was slightly higher than males, there was no evidence that gender could influence the emergence of hip complications.

All subject information contained in the image metadata was omitted from the present thesis for ethical reasons.

### 4.2.2 Image Artifacts

However, not all datasets from this group were in perfect conditions, i.e., some artifacts or misaligned datasets were found in that compromise femoral segmentation. Most of the artifacts were either due to the presence of metallic objects in the field of view of the CT scanner or by uncontrolled patient movement during the acquisition procedure. In this section, these artifacts will be

reviewed and a brief explanation of why they invalidate the femoral segmentation procedure will also feature.

The most common condition found in this image group that prevents an accurate and reliable femur segmentation is the misalignment of the individual's body. More specifically, when the alignment was not carefully planned, part of femur was left out of the ray incidence and therefore out of the image domain. This mostly affects the proximal part of the femur, as its the most lateralized in the image domain. Figure 4.4 shows an example of this.

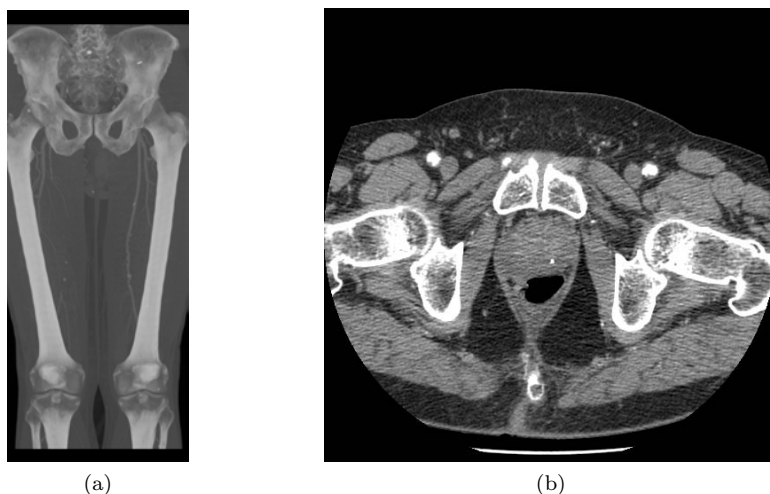


Figure 4.4: Example of a cropped femur due to body misalignment at the image acquisition. (a) shows a maximum intensity projection of the femur region and (b) is an axial image taken from the region of the neck of the femur.

Another common issue that excluded datasets from the study was severe osteoporosis and osteoarthritis, where the bone density is so low that is indistinguishable from the surrounding tissues. Furthermore, abnormal bone formations start to develop in crucial zones of the femur, as shown in Figure 4.5.

Lastly, in some of the datasets there was the presence of metallic objects in the field of view, as illustrated in Figure 4.6. Some individuals presented a prosthetic hip joint (Fig. 4.6a) and some other showed knee prosthesis (Fig. 4.6b). These metals have an extremely high attenuation coefficients which results in severe beam-hardening and bright streak-like artifacts on the image.

In total, 91 images were collected, which would ideally reflect in 182 in-image femurs. However, for the purpose of this thesis, scans that contained any of the abnormalities here described weren't considered as they would severely compromise the segmentation results. In sum, the following amount of images were discarded for the corresponding reasons:

**Metallic implants:** 3 femurs were not considered due to the presence of either a knee or an hip prosthesis;

**Abnormal bone formations or severe osteoporosis:** 3 femurs were not

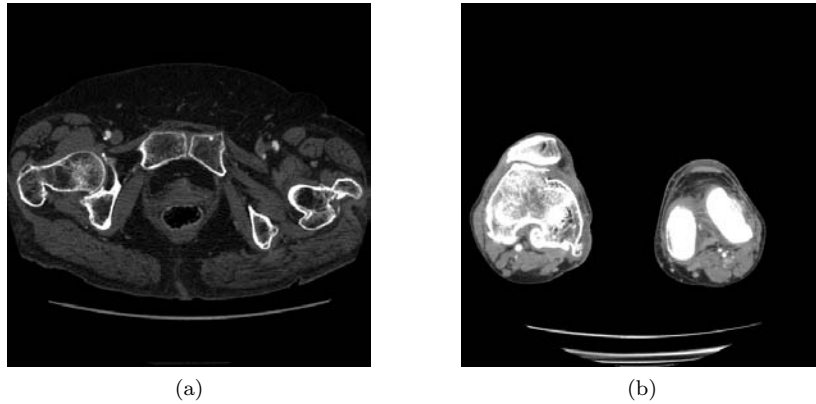


Figure 4.5: Example of a abnormal bone formations in two different patients. In (a) the patient has developed a tip-like structure at the level of the inferior trochanter of the right femur. (b) shows a misformed right condyle on the left femur.

considered due to abnormal bone formations or excessively low bone mass density;

**Occluded femur:** 28 femurs were not totally inside the image domain.

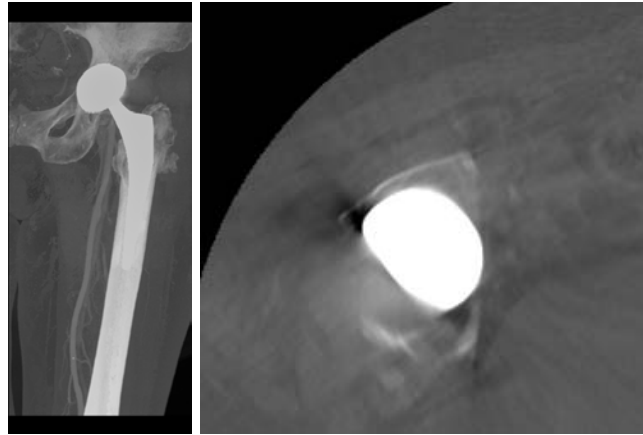
In sum, only 148 of the in-image femurs, both left and right, were eligible for the study.

### 4.3 Cadaveric Femurs

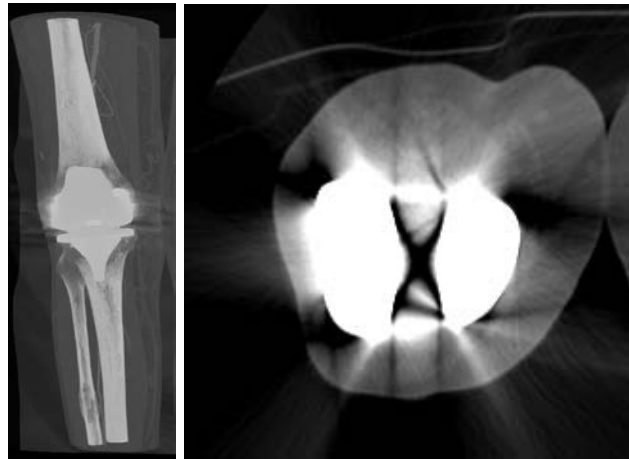
In addition to living patients' datasets, the author of the thesis also had access to CT scans of stacks of cadaveric femurs. They were made available by the UZ Gent Pathological anatomy and dissection department, in Ghent, Belgium. Even though not much is known about the origin of the femurs, it is assumed that they were part of a bone bank, i.e., an establishment that collects and recovers human cadaver tissue for the purposes of medical research and education. These banks allow the transplantation of human bones, procedure also known as bone allografts [166]. Studies show that bones can be preserved in banks up to five years [167].

Bone morphology and mechanical properties may be affected by the freezing or demineralization processes required for the bone preservation in a bank. However, embalmed femur bones and fresh frozen bones have similar characteristics by mechanical testing [168]. In what concerns size and shape changes, no significant information was found in the literature. Hence, it was assumed that these bones were eligible to take part of the statistical analysis for shape variances and integrate the shape model developed in the scope of the present thesis.

The femurs were stacked on top of each other and displayed in two rows on the CT scanner. There were 4 different scans of 15 femurs each, adding up to 60 femurs. The datasets presented, on average, 1700 axial slices. Similarly to the 'UZ Gent' image group, they were acquired using a GE Health care



(a) Hip implant.



(b) Knee implant.

Figure 4.6: Examples of metallic objects in the datasets that excluded them from this study. On the left, two maximum intensity projections of the area of interest, where it is clearly observable the much higher radiation attenuation coefficient of the metals compared to the bone tissue. On the right, two axial images of the radiation scattering and artifacts produced. In (a) the image is taken from the sub-trochanteric region and in (b) the image is taken from the distal epiphysis of the femur, just superior to the epicondyles.

LightSpeed VCT scanner. The acquisition of such volumes is of much lower degree of complexity, as there are no involuntary movements of the bone or any surrounding entity capable of interfering on the radiation absorbance, therefore no image artifacts were observed in any of the four datasets. Table 4.3 lists the relevant scanning parameters used for the acquisition of the cadaveric femurs.

As it is observable in Table 4.3, image resolution of the datasets is considerably high and capable of capturing the femur anatomical shape variances. The voxel size of 0.815 mm x 0.815 mm x 0.6 mm is lower than a cubic millimeter.

Segmentation of these femurs was not as straightforward as one may in-

Scan Type	dynamic
Slice Thickness	0.625 mm
Slice Spacing	0.6 mm
Slice Overlap	0.25 mm
Pixel Spacing	$0.815 \pm 0.038$ mm x $0.815 \pm 0.038$ mm
Rows x Columns	512x512
Typical Resolution (Avg.)	1.23 pixels per mm

Table 4.3: CT scanner parameters for the cadaveric femurs acquisition.

tuitively think: they were in contact among them, causing general edge and region based approaches to fail redundantly. In addition, computationally handling image sets this big requires a significant amount of physical memory. Moreover, it exponentially increases if gradient descent methods are applied, such as active contours. Therefore, these femurs were manually segmented using 3DSlicer<sup>3</sup>, a free, open source software package for visualization and image analysis that takes advantages of the Insight Segmentation and Registration Toolkit (ITK)<sup>4</sup> library. An example of a segmented image domain is shown in Figure 4.7, where the segmented volumes are still placed in the original relative positions.

#### 4.4 The Crop Algorithm

In this section, an algorithm that locates the femur and crops its bounding box from the dataset domain is presented. Due to the image resolution and the consequent virtual and physical memory requirements that transformations on these require, there was the need to either crop or down-sample the original datasets. As down-sampling could compromise the capture of small femoral shape variances, an algorithm to crop the images was developed. The algorithm is fully automated as it is tedious and especially very time consuming to do it manually for such a large number of datasets.

The Hough Transform (HT) is a feature extraction technique widely used in digital image processing and computer vision. Its potential is considerable and it has been applied to the most diverse applications. It was first introduced by Paul Hough in 1962 and first applied to pattern recognition in 1972 [169], but only a few years later it was generalized as we know it nowadays, which is under the name 'generalized Hough Transform' [170]. Originally, it was used to identify parametric forms in the image, such as lines, circles or ellipses but the latter revision made possible its application where the analytic description of features is not possible. This proved to be particularly relevant to medical imaging analysis. Over the years, it has been improved several times and made computationally less complex. An extensive review on the history of the modern HT can be consulted in the paper presented by Hart [171].

<sup>3</sup><http://www.slicer.org/>

<sup>4</sup><http://www.itk.org/>

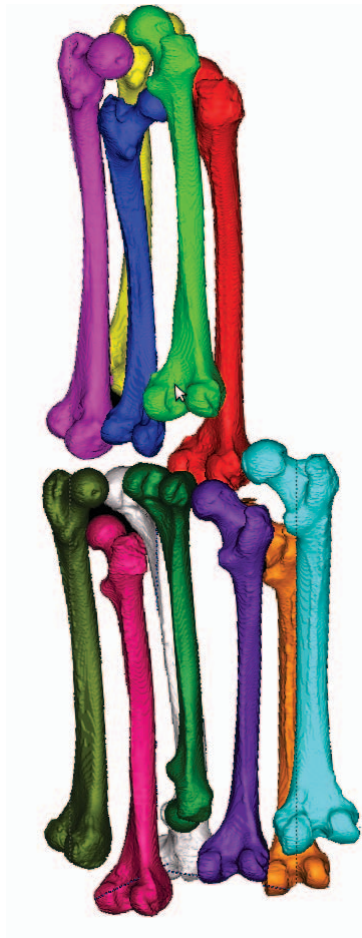


Figure 4.7: Preliminary results of manual segmentation. Different femurs are represented in different colors.

#### 4.4.1 The Generalized Hough Transform

The classical HT was limited to analytically defined shapes, i.e., shapes which could be defined parametrically. Only later, an extension was proposed which allows the detection of more complex patterns without a parametric definition [170]. In other words, it generalizes the application of HT to any object described within its model, thus named GHT (Fig. 4.8). Instead of considering parametric models, the GHT first builds an R-table, which, for every point in the boundary of the object, stores the distance to a reference point, chosen arbitrarily, in the gradient direction.

The R-table works as a look-up table. When searching for patterns, the algorithm follows the boundary pixels of a given shape in the image, looks up in the table for a reference point in the model, according to its properties, and increments that cell in the accumulator matrix. In the end, the cell with higher number of votes is the most probable reference for the shape.



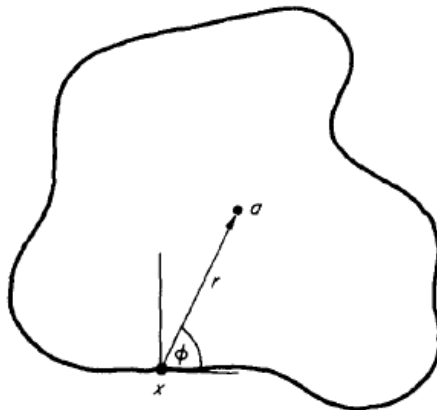


Figure 4.8: Generalized Hough Transform example.

#### 4.4.2 The Circle Hough Transform

The Circle Hough Transform (CHT) is a circle detecting variation of the HT. Its purpose is to detect imperfect circles in images. The best circle candidate is found by looking at the local maximum of the accumulator matrix, e.g., the most voted circle in the Hough parameter space.

In 2D, a circle is defined by

$$(x - a)^2 + (y - b)^2 = r^2 \quad (4.1)$$

where (a,b) are the coordinates of the circle center and r is the radius. These are the parameters that the CHT will approximate. The procedure starts to consider a fixed radius and find the optimal center of circles in a two dimensional parameter space (the coordinates of the position) followed by the location of the optimal radius in a one dimensional parameter space. In the first step, the initial radius guess is given by the user as input and for each (x,y) in its perimeter another circle is defined. The objective is to find the (a,b) coordinates of the center – Figure 4.9. The true center point will be common to all parameter circles and can be found with a Hough accumulation matrix. The accumulator matrix tracks the intersecting points of these circles and the local maxima point is where the most circles intersect.

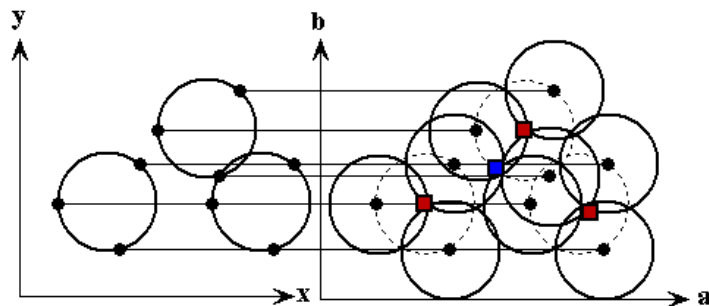


Figure 4.9: Circle Hough Transform (CHT).

### 4.4.3 3D Extension of the Hough Transform

The reasoning used in CHT may easily be extended to the 3D case, where we aim to detect spheres. A sphere can be expressed as:

$$(x - x_0)^2 + (y - y_0)^2 + (z - z_0)^2 = R^2 \quad (4.2)$$

and, in consequence, the HT be written as:

$$|(x - x_0)^2 + (y - y_0)^2 + (z - z_0)^2 - R^2| < \epsilon \quad (4.3)$$

where  $(x_0, y_0, z_0)$  is the sphere center,  $(x, y, z)$  the points coordinates in the sphere surface,  $\epsilon$  the tolerance and  $R$  the sphere radius. Then, by iterating over the boundary pixels of shapes in the image, we are able to vote in the accumulator space, by incrementing all the points within the given tolerance. In practice, the direct use of 3D CHT extension is not feasible due to the highest computation and memory cost it demands in the accumulator storage space. However, some alternatives have been proposed which explore properties of the systems to alleviate this cost, for instance, by dividing the problem into sub-problems with lower accumulator space storage requirements [172].

### 4.4.4 The developed method

The goal is to detect the sphere-like shapes in medical images, as they approximate the femoral head and both condyles. For this task, a method based on the GHT was developed. The classical HT can also be used in this scenario, given that we are able to define a parametric model of a 3D sphere. However, there is a major drawback restricting its use: with the use of parametrical models we are restricted to look into spheres with a particular radius. This is not the general case, given that the femur size varies from person to person. In turn, the GHT provides a flexible framework which can be adapted to accommodate the search for a range of radii. The original formulation of the GHT requires the construction of a R-table, which stores the gradient direction of the model with regard to the angle. For this algorithm, the voting procedure is modified. Instead, the method is based on a radial voting such that, for every edge pixel, points along the normal drawn from that point and within a given radius range, receive a vote. The implementation was based in the ITK library [173]. In the end, the accumulator can be drawn over the original image, where each pixel value indicates its vote number.

In order to optimize the search for the spherical features, their radius should be limited to an interval which should be as narrow as possible, for the sake of computational efficiency. However, the interval should also be wide enough to contain the expected radius of the femoral head and the condyles. A literature review [174, 175] pointed to different values for radius estimation, therefore a battery of tests was conducted to tune the algorithm. An additional tweak that enhanced the speed of the algorithm was the down-sampling of the original high resolution ('UZ Gent') images. The down-sampling was only conducted in the axial slices, where only one slice in every five was considered. Image resolution in this axes was then reduced from 0.6 mm to 3 mm which is still enough to accurately define the sphericity of the head of the femur and the condyles.

Since the sphere-like structures are bone tissue, which has a high CT value, a simple threshold is used at the beginning to remove soft tissues and thus

making the detection faster. In the following Figure 4.10, the accumulator results for the tuned radius expectancy  $R \in [25, 30]$  pixels are shown. The most voted pixels are represented in warm colors and they represent the best candidates for the center of a sphere-like feature.

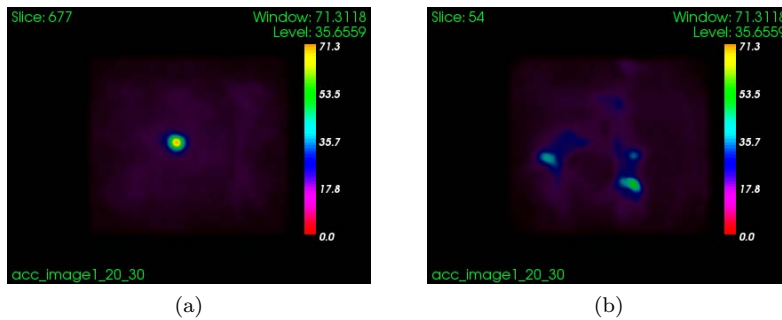


Figure 4.10: Two axial slices of the accumulator image. The color-scale represents the amount of votes for every candidate (pixel) according to the side scale. (a) is a slice on the maximum peak found and corresponds to the location of the femoral head. (b) shows two nearby peaks who stand for stand for the pixels that represent the center of the spherical femoral condyles. This proved to be enough to accurately locate the femoral bounding box and crop the original image in a way that transformations become more time efficient.

As seen in figure 4.10, the best candidate, i.e. most voted, is the center of the femoral head. Even without any radius limitation, the femoral head will still have the maximum vote into the accumulator space. Hence, the maximum peak in the image scale is found in the center of the femoral head center (Fig. 4.10a). The two less voted peaks in figure 4.10b represent the femoral condyles. Even though they are not as evident as the femoral head, it was enough to label them successfully and use their locations on the image domain to predict the limits for the femoral bounding box.

At this point, the center of the three sphere-like structures of interest is identifiable. It is important to note that a rough estimate of this center is enough to locate the bounding box that contains the femur in the image domain and crop it. Due to the fact that these structures are located in the extremities of the femur, the crop box will be limited by their coordinates in the superior inferior axis, with a tolerance limit that can be easily estimated as the image group presents nearly the same voxel size among all images. Figure 4.11 shows a slice in the coronal plane with the location of the femoral head and condyles in green and red for the right and left femur, respectively.

Left and right femur cropping is done in a similar way: a predefined tolerance is added in the axial directions to the location of the left and rightmost node of interest and then the image is cropped. If there are domain restrictions to the tolerance level, i.e., the femur is not entirely defined within the image domain, the cropping is consequently restricted by the domain. Figure 4.12 shows a maximum intensity projection of the left and right femur bounding boxes.

In sum, even though the method is not very time efficient, it proved to be very reliable and managed to successfully crop the femur bounding boxes for

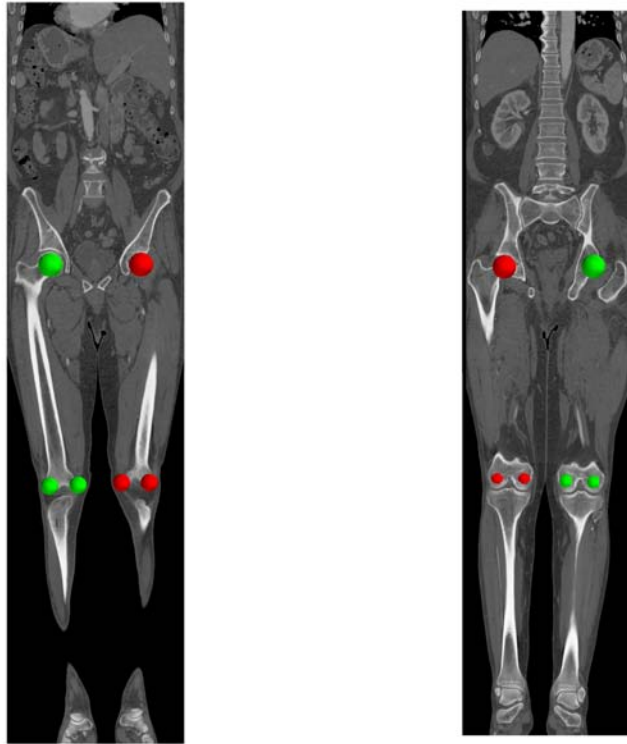


Figure 4.11: Anterior and posterior views of the superior-inferior plane of the original dataset image domain, containing information from the superior torso to just inferior of the ankle. Femoral heads and condyles are identified in green and red, respectively for the right and left femur.

all of the datasets in the 'UZ Gent' group. Moreover, this algorithm's pipeline is only performed once and all posterior transformations are performed in the resulting images, with a much smaller domain. Hence, a lot of processing time in the active shape model training and its application to segmentation was saved. The femoral bounding boxes are able to define the femoral volume in approximately 800 axial slices, slightly less than half of the original images. The resolution of this cropped images is the same as no other parameter was changed in the process.



Figure 4.12: Maximum intensity projections of the left and right femur image domains, respectively. The algorithm crops the original dataset image in a way that ideally only the axial slices corresponding to the femur bone are selected.



## Chapter 5

# Femur Active Shape Model: Training

In this chapter, the training of the femoral shape model will be reviewed. This is the basis for the automatic segmentation pipeline presented in chapter 6. The femoral volume is described by a piece-wise parametric mesh that was fitted to previously segmented femurs. As seen in chapter 3, this provides a correspondent distribution of fitted mesh nodes across the entire training set, particularly at well-conserved geometry features. The shape model training was done by fitting the mesh to each training femur, before statistical modeling using PCA [118]. The training pipeline is summarized in Figure 5.1.

In the first section, the segmentation of the initial population of femurs is described extensively. A semi-automatic procedure was developed in order to create triangular meshes that describe the femur shape from the image datasets described in previous chapter 4.

The following sections sections 5.2 and 5.4 cover the theory behind the key methods used to create the SSM and the LAM of the femur, focusing on its formulation and implementation and presenting examples for an easier understanding. Section 5.2 is subdivided in subsection 5.2.1 which covers the Lagrange piece-wise parametric meshes used to describe the femur shape and the correspondence among the population; and subsection 5.2.2 which accounts for the fitting of a generic point cloud mesh to the parametric mesh used in the present thesis. Section 5.3 describes the alignment and dimensionality reduction method used - the PCA. Section 5.4 briefly describes the adaptation of the ASM theory for Lagrange parametric meshes and the subsequent creation of the LAM.

In the latter sections, the training of the model based on the image datasets presented in the previous chapter is thoroughly described. This shape model will serve as basis for the automatic segmentation pipeline presented in this thesis. Section 5.5 summarizes the femoral shape mesh design, while section 5.6 describes the training process. The chapter ends with section 5.7 where the final remarks on the technique are featured.

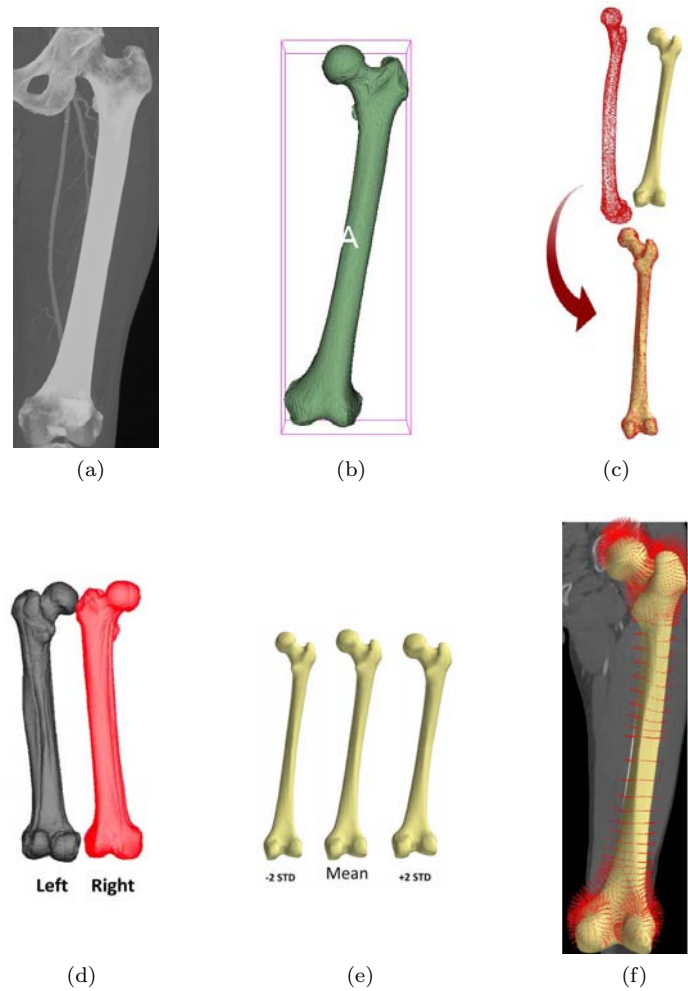


Figure 5.1: Overview of the femur shape model training pipeline. The starting point are the CT Scan datasets (a) from where a semiautomatic segmentation process generates the triangulated meshes of the femoral volume (b). In (c), the fitting of the triangular mesh to the piece-wise parametric mesh is shown, enabling correspondence between the mesh nodes across the femur population. A Procrustes Analysis is performed to remove all translational, rotational and scaling variations from the femur population, as illustrated in (d). The creation of the statistical shape model and local appearance model based on a Principal Component Analysis of the available data is shown in the last two figures: in (e) the mean shape is illustrated, along with a couple of variations of the first principal component and (f) shows a plot of the mesh normals along which the image gradient profiles are acquired.



## 5.1 Segmentation

In order to train the shape model, a set of 30 datasets was randomly selected for the effect. The images were exclusively taken from the 'UZ Gent' group as they image resolution is significantly higher. The semi-automatic segmentation was done using 3DSlicer<sup>1</sup>, a free and open source software package for visualization and medical image computing based on ITK<sup>2</sup>. The segmentation took advantage of the techniques implemented in the software but also required some manual adjustments. Figure 5.2 shows a screen-shot of the 3DSlicer software.

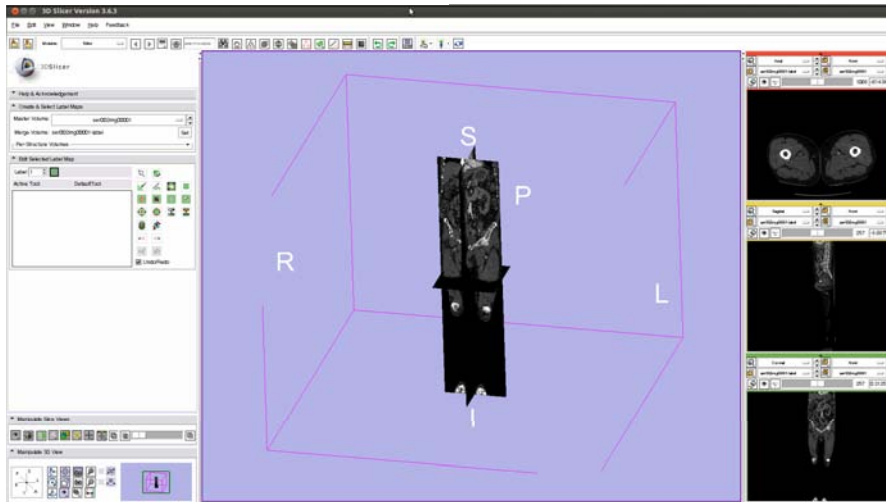


Figure 5.2: Screen-shot of 3DSlicer. On the left there is the Module panel, where the segmentation functions are visible; on the center, the 3D viewer where an example dataset is shown; and on the right the axial (red), sagittal (yellow) and coronal (green) views of the dataset.

A step-by-step description of the pipeline is presented in the following paragraphs:

1. The femoral region on the dataset was cropped for the sake of computational efficiency - Fig. 5.3a.
2. Based on the Hounsfield value interval for bone tissue, the image is thresholded in order to isolate the tissue of interest from the surrounding soft tissues. However, the range of bone tissue sometimes includes soft tissues that absorb as much radiation as cancellous bone, mainly in the distal parts of the femur. Figure 5.3b shows the volume reconstruction of all the regions that belong to the predicted range of pixel intensity values. Due to the use of a special dye, the blood vessels are highlighted in these scans and therefore present a value on the Hounsfield scale in the same range as bone tissue.
3. The resulting image from last step includes different islands. An island, also known as connected region, is defined as a group of pixels which

<sup>1</sup><http://www.slicer.org/>

<sup>2</sup><http://www.itk.org/>

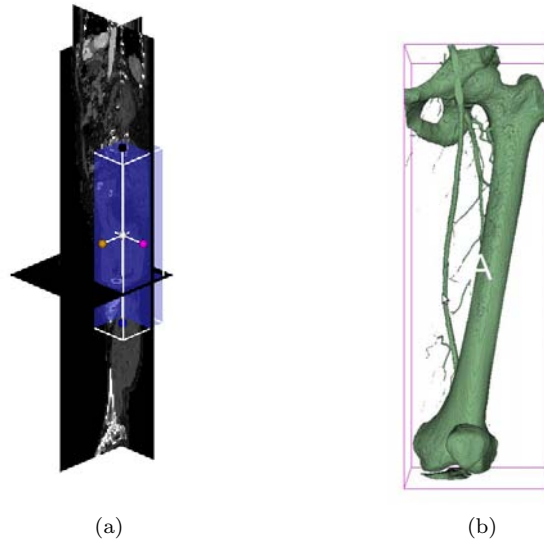


Figure 5.3: 3D view of the full image domain in (a) and cropped image limits in blue. (b) shows the 3D reconstruction of the initial thresholded region, expected to be bone tissue.

touch each other but are surrounded by zero valued voxels. The idea is to minimize user manual interaction. Even experienced users will take a serious amount of time if manually editing the image slice per slice as the femur in these datasets is defined in about 1000 axial slices. Therefore, functions like Identify Island and Save Island will significantly reduce the amount of time in isolating the island corresponding to the femur. Figure 5.4 shows a volume reconstruction after the deletion of all non-connected pixel groups. Coincidentally, in this specific example, the patela, the tibia and the fibula are not connected to the femoral island. However, the femoral artery and the profunda femoris artery are attached to the linea aspera and can not be segmented in this way.

4. Hence, some manual segmentation is required. The blood vessel attachment to the femur (Fig. 5.5a) is singular and limited to the neighboring axial slices. It can, therefore, be manually separated within a couple of minutes. Figure 5.5b shows the volume reconstruction of the volume of interest at this point, where it is observable that the acetabular bone is still an issue.
5. This step is the most time consuming part of the segmentation process. It is hard to generalize how long this task would take as it depends not only on the contact area of the femur and the acetabular cup but also on the quality of the bone mass, as sometimes the femoral head border is not easy to manually identify. Figure 5.6a shows the threshold estimation of the segmentation and the contact area is highlighted. Erode and Dilate functions might be helpful at this point: these are two morphological operations that consist of convoluting an image  $\mathcal{A}$  with some kernel  $\mathcal{B}$

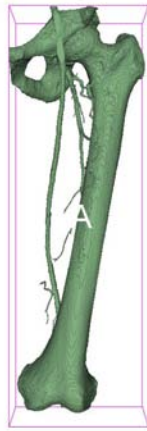
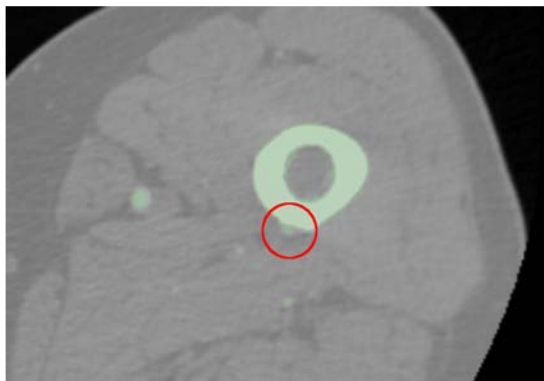
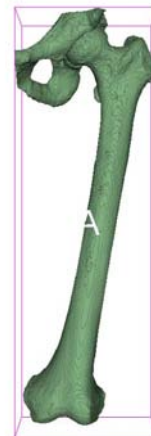


Figure 5.4: 3D reconstruction of the largest pixel island in the cropped image domain. The patella, the tibia and the fibula no longer figure on the image as they were not connected to the femoral island in the binary map.



(a)



(b)

Figure 5.5: An axial slice of the region where the blood vessel attaches to the bone is shown in (a). After manual island separation, the resulting volume reconstruction is shown in (b). Only the acetabulum and the femoral volumes are shown at this point.

with a defined anchor point, usually being the center of the kernel. As the kernel  $\mathcal{B}$  is scanned over the image, the minimal, or maximal in the case of dilation, pixel value overlapped by  $\mathcal{B}$  is computed and replaced by the image pixel under the anchor point with that minimal, or maximal, value. Erosion causes the label to get thinner and it often leads to the separation of the head of the femur and the acetabulum. A posterior dilation can compensate the volume loss with the erosion. This technique can decrease the amount of manual interaction but never completely.

- The creation of the 3D models from the gray-scale data made use of the Marching Cubes [80] algorithm to build a surface that consists in a triangle mesh. The exported femoral model from 3DSlicer is shown in Figure 5.6b.

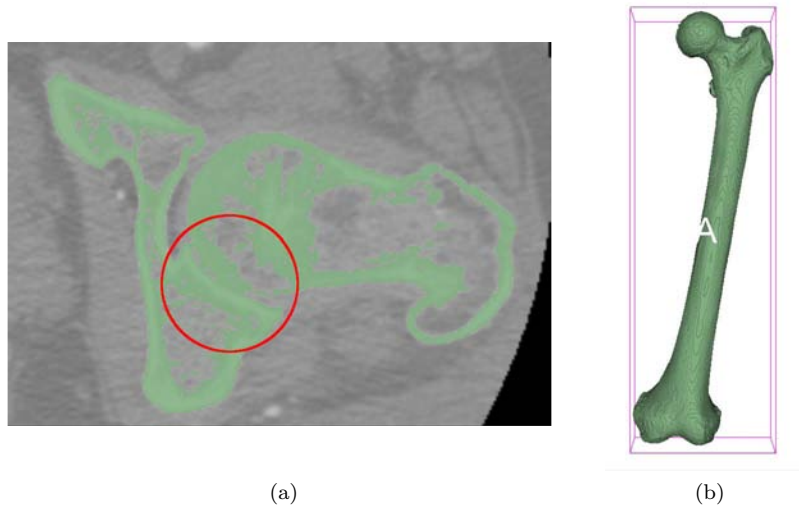


Figure 5.6: (a) shows an axial slice where the femoral head and acetabular cup border definition problem is present. Due to low bone mass density and proximity of both surfaces, the femoral segmentation problem is often complex with conventional segmentation methods. For the shape model training, it was done manually and the resulting volume is shown in (b).

- The 3D models were imported to pyFormex<sup>3</sup>, an open source program for generating, transforming and manipulating large geometrical models of 3D structures. Then, the GNU Triangulated Surface Library<sup>4</sup> is used to reduce the number of edges of the triangulated surface for the sake of computational efficiency. The edge reduction algorithm [176] allowed a shape, boundary and shape optimization while the smoothing algorithm [177] allowed the suavization of the voxel-size stair-effect of the volume. The final volume is presented in Figure 5.7.

## 5.2 Statistical Shape Model

As seen in chapter 3, the first key step in the construction of a SSM is the choice of a shape descriptor to describe each object in the training set. These were extensively reviewed in the subsection 3.3.3.1 of the same chapter and their advantages and disadvantages were compared in Table 3.3. Based on that, a piece-wise surface mesh of patches, or 2D elements, each interpolated by polynomial basis functions was chosen as a natural and flexible way to represent the femoral volume. When compared to data point clouds, e.g. triangulated

<sup>3</sup><http://www.nongnu.org/pyformex/>

<sup>4</sup><http://gts.sourceforge.net/>

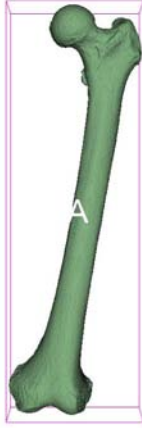


Figure 5.7: Final smoothed and decimated 3D reconstruction of the segmented femoral volume.

surfaces as the ones resulting from the method described on previous section 5.1, they offer a number of advantages [100]:

- High-order polynomial parametric meshes typically require fewer degrees of freedom to represent complex surfaces. This reduces the size of the correspondence problem and the complexity of the statistical model;
- A triangulated surface has a fixed number of vertices on which image analysis can be performed. In contrast, parametric meshes can be discretized to any desired number of nodes, increasing the resolution of the mesh;
- The basis function of the mesh elements constrains the way they fit to a certain geometry which helps to preserve the correspondence when fitting meshes to a population of shapes;
- They are more robust and suitable for representing noisy data.

### 5.2.1 Shape Descriptor

The femoral shape is described with use of a piece-wise parametric mesh of Lagrange elements. For each element in this mesh, the basis function  $\phi_1, \dots, \phi_p$  are defined over the element's bi-dimensional parametric space, with coordinates  $(\xi_1, \xi_2)$  such that

$$\mathbf{x} = \sum_{i=1}^p \mathbf{x}_i \phi_i(\xi_1, \xi_2) \quad (5.1)$$

where  $\mathbf{x} = (x_1, x_2, x_3)$  are the coordinates of the mesh in  $\mathbb{R}^3$  at  $(\xi_1, \xi_2)$ .  $\mathbf{x}_1, \dots, \mathbf{x}_p$  are known  $\mathbb{R}^3$  surface coordinates at fixed element coordinates, also named nodes or control points.

When elements are joined to form a mesh, adjacent elements share the coordinates of their nodes on the common boundary in order to create a continuous surface across elements, as shown in Figure 5.8.

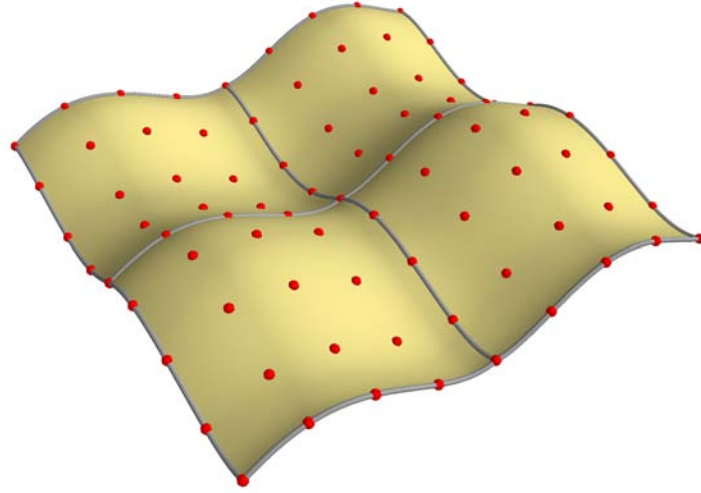


Figure 5.8: A quartic four-element Lagrange piece-wise parametric mesh. The element boundaries are marked in gray and the mesh nodes are marked in red.

A point in the mesh can be uniquely defined by a set of element coordinates and the element it is in. These points will be referred to as material points as their defined in the coordinates of the material or surface. The term mesh parameters shall refer to the set of all nodal coordinates of a mesh and is defined as

$$\mathbf{X} = (\mathbf{x}_1, \dots, \mathbf{x}_n) \quad (5.2)$$

where

$$\mathbf{x}_i = (x_i^1, x_i^2, x_i^3) \quad (5.3)$$

denotes the coordinate direction in  $\mathfrak{R}^3$ .

The overall 3D geometry is altered by changing its mesh parameters or nodal coordinates (Eq. 5.2). The theory behind altering mesh parameters to fit a triangulated mesh is the focus of the subsection 5.2.2. Furthermore, the process of fitting the meshed derived from previous section 5.1 is also extensively described in sections 5.5 and 5.6. As no derivative information is carried at nodes of Lagrange elements, there is no inherent smoothness across elements and therefore Lagrange meshes are  $C^0$  continuous. Hence, methods to emphasize smoothness between elements will also be presented.

### 5.2.1.1 Quartic Lagrange Basis Function

Mesher with quartic, i.e., that use 4<sup>th</sup> order polynomial basis functions, are fitted to the femur geometry in order to model its shape. A combination of quadrilateral and triangular elements were used to allow greater flexibility in the mesh design, as the topology of the mesh is not constrained to a regular grid of quadrilateral elements. Furthermore, there is no requirement for continuous element coordinate directions across elements as Lagrange elements do not have derivative parameters.

The basis for a 1D quartic Lagrange element are:

$$\begin{aligned}
\phi_1 &= \frac{1}{3}(32\xi^4 - 80\xi^3 + 70\xi^2 - 25\xi + 3) \\
\phi_2 &= \frac{1}{3}(-128\xi^4 + 288\xi^3 - 208\xi^2 + 48\xi) \\
\phi_3 &= \frac{1}{3}(192\xi^4 - 384\xi^3 + 228\xi^2 - 36\xi) \\
\phi_4 &= \frac{1}{3}(128\xi^4 - 224\xi^3 + 112\xi^2 + 16\xi) \\
\phi_5 &= \frac{1}{3}(32\xi^4 - 48\xi^3 + 22\xi^2 - 3\xi)
\end{aligned} \tag{5.4}$$

and correspond to the node numbers in Figure 5.9.

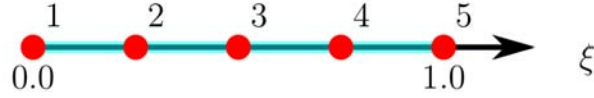


Figure 5.9: 1D Quartic Lagrange line element.

The tensor product of equation 5.4 quadrilateral elements results in 25 2D element basis functions (Eq. 5.5). For a triangular element instead (Fig. 5.10b), the 15 basis functions are shown in Equation 5.6, which correspond to the nodes in Figure 5.10.  $(l_1, l_2, l_3) = (1 - \xi_1 - \xi_2, \xi_1, \xi_2)$  are the area coordinates defined over a standard triangle with vertices  $[(0, 0), (1, 0), (0, 1)]$  in element coordinates.

$$\phi_{ij} = \phi_i(\xi_1)\phi_j(\xi_2) \quad \text{for } i, j \in \{1, 2, 3, 4, 5\} \tag{5.5}$$

$$\begin{aligned}
\phi_{11} &= \frac{32}{3}(l_1 - 3/4)(l_1 - 1/2)(l_1 - 1/4)l_1 & \phi_{12} &= \frac{128}{3}(l_1 - 1/2)(l_1 - 1/4)l_1l_2 \\
\phi_{13} &= 64(l_1 - 1/4)l_1(l_2 - 1/4)l_2 & \phi_{14} &= \frac{128}{3}(l_2 - 1/2)(l_2 - 1/4)l_1l_2 \\
\phi_{15} &= \frac{32}{3}(l_2 - 3/4)(l_2 - 1/2)(l_2 - 1/4)l_2 & \phi_{21} &= \frac{128}{3}(l_1 - 1/2)(l_1 - 1/4)l_1l_3 \\
\phi_{22} &= 128(l_1 - 1/4)l_1l_2l_3 & \phi_{23} &= 128l_1(l_2 - 1/4)l_2l_3 \\
\phi_{24} &= \frac{128}{3}(l_2 - 1/2)(l_2 - 1/4)l_2l_3 & \phi_{31} &= 64(l_1 - 1/4)l_1(l_3 - 1/4)l_3 \\
\phi_{32} &= 128(l_3 - 1/4)l_1l_2l_3 & \phi_{33} &= 64(l_2 - 1/4)l_2(l_3 - 1/4)l_3 \\
\phi_{41} &= \frac{128}{3}(l_3 - 1/2)(l_3 - 1/4)l_1l_3 & \phi_{42} &= \frac{128}{3}(l_3 - 1/2)(l_3 - 1/4)l_2l_3 \\
\phi_{51} &= \frac{32}{3}(l_3 - 3/4)(l_3 - 1/2)(l_3 - 1/4)l_3
\end{aligned} \tag{5.6}$$

Each element has two points of inflection in each element-coordinate direction, as seen in Figure 5.11. In other words, a single 2D element can represent ridge or valley-like features, protrusions and depressions, which are all present

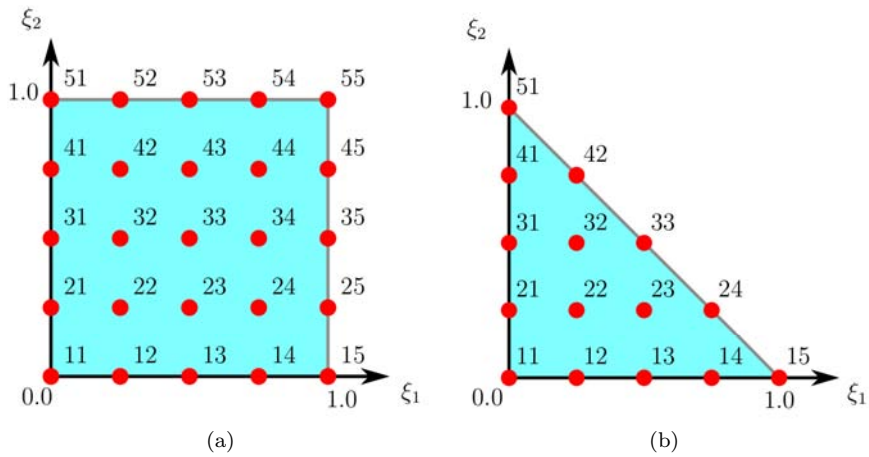


Figure 5.10: 2D Quartic Lagrange quadrilateral (a) and triangular (b) elements. Node numbers correspond to basis functions in equations 5.5 and 5.6, respectively.

in the femoral surface. Therefore, they are guided to these features by a mesh fitting process [178] which is going to be detailed in next section. This process improves the correspondence of elements between different fitted meshes. This proved to be of major importance in designing the femur mesh topology, as the elements' interior part is placed over high-curvature features while element boundaries are placed in regions of low curvature.

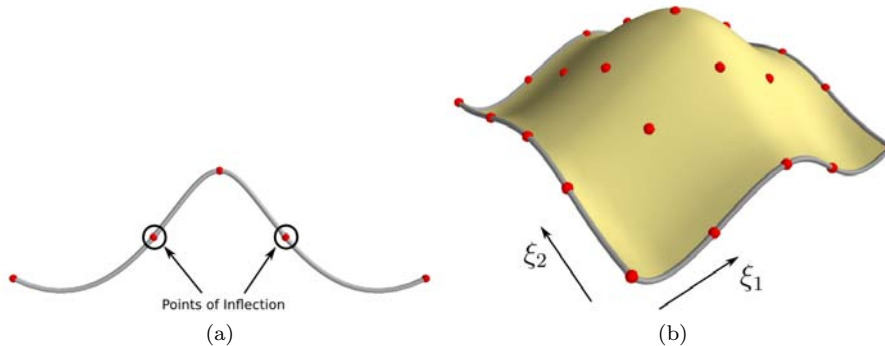


Figure 5.11: Flexibility of quartic Lagrange elements. (a) shows the inflection points on a 1D line element and (b) illustrates a 2D element that efficiently models protrusions and ridges, present on the femoral surface.

Advantages of such a choice for a shape descriptor have been listed in the beginning of this section. However, the choice of Lagrange basis functions brings along some limitations. The first obvious limitation of Lagrange elements is that they are not smooth in the element boundaries, i.e., there is only  $C^0$  continuity across elements and therefore additional regularization is required during the mesh fitting process to force smoothness across boundaries



(see subsection 5.2.2). Nevertheless,  $C^0$ -only continuity allows rectangular and triangular elements to be simply connected by sharing boundary nodes, leading to a more flexible mesh design when compared to other used piece-wise parametric basis functions that present  $C^1$  or higher, such as Hermite [178] or B-Splines [108, 179]. These approaches also require a more complicated subdivision or blending operations of the surface to ensure continuity. Another advantage of Lagrange elements over its alternatives is that the mesh parameters are merely the node coordinates in the same Euclidean space, which is in conformity with the assumptions of statistical methods such as the PCA (see section 5.3). Hermite meshes, on the contrary, are ruled by both coordinates and derivative values, while splines are ruled by control point and knot coordinates in the parametric space. In sum, the choice of Lagrange basis functions is due to their flexibility and straightforward mesh design and compatibility with statistical analysis.

## 5.2.2 Mesh Fitting

The geometry of the segmented femurs was customized by fitting the data points generated by the Marching Cube algorithm (see section 5.1) to the data points of the Lagrange elements. Fitting involves optimizing nodal parameters  $\mathbf{X}$  in a way that minimizes a weighted combination of data error  $\epsilon_d$  and smoothing errors  $\epsilon_s$ :

$$\epsilon(\mathbf{X}) = \epsilon_d(\mathbf{X}) + \omega_s \epsilon_s(\mathbf{X}) \quad (5.7)$$

The error  $\epsilon_d$  describes how close a fit is to data, but its minimization does not guarantee a flawless mesh, i.e., without self-intersections or sharp creases. Therefore,  $\epsilon_s$  is introduced to smooth the mesh. This subsection will present formulations of  $\epsilon_d(\mathbf{X})$  and  $\epsilon_s(\mathbf{X})$  and the ways in which mesh nodes are optimized. These methods describe the mesh fitting process used throughout the thesis.

### 5.2.2.1 Data Error

There are several ways do describe the distance between the data points and the mesh surface  $\epsilon_d$ . Three common methods were looked into: data projection, nearest material point and nearest data point. In this subsection, a brief description with schematic representations of the methods is presented and their efficient is compared.

#### Data Projection

This first method finds the orthogonal projections  $\mathbf{p}_i$  of each point  $\mathbf{d}_i$  to the mesh, as Figure 5.12 illustrates, so that

$$\epsilon_{DP} = \sum_{i=1}^D \|\mathbf{d}_i - \mathbf{p}_i\|^2 \quad (5.8)$$

This projection translates the closest distance between both. When the mesh is composed of non-linear elements, e.g. quartic Lagrange elements, a non-linear search is required for each data point and therefore the method is

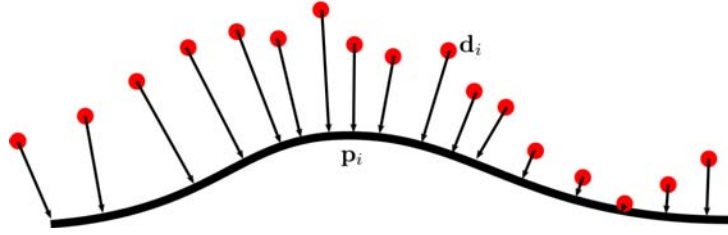


Figure 5.12: Fitting error defined as the distance between each data point and its orthogonal projection on the mesh, i.e., the minimum distance between both.

not computationally effective. In addition, as all distances from all data points are involved, outliers can adversely influence the fitting process.

### Nearest Material Point

This method, as the name points out, is a nearest material point search. The mesh is discretized by evaluating a fixed set of material points  $\mathbf{M} = \{\mathbf{m}_1, \dots, \mathbf{m}_M\}$  and the closest material point  $\mathbf{m}_i$  for each data point  $\mathbf{d}_i$  is predicted (Fig. 5.13) so that

$$\epsilon_{\text{DM}} = \sum_{i=1}^D \|\mathbf{d}_i - \Omega(\mathbf{m}_i)\|^2 \quad (5.9)$$

where  $\Omega(\mathbf{m}_i)$  stands for the mesh  $\Omega$  evaluated at the material point  $\mathbf{m}_i$ . An iterative mesh fitting pipeline was implemented for efficient searching of this point and will be reviewed further on the thesis. As the density of the material points increases,  $\epsilon_{\text{DM}}$  converges to  $\epsilon_{\text{DP}}$ .

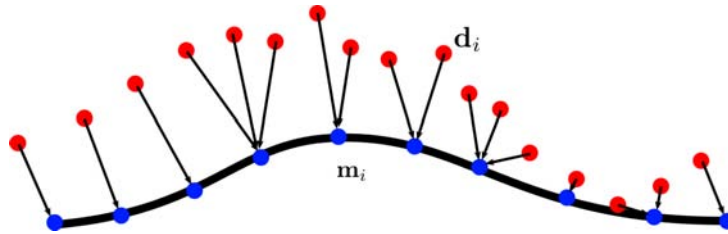


Figure 5.13: Fitting error defined as the distance between each data point and its closest material point sampled on the mesh.

### Nearest Data Point

The last method approaches the problem in an opposite way when compared to the nearest material point: similarly, the mesh is discretized at material points but now, for each material point  $\mathbf{m}_j$ , the closest data point  $\mathbf{d}_j$  is found (Fig. 5.14). Hence, the distance is

$$\epsilon_{\text{MD}} = \sum_{j=1}^M \|\Omega(\mathbf{m}_j) - \mathbf{d}_j\|^2 \quad (5.10)$$

This proved to be the most efficient method, where expensive non-linear searches are avoided and there is no need for iterative mesh fitting as the material point is not updated throughout the process. Moreover, outlier data points are ignored for closer points. However, distant but accurate data points may also be ignored so the average distance to the data points is taken in account in the search algorithm.

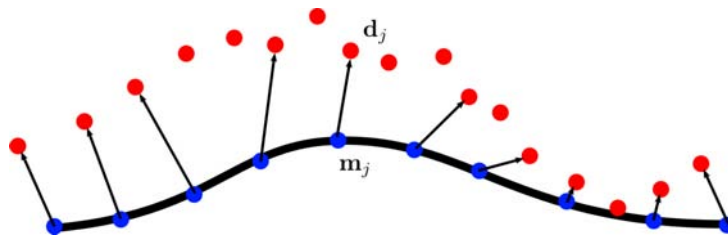


Figure 5.14: Fitting error defined as the distance between each sampled material point and its closest data point.

### 5.2.2.2 Smoothing Errors

Coupled with mesh fitting, smoothing errors result from under-constrained mesh fitting or noisy data points which lead to mesh defects. Both are illustrated in Figure 5.15 and penalization methods are used to solve such issues. Sobolev smoothing has to be used in order to penalize high curvature within elements and element boundary normal smoothing is used to encourage smoothness across element boundaries. The usage of such methods decreases the occurrence of mesh self-intersections and creasing.

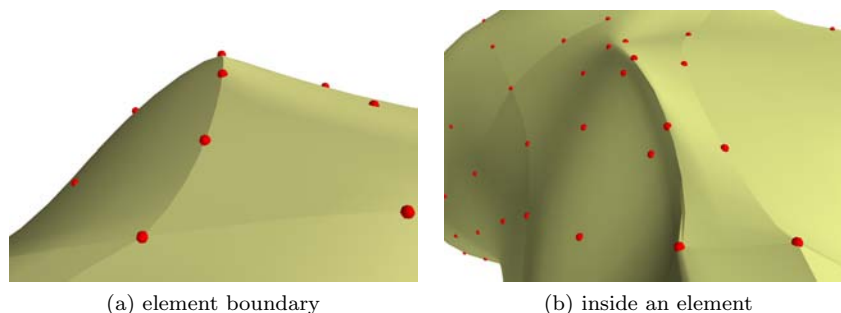


Figure 5.15: Mesh defects resulting from a lack of smoothing penalties. In (a) a sharp crease was formed at the element boundary and in (b) the crease was formed within an element. Different penalty functions are used to suppress both defects.

### Sobolev Smoothing

The second order weighted Sobolev norm [180] is calculated from the derivatives of the geometry of each element. For a curve with  $n_e$  1D elements, it is defined as

$$\epsilon_{sob}^{1D}(\mathbf{X}) = \sum_{i=1}^{n_e} \int \omega_1 \sum_{j=1}^3 \left( \frac{\partial \Omega_i^j}{d\xi} \right)^2 + \omega_2 \sum_{j=1}^3 \left( \frac{\partial^2 \Omega_i^j}{d\xi^2} \right)^2 d\xi \quad (5.11)$$

where  $\Omega_i^j$  is the geometry in element  $i$  in direction  $j$ .

For a mesh with  $n_e$  2D elements, the Sobolev term is

$$\begin{aligned} \epsilon_{sob}^{2D}(\mathbf{X}) = & \sum_{i=1}^{n_e} \int \int \omega_{11} \sum_{j=1}^3 \left( \frac{\partial \Omega_i^j}{\partial \xi_1} \right)^2 + \omega_{12} \sum_{j=1}^3 \left( \frac{\partial^2 \Omega_i^j}{d\xi_1^2} \right)^2 \partial \xi + \\ & \omega_{21} \sum_{j=1}^3 \left( \frac{\partial \Omega_i^j}{\partial \xi_2} \right)^2 + \omega_{22} \sum_{j=1}^3 \left( \frac{\partial^2 \Omega_i^j}{d\xi_2^2} \right)^2 \partial \xi + \\ & \omega_{211} \sum_{j=1}^3 \left( \frac{\partial^2 \Omega_i^j}{\partial \xi_1 \partial \xi_2} \right)^2 \partial \xi_1 \partial \xi_2 \end{aligned} \quad (5.12)$$

The first order derivatives regularizes the length of elements along  $\xi$  directions while the second order derivatives penalize high curvature. The cross derivative in the 2D case penalizes against very large or very small areas in 2D elements [181].

### Element Boundary Smoothing

As seen in previous subsection, Lagrange elements are  $C^0$  continuous, i.e., they are only continuous in position but not tangent direction or curvature across elements. However, for geometric accuracy, it is mandatory for these properties to be continuous as well. Thus penalty functions are applied against smoothness discontinuities across element boundaries.

For 1D line elements, the penalization aims to minimize differences in tangent directions at element junctions. Given a 1D mesh with  $n_t$  connections between line elements, the tangent smoothing penalty is:

$$\epsilon_b^{1D} = \sum_{i=1}^{n_t} 1 - t_{i,1} \cdot t_{i,2} \quad (5.13)$$

where  $t_{i,1}$  and  $t_{i,2}$  are the normalized tangent vectors at the joining ends of the two elements at connection  $i$ . Figure 5.16a illustrates precisely this.

For 2D elements, differences in element boundary normals are penalized. Given a mesh with  $n_b$  shared element boundaries, the penalty is:

$$\epsilon_b^{2D} = \sum_{i=1}^{n_b} \int 1 - N_{i,1} \cdot N_{i,2} d\xi_b \quad (5.14)$$

where  $N_{i,1}$  and  $N_{i,2}$  are normalized mesh surface normals evaluated in the two adjacent elements along the shared boundary  $i$ , with element coordinates  $\xi_b$  (Fig. 5.16b).

### 5.2.2.3 Fitting Methods

The methods used for adjusting the mesh parameters will be reviewed in the following paragraphs. These methods are postulated in a way that errors defined in subsections 5.2.2.1 and 5.2.2.2 are minimized.

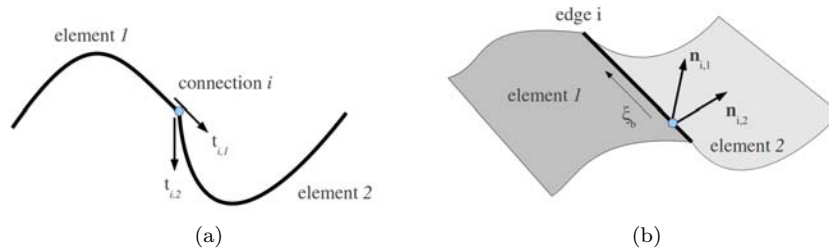


Figure 5.16: Tangent smoothing for 1D line elements (a) and normal smoothing for 2D surface elements (b).

### Nodal Fit

In a nodal fit pipeline, the mesh parameters are free to adjust independently to minimize the least-squares distance. Even though it produces accurate fits, these are computationally expensive as the number of degrees of freedom is considerable and it requires tuning of smoothing weights.

### Free-Form Deformation

Free-Form Deformation (FFD) [182] is a method that allows mesh fitting on a coarse scale, used to perform geometric transformations consisting of both Euclidean (translation and rotation) and Affine (Euclidean plus scaling and shearing) operations on arbitrary point cloud meshes. As illustrated in Figure 5.17, the slave mesh is embedded in a coarse host mesh with fewer degrees of freedom. The fitting adjusts the parameters of the host mesh and, as the host mesh deforms, the slave mesh deforms according to the warping of the space internal to the host mesh.

The host mesh is typically composed of a small number of low-order tricubic elements that completely envelop the slave mesh. The slave mesh, on its turn, is embedded by calculating the host mesh material coordinates of the slave mesh nodes (slave nodes). As the host mesh deforms, slave node coordinates are updated by evaluating the host mesh at these material coordinates. Since the host mesh has far fewer degrees of freedom than the slave mesh, the complexity of the fit is greatly reduced at the cost of fitting accuracy. FFD is used to bring a template mesh close to the data efficiently before nodal fitting fine tunes the fit.

The design of the piece-wise parametric femur mesh and its fitting to the data point cloud meshes resulting from the segmentation described in section 5.1 will be extensively reviewed and commented on section 5.6, but first the shape correspondence method used for correlate information on the initial segmented femurs population will be presented.

### Principal Component Fit

Given a set of  $k$  principal components trained from a set of meshes, mesh parameters  $\mathbf{x}'$  can be generated from the weighted sum of the principal components  $\mathbf{b}$  and the mean shape  $\bar{\mathbf{x}}$ , according to

$$\mathbf{x}' = \bar{\mathbf{x}} + \sum_{i=1}^k \mathbf{b}_i a_i \quad (5.15)$$

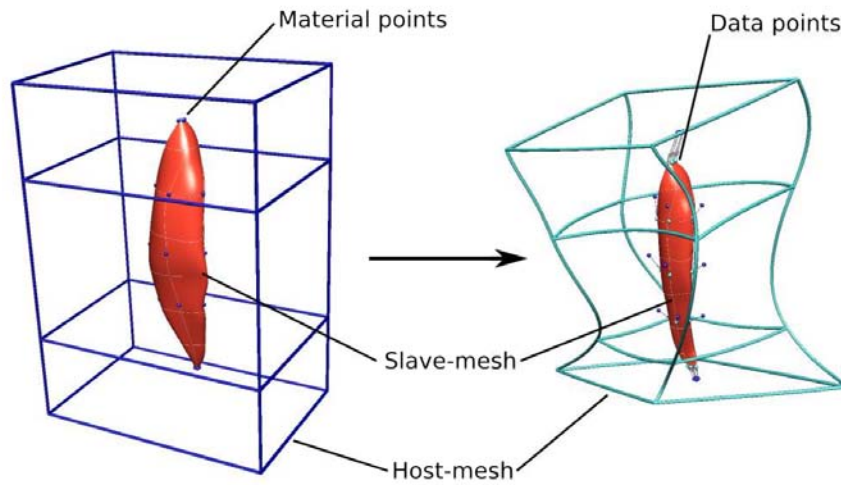


Figure 5.17: Free-Form Deformation of a rectus femoris muscle. The mesh of the muscle is embedded as a slave mesh in a simple host mesh. Material points on the slave mesh are fitted to data points by deforming the host mesh, which deforms the embedded slave mesh [178].

For a more extensive description of the PCA technique, a reading of the following section 5.3 is suggested. By adjusting the weights, or principal component scores  $\alpha$ , plus a rigid body translation  $\mathbf{t}$ , rotation  $\mathbf{r}$  and scaling  $s$ , a mesh can be customized to minimize error.

Principal component fitting has three clear advantages, added to the two previous methods:

1. Far fewer degrees of freedom are involved in the fitting, which reflects in added efficiency;
2. Robust to unrealistic mesh geometries or defects, due to the weights constraints on the reconstruction;
3. Principal component fitting distributes mesh nodes in a way that is correspondent across the population, so that iterative fitting (Sec. 5.6.1) and training can be used to improve the correspondence of fitted meshes.

### 5.3 Alignment and Dimensionality Reduction

Simultaneously to the choice of the shape descriptor, a decision has to be made to accurately cross the information of the population of femurs. In order to remove the whole-femur translational and rotational variations, all femurs were aligned by their centers of mass and principal axes of inertia before the PCA took place (Sec. 3.3.3.2).

The use of a piece-wise parametric mesh, described with detail in last section 5.2, where node points coordinates are described in the same Euclidean space, made the choice of PCA obvious and allowed a straightforward implementation as the mesh parameters are coincident across the same femur population.

Moreover, as seen in section 3.3.3.3, in 3D statistical shape analysis problems as over-fitting or lacking robustness of non-linear methods are more present and, depending on the complexity of the shape variances to model, the PCA suits the majority of the demands.

PCA is the most widely used dimension reduction method for statistical shape analysis [118]. It decomposes multi-dimensional data into orthogonal components of maximum variance. Given  $n$  observations of  $m$  variables, or  $n$  data points in an  $m$ -dimensional space, PCA can be thought of as a rotation of axes in  $m$ -dimensional space so that the first axis is aligned with the direction of maximum variance among the  $n$  points. The second axis will be aligned according to the next greatest direction of variance which is orthogonal to the first one and so on. This is illustrated in Figure 5.18, where an example for 2D data is presented.

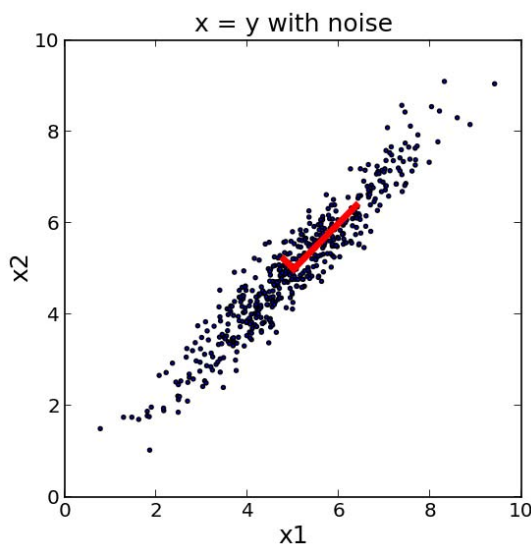


Figure 5.18: PCA on 2D data. The longest of the principal components (in red) is the first and the orthogonal is the second. This length depends on the standard deviation in each direction.

The directions of the new axes are named the principal components and the projections of the data points on the axes are usually referred to as weights or scores. For a shape model, the axes are centered at the mean shape of the population. Since the principal components are orthogonal, an observation can be reconstructed by a linear combination of these principal components weighted by its scores, or closely approximated by the first few principal components and its corresponding scores. This allows a number of advantages in statistical shape analysis which will be focused further on this section. However, the PCA assumes the data to be Gaussian, i.e. can be described by the mean and variance, and that the data has a high signal-to-noise ratio so that high variance has considerable significance.

### 5.3.1 Computation

The PCA can be computed in two distinct ways: eigen-decomposition of the covariance matrix of the centered data and SVD [183]. Both approaches start by concatenating the  $n$  observations of each of the  $m$  variables in a  $m$  by  $n$  data matrix  $\mathbf{X}$

$$\mathbf{X} = \begin{pmatrix} x_{1,1} & \cdots & x_{1,n} \\ \vdots & \ddots & \vdots \\ x_{m,1} & \cdots & x_{m,n} \end{pmatrix} \quad (5.16)$$

In the first method, the calculation of the principal components of the matrix is done by diagonalizing the covariance matrix of  $\mathbf{X}$

$$\mathbf{C}_{\mathbf{X}} = \frac{1}{n-1} \mathbf{X}\mathbf{X}^T = \mathbf{E}\mathbf{D}\mathbf{E}^T \quad (5.17)$$

The eigenvectors of  $\mathbf{C}_{\mathbf{X}}$  are the principal components and correspond to the columns of  $\mathbf{E}$ . The eigenvalues  $\lambda_1 > \lambda_2 > \cdots > \lambda_m$  are the variances along each component, but also the diagonals of  $\mathbf{D}$ .

When  $m$  is equal or greater than  $n$ ,  $\mathbf{C}_{\mathbf{X}}$  is rank deficient as there can only be as many principal components as the number of observations minus one. In this case, the SVD method can be used. In addition, it is also more computationally efficient. Hence, a different data matrix  $\mathbf{Y}$  is constructed so that

$$\mathbf{Y} = \frac{1}{\sqrt{n-1}} \mathbf{X}^T \quad (5.18)$$

and  $\mathbf{Y}^T\mathbf{Y} = \mathbf{C}_{\mathbf{X}}$ . Carrying out the SVD on  $\mathbf{Y}$

$$\mathbf{Y} = \mathbf{U}\mathbf{\Sigma}\mathbf{V}^T \quad (5.19)$$

yields the principal components as the columns of  $\mathbf{V}$  and the square root of their variances in the diagonals of  $\mathbf{\Sigma}$ . The weights  $\mathbf{a}$  of an observation  $\mathbf{x}$  on the principal components  $\mathbf{b}_1, \dots, \mathbf{b}_{n-1}$  can be calculated by

$$\mathbf{a} = \mathbf{x} \cdot \begin{pmatrix} \vdots & & \vdots \\ \mathbf{b}_1 & \cdots & \mathbf{b}_{n-1} \\ \vdots & & \vdots \end{pmatrix} \quad (5.20)$$

Conversely, an observation  $\mathbf{x}'$  can be approximated by a linear combination of the first  $k$  principal components and the mean  $\bar{\mathbf{x}}$

$$\mathbf{x}' = \bar{\mathbf{x}} + \sum_{i=1}^k \mathbf{b}_i a_i \quad (5.21)$$

as illustrated in Figure 5.19, where the 2D data from Figure 5.18 is reconstructed using just the principal component, resulting in the removal of noise in the  $x_1 = -x_2$  direction.

The distance of an observation to the training set mean is the Mahalanobis distance



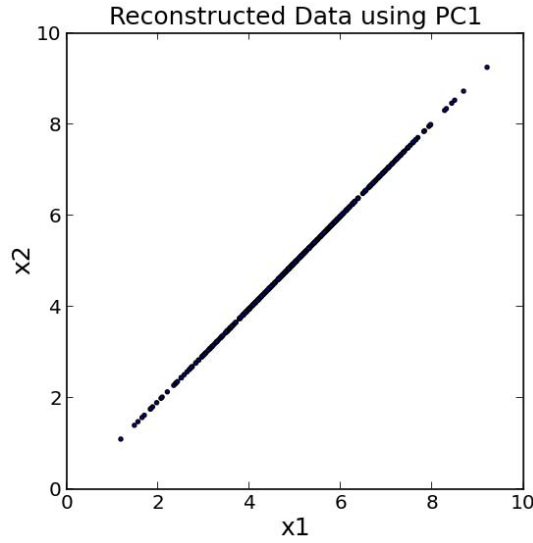


Figure 5.19: Reconstruction of the PCA on 2D data using just the first principal component.

$$h = \sqrt{\sum_{i=1}^k \frac{a_i^2}{\lambda_i}} \quad (5.22)$$

that quantifies the unlikeliness of an observation and can be used to identify outliers or penalize the generation of unrealistic observations.

The number of principal components  $k$  is usually chosen so that the variance accounted for  $\sum_{i=1}^k \lambda_i$  reaches a certain proportion of the total variance  $\sum_{i=1}^n \lambda_i$ . The proportion is usually arbitrarily chosen at 0.95 although more objective methods for determining  $k$  have been proposed in the literature [118, 184].

## 5.4 Active Shape Modeling

ASMs were first introduced as an application of statistical shape modeling to image segmentation [99]. Although the method is not new, it is still widely used [86] due to its simplicity and efficiency. Section 3.3.3 extensively reviews its literature and provides a background for its use in the present thesis. This section will describe the methodology adapted for piece-wise parametric meshes. More details and discussion can be found in a paper by the same original author [185].

### 5.4.1 Training

ASM also requires a LAM, besides the previously described shape model. The LAM is a statistical model of the normalized image gradient – based on the voxel intensity values – normal to the object surface at specific landmarks. This model is trained on a set of images and their segmented surfaces.

If the profiles through each model point along the model boundary are analyzed, edges where the intensity abruptly changes can be identified. However, these profiles often do not correspond to the strongest edge of the profile, as for example the profiles in the femoral head where the acetabular cup edge is also present. The best approach is then to learn from a training set what to look for in the target image. This is achieved by sampling along the profile normal to the boundary in the training set and building a statistical model of the gray-level structure - the LAM.

For each dataset, the image intensity profiles are sampled in evenly spaced mesh material points,  $\mathbf{q}^{\text{ASM}} = \{q_i^{\text{ASM}} | i = 1, \dots, Q^{\text{ASM}}\}$ . These are a discretization along the surface of the mesh node points, decreasing the distance between them. Figure 5.20 shows the evenly spaced normals along the mesh surface.



Figure 5.20: Anterior and posterior views of the active shape model with its normals to material points (in red), along which the image gradient profiles are sampled.

In order to reduce the effects of global intensity changes, the derivative along the profile is sampled rather than the absolute gray-level profiles. These gradients of the profiles are then calculated and normalized by dividing through the sum of absolute element values, hence removing variations in global intensity between datasets with different origin. As proposed by Cootes et al. [99], the gradient of a profile  $\mathbf{g}'$  with  $2l$  samples along its domain, is normalized to  $\mathbf{g}$  according to:

$$\mathbf{g} = \frac{\mathbf{g}'}{\sum_{i=1}^{2l+1} |g'_i|} \quad (5.23)$$

where  $l$  is the number of profile samples in each of the directions of the normal, added to the model point itself. This is repeated for every training image in order to get normalized profiles  $\{\mathbf{g}_i\}$  for every model point. The normalized profiles of two sample model points are shown in Figure 5.21.

Then, at every material point  $q^{\text{ASM}}$ , a PCA is computed over the normal extent  $\mathbf{g}_i | i = 1, \dots, m$ , producing a mean profile with principal components  $\mathbf{b}_i | i = 1, \dots, m$  and eigen-values  $\lambda_i | i = 1, \dots, m$ .  $m$  is the size of the training set. The Mahalanobis distance  $h$  [186] of a mean-subtracted unseen profile  $\mathbf{g}^*$  is calculated by projection onto the principal components:

$$h = \sqrt{\sum_{i=1}^k \frac{(\mathbf{g}^* \cdot \mathbf{b}_i)^2}{\lambda_i}} \quad (5.24)$$

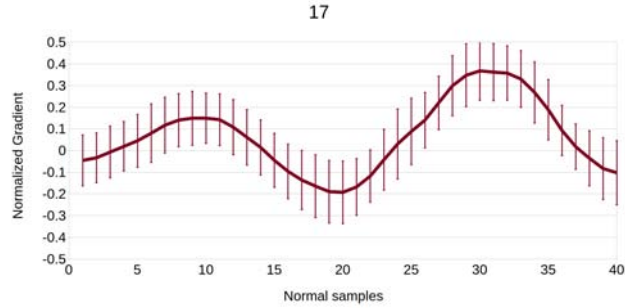
The Mahalanobis distance quantifies how similar is the profile  $\mathbf{g}^*$  and the profiles sampled from the training set. The smaller  $h$ , the greater the similarity. In the ASM segmentation (Chapter 6), the profile models are used to identify probable matches for the femoral surface in the image.

Image gradient quantifies the directional change in the intensity of a gray-scale image. For both of the above images,  $m = 40$  points were sampled, 20 to each direction of the surface normal. In image 5.21a, the material point is located in the femoral head. Its gradient is rather noisy due to the varying bone mass density among the femur population, which is reflected in a significant standard deviation of the training data. The rise past the half-way point of the profile is due to the presence of the pelvic bone. On the contrary, the profile in image 5.21b shows a very clean profile on the positive side of the normal, where the samples are in a soft tissue only region. This is in concordance with what was expected for a material point located in the femoral shaft.

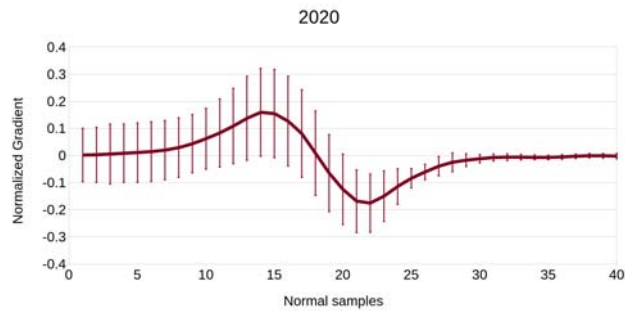
The segmentation process is described in the following chapter 6 and it is based on both the SSM (section 5.2) and the LAM. Basically, it will start with an estimation of the pose and shape of the in-image femur and search the image along the normals of the surface mesh with the same discretization of the LAM. It then compares the sampled profiles to the corresponding trained profiles and the surface is moved to the new center of the profile. Posteriorly, outlier predictions will be corrected and the mesh is iteratively updated until convergence.

## 5.5 Femur Mesh Design

The femur was partitioned into six correspondent regions, based on the Gaussian curvature of their nodes, which were then fitted to the femur training set. This fact enabled correspondence among the training shapes as they now have the mesh nodes specifically located along their geometry. Therefore, statistical shape modeling was allowed to accurately cross statistical information across the population and consequently its training (section 5.6). The femur volume partitioning into correspondent regions that could be accurately fitted by Lagrange elements (see subsection 5.2.1) was done in two steps: the design of a femur mesh with regions that share some property and their fitting to each of the 30 training femurs.



(a) Material point 17



(b) Material point 2020

Figure 5.21: Image profiles sampled normal to material points (a) and (b). On the left, the model with the corresponding normal is shown and on the right the average normalized gradient profiles. (a) corresponds to a point in the femoral head and (b) to the femoral shaft. Error bars show one standard deviation from the mean at each sample point. For the femoral head, the rise in value past the half-way point of the profile is due to the pelvis. The shaft shows a much cleaner profile with only soft-tissue on the side of the cortex.

Correspondent description can be achieved by partitioning surfaces into correspondent regions and optimizing correspondence within each region [187, 188, 138]. Some authors approach the problem manually, which can be subjective and is definitely time consuming, or semi-automatically, with use of some intrinsic surface property, such as curvature, which reduces the manual interaction but still leaves the problem of having to manually designate the regions between the shapes. Zhang [100] proposed to approach this problem by automatically partitioning the femur volume based on the Gaussian curvature and

finding similar regions across the training set by clustering and ranking them in their correspondence. Due to the good results the approach offered, it was adapted to the femoral mesh design presented in this section.

The Gaussian curvature [189] is defined at the cost of the two principal curvatures,  $\kappa_1$  and  $\kappa_2$ , which determine the local shape of a point on a surface. One characterizes the rate of maximum bending of the surface and the tangent direction in which it occurs, while the other characterizes the rate and tangent direction of minimum bending, respectively. The rate of surface bending across any tangent direction at the same point is determined by the two principal curvatures. If the surface patch  $\sigma(u, v)$  is considered, the Gaussian curvature of  $\sigma$  is given by

$$K = \kappa_1 \kappa_2 \quad (5.25)$$

and its independent of the unit normal  $\mathbf{n}$ . However, the sign of  $K$  at a point  $\mathbf{p}$  on a surface  $\sigma$  has an important geometric meaning:

1.  $K > 0$  The principal curvatures  $\kappa_1$  and  $\kappa_2$  have the same sign. The normal curvature  $\kappa$  in any tangent  $\mathbf{t}$  is equal to  $\kappa_1 \cos^2 \theta + \kappa_2 \sin^2 \theta$ , where  $\theta$  is the angle between  $\mathbf{t}$  and the principal vector corresponding to  $\kappa_1$ . The surface is bending away from its tangent plane in all tangent directions at  $\mathbf{p}$ . Therefore, the quadratic approximation of the surface near  $\mathbf{p}$  is a paraboloid and  $\mathbf{p}$  is considered an elliptic point of the surface.
2.  $K < 0$  The principal curvatures  $\kappa_1$  and  $\kappa_2$  have opposite signs at  $\mathbf{p}$ . The quadratic approximation of the surface near  $\mathbf{p}$  is a hyperboloid. The point is then said to be a hyperbolic point of the surface.
3.  $K = 0$  There are two cases:
  - a) Only one of the principal curvatures is zero. In this case, the quadratic approximation is a cylinder and  $\mathbf{p}$  is called a parabolic point of the surface.
  - b) Both principal curvatures are zero. The quadratic approximation is a plane. The point  $\mathbf{p}$  is a planar point of the surface and the shape of the surface nearby can't be determined without examining the third or higher order derivatives.

Femoral mesh vertices were then classified according to their Gaussian curvature signs, as illustrated in Figure 5.22. Due to noise in Gaussian curvature or imperfect triangular meshes, there were many small spurious regions which were grouped to the nearest considerably large regions by iterative inclusion of faces with similarly classified vertices [190].

Regions of similar Gaussian curvature were then identified in the set of training femurs and based on that the femur was partitioned into six regions: the femoral head, the greater trochanter, the medial and the lateral condyle, and the proximal and distal shaft. Some regions, as the proximal and distal regions, do not show a uniform sign concordance within their domain. However, as Figure 5.22a shows, the curvature values are significantly lower than the condyles or trochanters and therefore suitable to group in the same region. The six regions were finally assembled into the ensemble mesh which describes

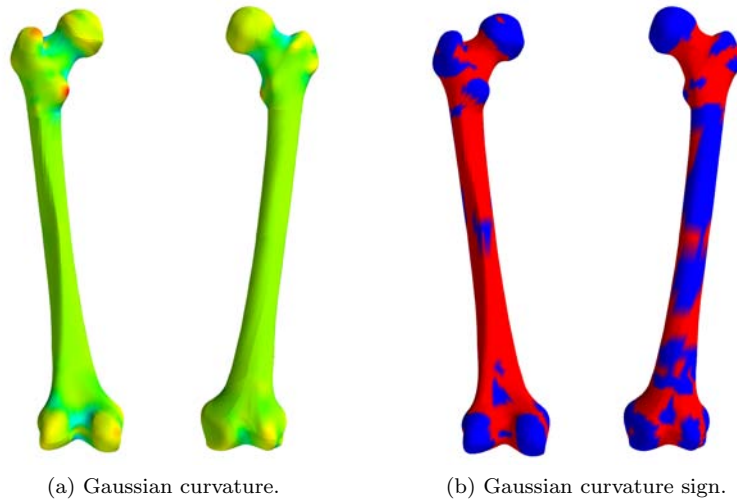


Figure 5.22: Partitioning regions on the femoral surface. (a) shows the Gaussian curvature of estimation at vertices, where hot colors (red) represent regions of high curvature and contrarily regions of low curvature are represented by cold colors (blue), and (b) shows the vertices classified by Gaussian curvature sign, where red and blue regions represent negative and positive curvatures, respectively. In both cases, left figure corresponds to posterior view and right figure to anterior view.

the shape of the whole femur, as illustrated in Figure 5.23. Region boundaries are shown in thick black and element boundaries are represented by thinner gray lines.

The meshes were composed of quadrilateral and triangular elements interpolated by quartic-Lagrange basis functions, described with detail in subsection 5.2.1, along with their principal advantages over their alternatives. Quartic-Lagrange basis allow elements to have up to three points of inflection in each element-coordinate direction, meaning that a single element can represent a ridge-like, valley-like, convex or concave feature, all of which present in the femur. Element boundaries were purposely placed in low curvature regions for greater flexibility in mesh design. Elements share the nodes in their boundaries in order to allow a simpler assembly. In sum, the femur mesh was composed of 63 elements and 634 nodes, giving 1902 degrees of freedom (Fig. 5.24).

## 5.6 Femur Shape Model Training

The training of the femur shape model using the femur mesh described in the previous section has two steps: the mesh fitting, where each region’s reference mesh is fitted to its corresponding set of region meshes in an iterative fitting process, in order to improve correspondence among them; and a second step, where the ensemble meshes are statistically evaluated with a PCA, creating a statistical model that compactly but accurately describes the femoral shape. Fitting errors and model compactness are discussed in the final paragraphs of this section.

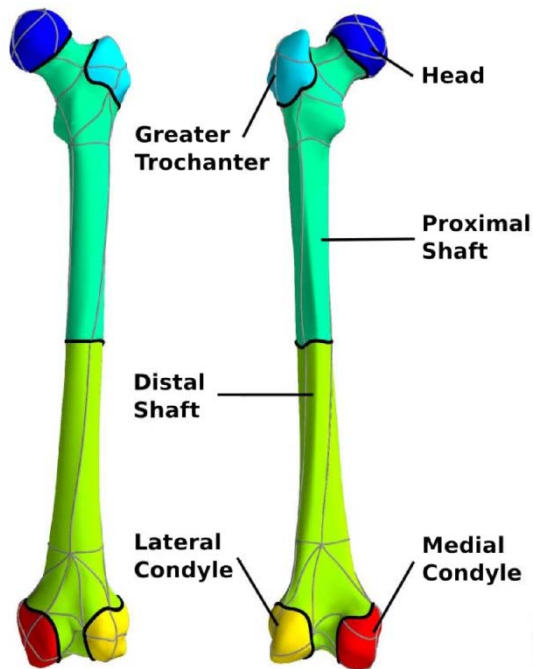


Figure 5.23: The ensemble femur mesh, composed by six region meshes. Region boundaries are shown in black and element boundaries in gray. Anterior view on the left and posterior view on the right [100].

### 5.6.1 Fitting Meshes

Figure 5.25 illustrates the data point cloud originated by the segmentation described in section 5.1 and the assembled piece-wise parametric mesh, also named reference mesh. The objective is to fit the parametric region meshes to the point cloud. The fitting pipeline will be described thoroughly in the following paragraphs. The fitting methods, objective function and smoothing functions referenced below are described in detail in section 5.2.2.

The fitting process can be summed up in the following steps:

1. The reference mesh was aligned to data points using iterative closest point;
2. The aligned mesh was coarsely fitted to the surface by free-form deformation or shape model approximation;
3. Mesh boundary nodes were fixed to the boundary curve nodes;
4. Mesh was fitted to data points by optimizing unconstrained nodes - nodal fit.

The initial position of the data point can't be predicted: in this example (Fig. 5.25), the reference mesh is rotated nearly 90 degrees in relation to the point data cloud and at the distance of an also random translation and scaling. The reference region mesh  $\Omega^R$  was fitted to the data points of training

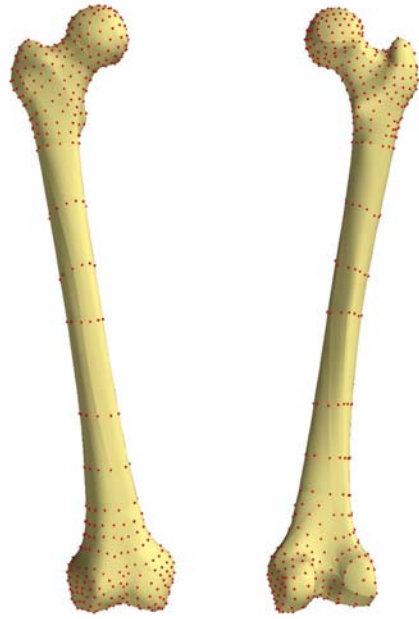


Figure 5.24: From left to right, anterior and posterior views of the template mesh of the femur. The 634 nodes are shown in red.

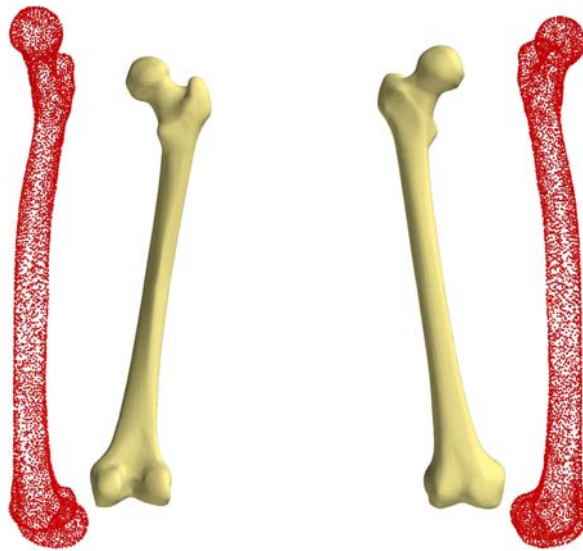


Figure 5.25: Posterior and anterior views of the data point cloud originated by the segmentation (in red) and the reference mesh.



regions  $\mathbf{V}^R$ , with its boundary nodes  $\mathbf{x}_{b_1, \dots, b_{n_B}}^R$  fixed to the nodes of the fitted boundary curves  $\mathbf{x}_{1, \dots, n_B}^B$ .

The mesh  $\Omega^R$  was aligned to the data point cloud vertices by finding the optimal translational ( $\mathbf{t}$ ), rotational ( $\mathbf{r}$ ) and scaling ( $s$ ) transformations

$$\mathbf{T} = (t_x, t_y, t_z, r_x, r_y, r_z, s) \quad (5.26)$$

that the minimized sum of the squared distance between the data points and their closest points on the data point cloud. Figure 5.26 illustrates the data point cloud originated by the segmentation described in section 5.1 and the aligned assembled piece-wise parametric mesh.

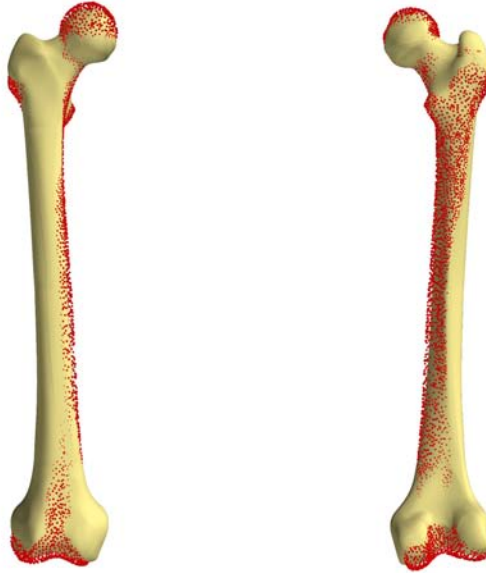


Figure 5.26: Posterior and anterior views of the rigid scale aligned data point cloud (in red) and the reference mesh.

Then, Quartic-Lagrange curves were fitted to data points, or vertices, on the boundaries of the training region surfaces, in order to ensure continuity along adjacent regions. One to one correspondence was chosen due to its simplicity and an example can be seen in Figure 5.27.

The curve  $B$  was aligned to the boundary vertices  $\mathbf{V}^b = (v_i^b, \dots, v_{N_{BD}}^b)$  according to  $\mathbf{T}$  and fitted to minimize:

$$\epsilon_{\text{boundary}} = \epsilon_{\text{MD}}(B, \mathbf{V}^b) + \epsilon_{\text{DM}}(B, \mathbf{V}^b) + \epsilon_s(B) \quad (5.27)$$

where the term  $\epsilon_{\text{MD}}(B, \mathbf{V}^b)$  is the sum of the squared distance between the points of the curve and their closest data point, the term  $\epsilon_{\text{DM}}(B, \mathbf{V}^b)$  is the inverse, i.e., the sum of the squared distance between each data point and its closest point on the curve.  $\epsilon_s(B)$  is a smoothing term incorporating Sobolev terms which penalize high curvature within elements. The two-way distance measure improves the stability of the fit, especially in noisy boundaries. The

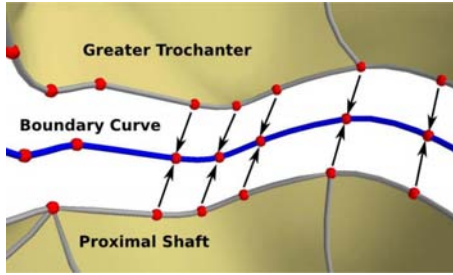


Figure 5.27: A segment of the boundary curve between the greater trochanter and the proximal shaft regions in blue, with the boundary nodes in red. One to one correspondence between both meshes and the curve nodes ensures continuity when assembled.

smoothing weights encouraged smooth curves that capture the general shape of the boundaries.

The coarse fit is a two step procedure: the first is based on the free-form deformation followed by a principal component fitting, both described in section 5.2.2. More specifically, it iteratively minimizes squared distances between the data point cloud and the parametric mesh according to

$$\epsilon_{\text{coarse}} = \epsilon_{\text{MD}}(\Omega^R, \mathbf{V}^R) + \omega_b \sum_{i=1}^{n_B} \|\mathbf{x}_{b_i}^R - \mathbf{x}_i^B\|^2 \quad (5.28)$$

where  $\epsilon_{\text{MD}}(\Omega^R, \mathbf{V}^R)$  is the sum of the squared distances between points sampled on the mesh and their closest data points (see subsection 5.2.2.1). The second term is the sum of the squared distances between the mesh boundary nodes and the boundary curve nodes. After this coarse fit, region boundary nodes were fixed to boundary curve nodes by assigning  $\mathbf{x}_{b_i}^R = \mathbf{x}_i^B$  for  $i = 1, \dots, n_B$ .

This smoothly deformed the mesh to fit large geometric features, allowing better convergence for the subsequent nodal mesh fit. In addition, it ensured that the boundary nodes were close to their corresponding nodes on the boundary curve, so that there would be minimal change in mesh geometry when boundary nodes were fixed. Figure 5.28 illustrates precisely this, i.e., the coarsely fitted mesh to the data points.

The final nodal mesh fit optimized all nodal coordinates except the ones at the boundary of each region, thus minimizing

$$\epsilon_{\text{nodal}} = \epsilon_{\text{MD}}(\Omega^R, \mathbf{V}^R) + \epsilon_s(\Omega^R) \quad (5.29)$$

where  $\epsilon_s(\Omega^R)$  is a smoothing term incorporating Sobolev penalizing terms, which avoid high curvature within elements and a penalty against mismatched normal vectors at element boundaries. The result of the fitting example here presented is shown in Figure 5.29.

## 5.6.2 Mesh Training

After iteratively fitting each femur region, the fitted region meshes for each femur in the training set were assembled into ensemble femur meshes. These underwent a final nodal mesh fit to the training set femur surfaces, with all



Figure 5.28: Posterior and anterior views of the coarsely fitted reference mesh to the data point cloud (in red).



Figure 5.29: Posterior and anterior views of the final result of the fitting of the aligned data point cloud (in red) and the reference mesh.

nodal coordinates unconstrained, in order to minimize error that may have been caused by fixed boundary nodes. The procedure is extensively described in previous subsection 5.6.1. The fitted meshes were aligned and a PCA (section

5.3) was carried out on the nodal coordinates to produce the full femur shape model.

Iterative fitting and training proved to improve accuracy and shape model compactness. Each of the training samples underwent a parametric study in order to estimate the optimal fitting method (subsection 5.2.2.3) and fitting parameters, e.g. number of iterations and the Sobolev weights. This procedure helped minimizing the mean Root Mean Square (RMS) error without compromising mesh design and boundary smoothness. The 30 fitted femurs are shown in Figure 5.30.

The femurs shown are aligned according to the first one and the variances among the training set such as femur length or shaft thickness are well observable in the figure. Approximation errors and compactness stabilized after the third iteration of the nodal fit (step 5 in Figure 5.31). However, the mesh fitting error continued to slowly decrease.

The final fitting error averaged  $0.8895 \pm 0.0179$  mm (Table 5.1). Nonetheless, fitted meshes from the third iteration were used, where the error averaged  $0.9902 \pm 0.0570$  mm. This is roughly the size of the voxel resolution in the high resolution image group (UZ Ghent) described in the chapter 4. Therefore, the fitted meshes were considered reliable representations of the manually segmented femur geometry.

<b>Step</b>	<b>Mean RMS error <math>\pm</math> SD (mm)</b>
Initial	$62.1462 \pm 25.1542$
Rigid-scale Alignment	$4.9791 \pm 0.4382$
Coarse fit (FFD)	$2.9704 \pm 0.1730$
Nodal fit	$0.8895 \pm 0.0179$

Table 5.1: Averaged fitted RMS errors for each of the steps in the fitting pipeline.

Shape model compactness was measured as the fraction of variance explained by the first five components. The first four components of the femur shape model accounted for more than 95% (Table 5.2) of total variation, and reflected obvious changes in shape and size as Figure 5.32 illustrates. Therefore, the trained femur shape model can be considered a compact representation of the variations of the femur geometry.

<b>Component</b>	<b>Percentage Significance</b>
1	90.54%
2	2.01%
3	1.63%
4	1.11%
$95.29\%$	

Table 5.2: Percentage significance of the first four principal components of the femur shape model.

The first component (Fig. 5.32a) was dominated by size variation, plus a small increase in the femoral neck angle with size. Figure 5.32b shows the second principal component, which accounted for the femur thickness, namely the widths of the proximal and distal epiphysis as well as the shaft. Inversely



Figure 5.30: Aligned ensemble meshes fitted to the segmented data. These were the 30 femurs that were used to build the statistical shape model.

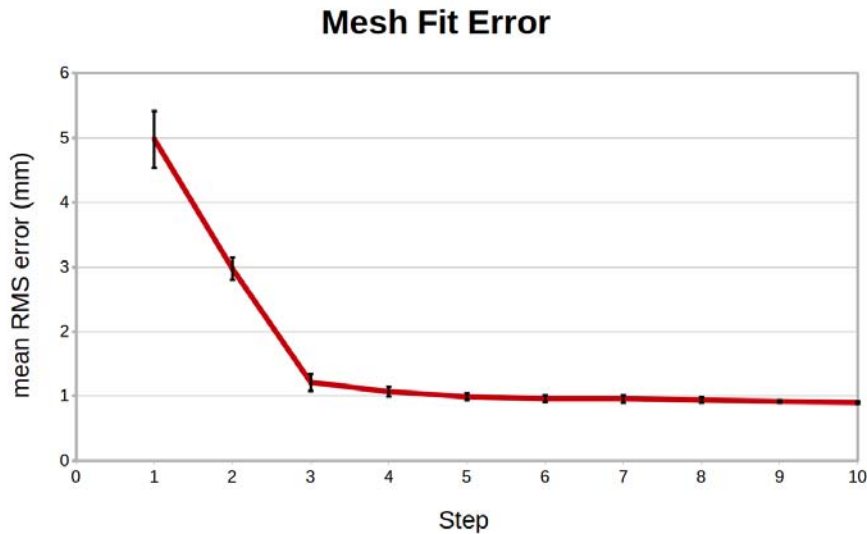


Figure 5.31: RMS distance between points sampled on the mesh and their closest data point, averaged across the training set, of the iterative fitting pipeline. Values are presented connected through the line in red with standard deviations of each step in black. Step 1 corresponds to the mean RMS error after the rigid-scale alignment. Step 2 shows the RMS error after the free-form deformation described above. Iterations 3 to 10 are part of the nodal fit. The errors gradually decrease with the step number.

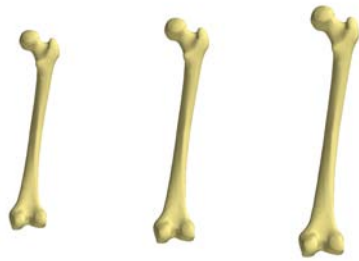
proportional is the femoral neck angle variation in the second component. The third component (Fig. 5.32c) reflected an increase in the neck angle correlated with an increase in the sizes of the proximal and distal femur. The fourth component (Fig. 5.32d) accounts for variation in the anteversion angle, i.e., the twisting of the femur along the shaft axis.

Besides fitting accuracy and compactness, the model was validated using leave-one-out cross-validation for shape model generality. For each of the fitted meshes, a shape model was trained using the remaining fitted meshes and used to approximate the left out mesh. The RMS error between the mesh and the closest points in the approximated was measured in order to quantify the ability of the shape model to accurately approximate unseen shapes.

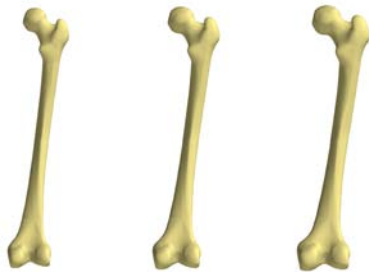
The leave-one-out approximation errors decreased as the number of principal components considered increased. For a total of 5 components the average RMS was  $1.42 \pm 0.45$  mm but when considering 20 components the value decreased to  $1.02 \pm 0.05$  mm. Errors were calculated against left out meshes and not the manually segmented surfaces.

## 5.7 Conclusions

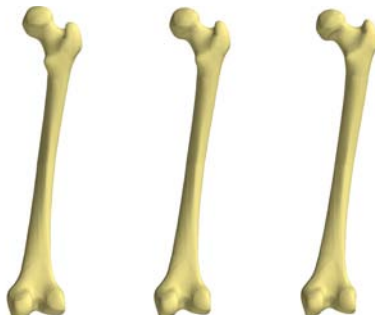
This chapter described the training of the initial femur statistical shape model, based on a training set of 30 distinct femur geometries. This model, along with the active shape model, allowed the segmentation of new training data from



(a) Component 1



(b) Component 2



(c) Component 3



(d) Component 4

Figure 5.32: Principal components of the femur shape model. (a) to (d) show shape variations along the first four principal components at  $-2$  and  $+2$  standard deviations.

CT-scan images. The segmentation pipeline will be covered in the following chapter 6. Newly segmented geometries can be automatically appended to the statistical shape model in order to broaden the incidence of the statistical analysis.

Training femurs were automatically partitioned into six regions based on their Gaussian curvature. A reference piece-wise Lagrange parametric mesh was created for each region and then assembled together into a full femur shape model. A PCA was performed in the training data and its principal components of variation were identified and studied. The creation of the SSM allowed us to identify the principal modes of variation of the human femur and perform a morphometric study on the human femur. It can be used to characterize the Belgian population's femoral shape variations and infer statistical variables valuable of all sorts, as prosthesis shape and size prediction. The image set contained both male and female patients, with a considerable age range. Therefore, some of the bones with various degrees of age-related bone loss and osteoporosis were present. It will be interesting to study how the principal components vary with the inclusion of newly segmented femur geometries.



## Chapter 6

# Femur Active Shape Model: Segmentation

This chapter details the fully automated adaptation of the ASM to medical image segmentation<sup>1</sup>. The in-image femur volume definition is possible based on the trained SSM and LAM, which were detailed in previous chapter 5, and through a mesh adaptive process initially proposed by Cootes et al. [99]. This way, it is ensured that the user is not required to have any knowledge on the techniques behind the segmentation method and can have a straightforward, fast and reliable experience with the software.

From an anthropological and forensic perspective, the femoral cortex morphology varies with factors such as age, height and ethnicity [6, 191]. It can also be used to predict the hip fracture risk [192, 193]. Determining the size and shape of the medullary canal will improve the finite-element analysis and allows the optimization of the prosthesis' geometry and stem placement.

The subsequent 3D reconstruction of the femoral volume allows kinematic, finite-element and morphometric analysis over its geometry. The segmentation method presents a novel femur pose and shape estimation procedure that significantly shortens the iterative segmentation step. This pipeline was validated and tested extensively, proving to be a reliable and time effective alternative to the reported alternatives in the literature. Therefore, this methodology is suitable to integrate a THA planning software.

In medical imaging, the accuracy of the segmentation is limited by the image resolution, as seen in chapter 4. Proposed methods for femur segmentation were reviewed in chapter 3 and will be used as comparison references to the proposed method. Figure 6.1 shows a schematic of the proposed adaptation of ASM to image segmentation, adapted for the piece-wise parametric mesh of the femur.

Section 6.1 will cover the initialization method, based on iterative point cloud fitting to find the femur pose and shape estimation of the in-image femur. Following section 6.2 will review the iterative mesh fitting to the in-image femur, for both dataset groups described in chapter 4. The segmentation of the medullary canal is reviewed in section 6.3. Sections 6.4 and 6.5 present

---

<sup>1</sup>This study was published: Diogo F. Almeida, Rui. B. Ruben, João Folgado, Paulo R. Fernandes, Emmanuel Audenaert, Benedict Verhegghe, Matthieu de Beule. "Fully Automatic segmentation of femurs with medullary canal definition in high and in low resolution CT scans", *Medical Engineering and Physics* 38.12 (2016): 1474-1480

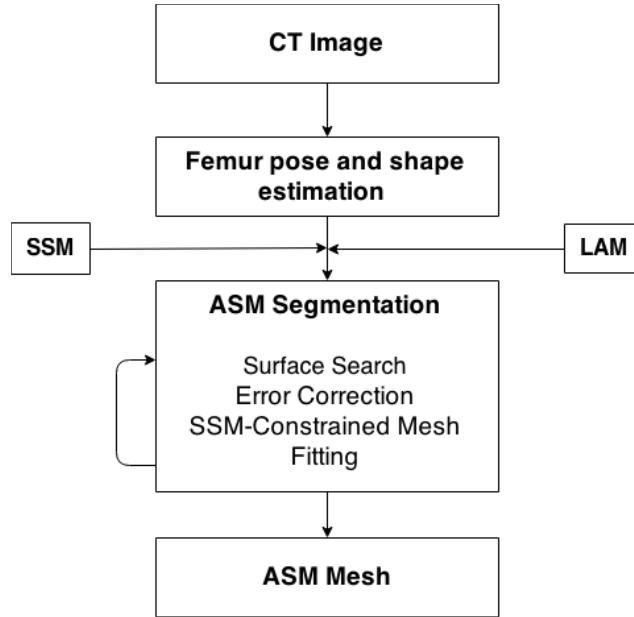


Figure 6.1: Schematic overview of the ASM segmentation pipeline.

the method validation and obtained results. The novel contributions of the developed work as well as some comparative considerations with the available methods in the literature are also accounted in these last sections.

## 6.1 Initialization

The iterative segmentation process that adapts the mesh  $\Omega$  to the in-image femur will strongly depend on the parameters of the initial guess, which account for the translation, rotation and principal components estimation. In other words, the closer the initial approximation to the in-image femur is, the faster the segmentation process converges. The initial solution to this issue was a multi level approach [99]: the training of a coarser ASM that would deal with larger deformations and then repeat the pipeline with a finer scale [194]. However, this method is very time consuming and still requires some additional image processing for the estimation of the coarser scale ASM.

The HT has also been used in this process as it allows the location of imperfect instances of objects within a certain class of shapes by a voting procedure. The assumption that some parts of the femur can be represented by geometrical shapes – namely sphere and cylinder – allows the detection of the femoral head and diaphysis, respectively [150]. Although the automation of the process was achieved with such approach, the technique is very time consuming and lacks in describing with relative precision the size of the identified shapes.

Lastly, a SSM reconstruction based on a few manually easy to identify femoral landmarks was also considered. The statistical model is able to extrapolate a synthetic femur shape based solely on the relative location of a few mesh nodes, due to the shape correspondence of the piece-wise parametric

mesh. The approximated shape provides an accurate pose estimation as it represents the statistical extrapolation of the femur shape to the in-image object. Figure 6.2 shows an example of a manual initialization of the method. Both condyles, the lesser trochanter and the fovea capitis were located manually (in green) and the model in red was extrapolated. However, this approach depends on the experience of the user to quickly identify the femoral landmarks - an experienced user would take roughly two minutes in the task. Therefore, a novel mesh fitting approach is presented in the subsequent paragraphs as a result of this doctoral work, which is computationally easy to handle and requires no input from the user.

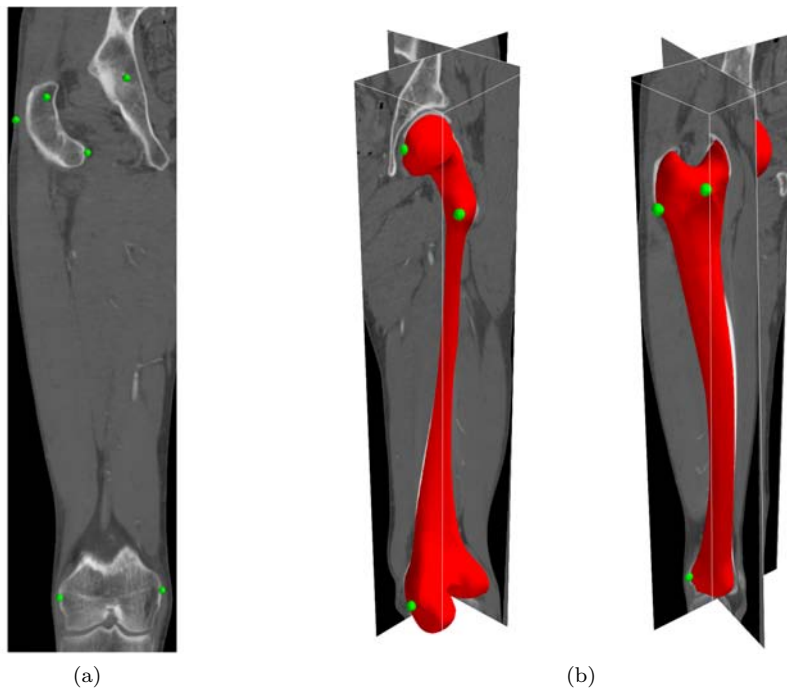


Figure 6.2: Manual initialization of the ASM segmentation. In (a), the manually extracted landmarks (in green), which correspond to easily identifiable anatomic prominences, are shown. (b) also features the landmarks together with shape reconstruction based on the SSM (in red).

As already mentioned, the intent of the proposed method is to approximate the template mean mesh to the in-image object in order to minimize the segmentation iterative process and consequently the overall computational time. This would undoubtedly improve the user experience in the THA planning software as the waiting time and knowledge required are minimized this way. The approach should be able to accurately estimate the pose and orientation of the in-image femur and place and orient the SSM, with no user input. Furthermore, it should also be robust to image artifacts and predict partially occluded femurs.

Datasets used to acquire three dimensional representations of the human body parts are slow to manipulate due to their resolution. This is unfortunately

difficult to avoid without compromising the acquisition of the level of detail of the organ’s morphology. Therefore, it was chosen to keep operations with the datasets to a minimum and instead work with a data point cloud framework. Figure 6.3 contains a step-by-step illustration of the pipeline of the proposed algorithm for the ASM initialization.

Firstly, a binary image is generated based on a band-pass threshold filter with fractions  $m$  and  $M$ , easily estimated based on the Hounsfield scale (Sec. 3.1) applied to the image. The resulting image contains bone tissue, regardless of the anatomical structure it represents, and also all the noisy data that also fulfills the filter parameters. This noisy data is mainly represented by acquisition errors due to the patient’s movements during the examination and reflectance from metallic implants the subject might have. Seldom, contrast liquids are used to enhance blood vessels visibility and some of them have their maximum coincident with the bone tissue region in the gray-scale spectrum. This means that they will also be present in our binary image, although the method is robust to their presence as we will see in the following section.

The Marching Cubes algorithm, proposed by Lorensen and Cline [80] in 1987, was used to create a triangle mesh model of the constant density surfaces of our binary image. Using a divide-and-conquer approach to generate inter-voxel connectivity, it creates a mesh using linear interpolation. It is still a very rough approximation to the in-image femur, as pictured in Figure 6.3a, but it proved to be a good starting point for the proposed method.

The template mesh that best fits a generic femur is the mean model of our SSM. Picture 6.3b shows the mean model translated to the image domain and scaled taking in account the values of the pixel spacing stated in sections 4.1 and 4.2.

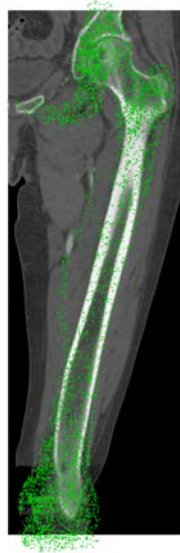
At this point, there is the need to approximate the mean model mesh to the segmented point cloud. An iterative algorithm for surface registration based on least-squares estimation to reduce the average distance between points in the two surfaces was used [195]. Its significant advantage is that the closest points in the two surfaces do not necessarily correspond to a single point in space at the cost of the iterative process.

Given the 3D coordinates of two surfaces  $\mathcal{S}_i (i = 1, \dots, m)$  and  $\mathcal{S}'_k (k = 1, \dots, n)$ , let  $\mathbf{x}_{i,j} (j = 1, \dots, N_i)$  and  $\mathbf{x}'_{k,l} (l = 1, \dots, N_k)$  be the points on the surfaces  $\mathcal{S}_i$  and  $\mathcal{S}'_k$ , respectively. The objective is to find the motion between the two point clouds, i.e.,  $\mathbf{R}$  for rotation and  $\mathbf{t}$  for translation, such that the following criterion

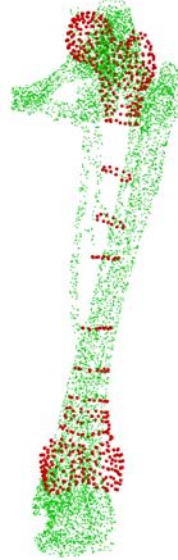
$$\mathcal{F}(\mathbf{R}, \mathbf{t}) = \sum_{i=1}^m \sum_{j=1}^{N_i} p_{i,j} d^2(\mathbf{R}\mathbf{x}_{i,j} + \mathbf{t}, \mathcal{S}'_k) + \sum_{k=1}^n \sum_{l=1}^{N_k} q_{k,l} d^2(\mathbf{R}^T \mathbf{x}'_{k,l} - \mathbf{R}^T \mathbf{t}, \mathcal{S}_i) \quad (6.1)$$

is minimized, where  $d(\mathbf{x}, \mathcal{S})$  is the distance of the point  $\mathbf{x}$  to the surface  $\mathcal{S}$ ,  $p_{i,j}$  and  $q_{k,l}$  take the value 1 if the point  $\mathbf{x}_{i,j}$  or respectively  $\mathbf{x}'_{k,l}$  can be matched on the corresponding surface and 0 otherwise. The solving of equation (6.1) is done iteratively, where at every iteration the motion estimate  $(\mathbf{R}, \mathbf{t})$  is recovered from the last and a least-squares estimate reduces the average distance between both surfaces.

The identification of the closest points is done with the use of the computationally very effective  $k$ -D trees [196]. For every point  $\mathbf{x}$ , a closest point



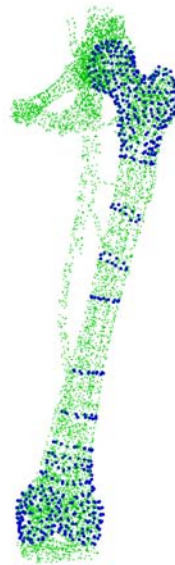
(a) Initial data.



(b) Mean mesh.



(c) First pairing.



(d) Final alignment.

Figure 6.3: ASM initialization pipeline. (a) shows the data cloud that represents the bone tissue region. The mean model (in red) is then translated and scaled to the image coordinate space (b) and the initial  $k$ -D tree correspondence is shown in (c). The final result of the iterative fitting is shown in (d).

$\mathbf{y}$  in the matching surface can always be found, even if it likely won't make sense. There was therefore the need to impose constraints to the matching algorithm for maximum distance and rotation tolerance. Furthermore, a threshold parameter  $D$  is defined which evaluates when the registration between the surfaces is good. This way, instead of considering all the matches recovered, the algorithm can iterate adaptively based on the statistics of the distances and relatively filter big motion and gross outliers.

The  $k$ -D tree is a generalization of the bisection method in one dimension to  $k$  dimensions, which in our case  $k = 3$ . Hence, a  $k$ -D tree is constructed as follows. Firstly it chooses a plane parallel to the  $yz$ -plane passing through a data point  $P$  to cut the whole space in two (generalized) rectangular hyper-rectangles such that there are approximately equal number of points on either side of the cut, originating a left and a right son. Secondly, each son is further split by a plane parallel to the  $xz$ -plane in a similar way, originating respectively two grandsons. The splitting continues with alternating directions until a hyper-rectangle not containing any point is reached: the corresponding node is the leaf of the tree. Figure 6.3c, shows the data set originated by the Marching Cubes and its nodes paired with the mean model.

A complete set of  $N$  coordinates  $\{\mathbf{x}_i\}$  and  $\{\mathbf{y}_i\}$  has been reasonably paired, so now the tree can be queried for the  $r$  closest neighbors of any given point (optionally returning only those within some maximum distance of the point). It can also be queried, with a substantial gain in efficiency, for the  $r$  approximate closest neighbors. The minimization of the mean-squares objective function

$$\mathcal{F}(\mathbf{R}, \mathbf{t}) = \frac{1}{N} \sum_{i=1}^N \|\mathbf{R}\mathbf{x}_i + \mathbf{t} - \mathbf{y}_i\|^2 \quad (6.2)$$

can be solved by any generic least-squares solver for a linear matrix equation. In the present thesis, the dual quaternions was used [197].

Because the registration algorithm expects the use of initial small distances, a two step data fitting was implemented. Firstly, it finds the translation that best fits the mean model to the in-image object by minimizing the least square distance of both meshes and then the process is repeated for a transformation that allows rotation and scaling of the template mesh. The two step rigid-scale alignment is featured in Figure 6.3d.

## 6.2 Segmentation

In this section, the adaptation of ASM segmentation to piece-wise parametric meshes will be described thoroughly. Its goal is to produce a mesh  $\Omega$  with parameters  $\mathbf{X}$  that approximates the in-image object surface.  $\mathbf{X}$  results from a rigid-body translation  $\mathbf{u} = (u_x, u_y, u_z)$  and rotation  $\mathbf{r} = (r_x, r_y, r_z)$  of mesh parameters, generated by the shape model with principal component weights  $\mathbf{a} = (a_1, \dots, a_{n_p})$ . Thus  $\mathbf{\Gamma} = (\mathbf{u}, \mathbf{r}, \mathbf{a})$  is optimized to give  $\Omega$  that matches the predicted surface. For convenience,  $\Omega(\mathbf{\Gamma})$  will denote the mesh with parameters produced by  $\mathbf{\Gamma}$  and

$$\mathbf{p}_i = \Omega(q_i^{\text{ASM}}, \mathbf{\Gamma}) \quad (6.3)$$

is the  $\mathbb{R}^3$  coordinate of  $\mathbf{p}$  evaluated at material point  $q_i^{\text{ASM}}|_{i=1, \dots, Q^{\text{ASM}}}$ , which coincide with the coordinates of the LAM. The initial  $\mathbf{p}$  is estimated by the method proposed in previous section 6.1 and a three step iterative segmentation pipeline follows:

1. Surface prediction by profile matching;
2. Element-wise error correction;
3. Mesh update with the optimization of the parameters  $\mathbf{p}$  until convergence.

### 6.2.1 Surface Prediction

In this step, the image is searched along its normal to the surface mesh at material points  $\mathbf{q}^{\text{ASM}}$  to find the best match for the LAM, as Figure 6.4 shows.

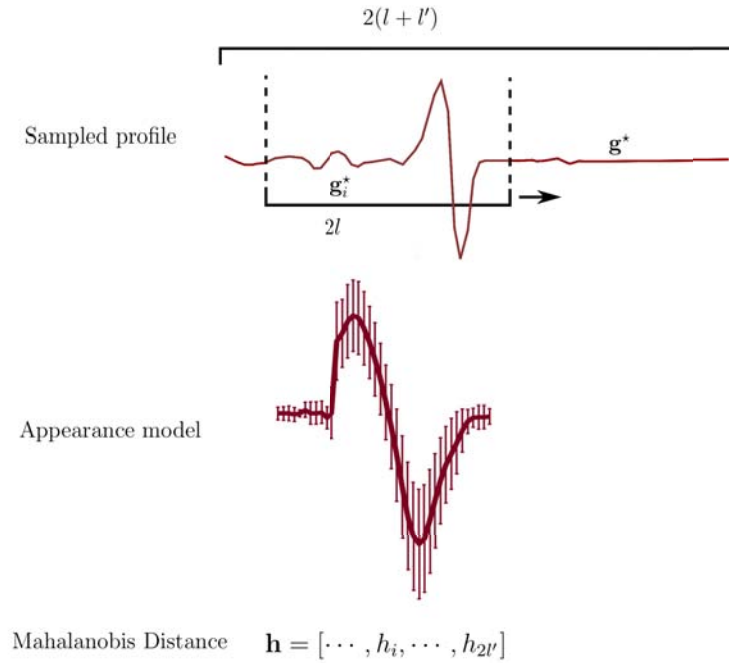


Figure 6.4: Surface prediction along a sampled profile in the ASM segmentation. A 1D profile of length  $2(l + l')$  is sampled from the image and portions of length  $2l$  are used to calculate the Mahalanobis distances against the LAM to quantify its likelihood of being from the object surface.

The sampled profile  $\mathbf{g}^*$  is usually longer when compared to our model but with the same resolution. If we consider the appearance model profiles to have a length of  $2l$ , the length of the sampled profile is considered to be  $2(l + l')$ . Hence, sub-profiles  $\mathbf{g}_i^* = (g_i^*, \dots, g_{i+2l}^*)$  are extracted from  $\mathbf{g}^*$ ,  $i \in [0, 2l']$ . The Mahalanobis distance vector  $\mathbf{h}$  of each  $\mathbf{g}^*$  is given by equation 5.24. The best matching profile is calculated according to  $\mathbf{g}_{\text{argmin}(\mathbf{h})}^*$ . By construction of the

model, the object surface is moved to the center of the profile, so a matched position of the surface along the profile is  $d = \operatorname{argmin}(\mathbf{h}) + l$ . Equation 6.4 converts this 1D coordinate to 3D coordinates  $\mathbf{d}$ ,

$$\mathbf{d} = \rho[d - (l + l')]\mathbf{n} + \mathbf{p} \quad (6.4)$$

where  $\rho$  is the profile's resolution,  $\mathbf{n}$  is the surface normal at node  $\mathbf{p}$ . The cloud data points  $\mathbf{D} = \{\mathbf{d}_i | i = 1, \dots, Q^{\text{ASM}}\}$  is constructed from the coordinates  $\mathbf{d}$  at every material point and represents the predicted surface.

### 6.2.2 Element-wise Error Correction

Profiles with  $\tilde{\mathbf{d}}$  greater than one standard deviation away from its corresponding median  $\bar{\mathbf{d}}$  are considered as possibly erroneous. This is mainly due to unexpected variations in bone morphology, artifacts or joint positioning that influence the image intensity distribution over the normal of the profiles. Nevertheless, the assumption that realistic surface points will closely follow the surface mesh, which is constrained by the shape model, allows an error correction of these erroneous predictions. For each of these profiles, all local minima of  $\mathbf{h}$  are found and the closest to  $\tilde{\mathbf{d}}$  is selected as corrected. The 3D coordinates of this match is recalculated based on the new  $\mathbf{d}$ . This proved to significantly improve the surface prediction as noticeable on Figure 6.5.

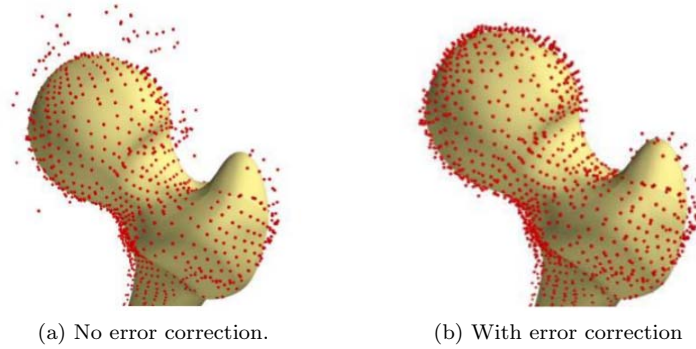


Figure 6.5: Error correction for the ASM segmentation. (a) shows femoral head with erroneous predictions (in red) that are corrected in (b).

### 6.2.3 Mesh Update

At the end of every iteration, the mesh  $\Omega$  needs to be updated to fit the surface predicted by the resulting data cloud  $\mathbf{D}$ . This occurs according to the objective function

$$\min_{\Gamma \in \text{ASM}} = \sum_{i=1}^{Q^{\text{ASM}}} \|\mathbf{d}_i - \Omega(q_i^{\text{ASM}}, \Gamma)\|^2 + h^{\text{mesh}}(\Gamma) \quad (6.5)$$

where  $h^{\text{mesh}}$  is the Mahalanobis distance of the current mesh, with shape model weights  $\mathbf{a}$  (which are part of  $\Gamma$ ), and acts as a smoothing term, penalizing



unlikely mesh shapes from being produced in the next fit. The iterative process concludes when one of the following set of criteria of success is achieved:

1. A maximum number of iterations is reached;
2. When the optimum mesh parameters have not changed between iterations;
3. When at least 80% of  $q^{\text{ASM}}$  have matched the central 20% of their sampled profiles.

Criteria one terminates segmentations that do not converge and usually occurs when the mesh is too far from the in-image object. Criteria two is satisfied when the mesh has converged. Even though it does not ensure that it has converged to the optimum shape, it stops the process if no further improvements are observed. The last criteria is satisfied if the mesh has successfully converged, within tolerances proposed by Cootes et al. [185]. An example of a segmented volume by the process above described is presented in Figure 6.6.

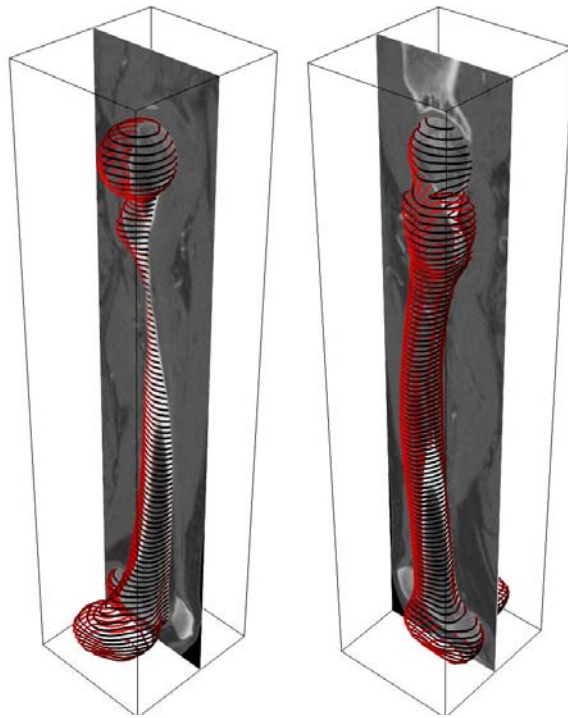


Figure 6.6: Achieved ASM segmentation example, initiated by the proposed method.

### 6.3 Segmentation of the medullary canal

As seen in section 2.4.2, the femur presents a dense cortical bone layer, also named cortex, forming the shell of the femur. In the proximal and distal femur, cancellous bone fills most the interior space, presenting an anisotropic lattice

of trabecular bone elements in the shape of plates, rods and struts which tend to align parallel to the directions of principal stress. Inside the femoral shaft, however, the medullary canal, or cavity, is filled with bone marrow.

From a femoral modeling point of view, it is interesting to locate the boundary between cortical and the medullary cavity within the femoral domain which, at this point, is determined (Fig. 6.6). Aamodt et al. [198] proposed the HU value of 600 as the CT density of the corticocancellous interface in previously reamed bones, i.e., 600 HU is the value of the boundary where bone tissue is not removable by conventional reamers. Figure 6.7 shows the contours at suggested threshold with a small error margin of 20 HU.

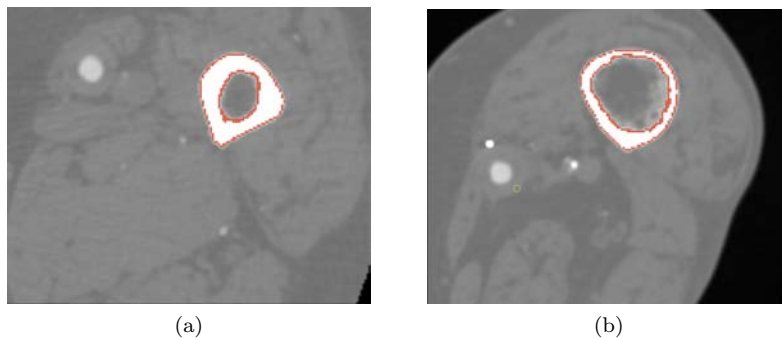


Figure 6.7: Examples of the contours generated by thresholding the dataset at the suggested values. (a) is located at mid-shaft, where the linea aspera is visible, and (b) is located in the distal shaft, hence the higher section area.

The inner contour matches the desired medullary canal border and is therefore extracted. The bone in the proximal and distal parts of the canal is less dense and therefore the classification of a voxel as cortical or cancellous bone is more controversial. However, prosthesis fixation after THA is usually done at the distal stem area, which coincides with the mid-shaft region. For the sake of automation and computational cost, the segmentation of the medullary canal is limited in both the proximal and distal parts of the shaft. The obtained results are shown in Figure 6.8, where the segmented bone geometry is represented in beige while its medullary canal is shown in red.

Full cortex segmentation problem has been addressed [111, 199] but its degree of complexity is of a higher order of the simple medullary canal extraction. Moreover, a different approach based on the gradient profiles along the inner surface normal of the shape model would be a good starting point for a full cortex mapping. Nevertheless, the method here proposed is both automatic and accurate, hence proving to be suitable for a THA guidance software, as following chapter 7 reviews.

## 6.4 Results

For the testing and validation of the proposed method, 30 different and randomly chosen datasets from the 'UZ Gent' group (Sec. 4.2) were chosen. This group was chosen over the 'Quadrantes' group due its higher inhomogeneity, i.e., includes different age and gender considerations which reflects in a variety



Figure 6.8: Anterior and posterior views of a segmented femur, in beige with 50% opacity, and its correspondent medullary canal in red.

of femur morphologies, and also due to their clearly superior voxel resolution. This way, we ensure that the propose method is extensively tested. Nevertheless, the final subsection 6.4.3 includes results from the 'Quadrantes' image group, where the proposed segmentation method excelled in performance. In some of the patients, the voxel resolution was higher than the interstitial space between the distal femur and the proximal tibia and fibula and the algorithm managed to predict the femoral shape with sub-voxel resolution.

#### 6.4.1 Initialization results

The iterative process of least-squares minimization based on  $k$ -D trees was tested on this sample and the obtained results are shown in Figure 6.9. Time-wise, it took the initialization procedure an average of 32.41 seconds to complete. An Ubuntu 14.04<sup>2</sup> machine with an Intel® Core™ i7-2600K CPU @ 3.40GHz and 8GB of RAM was used for the matter. Python<sup>3</sup> was the language on which the algorithm was implemented. Another quality indicator of the proposed method is the square root of the mean of the squares of the optimization procedures. This statistical measure, most commonly known as RMS error, can determine how good was the fitting of our mean model to the  $k$ -D tree pairings of Marching Cubes nodes. Table 6.1 shows the average RMS

---

<sup>2</sup><http://www.ubuntu.com/>

<sup>3</sup><https://www.python.org/>

error of the different steps of the alignment, as well as the final average RMS error of the manual initialization method.

Step	Proposed method $\pm$ SD	Manual $\pm$ SD
Initial	18.938 $\pm$ 7.419	
After translation	10.261 $\pm$ 3.998	
Final	5.539 $\pm$ 0.853	5.757 $\pm$ 1.009

Table 6.1: Averaged fitted RMS errors for the the proposed initialization method and the manual initialization, in mm.

The first fact that one can state from the above table is that the final value of the RMS error is, on average, one third of the initial. The initial value is merely figurative, as it depends on the  $k$ -D pairing which is not controlled in the initial stage, as explained in section 6.1. However, the final value of 5.539 is important: if we take in account that the datasets considered have sub-millimeter resolution, it reflects in an average of 5.1 pixels, which is relatively close for a mere rigid alignment. Moreover, the intent of the initialization method is a quick femur pose and shape estimate rather than an accurate femur domain definition. The advantage is clear: such low RMS values at this stage will ultimately reflect in a faster ASM segmentation, as the iterative process is shorter. Figure 6.9 shows the initialization of the ASM segmentation. It is noticeable that the rigidity constraint of the proposed method may be a limiting factor of the initialization procedure, as shown in the example that follows. The shaft thickness and the greater trochanter have a better approach in the manual approach. Nevertheless, these differences are not significant as it will be extensively described in the following paragraphs.

#### 6.4.2 'UZ Gent' datasets results

The same 30 datasets were considered to evaluate how time-consuming and accurate the ASM segmentation process described in section 6.2 was. Time-wise, the proposed method makes the segmentation slightly slower when compared to manual initialization. Even though the SSM has to extrapolate shape information based on the manually extracted landmarks, the segmentation converges in less time. For the proposed method, the average running time is  $31.12 \pm 3.21$  seconds and for the manual initialization makes the segmentation process converge in  $29.32 \pm 2.31$  seconds. However, the time difference of  $2.20 \pm 0.90$  seconds is not considerable when the landmark extraction time is taken in account. For an experienced user this time is never less than two minutes. Due to the Cython<sup>4</sup> implementation of this step, the iterative process is very efficient. This fact explains the very small difference in time of both approaches that converge to similar results. The following Table 6.2 shows the processing time for several other femur segmentation methods found in the literature. Other authors have mentioned using 16GB or more of RAM memory.

Since it's a very subjective analysis due to its dependence on the workstation capabilities, it's important to again refer to the high resolution of the datasets used in this report. In addition, the HT and active contours are known to

<sup>4</sup><http://cython.org/>

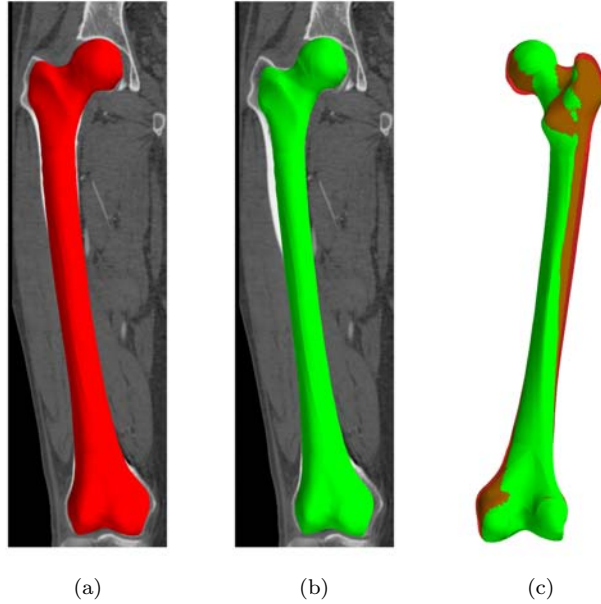


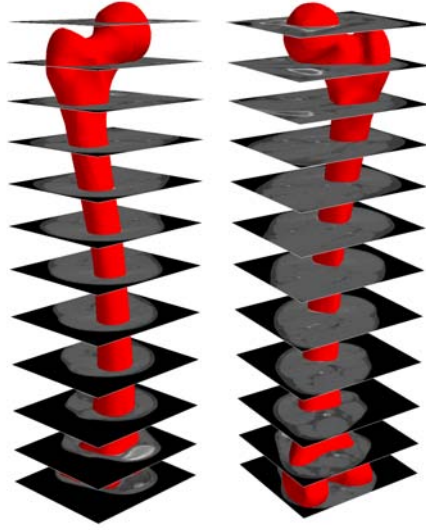
Figure 6.9: ASM initialization comparison: manually extracted landmarks (red) and the proposed method (green). (c) shows a superimposition of both shapes.

Method	Processing time $\pm$ SD (s)
Proposed	$31.12 \pm 3.21$
Manual initialization	$29.32 \pm 2.31$
Younes et al. [150]	about 180
Teodoro [79]	about 222

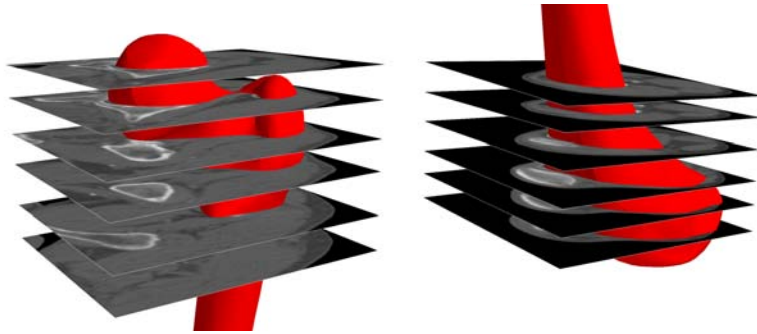
Table 6.2: Processing times for femur segmentation of the proposed method and others found in the literature.

have high computational processing times. The obtained results were very satisfying in terms of accuracy. An example of the results achieved on the proposed method is shown in Figure 6.10. Figure 6.10a shows two isometric views of the full femur volume and Figure 6.10b focus the segmentation results on the femur extremities where the segmentation is more problematic. Figure 6.11 allows the comparison of the ASM segmentation (in red) results against manual segmentation (in beige).

Every of the 30 datasets considered has converged before the maximum iteration numbers was reached. Because the convergence criteria considered on the ASM segmentation is the same regardless the initialization process, no significant difference was found on the quality of the obtained results. In order to validate the proposed method, two metrics were considered. The first is a volume overlap technique that measures the error in the meshes' agreement. It's named Dice coefficient and it is calculated as the volume of the union of



(a) Full geometry.



(b) Proximal and distal epiphysis, respectively.

Figure 6.10: Multiple views of an example of a femur ASM segmentation. In (a) the whole femur geometry is represented and in (b) the femoral epiphysis are represented.

the two meshes over the average of the volume of both sets - equation 6.6.

$$D(S, S') = \frac{2|S \cup S'|}{|S| + |S'|} \quad (6.6)$$

More simply, it's the ratio of the volume of the intersection of the red and beige meshes of Figure 6.11 and the average volume of the intersecting meshes. A value of 0 indicates no overlap and a value of 1 indicates perfect agreement. In the case of segmentation, if the value is one it means that the results match the gold standard perfectly. The second validation metric is the Hausdorff Distance (HD) [200] and is calculated according to equation 6.7.

$$d(S, S') = \max_{p \in S} d(p, S') \quad (6.7)$$

It presents the maximum difference between the minimum distances of every point of the two surfaces  $S$  and  $S'$ , across the entire geometry. The HD was then



Figure 6.11: Anterior and posterior views of a ASM segmentation example initiated by the proposed method of a 'UZ Gent' image. Manual segmentation is represented in beige and the obtained result is represented in red.

set to correspond to the maximum distance error between the surfaces. The ground truth for this validation was considered to be the manually segmented datasets using 3DSlicer. Because of the image resolutions, to manually segment a femur is very time consuming, hence only 10 were considered for the method validation. Figure 6.12 maps the errors on both resulting meshes and Figure 6.13 shows the absolute error mapping of the in-image segmented femur.

It is relevant at this point to show some other segmentation meshes obtained with the method proposed in the present method. Four patients randomly chosen were considered and their femur reconstruction is shown in Figure 6.13.

For the 10 datasets considered in this validation, the average for the Dice coefficient was  $0.94 \pm 0.016$  and for the error was  $1.014 \pm 0.474$  mm. Overall, these values are relatively low, particularly if we take in account the processing time of the proposed method. In Figure 6.13, the HD was set as the maximum value in our label color scheme. It's important to bear in mind that a reliable manual segmentation, set as ground truth, is often hard to obtain due of the dubious bone tissue region edge. Even an experienced user will have trouble considering pixels on the bone region edge as part of bone tissue or part of the surrounding soft tissues.

Error peaks can be clearly identified in Figure 6.13. These are mainly due to the nature of the proposed method: the ASM segmentation is prone to small unexpected variances of the femur shape model. In contrast, it presents a ro-

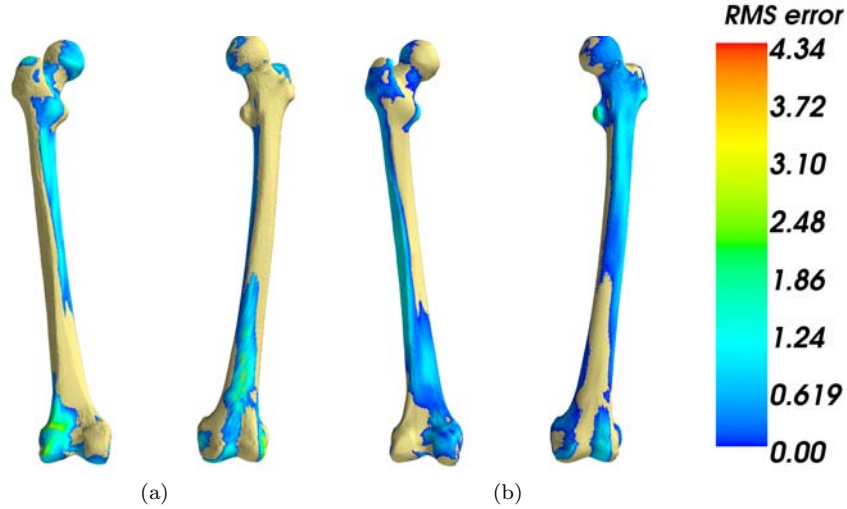


Figure 6.12: RMS error in mm. (a) is the distance mapping between the result of the proposed method and the manually segmented femur and (b) is the opposite.

bust and efficient segmentation of the volume of interest. More specifically, these can be found in the greater trochanter and the anterior medial condyle of 6.13a and the lesser trochanter of 6.13c. Image artifacts or other acquisition errors might also influence the values obtained in this regions. Table 6.3 following table sums the comparison on the average error for the proposed method against two other found in the literature.

Method	Mean RMS (mm)	HD (mm)	Mean Dice
Proposed	$1.014 \pm 0.474$	$4.336 \pm 0.861$	$0.94 \pm 0.016$
Younes et al. [150]	$1.48 \pm 0.28$	$10.53 \pm 3.19$	$0.87 \pm 0.026$
Teodoro [79]	$0.152 \pm 0.144$	2.33	$0.98 \pm 0.012$
Krčah et al. [159]	5.4	< 8	N/A

Table 6.3: Averaged RMS error, Hausdorff Distance (HD) and Mean Dice Coefficient of the proposed method against three other found in the literature.

The obtained average Dice coefficient highlights the reliability and accuracy of the segmentation method. On the one hand it was able to segment all of the datasets considered in this thesis and with a volume difference of less than 6% when compared to the manually segmented. Moreover, the average RMS error of  $1.014 \pm 0.474$  mm is similar to voxel resolution of the dataset, mentioned in chapter 4, which validates the high accuracy of the proposed method. In addition, these errors are of very little significance when the main goal of the segmentation is the assistance in a THA, where the modeling of the most significant total femoral volume variations is clearly of more importance than small localized variations. Again, it is important to mention the very low processing time. The obtained results can be improved if we consider



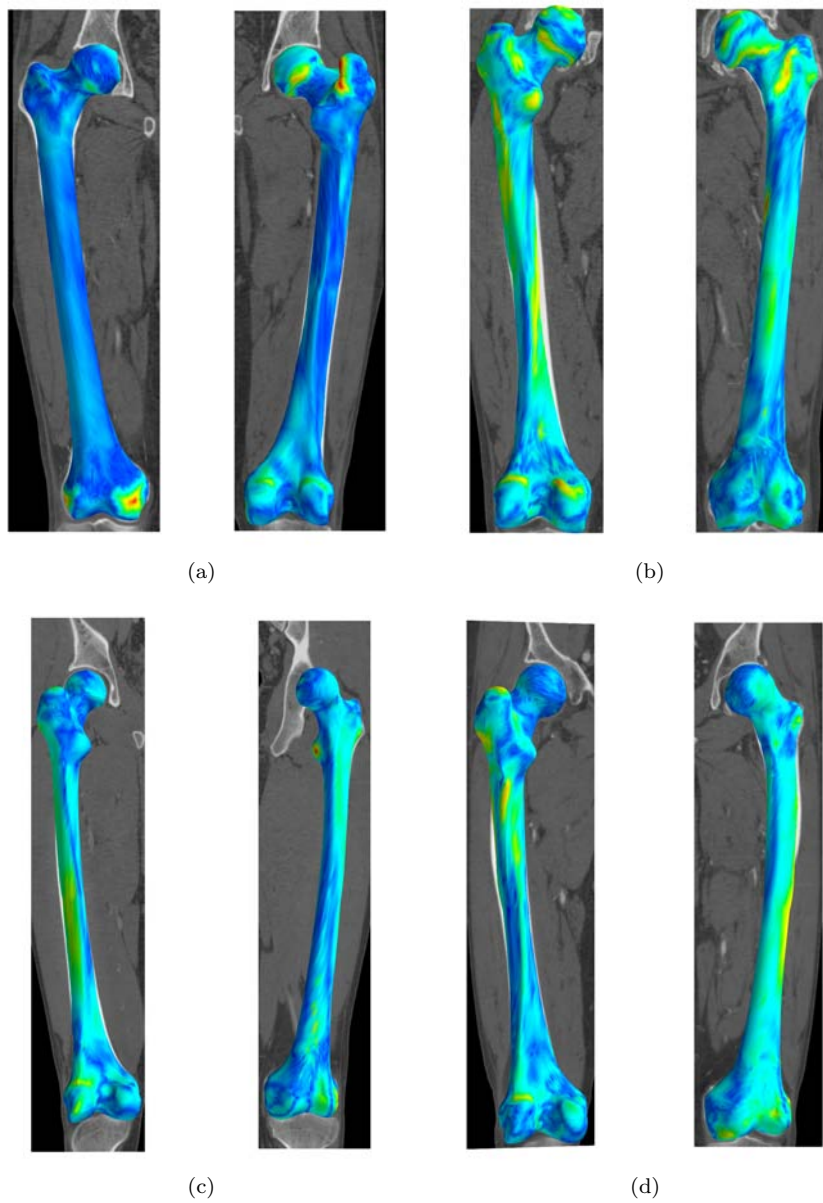


Figure 6.13: RMS error plotting of four segmented femurs (a-d) by the proposed method to the corresponding manually segmented femur, assumed to be the ground truth. Scale goes from cold to hot colors and maximum Hausdorff distance (HD) value is again 4.336 mm.

different parameters for the success of the ASM segmentation convergence and perhaps we could achieve sub-voxel values for the mean HD and an even smaller difference in volumes towards the ground truth.

Lastly, the full 'UZ Gent' dataset group was segmented. As seen in section 4.2.2 out of the 182 expected femurs only 148 were eligible for segmentation, as some of the images show the presence of disease, prosthesis or severe image artifacts. The addition of newly segmented femurs to the model showed no significant improvement in the segmentation success rate. However, ASMs specific to certain populations may offer an improvement, e.g., there are significant shape and appearance differences between genders and age groups. Hence, ASMs trained with data specific to a particular group could be more sensitive and robust for scans from that same group. The mirroring of the ASM enabled both right and left femurs to be modeled together, doubling the training set size. This didn't increase the success rate of the segmentation pipeline as seen above but takes in account more shape variations in a SSM morphometric study. Figure 6.14 shows two examples in the most critical segmentation regions, the proximal and distal femur.

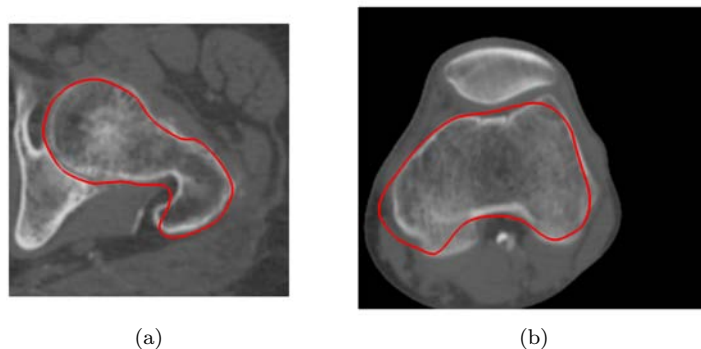


Figure 6.14: Two examples of mesh defects in the proximal (a) and distal (b) femur.

No ground truth data was available, so the quality rating given to the resulting meshes was based on visual inspection. Table 6.4 sums up the classification of the obtained results.

Classification	Occurrences
No apparent defects	68
Apparent defects at 1 or 2 isolated locations	59
Apparent defects at 3 or more locations	18
Segmentation failed to converge.	3

Table 6.4: Classification of the segmentation results together with the number of occurrences verified for each category.

Out of the 148 in-image femurs, 68 showed good quality results with no apparent inaccuracies, 59 showed minor inaccuracies, 18 showed significant inaccuracies and only 3 didn't converge or the automatic initialization procedure failed. In other words, 86% of the datasets were segmented with acceptable

quality (up to two defects) and the ASM segmentation pipeline converged in 98% of the cases. When present, most defects are on the anatomical prominences of the femur: the trochanters or the condyles. In addition, despite removing 34 datasets with severe abnormalities, significant variances to the femur shape were still present, as the variability of gender and age is significant. Bones with various degrees of age-related bone loss and osteoporosis were present.

### 6.4.3 'Quadrantes' datasets results

The proposed method was put under demanding tests with this image group, mainly due to its very low voxel resolution (slice spacing is either 5 or 7 mm). Due to this fact and as seen in chapter 4, it was impossible to manually predict some of the femur's boundaries. Moreover, methods that are based exclusively in regional properties or edge detection will also ultimately fail. The 5mm distance between axial slices is superior to the spacing between the femur and the fibula and the tibia, therefore making it impossible to identify the lower in-image femur boundary. Figure 6.15 shows precisely this: it is unclear whether the axial slice in Figure 6.15a intersects the femoral head or not and if it does, it is also not straightforward how to estimate its boundaries.

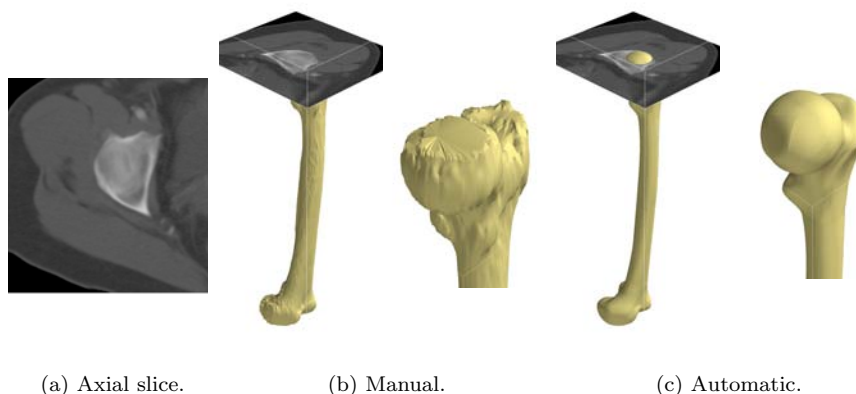
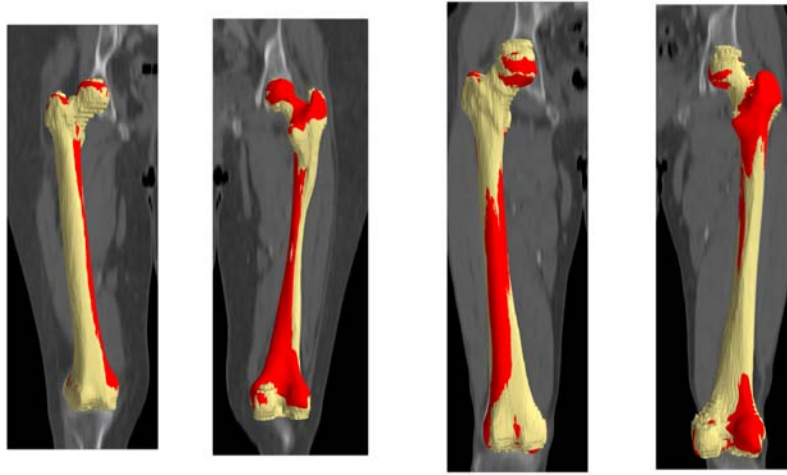


Figure 6.15: Low resolution femur segmentation. (a) shows an axial slice of the dataset 'Patient 1' in the 'Quadrantes' image group. (b) and (c) illustrate the manual and automatic prediction of the femoral head boundaries, respectively. The whole femur is shown next to a detailed view of the head surface.

However, as seen on section 6.2, the proposed method looks at the whole gradient profile along the normal and not merely to the border which allowed femur boundary estimation even in sub-pixel resolution. This is a major breakthrough, as this is the CT image resolution used in some of the Portuguese health institutions. Moreover, in Figure 6.15b it was assumed the slice plane didn't intersect the femoral head and its sphericity was influenced as a consequence. On the other hand, in Figure 6.15c the shape model influenced the convergence of the proposed method through the gradient profiles and an spherical femoral head was achieved. Although it would be far-fetched to empirically

say that the proposed method achieves a better femoral shape estimation than the author's manual prediction, the aspect of the obtained surfaces points so.

Within this context, 10 femurs were automatically segmented and compared against their corresponding manually segmented femurs. These femurs correspond both to the left and right femurs of all patients of the 'Quadrantes' image group. Time-wise, the procedure took less time than the 'UZ Gent' image group due to the lower image resolution. On average, the algorithm achieved convergence in  $25.27 \pm 2.21$  seconds. Two examples of the automatically predicted femur surface mesh (in red) and the manually segmented mesh is shown in Figure 6.16. The staircase effect is a consequence of the high slice spacing.



(a) Patient 4, right femur.

(b) Patient 5, right femur.

Figure 6.16: Anterior and posterior views of two ASM segmentation examples initiated by the proposed method on the 'Quadrantes' image. Manual segmentation is represented in beige and the obtained result is represented in red.

The mesh in beige presents mis-segmented areas which are mainly due, again, to the low image resolution, as seen above. Even for an experienced user, it was not straightforward to identify the femur border in its epiphysis, which are regions of higher level of detail. On average, the femoral head diameter is 42.2 mm for females and 48.4 mm for males [11], respectively 8 and 10 voxels in the inferior-superior direction. In addition, the interstitial spaces on the femoral joint and on the distal femur, between the condyles and the tibia and fibula, are often smaller than the average 'Quadrantes' voxel size. Nevertheless, the algorithm converged to a smooth and relatively accurate mesh in all cases. Similarly to the results presented in the previous section, Figure 6.17 shows the error distance mapping in both the manually segmented and the proposed method convergent meshes.

Average RMS error distance for the 10 segmented femurs is  $1.446 \pm 1.101$  mm which is twice the value of pixel spacing in the axial slices but 3 or more times lower than the space between slices. As seen on Figure 6.15, the areas

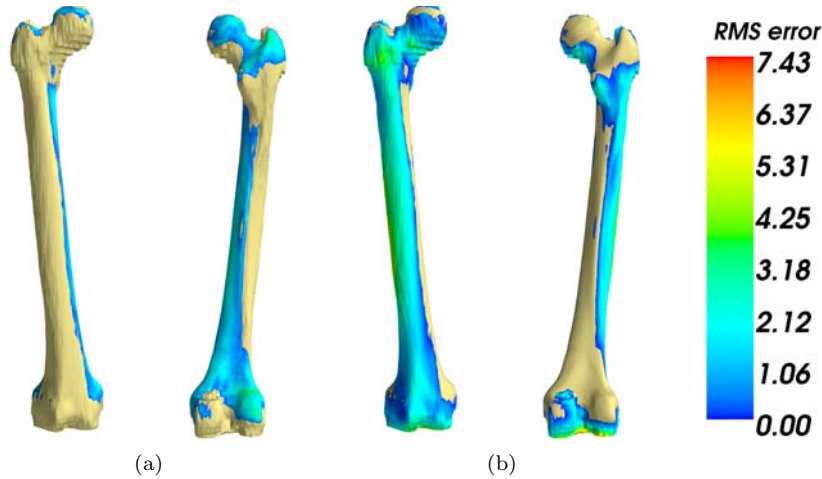
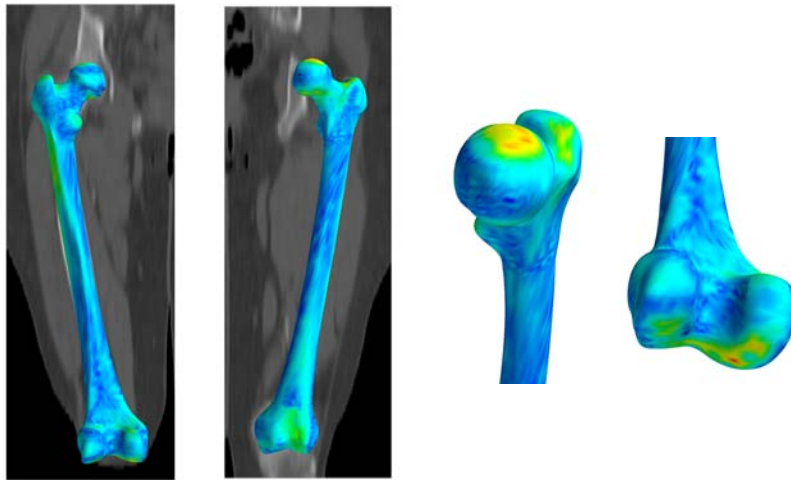


Figure 6.17: RMS error distances measured on patient 4 in mm. (a) is the distance mapping between the result of the proposed method and the manually segmented femur and (b) is the opposite. Hausdorff distance was 7.43 mm.

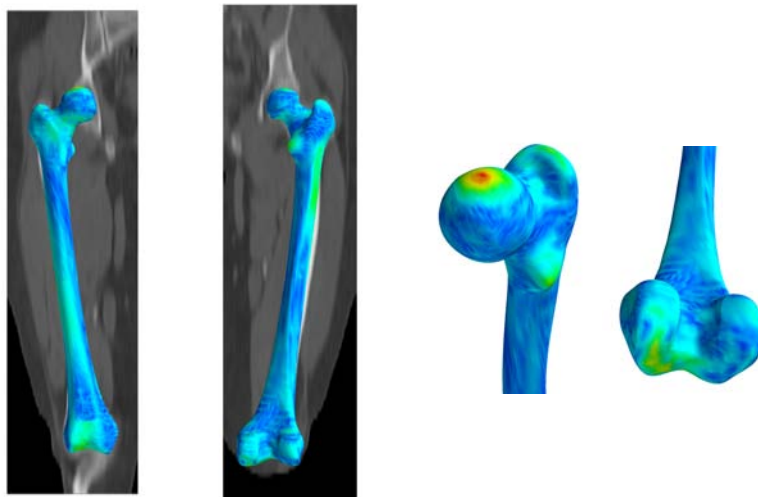
where the error distance is the highest are the areas of the femoral head and both femoral condyles. The average HD measured was  $10.135 \pm 5.9478$  mm which is a relatively high value. However, as the manual segmentation accuracy in these regions is very controversial due to the low detail level, it is not legitimate to infer that the relatively high Hausdorff distance values are due to an automatic segmentation error but instead a manual mis-segmentation. On the other hand, the average error distance distribution throughout the whole femoral surface confirms the average low values. It is also important to notice that pixel resolution in axial plane is on average 7 to 8 times higher than in the inferior-superior direction, so the distance is maximum in this axis. In addition, the femoral shape is overall in concordance which allowed the author to infer that the proposed method presents a good femoral shape estimation even in very low resolution CT-Scans.

As the method was validated in the previous section, instead of extensively presenting all results of the 10 segmented femurs, Figure 6.18 shows merely the obtained results for both femurs of patient 2. This patient was chosen due to its maximum slice spacing of 7 mm, which is reflected in minimum image resolution in the inferior-superior direction. The obtained results were overall good and the RMS error is plotted over the obtained femoral mesh surfaces.

These error values obtained are of relatively low importance when the main goal of the method is the assistance in a THA, where the modeling of the most significant total femoral volume variations is clearly of more importance than small localized variations. Together with the reduced computational time, the presented method is suitable to integrate a real time software to help physicians in a surgical environment, even in the Portuguese or other countries where health care units use low resolution CT-Scans as basis.



(a) Left femur.



(b) Right femur.

Figure 6.18: RMS error of the automatically segmented femurs of patient 2, where slice spacing was 7 mm. From left to right, the figure shows the anterior and posterior view of the RMS error plotted over the whole femur surface and femoral head and the condyle region in detail, where the RMS error is the highest. Scale goes from cold to hot colors and maximum value is 10 mm, slightly over slice thickness.

## 6.5 Conclusions

Firstly, it can be concluded that a robust and automatic method for segmentation and reconstruction of the human femur was developed with success from clinical CT images, both high and low resolution. The method is patient-specific and computationally very efficient. The leg posture was not strictly

controlled at the time of the image acquisition, hence the femur orientation was also highly variable. Nevertheless, in roughly half a minute, it was capable of accurately segmenting without any user input, as noticeable in Figures 6.10 and 6.11. These facts are supported by its 100% the success rate on the 30 datasets considered for the present study, with error below a reasonable threshold.

Its initialization algorithm is based on point cloud registration. When compared to the manual estimation of the initial pose, it is clearly less time consuming and does not rely on any user input. Even an experienced user would take more than a couple of minutes to identify a few femoral anatomical landmarks so that the in-image femur initial pose and scaling would be estimated. The average RMS error between the manual initialization of our 30 datasets and the corresponding  $k$ -D tree best pairing of the binary image nodes is 5.539 mm. The value is slightly higher than our method. This means that the automation of the procedure didn't compromise its accuracy. The standard deviation of the average distance of the manual shape and pose estimation presents a value of 0.853, which is 15% lower than the one from the proposed method. Both of the values obtained are due to the fact that manual estimation of the shape and pose is based on the statistic model, as seen on Figure 6.9, and hence is not able to extrapolate information to predict a femoral shape that lies outside of the population of the SSM. In addition, and for the sake of computational load, the PCA reduces the dimensionality of the problem by considering only a few variation modes, reducing the variability specter for variations of low significance. Ultimately, what was concluded was that the better the estimation of the parameters is, the more straight-forward the segmentation process is, i.e., less deformation iterations on the nodes of the mesh to fit the in-image femur. Another advantage of this method is that its dependence on the size of the population of the SSM is less significant over the increase of the size of the population, i.e., the inclusion of over 100 femurs didn't show significantly better results when compared to the initial shape model of 30 femurs. The training of the SSM can be very time consuming and is often limited by the available sample datasets. It is common that they grow as they're used and hence broadening their specter and therefore becoming more effective. The method here proposed does not depend on any of these parameters and proved to be effective on all the cases tested without any previous training or classification procedures.

The accuracy of femoral segmentation was validated using the Dice coefficient and the average distance error against a set of manually segmented meshes. Figure 6.11 shows the comparison between the two meshes used for the calculation of the Dice coefficient and Figures 6.12 and 6.13 present respectively the error distances mapping against the corresponding manual segmentation in beige and several other examples of the error distances. As one can observe, precise and prompt results were obtained: the Dice coefficient is  $0.94 \pm 0.16$ , the average distance error is  $1.014 \pm 0.474$  mm and its average running time was  $31.12 \pm 3.21$  seconds.

Krčah [159] chose to approach the problem with active contours and had a success rate of 81% on the segmentation of 197 femurs, significantly lower than the proposed method. The mean error distance presented of 5.4 mm is also higher than the one achieved in the present method by a factor of 6. The author didn't present the average Dice coefficient obtained. Although he

managed to achieve an automatic segmentation method not based on shape priors, the convergence of his method is far from ideal and the precision of the results presented is significantly surpassed by the values of the present work.

Teodoro [79] with his active contour approach presented better results than Krčah. He claims to have an average error of  $0.152 \pm 0.144$  mm and a maximum error of 2.33 mm. It is slightly better than the values achieved in this study although at a cost of significant processing time. If statistical analysis of general morphology is the goal, then accurately representing small features will be more important than robust and quick acquisition of large features. Figure 6.13 shows precisely that. The small, localized segmentation imperfections that would be of minor impact in a prosthesis fitting optimization. At this cost, the presented algorithm performs 7 times faster which in a surgical environment or even in a interactive THA planning software is of major importance.

When compared against other ASM segmentation implementations, it proved to outperform the application of the HT by Younes [150] to initialize the model, both in terms of accuracy and time. The HT is a very powerful method but at a cost of a huge amount of calculation when extended to three dimensions. In addition, algorithm is unable to estimate the sphere radius and shaft diameter with consistency. Their algorithm takes around 3 minutes to perform, which is 6 times more than our method. In addition, the average distance error measured for our method is smaller than theirs, which might be related to the ASM training or the parameters chosen for the segmentation convergence. The HD presented by the authors is of higher level of magnitude, which clearly highlights our algorithm accurate and reliable performance.

The proposed method can be extended to other bones or soft-tissue organs. Regarding the diagram of Figure 6.1, the algorithm can be easily adapted to retrieve information about the volume of interest in different image modalities as MRI imaging, for example. As the size and pose estimation is merely based in data cloud point optimization, it is also adaptable to other shapes. The rest of the method has already well known applications to the most diverse segmentation problems. Therefore, at the cost of a mean template mesh definition, a SSM can be trained and extended to ASM so that a straightforward segmentation is automatically performed.



## Chapter 7

# Total Hip Arthroplasty planning

In this chapter, the development of a framework for the planning of the THA will be described in detail<sup>1</sup>. Following the patient-specific segmentation described in previous chapter 6, the femur is oriented and its anatomical prominences are extracted in a way that facilitates the planning of the implant insertion. The surgical procedure is described in subsection 2.8.3. The contents of this chapter have been published in a peer reviewed journal, as mentioned in chapter 1.

The chapter starts by presenting a historical note on the planning of the THA, featuring a literature review on femoral landmark extraction and prosthesis placement optimization (Sec. 7.1). Section 7.2 extensively describes the methodology used for landmark extraction and axis definition and following section 7.3 presents the framework for cutting the femoral neck. Then, the prosthesis modeling is described in section 7.4 and their coupling with the femur is described in section 7.5, namely its size and position optimization. Automatic Finite Element (FE) hexahedral mesh generation is done according to the methodology featured in section 7.6. The chapter ends with the presentation of the results achieved (Sec. 7.7) as well as their discussion (Sec. 7.8) and some final remarks on the methodology presented (7.9).

### 7.1 Introduction

Even though the THA surgical procedure is considered to be among the most successful, safe and cost-effective surgical procedures, implant failures related to prosthesis design and placement still occur in a considerable number [1]. The absence of reliable landmarks defining the alignment of the femur and pelvis accessible intraoperatively difficults the implant placement in the surgery. Hence, a proper planning of the surgical procedure based on patient-specific image processing will reduce the intraoperative risk of human error and consequently increase the durability of the implant [201]. Moreover, the automation of such methods will thoroughly improve the surgical planning experience and will ul-

---

<sup>1</sup>This study was published: Diogo F. Almeida, Rui. B. Ruben, João Folgado, Paulo R. Fernandes, João Gamelas, Benedict Verhegghe, Matthieu de Beule. “Automated femoral landmark extraction for optimized prosthesis placement in total hip arthroplasty”, *International Journal For Numerical Methods In Biomedical Engineering*. Accepted. 2016.

timately decrease the time of the surgical procedure and risk of unexpected complications.

The durability of the implant is determined by its interaction with the bone tissue, which is a complex, continuously evolving structure. The femoral anatomy differs in anteversion angle, antero-lateral bowing of the femur and neck shaft angle between individuals. The knowledge of this anatomy may help reduce the high incidence of implant dislocation [202]. Moreover, clinical and experimental studies have demonstrated that a close geometric fit between the femoral component and supporting bone is essential for durable implant fixation [175]. Therefore, it is safe to assume that the success of THA is critically related to the knowledge of the femur geometry and the predictability of the key femoral dimensions. These two allow the optimization of the design and placement of hip implants in the femur for a better coupling. Consequently, the design and the prosthesis placement can provide a load transmission system that optimizes the longevity of the implant.

Patient-specific modeling from image datasets is recognized as the gold standard technique to computationally represent the hip joint in preoperative planning, although it can be susceptible to slight error variations [203]. Classic techniques such as two-dimensional templating lack in repeatability and three dimensional insight of the anatomy, i.e., anteroposterior and lateral radiographies merely provide one projection of the pelvis and the femur and therefore one of the dimensions is lost in the acquisition. CT-scans allow the visualization of the hip joint anatomy in three dimensions and consequently plan the implantation of the femoral and acetabular components with superior accuracy. In addition, recent developments in image acquisition techniques with special low dose CT-Scan protocols are being presented [204, 205, 206], which reduces significantly the radiation exposure of the patients. This way, restoration of leg length, center of rotation, range of motion of the joint and points of bony and prosthetic impingement can be analyzed preoperatively by the surgeon [207].

When computationally recreating an anatomical environment, the identification and location of prominent features of the organism as reference parameters, such as distances or angles, is of great utility: they can be helpful for objective diagnosis purposes [208, 209]; preoperative planning [209, 210, 211]; computer aided surgery [212, 213]; and post-operative follow-up [214, 215]. Manual landmark extraction is time-consuming and its repeatability and accuracy rely on the level of expertise of the observer. Later, a semi automatic landmark detection based on the local curvature of iso-contours initiated manually was proposed [216]. More recently, fully automatic landmark detection methods based on statistical models [217, 218] were also proposed. These methods are more prone to accuracy errors, due to their dependency on the population size of the trained model. In addition, the training of this model can be very time consuming. Pure geometric analysis methods achieve high reproductibility and are the computationally less expensive, although they highly depend on the level of discretization of the surface mesh [219].

Within this context, a set of tools to properly plan the THA based on the landmark extraction of the hip joint was developed under pyFormex<sup>2</sup>. Its aims are not only an improved alignment of the hip prosthesis but also to provide instant information and feedback to the surgeon, which may make the surgical

---

<sup>2</sup><http://www.nongnu.org/pyformex/>

technique easier to perform leading to better clinical outcomes.

The toolbox automatically extracts femoral landmarks and measurements from a triangular surface mesh over which the prosthesis placement is planned. For instance, with the definition of the femoral neck axis and the femoral medial diaphysis axis it is possible to promptly infer the femoral angle of anteversion and neck shaft angle and diagnose excessive retroversion or anteversion, as well as above normal femoral neck angles. In addition, these axes allow an ideal pre-surgical alignment of the prosthesis' stem and neck. Landmarks such as the greater and lesser trochanters or the inflection point of the femoral neck allow improvements in the osteotomy planning, such that the amount of bone mass removed is minimized. The definition of the femur medullary canal and the knowledge of its endosteal's anatomy allows prosthesis sizing and ultimately reduces the unnecessary broaching of the cavity for prosthesis fixation. The sizing of the implant can be such that it maintains the anatomical leg length and femoral offset.

In sum, the toolbox here presented allows the surgeon to better plan the patient-specific THA without the knowledge of the techniques used behind the methods. Combining a three dimensional reconstructed surface mesh of the femur with a set of commercially available implants, the planning here presented will reduce the surgical time and cost. Three dimensional finite element meshes can be generated of the femur-implant coupling and the performances of different implant sizes and designs can be compared preoperatively.

## 7.2 Automatic extraction of femoral landmarks

Within this section, the femoral landmark extraction and axis will be thoroughly described. Anatomically relevant femoral landmarks and axes have been previously listed and described in section 2.4.

### 7.2.1 Standardized coordinate system

The presented feature extraction process is invariant to the orientation of the bone. Therefore, in order to standardize the coordinate system for the complete femur, the origin and a system of axes that is common to all femurs has to be defined. In order to do so, the affine transformation matrix that transfers the femur from the CT image coordinates to the new standardized coordinate system is calculated and applied to the femur in the CT image coordinates, i.e., so that any translational and rotational variations are removed.

The first step of the alignment is to determinate the center of gravity (C) of the surface mesh and set it as the origin. Then, the calculation of the principal axes of inertia of the outer surface estimates the antero-posterior (AP), right-left (RL) and disto-proximal (DP) directions of the femur. A pipeline based on volumetric splitting and part size comparison [211] was established in order to classify the femur as right or left. An example of a surface mesh translated to the origin and without any rotational variation is shown in Figure 7.1. The definition of such coordinate system proved to be of added value to the extraction of the anatomical landmarks of the femur and geometrical entities fitting, as relative positioning can be assumed *a priori*.

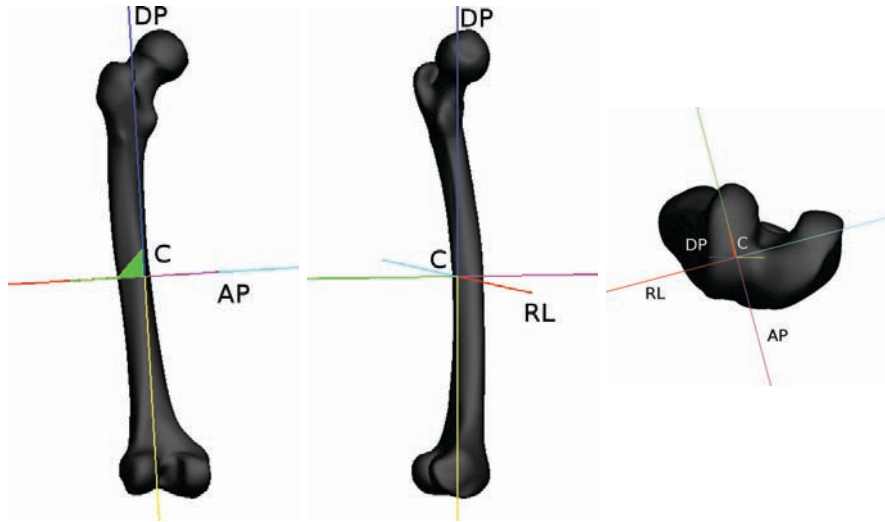


Figure 7.1: Principal axes of inertia of a femur model, respectively frontal, lateral and bottom views. For labeling simplifications, the RL, AP and DP axes will be respectively referred to as  $x$ ,  $y$  and  $z$ .

### 7.2.2 Femoral middle diaphysis axis and prosthesis insertion axis

The Femoral Middle Diaphysis Axis (FMDA) is defined as the straight medial axis of the femoral diaphysis or shaft. It is computed firstly by clipping the surface along DP, i.e., symmetric around the origin, over a height that is equal to half of the femoral length along the DP direction. Then, a circle is fitted to the points of each cross section boundary and the centroid point is calculated. The FMDA is then calculated by defining the covariance matrix  $\Sigma$  of the mean-centered data points  $X$ ,

$$\Sigma = \frac{X^T X}{m} \quad (7.1)$$

where  $m$  is the number of points, and performing singular value decomposition on  $\Sigma$ . This will return the direction vector of the line that best fits FMDA in the least squares sense as the first principal component. Figure 7.2 shows an example of the estimated FMDA for the human femur.

However, due to the medullary cavity present on the femur, to define the FMDA as the ideal prosthesis insertion axis may result in unnecessary cavity reaming, i.e., excessive removal of cortical bone on the inner wall of the femoral shaft. This will ultimately result in a decreased femoral shaft load bearing capacity. Hence, an estimate of the middle medullary cavity axis was estimated, based on the same pipeline as the FMDA. In addition, the medullary isthmus, which is defined as the smallest cross sectional area in the medullary cavity, is also extracted for prosthesis placement purposes. Figure 7.3 illustrates both the middle medullary canal axis and the isthmus of a femur. The position isthmus is highly variable and if located too superiorly, it may require intramedullary reaming to adapt the canal to the prosthesis stem design.

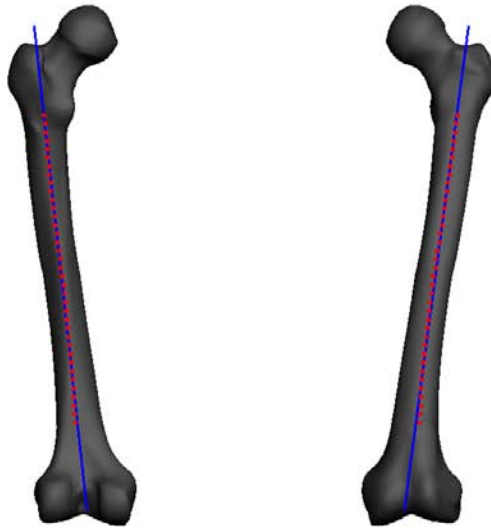


Figure 7.2: Anterior and posterior views of the femoral diaphysis medial axis. The axis (in blue) is the principal mode of variation of the medial points (in red) of the centroids obtained by cross-sectioning the femoral shaft along the inferior-superior direction.

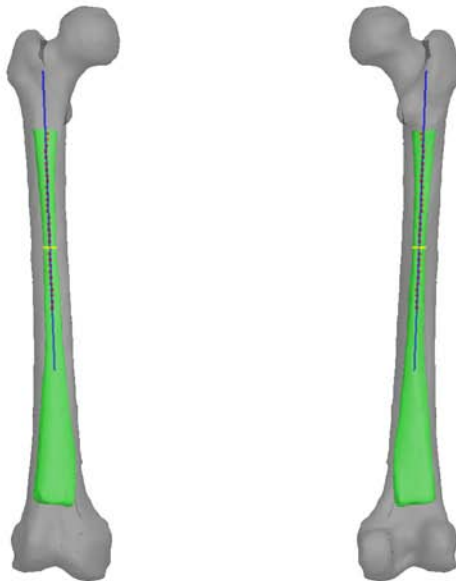


Figure 7.3: Anterior and posterior views of the prosthesis insertion axis and the cavity isthmus. The axis (in blue) is the principal mode of variation of the medial points (in red) of the medullary canal (in green). The isthmus (in yellow) is defined as the minimum cross-section area of the cutting planes along the prosthesis insertion axis.

### 7.2.3 Femoral neck axis and head center extraction

In addition to the prosthesis' stem insertion axis, the computational estimation of the femoral neck axis is also important to try to optimize the prosthesis placement in preoperative planning. CT-scan is considered as accurate and reliable as gold-standard techniques for locating the femoral head center due to its three-dimensional nature [220].

The Femoral Neck Axis (FNA) is defined by the line that connects the center of the head of the femur and the centroid of the smallest cross section on the neck of the femur. The cross-sectional area depends on the position and orientation of the slicing plane. Therefore, and based on the standardized coordinate system defined in the previous subsection, the neck was sliced along a normal with coordinates  $(1, 0, 1)$ . Each slicing of the mesh will result in a polygon defined by  $P_i$  vertices and its area can be computed using:

$$A = \mathbf{n} \cdot \sum_{i=0}^{N-1} \frac{P_i \times P_{i+1}}{2} \quad (7.2)$$

where  $\mathbf{n}$  is the normal to the plan containing the polygon and  $N$  is the number of points on the border of the polygon.

From here, we can obtain the smallest cross section along the femoral neck. Figure 7.4a shows the cross-section on the neck of the femur considered to be the smallest and the normal used to estimate the slicing planes.

The center of the head of the femur is estimated by fitting a parametric spherical surface to the partial sphere defined by the head of the femur. For that, the proximal femur is sectioned again perpendicularly to the normal defined before and the relative difference in the sectional area allows the estimation of the nodes in the mesh that define the femoral head. Then, a quartic surface is fitted to those nodes of the triangular mesh and a well-approximated femoral head is obtained. Figure 7.4b shows the best fitting sphere to the femoral head vertices, whose normals are represented in red.

The axis defined by the two points estimated in the previous paragraphs, the center of the smallest cross section and the center of the head, defines the FNA. Together with the FMDA, it allows us to calculate the femoral neck-shaft angle if measured in the coronal plane (see Subsection 7.2.6). Moreover, combined with the prosthesis insertion axis, it will be used to better plan the prosthesis placement. Also in Figure 7.5, the FNA is represented in a generic femur mesh.

### 7.2.4 Greater and lesser trochanters

Proximal femoral resection is the surgical removal of the femoral head and part of the proximal femur. This is done in case of injury and in order to replace the hip joint. The portion of removed femur depends on the lesion of the femur. Therefore, the femur osteotomy location and cutting plane are planned so that the portion of removed femur is minimized. In order to locate and position the femoral osteotomy, pipelines for the automatic detection of both femoral trochanters were implemented.

Again taking advantage of the standardized coordinate system defined in subsection 7.2.1, the extraction of both the greater and the lesser trochanter was based on volume sectioning along their normal. Its accuracy depends on

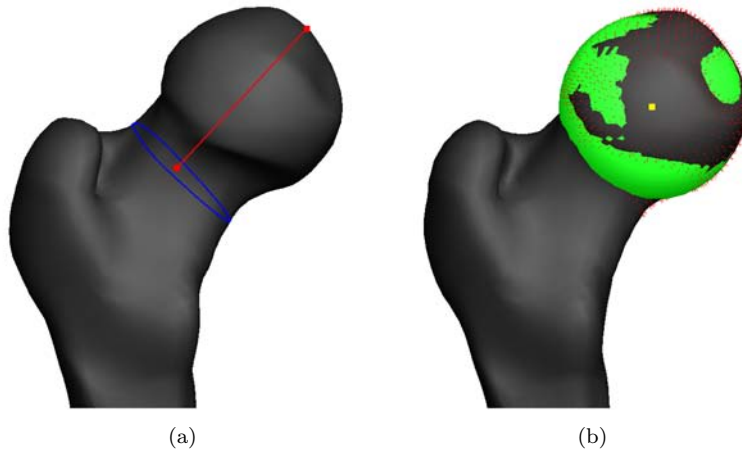


Figure 7.4: Posterior view of the proximal femur. In (a) the smallest cross section of the femoral neck is shown in blue. The red line shows the normal vector of the slicing plane, positioned at the center of the cross-section. In (b) the sphere fitted to the femoral head is shown in green. The red lines show the normal of the vertices considered for the fitting and the yellow mark at the center of the femoral head represents the geometrical center of the fitted sphere, also assumed the center of the femoral head.



Figure 7.5: Posterior view of the femur and the femoral neck axis (FNA) shown in red.

the level of discretization of the mesh and the size of the triangle faces of the mesh. Nevertheless, a mesh refinement proved to compensate accuracy of the method at the cost of an additional computational time.

For convex or concave structures, the extreme point along one direction is computed as the mesh vertex for which the length of the projection on the direction vector is maximal. As shown in Figure 7.6, the mesh was sectioned perpendicularly to an approximated direction of the normal to the mesh on the saddle point and the maximum value of the centroids of the sections in red is assumed to be the point of interest. The search process initiates in the center of gravity of the proximal femur. Expected curvature variances define the iterative algorithm's convergence criteria. Both trochanters are shown in yellow.

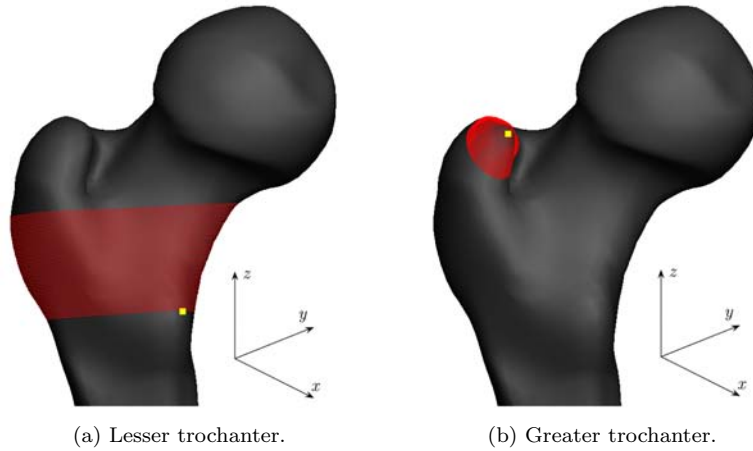


Figure 7.6: Lesser (left) and greater (right) femoral trochanters shown in yellow. The extraction algorithm starts in a automatically predicted point and segments the surface mesh perpendicularly to a given normal as shown in red. The normals are  $\mathbf{n} = (0, 0, -1)$  for the lesser trochanter (left) and  $\mathbf{n} = (1, 0, 1)$  for the greater trochanter (right).

In Figure 7.6a, the largest axis of inertia was chosen as the normal of the iterative slicing plane and the algorithm looked for the maximum  $x$  value. Similarly, on the right, the greater trochanter extraction. The initial direction for the normal of the slicing plane was chosen as  $\mathbf{n} = (1, 0, 1)$ , which is roughly the direction of the FNA. However, the resulting section can have two islands: one formed by the trochanter and other by the neck of the femur. Due to this fact, the algorithm will assume that the one with smaller area corresponds to the greater trochanter.

### 7.2.5 Neck saddle point

The extraction of neck saddle point is due, in order to properly plan the osteotomy. Due to the saddle-shaped nature of the femoral neck, its curvature is different according to the direction considered. Therefore, and taking advantage of standardized coordinate system, the neck saddle point was considered to be the closest point to the FNA. Its location is straightforward as it will be the point with the maximum value in the  $z$  axis on the minimum cross-section perimeter of consecutive slices of the femoral neck perpendicular to the FNA. The neck saddle point is shown in Figure 7.7.



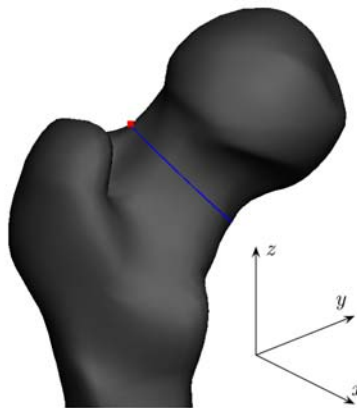


Figure 7.7: Extraction of the femoral neck saddle point. The minimal femoral neck cross-section perimeter is shown in blue and the neck saddle point, shown in red, is considered to be the point with the highest value in the  $z$  axis.

### 7.2.6 Femoral neck-shaft angle and anteversion angle

The landmark extraction and axis definition allows the calculation of the femoral neck-shaft angle and the femoral anteversion angle. The first is defined as the interior angle between the FMDA and the FNA and is used to diagnose the occurrence of coxa vara and coxa valga. It can vary within normality values between  $126 - 139^\circ$ . In the presence of an increased neck-shaft angle (equal or superior to  $140^\circ$ ) or a decreased neck-shaft angle (equal or inferior to  $125^\circ$ ), respectively coxa valga and coxa vara, it can cause hip pain and degeneration. There are implants that compensate for these deviations in order to maintain equal leg length and femoral offset. Figure 7.8a features a visual representation of the neck-shaft angle.

The anteversion angle is used to measure the femoral torsion along its shaft. It can be defined as the angle between the condylar axis and the FNA, which is undetectable in 2D radiographies. Normal version is a forward angle of  $12 - 15^\circ$ . In individuals with version abnormalities, the femoral neck may be rotated either too far forward (excessive anteversion) or too far backward (retroversion). These conditions result in the ball portion of the hip joint being situated at an unhealthy angle to the cup portion of the socket and can lead to damage to the hip joint surfaces and surrounding structures. Figure 7.8b also shows an example of the anteversion angle measurement in three dimensions.

## 7.3 Osteotomy

Osteotomy is the surgical act of cutting a bone to shorten or lengthen it, in order to realign it. It is often used to correct bone deformities, straighten a bone that has healed crookedly following a fracture or to replace part of the bone by an implant. It is a significantly invasive procedure and therefore the recovery may be extensive. Femoral osteotomies involve adjustments made to the femur and are part of the THA procedure. Intuitively, the ideal situation would involve the minimal bone mass removal for the prosthesis insertion, hence

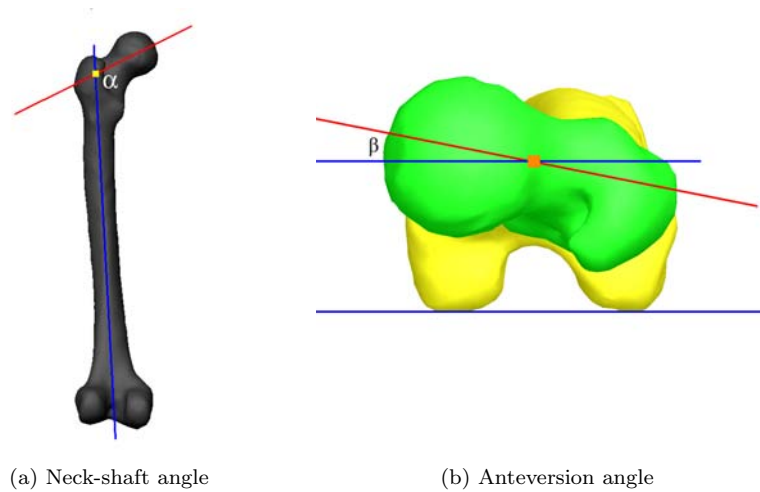


Figure 7.8: The femoral neck-shaft angle  $\alpha$  is represented in (a). It is the angle around the yellow intersection point of the FNA (in red) and the FMDA (in blue). This measure is clinically relevant as it diagnosis coxa vara and coxa valga abnormalities. Similarly, the anteversion angle  $\beta$  is shown in (b). It is the angle around the intersection (in orange) of the condylar axis (in blue, a parallel axis is shown for better visual understanding) and the FNA (in red). For visualization purposes, the proximal femur is represented in green and the femoral shaft and distal femur in yellow.

resulting from a higher femoral neck incision which gives a better rotational stability to the stem. There are several approaches to make room for the prosthesis insertion, which depend mainly on the location and extension of the injury, the design of the implant and the bone mass quality of the patient. Therefore, it is a very empiric therapy. Our experienced orthopedic partners consider that, ideally:

1. The cutting plane should be approximately perpendicular to the axis of the femoral neck;
2. In general, the osteotomy should be performed about 2 cm proximal to the lesser trochanter, to, together with leg length and global offset, avoid inappropriate muscle tension.

Due to the empiric nature of the procedure, it is the surgeon's decision where to perform it. Therefore, instead of an automatized osteotomy location, the computational implementation was done as follows: a reference osteotomy plane is defined as perpendicular to the axis of the femoral neck and containing the neck saddle point, so the prosthetic neck angle can be corrected.

The femoral offset is defined as the distance along the femoral neck axis between the anatomical center of the femoral head and the intersection of its projection in the coronal plane with the FMDA. A slight change in the post surgical femoral offset may reflect in a defective patient gait cycle and consequent limb pain [221], as shown in Figure 7.9.

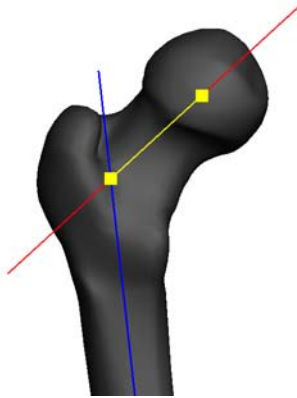


Figure 7.9: Posterior views of the proximal femur. The femoral offset (in yellow) is defined as the distance along the femoral neck axis (in red) between the anatomical center of the femoral head and its intersection with the FMDA (in blue). The limits of the femoral offset are also shown in yellow.

Because femur neck fractures occur in distinct regions of the femur, e.g. subcapital and trans-cervical fractures, the developed approach is able to perform the osteotomy based on the the deviance in distance to the saddle point and in angle to the perpendicular plane of the FNA, which are introduced by the user. At any point the user can check whether the distance to any of the trochanters is enough to avoid insufficient muscle tension. In addition, whatever the planned osteotomy is, changes on the femoral offset can be compensated with prosthesis sizing and placement, which will be looked into in the following subsection.

Figure 7.10 shows the reference cutting plane that passes through the femoral neck saddle point and is perpendicular to the femoral neck axis in white. Depending on the size and location of the injury, the cutting plane may vary its position and angle according to the user. In order to simplify the planning, this variation is translated in deviation to the reference plane and can be user defined. Also in Figure 7.10, in yellow, other planes equidistant from the reference plane in opposite directions and whose cutting plane normal is equally deviated from the femoral neck axis in opposite directions are also shown as examples of the implementation.

As the intention is to remove as little bone mass as possible, the osteotomy to the right is more suitable for a subcapital fracture and the one to the left to a transcervical neck fracture. Pauwels observed that the obliquity of the fracture line with the horizontal plane significantly affected the prognosis of the fracture [222]. The Pauwels' angle is defined as the angle formed by extending the fracture line upwards to meet an imaginary horizontal line drawn on left-right plane and can also be used to predict the best cutting plane for the osteotomy.

## 7.4 Prosthesis modeling

In order to compare the different prosthesis designs, some of the commercially available prosthesis were computationally modeled. The hip joint implant systems, namely their design and the materials used in their fabrication, were

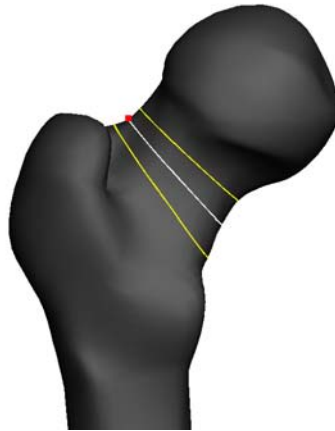


Figure 7.10: Posterior views of the proximal femur. Three planned osteotomy cutting planes are visible. As a reference, the saddle point of the femoral neck (in red) and the cutting plane perpendicular to the femoral neck axis (in white). The cutting planes shown in yellow are 2 cm deviated from the saddle point in both senses of the left-right direction and their normal is 6 degrees deviated from the reference cutting plane, respectively.

extensively reviewed in section 2.9. The modeling was based on the manufacturers templates and is fully parameterizable, i.e., the way the modeling was implemented allows the prosthesis' components dimensioning, so that it is adaptable to the patients' femur dimensions.

Firstly, it is possible to make the size of the femoral stem adaptable to the medullary canal. It is postulated that a cementless hip system consisting of a finite number of femoral components can accommodate all of the anatomic range of cavities. In a cemented hip system, due to the void-filling capacity of the cement layer the number of femoral components that accommodates the whole range of cavity geometries is even smaller [175].

With best femoral stem size estimation, the endosteal broaching is minimized and the most bone mass in the interior walls of the canal is preserved. Hence, the diameter of the medullary canal is calculated along the inferior-superior direction in the perpendicular cross-sections. In order to minimize cavity broaching, the femoral stem component diameter is adjusted to the minimum medullary cavity diameter on the cross-sections for uncemented prostheses and with a small tolerance to cemented prosthesis, so that room is left for cement filling.

The prosthesis design also takes in account the measured FNA (Subsec. 7.2.3) of the patient's femur. Excessively retroverted or antroverted femurs as well as coxa vara and coxa valga femurs can be compensated in the implant design as the toolbox here presented allows its diagnosis beforehand. Implants that contain a neck collar were not considered, because its role in preventing the loosening of a stem has not been clearly established and are said to decrease bone resorption in the proximal medial femur [223]. Similarly, neck preserving stems were also added to the implants database as their use requires less bone mass to be removed and therefore minimizes the complications associated with a second THA [224]. Finally, cemented and uncemented prosthesis were also

modeled as both fixation methods are in use. In sum, the idea is to have a prosthesis database as broad as possible.

Figure 7.11 shows four examples of modeled prosthesis, together with a photograph of the actual prosthesis for comparison purposes.

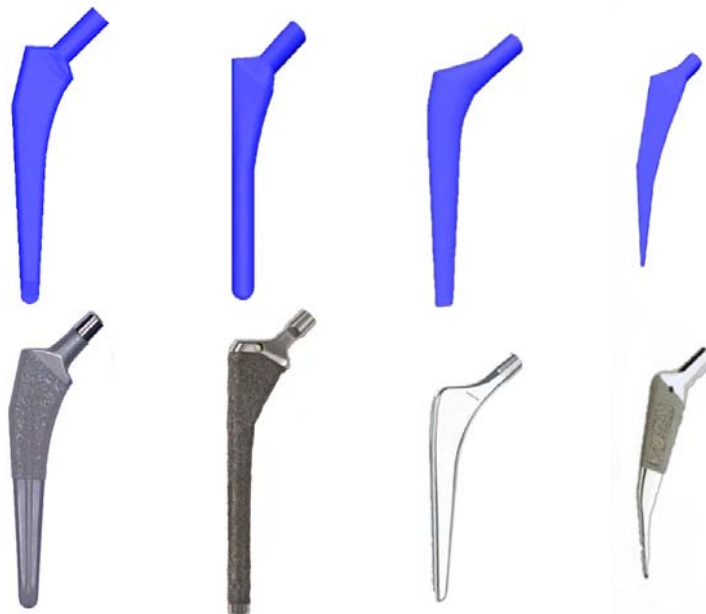


Figure 7.11: From left to right, DePuy Synthes TRI-LOCK<sup>®</sup> Bone Preservation Stem, the Zimmer<sup>®</sup> VerSys Epoch<sup>®</sup> FullCoat Hip System, the Zimmer<sup>®</sup> MS-30<sup>™</sup> stem and the the Zimmer<sup>®</sup> Mayo<sup>®</sup> Conservative Hip Prosthesis. The first row shows the computational models of the prosthesis and the second row shows their corresponding real aspect.

## 7.5 Prosthesis placement

Loosening is the most common long-term problem following the total hip arthroplasty. Moreover, the femoral component placement and the prosthesis stem design are among the factors that reportedly affect the incidence of loosening. On the other hand, the location of the hip center of rotation substantially affects the load on the hip and the kinematics of the hip joint. Long-term follow-up studies demonstrate significantly higher rates of femoral loosening with acetabular components placed in a superior and lateral (i.e., non-anatomic) positions, compared with acetabular components placed in a nearly anatomic position [225]. Another important fact that early studies point is that 2D prosthesis placement planning is often misleading, so 3D is compulsory for precise prosthetic components relation estimation [226]. Ultimately, there is still debate if acetabular and femoral implants should be orientated in such a way to reconstruct individual anatomy or fit within a safe zone. A recently published paper [227] has shown great variability in native hip joint anatomy and only a few fitted inside the component orientation criteria known

as safe zone. Therefore, the implant placement and sizing will be planned in order to mimic the native joint anatomy, i.e., in such a way that the femoral neck angle, the inclination or version of the femur and the femoral offset remain unaltered. In cases of femur valgus or varus the prosthetic neck should be adjusted, respectively reduced and increased, in order to compensate such abnormalities. Together with orthopedic surgeons, a workflow to restore the center of rotation of the femoral head was implemented and will be described in the following paragraphs.

The fitting problem can be described as finding the set of parameters (translation, rotation and prosthesis size) that minimize the distance between the input points, strategic on the prosthesis, and the geometrical entity, which is the respective femoral axis in this case. The computational cost of this pipeline is very low as it relies merely on algebraic operations with the surface meshes.

The joint reaction force acting on the femoral head is principally oriented in the coronal plane, even though rotational loading for the implant stability also takes an important role. Therefore, the characterization of the shape of the endosteal cavity in the anterior-posterior plane is of major importance to implant stability. In this context, the medullary canal can be characterized as normal, stove-piped if they are relatively straight sided and champagne-fluted if they are highly tapered [175]. The shape of the canal is non-proportional to the femoral length, as opposed to neck length or head diameter. Therefore, implants can't be designed on the basis of an average canal size proportionally scaled for larger and smaller canals in the anatomic range. However, the majority (83%) [175] of the femurs has normal shaped cavities. Consequently, the proposed framework was planned so that it deals with the patient specific cavity in order to determine the best prosthesis placement.

Most femoral stems are designed to extend to the isthmus of the medullary canal (Fig. 7.3) to stabilize component alignment and prevent varus migration. Consequently, selection of an optimal length for components of different size is determined by the relationship between the canal width and depth of the medullary isthmus, which is extremely variable [175]. Hence, it may require intramedullary reaming to broaden the canal which can be considered unnecessary bone mass removal.

On the other hand, studies have shown the importance of a close match between the proximal cross section of the femur and the femoral component [175]. Moreover, stem-bone contact within the metaphysis can only be obtained in discrete areas of the endosteal surface rather than over a substantial portion of the potential interface. For this reason, few femoral components truly fill the femoral canal laterally. In cementless arthroplasties this can lead to excessive micro-motion and impaired clinical performance.

Therefore, the first step of the workflow is to make the interception of the neck and shaft axes of both the femur and the implant coincident and orient the implant according to the prosthesis insertion axis (Fig. 7.3). Then, the stem is scaled so that it is as large as possible with minimal removal of cortical bone from the endosteal. Because only a few predetermined stem sizes are available, the best fit is selected. If the implant stem is smaller than the medullary cavity, there is the risk of prosthesis subsidence, i.e., moving inferiorly along the femoral shaft. If, contrarily, the stem is too large for the cavity, the excessive removal of cortical bone can fragilize the load-bearing capacity of the endosteal wall and ultimately result in a femoral fracture. Moreover, intra-

operative femoral fractures have been reported due to the trial and error stem size estimation, still often used by the surgeon. According to our orthopedic partners, the stem and the endosteal wall should have an interference less than 1 mm for uncemented implants in order to be considered a good fitting. For cemented prosthesis, the workflow takes in account the spacing between the stem and the endosteal wall that it is filled with the cement and a clearance of around 2 mm, depending on the implant model, is left in between the contact surfaces.

Secondly, it is important to maintain the femoral offset, which will ensure that the center of rotation of the joint and leg length are kept unchanged. In order to do so, the prosthesis is rotated along the insertion axis in order to minimize the distance to the center of the femoral head. Most prosthesis have a fixed neck angle, so the position of the prosthesis stem is chosen such that the center of the femoral head is maintained in the prosthetic joint. With this alignment, we ensure that the prosthetic center of rotation matches the anatomical center of rotation. In sum, the purpose of the toolbox here presented is to aid the surgical planning and not to undoubtedly determine the optimal size of the prosthesis. It is ultimately the judgment of the surgeon that determines which prosthesis design and size to use in every patient-specific coupling.

## 7.6 Automatic finite element mesh generation

FE analyses provide quantitative results that can be used to evaluate the performance of the different implants positioned in a patient-specific femur. The accuracy of a FE method analysis depends on the mesh quality of the domain discretization. Moreover, hexahedral meshes present several numerical advantages over tetrahedral meshes and the automation of the process avoids the time-consuming manual work of subdividing the domain in hex meshable regions. Within this context, a method for automatically generating hexahedral FE meshes of the femur-implant coupling was also implemented.

Contrarily to prostheses with rectangular cross-sections, where the meshing is straightforward, the meshing of the prostheses with round cross-sections is done combining two techniques: grid-based [228, 229] and receding front [230]. As seen in Figure 7.12, an example of an oval cross-section of the implant, the meshing presents an external ring meshed using the receding front algorithm and a central part meshed with the a grid based algorithm.

The main objective of such approach is to avoid distorted elements, such as the element highlighted in Figure 7.12, at the contact surfaces. This distortion is due to the grid-based approach used to mesh the interior of the cross-section, which is not a perfect rectangle. Every section has the same number of quadrilateral elements and therefore the hexahedral elements are formed by the consecutive quadrilateral elements. There is the possibility of interactively choosing the number of elements per section and the number of sections along the implant, thus making it up to the user to balance the mesh refinement at the cost of computational effectiveness. Figure 7.13 shows the meshing of the same implant consecutively increasing the number of elements.

The meshing of the femur is done according to the meshing of the prosthesis. The cross-sections of the implant are made coincident with the cross sections of the femur and the medullary canal, as Figure 7.14 shows. The receding front

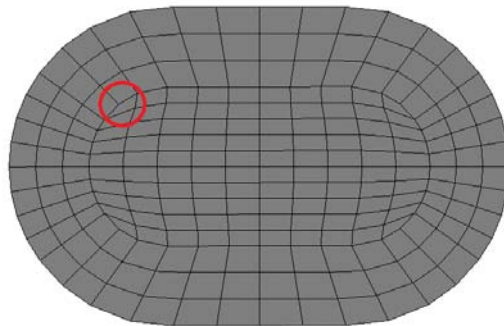


Figure 7.12: Meshing of an oval implant cross-section. The exterior part is meshed using receding front method and the interior part is using a grid-based algorithm. This way, distorted elements such as the one highlighted in red are avoided in the contact surface which is the external boundary in this case.

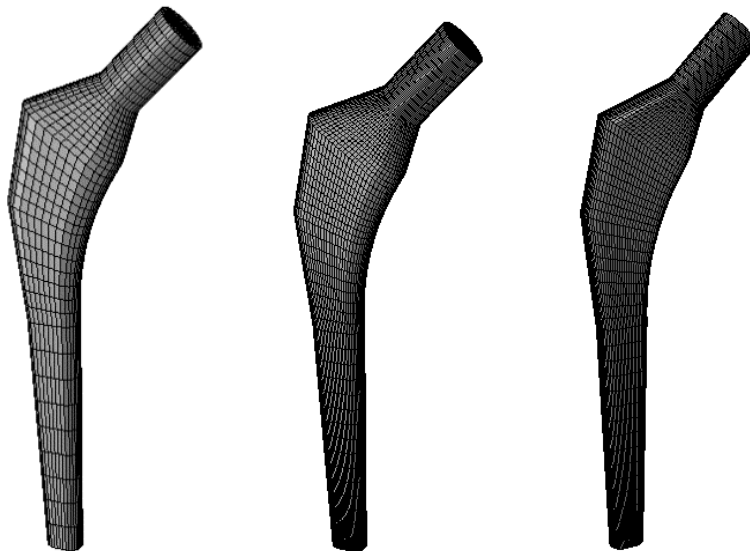


Figure 7.13: Meshing of the DePuy Synthes TRI-LOCK<sup>®</sup> Bone Preservation Stem, increasing its discretization from left to right.

technique is then used to mesh the femur domain up to its external boundaries.

To each element of the mesh of the femur there is a type of material associated: medullary cavity, cortical or trabecular bone, depending in which side of the segmented boundary they are located. This way, the resolution of the endosteal boundary is limited by the element size. Figure 7.15 exemplifies a cross-section along the femoral shaft, where the prosthesis stem is in contact with the endosteal. The area in lighter gray corresponds to the medullary cavity.



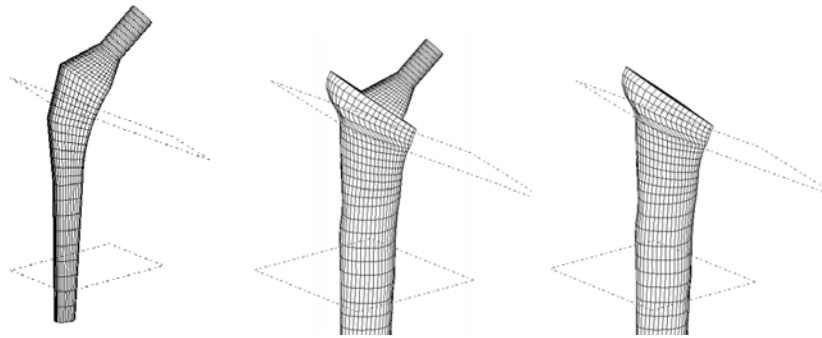


Figure 7.14: Meshing of the DePuy Synthes TRI-LOCK<sup>®</sup> Bone Preservation Stem and the femur.

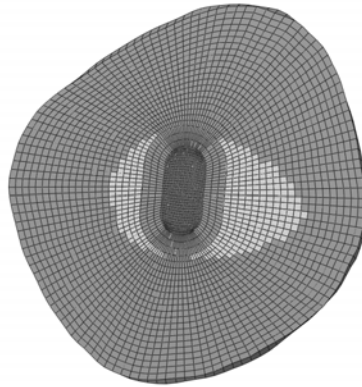


Figure 7.15: Cross-section of the femur-implant coupling in the femoral shaft. The meshing of implant stem was done combining the receding front method around a grid-based center. The femur was meshed using a receding method approach. The medullary cavity is represented with an higher intensity in the gray-scale. Elements have material properties according to the domain they belong to: implant, medullary cavity or cortical bone.

## 7.7 Results

The principal component of the singular value decomposition that stands as the direction vector of the FMDA represents 98.1% of the total point cloud scattering that represents the centroids of the cross sections along the femoral shaft. Similarly, the direction vector of the prosthesis insertion axis represents 97.7% of the total variation of the positions of the point cloud.

The sphere fitting to the femoral head was computed by minimizing the distances of the quadric surface that defines the sphere. The average error was  $0.42 \pm 0.06$  mm, which, represents less than 1% of the average  $46.1 \pm 4.8$  mm diameter of the femoral head [175].

In this section, some examples of the uses of the set of numerical methods here presented are shown. Figure 7.16 shows an example of a fitting of a TRI-LOCK<sup>®</sup> Bone Preservation Stem to a patient-specific femur.

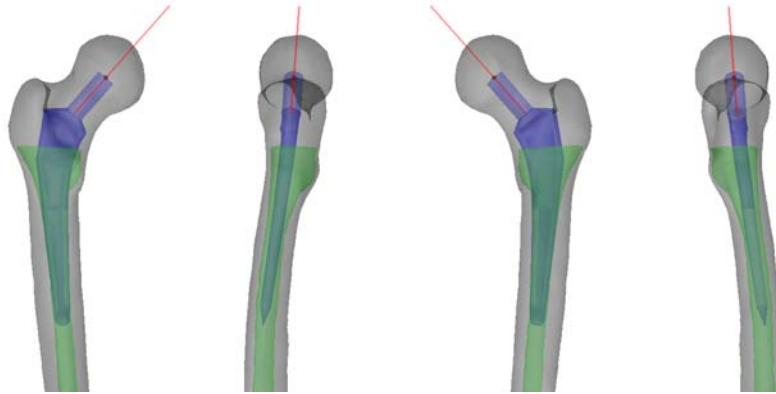


Figure 7.16: From left to right: posterior, left, anterior and right views of an example of a DePuy Synthes TRI-LOCK<sup>®</sup> implant fitting to a patient-specific femur. The femur is represented in translucent black with the center of the femoral head in black. The implant and the medullary cavity are shown in blue and green, respectively. In red, the prosthesis neck axis is visible.

It is ensured that the center of rotation of the joint is maintained with the proposed sizing and fitting. In this specific patient, the femoral head would be inserted halfway in the neck so that the center of the femoral head remains unchanged in the prosthetic joint. Moreover, due to the flattened nature of the stem in the anterior-posterior direction, the majority of the fitting to the endosteal is done in the coronal plane.

A second example of an uncemented prosthesis is illustrated in 7.17, where the sizing and fitting of an VerSys Epoch<sup>®</sup> FullCoat Hip System is shown. Intuitively we can verify the good sizing of the implant stem to promote maximum contact surface in the endosteal wall. With a fixed implant-shaft neck angle it is important also to ensure that the femoral head center lies within the neck axis of the implant, both frontally and sagittally.

Figure 7.18 shows the MS-30<sup>™</sup> cemented prosthesis, automatically sized and placed in a generic femur so that the implant size trial and error is avoided in the surgical intervention.

As is observed in Figure 7.18 the prosthesis fitted significantly well. The tip of the stem was placed at the medullary isthmus and the rotation center of the hip center is maintained, as the prosthetic hip rotation center is maintained. Although the stem fits the femoral walls in the frontal plane, its flattened design can be seen in the lateral views. This is because the MS-30<sup>™</sup> is a cemented stem and space needs to be taken in account for the cement filling.

Finally, an example of a fitting of a neck preserving implant achieved with the proposed toolbox is illustrated in Figure 7.19. The Mayo<sup>®</sup> Conservative Hip Prosthesis has a shortened distal stem that fixates distally against the endosteal that promotes minimal cortical bone removal which is one of the most determinant factors in a revision surgery. Due to that reason, the orientation of the prosthesis stem axis is done accordingly and not as the previous examples have shown.

As Figures 7.16, 7.17, 7.18 and 7.19 show, the alignment and sizing is in conformity with the pipeline described in the subsection 7.5. The prosthesis'

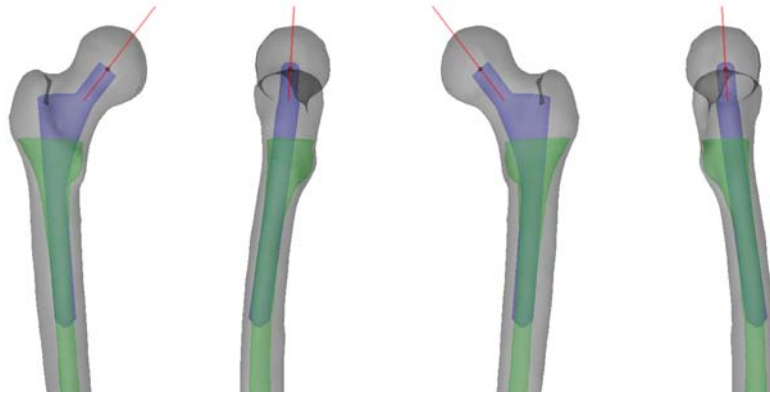


Figure 7.17: From left to right: posterior, left, anterior and right views of an example of a VerSys Epoch<sup>®</sup> FullCoat Hip System fitting to a patient-specific femur. The femur is represented in translucent black with the center of the femoral head in black. The implant and the medullary cavity are shown in blue and green, respectively. In red, the prosthesis neck axis is visible.

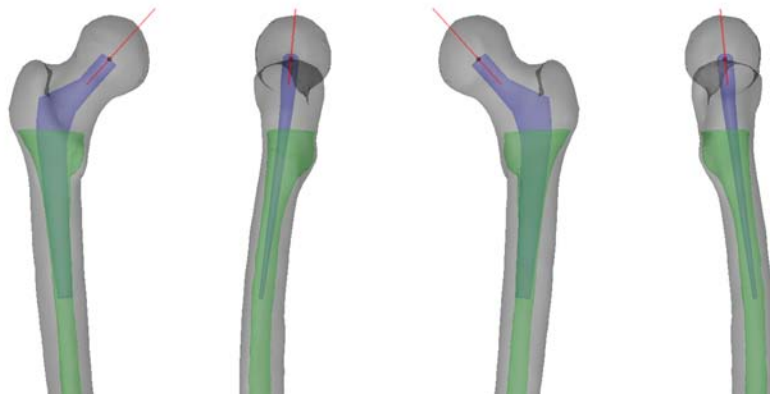


Figure 7.18: From left to right: posterior, left, anterior and right views of an example of a Zimmer<sup>®</sup> MS-30<sup>TM</sup> implant fitting to a patient-specific femur. The femur is represented in translucent black with the center of the femoral head in black. The implant and the medullary cavity are shown in blue and green, respectively. In red, the prosthesis neck axis is visible.

stem is aligned according to the prosthesis insertion axis and its size is fitted to the endosteal of the medullary cavity. This way the contact between the stem and the endosteal is maximized and an added support against the gait loads is expected.

Moreover, it is also observable that the prostheses are aligned with the femoral neck axis. This head center lies within the axis of the implant neckled to the minimization of the distance between the tip of the implant neck and the center of rotation of the femur. The distance between the tip of the femoral neck and the center of the femoral head is usually compensated by the configuration of the prosthetic head as the insertion socket can have controlled depth so that ultimately the femoral offset and leg length remains unchanged in the

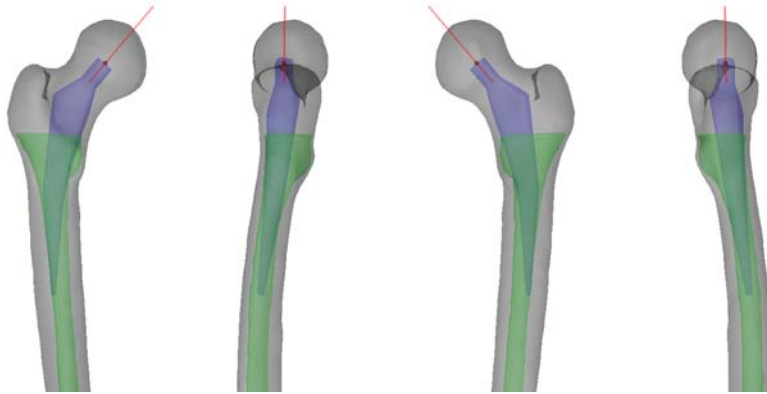


Figure 7.19: From left to right: posterior, left, anterior and right views of an example of a Zimmer<sup>®</sup> Mayo<sup>®</sup> implant fitting to a patient-specific femur. The femur is represented in translucent black with the center of the femoral head in black. The implant and the medullary cavity are shown in blue and green, respectively. In red, the prosthesis neck axis is visible.

prosthetic configuration.

The automatic FE generation proved to suit the problem with the achievement of hexahedral meshes of the patient's femur coupled with the chosen implant after the placement and sizing optimization. The mesh generation is fully parameterizable allowing the user to choose the desired balance between mesh discretization and computational effectiveness. Figure 7.20 shows two examples of different patient-specific femurs coupled with the TRI-LOCK<sup>®</sup> hip implant system.

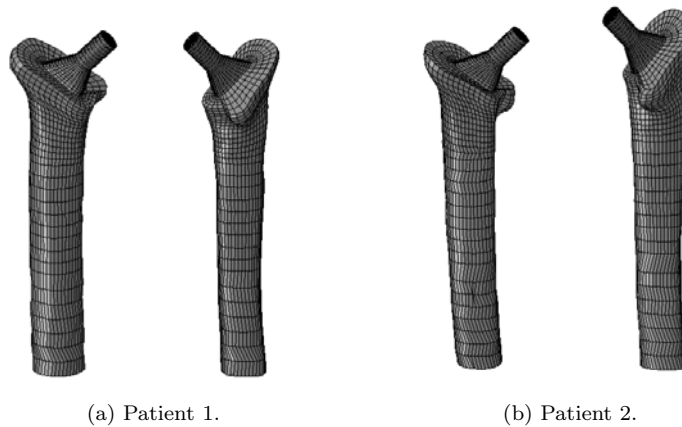


Figure 7.20: Examples of hexahedral meshes of two different patient's femurs, (a) and (b), coupled with the DePuy Synthes TRI-LOCK<sup>®</sup> Bone Preservation Stem.

Based on the presented FE mesh, a few preliminary analyses were run in order to test the mesh accuracy. For a chosen femur, the influence of the variation of the size of the implant was studied. Figure 7.21 shows the contact pressures

on the interface of the TRI-LOCK<sup>®</sup> hip implant system for its commercially available sizes 12.5 and 12.

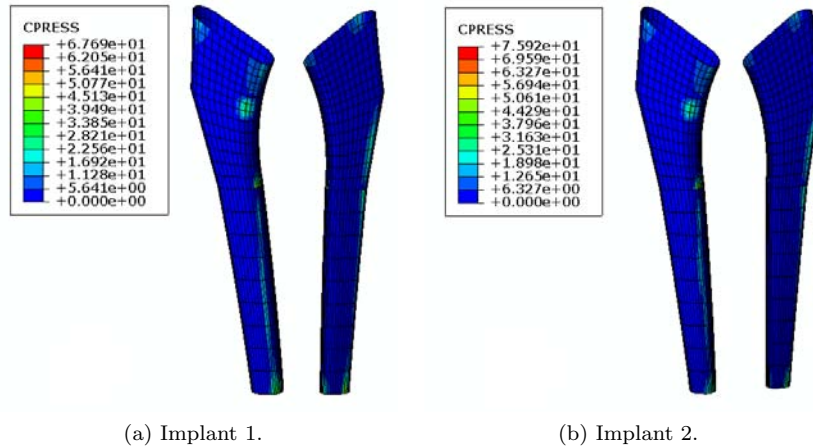


Figure 7.21: Examples of contact pressure (in MPa) on the interface of the implant resulting from the FE analysis of two different implant sizes. Implant 1, shown in (a), accounts for size 12.5 and implant 2, respectively shown in (b), stands for size 12.

The regions where the contact pressure is more evident are similar on both implants. However, the smaller implant presents higher contact pressure values. Similarly, Figure 7.22 shows the tangential displacement on the interface of the same implant and size variation.

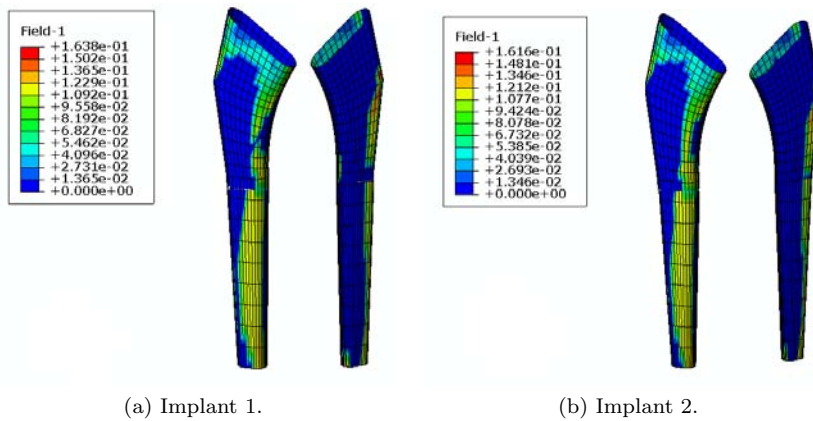


Figure 7.22: Examples of the tangential displacement (in mm) on the interface of the implant resulting from the FE analysis of two different implant sizes. Implant 1, shown in (a), accounts for size 12.5 and implant 2, respectively shown in (b), stands for size 12.

Contrarily to the contact pressure, it is the implant of higher dimension that presents higher tangential displacement values. The regions of the in-

terface where this variable is evident are similar in both implant sizes. It is believed that the higher contact pressure on the smaller implant is related to the increased medullary cavity space.

## 7.8 Discussion

Firstly, not only the linear regression of the FMDA and the prosthesis insertion axis but also the sphere fitting of the femoral head were performed accurately, i.e., presenting very low error values. Automatic 3D axes are therefore established for prosthesis insertion and take in account femoral anteversion or excessive retroversion in implant positioning, which is hard to achieve based on radiographic templating alone.

The values found for the neck-shaft and anteversion angles corroborate other values found in the literature [175, 221]. The proposed methodology can easily be adapted to diagnose femur valgus or vara and retroverted or excessively anteverted femurs merely by measuring the angles between the defined axes. In presurgical planning this allows the surgeon to correct the femur anteversion during the THA and potentially prevent future hip complications on the patient.

Overall, the landmark extraction is achieved within a few seconds, as it only relies on geometric transformations in its majority which are computationally very efficient. This is of critical importance when implemented in an interactive software where the surgeon is planning the THA. The methodology was able to accurately predict landmark location as well as estimate the axis and the angles above described for all of the 50 bone models, which stands as proof of the methods' repeatability and user independence. The accuracy error is inherent to the segmentation error and the coarsening and smoothing of the surface mesh which are beyond the incidence of the present study. It is however possible to implement mesh refinement in more detailed regions of the femur, e.g. the trochanters, in order to minimize the accuracy error.

The prosthesis placement workflow firstly ensured an accurate implant head rotation center reconstruction. Then, by orienting the implant neck as to mimic the anatomical femoral neck axis, femoral retroversion and excessive femoral anteversion can be previously measured so that the surgeon can place the implant to compensate these deviations. The femoral stem fixation to the endosteal is done by aligning the stem axis with the prosthesis insertion axis. The sizing of the implant is done such that the interference or clearance distance is in agreement with the surgeon's opinion. In order to do so, an interactive user interface is provided for the doctor to test or even to question the workflow's suggestion. This way the prosthesis subsidence is minimized even in cementless stems.

An experienced orthopedic surgeon can indeed achieve similar results to any of the four examples shown in section 7.7, at the cost of time and based on his experience and expertise. Hence, a positive clinical feedback relative to the implant dimensioning and positioning was given by the partner surgeon, since the developed workflow promotes a good fixation of the stem as well as a good implant neck orientation. This ensures that the offset remains unaltered and consequently equal leg length is maintained. The lateralization of the center of rotation directly influences the lever arm of abductor muscles which play an

important part during the gait cycle and can result in a defective gait cycle, i.e. limping. The restoration of the hip center of rotation can decrease the incidence of failures and reduce the need for revision surgery [221]. On the other hand, our method can be improved by fully mapping the cancellous and cortical bone boundaries. With so, a more accurate representation of the bone tissue's properties can be achieved, considering the bone mass density.

The work here presented is limited by the amount of different modeled prostheses. Recent approaches to hip replacement implants, namely geometries and coatings, have been developed and have not yet been used to test this workflow. Moreover, there are other optimization criteria that also need to be in agreement with the planning here, such as leg length and the femoral offset. Implants have various but limited sizes available, hence emphasizing the importance of the surgeon's final decision on which size is better suitable for one given femoral geometry, regardless the present workflows suggestion. It should be also noticed that landmark extraction depends on the bone surface mesh level of detail. However, if the same segmentation process is used for every surface mesh, the same data point structure is kept, even in low-resolution CT-Scans. Future improvements should also take in account acetabular component sizing and placement as well as look to maintain the biomechanics of the prosthetic joint as close to the anatomical joint as possible. Comparative leg lengths between legs are yet another limitation of this work and future work should consider the hypothesis of leg lengths need to be corrected.

To the author's knowledge, there is only one report of fully automated optimization methods of pre-operative THA planning based on computational anatomy [231]. The approach is formulated as maximum a posterior estimation based on statistical models derived from the training datasets prepared by a surgeon. The results shown are satisfactory and are said to improve the surgeon's planning. Nevertheless, if, on the one hand, the training of the shape model can be time consuming, an approach based on shape models might incorporate the errors of femur-prosthesis couplings population. The approach considers also the acetabular component of the hip implant which makes results quite difficult to compare [25].

Finally, the FE mesh generation was essential to achieve early results in patient-specific analysis. A fully automatic method for meshing the implant-femur coupling with hexahedral elements was implemented. The method is parameterizable, making it possible for the user to balance the precision of the mesh with the computational cost of the analysis. Due to time limitations, the extent of this work was shortened. Nevertheless, the tools for a THA planning were implemented so that even an inexperienced user can make use of the techniques here presented.

## 7.9 Conclusions

Even though the reduction of the incidence of hip implants failure on THA to zero is still difficult to achieve, the developed set of tools is a step forward towards better planning and hopefully to increase the longevity of the implants. The automated landmark extraction and consequent anatomical knowledge of the patient-specific femur allows an accurate and straightforward planning from the surgeon who, due to the automation of most of these methods, does not

need to have extensive knowledge of the implemented numerical methods. An accurate prosthesis sizing, fitting and placement can increase the precision of the surgery, shorten its duration and cost, reduce the incidence of prosthesis' loosening and minimize bone stock loss, which will ultimately influence the terms of a possible revision surgery. Moreover, by maintaining equal head rotation centers and if leg length is ensured to be kept unaltered, the risk of periprosthetic fracture is minimized as well as a normal gait cycle is more likely to be restored. In sum, a good planning reduces the risk of major errors but does not guarantee the everlasting success of a THA.

Within the scope of this thesis, the methods here presented were tested on 50 femur models. They proved to be both robust, precise and repeatable. The automated workflow developed can also be coupled to an automatic finite element model in order to infer quantitative data of a specific implant-femur coupling which can be used to presurgically compare the performance of different implant designs.



## Chapter 8

# Conclusions and Future Work

The main concern over the development and implementations of the methods presented in this thesis was their integration in a real-time THA software. Hence, the graphical user interface should be intuitive and straight-forward but most importantly automatic and time effective. Similarly, the implementation of the methods should generate robust and accurate results, so that the approach is as generic and case embracing as possible. Because the input data is heterogeneous and prone to image artifacts or acquisition errors, as seen in chapter 4, such method development and implementation were challenging and time consuming. Nevertheless, the approach presented in this thesis proved to be capable of solving the problem described in chapter 1 and ultimately of great utility in THA planning. Within the present chapter, the conclusions of the developed work will be presented and possible future directions will be discussed.

### 8.1 Conclusions and Key Achievements

In order to develop an automatic THA planning, the pipeline was divided in two phases, namely the femur segmentation and the prosthesis coupling. For the development of methods for segmenting, modeling and statistical femur analysis, an ASM based approach was implemented from a large population of CT-scan images. Hence, the first step was to create a SSM using a piecewise parametric mesh that in the end included 218 femurs resulting from both CT-scan image groups and the cadaveric femurs. This statistical model was analyzed and the characterization of the size and shape of the femoral anatomy of the population was possible, as well as the identification of its main modes of variance. Ultimately, this allowed the representation of the total variance of the femoral shape with only the first 4 principal modes and a significance of over 95%, which is computationally very effective.

The creation of the model was detailed in chapter 5 and based in two image groups described in 4: one large group of high resolution images acquired at the UZ Gent and a smaller group of images with significantly lower resolution acquired at the Quadrantes clinic in Lisbon. It was validated using leave-one-out cross validation experiments, proving to be accurate, compact and have a high generalisability. The application of the model to image segmentation, described in chapter 6, was capable of segmenting 158 femurs from both image

groups with a 98% success rate and with an average RMS error of 1.014 mm for the high resolution images and 1.446 mm for the low resolution images. The PCA was an appropriate method for statistical modeling since ranked orthonormal principal components allowed a very efficient fitting during the segmentation using only 5 to 6 components. A novel femur shape and pose estimation method based on a shape constrained iterative fitting was also presented, allowing the full automation of the segmentation pipeline. It proved to be cost effective and to optimize the iterative ASM segmentation process. The method was able to predict the medullary cavity of the in-image femurs with a thresholding approach.

The second phase, the development of a framework for implant placement and size estimation was also achieved using pyFormex<sup>1</sup>. Initially, a standardized coordinate system was developed in order to uniformly align and orient the whole femur population, hence remove all translational and rotational variations. Within this coordinate system, a series of algebraic transformations were implemented and allowed the extraction of key anatomical landmarks of the femoral shape, as well as defined important femoral axes and angles for implant orientation and size estimation. The trochanters, the center of the femoral head, the neck and shaft axis, as well as the medullary cavity medial axis were accurately defined. Moreover, the femoral anteversion, the neck-shaft angle or the femoral bowing are automatically predicted so that they can be taken into account in the THA preparation. Parallely, a set of known commercially available hip implant systems were parametrically modeled. Hence, an algorithm for the sizing and placement of four different known implant commercial prosthesis in a patient-specific femur was described in chapter 7.

Finally, an automatic hexahedral FE mesh generation was developed. The placed and aligned implant, as well as the femoral bone, are meshed with hexahedral elements taking in account the previously segmented medullary cavity. This way, a quantitative analysis of the performance of the different implant behaviors in a patient-specific bone can be evaluated and comparisons can be established by a doctor with very little knowledge on the background techniques.

## 8.2 Limitations and Future Work

Despite the achievements enumerated in previous section 8.1, there are limitations of the work developed that can give way to future developments in order to improve both phases, the ASM segmentation and the THA planning. Within this section, they will be reviewed and a line of work will be suggested to try to overcome these limitations and achieve better results with the proposed methodology.

### 8.2.1 ASM: Training and Segmentation

In the shape model training, 218 femurs were considered from both CT-scan image groups and the cadaveric femurs, after removal of abnormal and partially occluded femurs. Its application to segmentation was only tested in one image modality and therefore its results with other image modalities are unknown,

---

<sup>1</sup><http://www.nongnu.org/pyformex/>

even though it isn't far-fetched to assume the pipeline would work in MRI at the cost of minor adjustments in the training phase. The PCA model of 30 femurs was capable of segmenting the rest of the image datasets. The segmentation results did not change when the training set increased. In the presented pipeline, no effort has been made to find the optimum number of parameters needed to describe femoral shape nor appearance.

Moreover, the pipeline's robustness to abnormal or pathological femur morphologies is not quantified. Even though it is possible to assume that based on the *a priori* shape knowledge included in the model, the pipeline would be able to predict partially occluded femur boundaries. However, femurs may present oddly shaped prominences and for that reason be mis-segmented. Despite heterogeneity of the femur population seen on chapter 4, the solution to increase the accuracy of the model in such situations is not to modify the overall framework but to add oddly shaped femurs to the SSM. However, the inclusion of such oddly shaped femurs can be detrimental because it would create a highly non-Gaussian shape distribution. Because the PCA is sensitive to outliers, the resulting principal components may poorly model both normal and oddly shaped femurs. Because of this reason, it would be interesting to study the effect of the influence of the inclusion of the oddly shaped femurs and whether a classification step should be added to the pipeline initial parameters or not.

The initialization method proposed was efficient and minimized the segmentation iterative process. However, it has a considerable dependence on the femoral 3D image box estimation detailed in chapter 4, which, on the other hand, is not very time efficient. The estimation of a femoral bounding box in the image domain can be looked into either by reinventing the HT approach, or merely its implementation, or by extracting Haar-like features [232].

The method used for the medullary cavity segmentation served its purpose of THA planning although it can be significantly improved. Fully automated femoral cortex mapping has been reported and can provide additional information about the patients' age and weight. Moreover, the mapping of cortical and cancellous bone in the femoral domain gives way to a more accurate FE modeling of the femur and consequently more reliable results.

In the future, it would be interesting to relate the morphological variations to the anthropological information of the image datasets, such as age, gender or weight. This would enable the generation of template femur morphologies representatives of specific populations and used to improve the segmentation step and downstream analysis tasks such as FE analysis and prosthesis design and placement. In addition, the general methods proposed in this thesis are not specific to the femur. In other words, it is possible to segment and model other bones or anatomical soft-tissue organs at the cost of mesh generation, exemplified on chapter 5 for the femur. This would enable the possibility of automatically extracting and modeling several anatomical structures from large datasets as a routine and therefore detailed morphology could be readily studied.

### 8.2.2 THA Planning

The most intuitive and prominent direction of future work is to approach the acetabular component of the hip implant system. The ASM segmentation presented can be applied to the hip bone at the cost of the development of a new

mesh design. The study of its anatomy and curvature would serve as basis for the mesh design and Lagrange element fitting so that the hip bone could be computationally represented. With both femoral and acetabular bone modeling, as well as the complete hip implant systems, a more accurate and complete planning can be achieved. Decreased bone mass density or deteriorated bone in the acetabular region can be computationally represented and the acetabular cup fixation done in a way that minimizes bone loss without compromising the femoral offset and leg length.

The prosthesis database is subject of constant evolution. Initially, there is the need to enlarge the database of modeled prosthesis. Everyday more and more new solutions are released in the market and it is important to keep up-to-date to the modifications of the implant shape and design. Moreover, it would also be of interest to model modular prosthesis, i.e., different stem and neck combinations for the same implant design.

The prosthesis placement optimization pipeline is sequential, i.e., there is a series of decreasing importance directives that are respected to automatically place and size the implant. It would be interesting in the future to compare the obtained results with a multi-objective optimization pipeline, where the size and the location of the implant, among other criteria, are simultaneously optimized. This way, optimal decisions need to be taken in the presence of trade-offs between two or more conflicting objectives and therefore an increase or decrease on the size of the implant can be iteratively compensated by a translation or rotation. The complexity of such approach is considerable, as the formulation of the objective function has to take in account shape and space constraints, namely the endosteal wall and the center of the head of the femur.

Due to time limitations, the FE mesh generation potential was not fully taken advantage of. The FE mesh could be used to infer about the influence of alignment parameters such as the prosthesis and endosteal wall fitting or the stem position in the medullary canal in order to try to optimize stem design and orientation. Moreover, together with the enlargement of the implant database, comparative performance studies can be done among the different hip implant systems for a patient-specific femur and ultimately determine which would perform better in post-surgical conditions.

# Bibliography

- [1] U Holszarth and G Cotogno. Total hip arthroplasty - state of the art, challenges and prospects. Technical report, European Commission Joint Research Centre, Luxembourg, 2012.
- [2] J. Sobotta, R. Putz, R. Pabst, S. Bedoui, and R. Putz. *Sobotta Atlas of Human Anatomy: Head, Neck, Upper Limb*. Atlas of Human Anatomy (Sobotta) Series. Elsevier Urban & Fisher, 2006.
- [3] Philipp Damm, Joern Dymke, Robert Ackermann, Alwina Bender, Friedmar Graichen, Andreas Halder, Alexander Beier, and Georg Bergmann. Friction in total hip joint prosthesis measured in vivo during walking. *PLoS ONE*, 8(11):e78373, 11 2013.
- [4] Sofie Van Cauter. *Automatic Localisation of Landmarks on Virtual Bone Models*. PhD thesis, Institute Biomedical Technology, University of Ghent, 2013.
- [5] Julius Wolff. *The law of bone remodelling*. Springer Science & Business Media, 2012.
- [6] PK Bertelsen, JG Clement, and CDL Thomas. A morphometric study of the cortex of the human femur from early childhood to advanced old age. *Forensic science international*, 74(1):63–77, 1995.
- [7] MD Grynepas, B Alpert, I Katz, I Lieberman, and KPH Pritzker. Subchondral bone in osteoarthritis. *Calcified tissue international*, 49(1):20–26, 1991.
- [8] Iain Alexander Anderson. *Mechanics and Material Properties of the Femoral Head: From Microstructure to Continuum Modelling*. PhD thesis, Engineering Science–University of Auckland, 1996.
- [9] Jacqueline Lee Hislop-Jambrich. A 3d radiological study of age-related quantitative and morphological differences in the human femur: clinical and anthropological applications. 2010.
- [10] Mariana E Kersh, Marcus G Pandy, Quang M Bui, Anthony C Jones, Christoph H Arns, Mark A Knackstedt, Ego Seeman, and Roger Zebaze. The heterogeneity in femoral neck structure and strength. *Journal of Bone and Mineral Research*, 28(5):1022–1028, 2013.
- [11] George R Milner and Jesper L Boldsen. Humeral and femoral head diameters in recent white american skeletons. *Journal of forensic sciences*, 57(1):35–40, 2012.

- [12] Glen A Turley, Shahbaz MY Ahmed, Mark A Williams, and Damian R Griffin. Validation of the femoral anteversion measurement method used in imageless navigation. *Computer Aided Surgery*, 17(4):187–197, 2012.
- [13] Ge Wu, Sorin Siegler, Paul Allard, Chris Kirtley, Alberto Leardini, Dieter Rosenbaum, Mike Whittle, Darryl D D’Lima, Luca Cristofolini, Hartmut Witte, et al. Isb recommendation on definitions of joint coordinate system of various joints for the reporting of human joint motion—part i: ankle, hip, and spine. *Journal of biomechanics*, 35(4):543–548, 2002.
- [14] M Notelovitz. Osteoporosis: screening, prevention, and management. *Fertility and sterility*, 59(4):707—725, April 1993.
- [15] Duarte Pereira, Elisabete Ramos, and Jaime Branco. Osteoarthritis: Artigo de revisão. *Acta Médica Portuguesa*, 27(5), 2014.
- [16] S Agarwala, D Jain, VR Joshi, and A Sule. Efficacy of alendronate, a bisphosphonate, in the treatment of avn of the hip. a prospective open-label study. *Rheumatology*, 44(3):352–359, 2005.
- [17] S Agarwala, S Shah, and VR Joshi. The use of alendronate in the treatment of avascular necrosis of the femoral head follow-up to eight years. *Journal of Bone & Joint Surgery, British Volume*, 91(8):1013–1018, 2009.
- [18] Samuel Van de Velde, Ramona Fillman, and Suzanne Yandow. The aetiology of protrusio acetabuli. literature review from 1824 to 2006. *Acta orthopaedica belgica*, 72(5):524–529, 2006.
- [19] Lance C Brunner, Liza Eshilian-Oates, and Tony Y Kuo. Hip fractures in adults. *American family physician*, 67(3):537–542, 2003.
- [20] Andrew H Schmidt and Marc F Swiontkowski. Femoral neck fractures. *Orthopedic Clinics of North America*, 33(1):97–111, 2002.
- [21] Jun-Wen Wang, Liang-Kuang Chen, and Chin-En Chen. Surgical treatment of fractures of the greater trochanter associated with osteolytic lesions. *The Journal of Bone & Joint Surgery*, 87(12):2724–2728, 2005.
- [22] MB Coventry. Historical perspective of hip arthroplasty. In *Joint Replacement Arthroplasty*, pages 491–499. Churchill Livingstone New York, USA, 1991.
- [23] Pablo F Gomez and Jose A Morcuende. Early attempts at hip arthroplasty: 1700s to 1950s. *The Iowa orthopaedic journal*, 25:25, 2005.
- [24] Austin T Moore and Harold Ray Bohlman. The classic: Metal hip joint: A case report. *Clinical orthopaedics and related research*, 453:22–24, 2006.
- [25] Rui Miguel Ruben. *Projecto Ótimo de Próteses da Articulação da Anca*. PhD thesis, Instituto Superior Técnico–Universidade Técnica de Lisboa, 2009.
- [26] John Charnley. Arthroplasty of the hip: a new operation. *The Lancet*, 277(7187):1129–1132, 1961.

- [27] BM Wroblewski, PD Siney, and PA Fleming. The charnley hip replacement—43 years of clinical success. *Infection*, 22:1–53, 2006.
- [28] William H Harris. Conquest of a worldwide human disease: particle-induced periprosthetic osteolysis. *Clinical orthopaedics and related research*, 429:39–42, 2004.
- [29] Stephen Richard Knight, Randeep Aujla, and Satya Prasad Biswas. Total hip arthroplasty-over 100 years of operative history. *Orthopedic reviews*, 3(2), 2011.
- [30] Gwo-Chin Lee and Jonathan P Garino. Reliability of ceramic components. In *Seminars in Arthroplasty*, volume 22, pages 271–275. Elsevier, 2011.
- [31] DJW McMinn, J Daniel, H Ziaee, and C Pradhan. Indications and results of hip resurfacing. *International orthopaedics*, 35(2):231–237, 2011.
- [32] David R Marker, Thorsten M Seyler, Riyaz H Jinnah, Ronald E Delanois, Slif D Ulrich, and Michael A Mont. Femoral neck fractures after metal-on-metal total hip resurfacing: a prospective cohort study. *The Journal of arthroplasty*, 22(7):66–71, 2007.
- [33] Young-Min Kwon, Simon J Ostlere, Peter McLardy-Smith, Nicholas A Athanasou, Harinderjit S Gill, and David W Murray. “asymptomatic” pseudotumors after metal-on-metal hip resurfacing arthroplasty: prevalence and metal ion study. *The Journal of arthroplasty*, 26(4):511–518, 2011.
- [34] Inge HF Reininga, Wiebren Zijlstra, Robert Wagenmakers, Alexander L Boerboom, Bregtje P Huijbers, Johan W Groothoff, Sjoerd K Bulstra, and Martin Stevens. Minimally invasive and computer-navigated total hip arthroplasty: a qualitative and systematic review of the literature. *BMC musculoskeletal disorders*, 11(1):92, 2010.
- [35] Kyung-Soon Park, Chang-Seon Oh, and Taek-Rim Yoon. Comparison of minimally invasive total hip arthroplasty versus conventional hemiarthroplasty for displaced femoral neck fractures in active elderly patients. *Chonnam medical journal*, 49(2):81–86, 2013.
- [36] Organisation for Economic Co-operation and Development. *Health at a Glance: Europe 2014*. OECD, 2014.
- [37] Francette Koechlin, Paul Konijn, Luca Lorenzoni, and Paul Schreyer. Comparing hospital and health prices and volumes internationally. 2014.
- [38] R Otten and PM Van Roermund. en picavet sj. trends in aantallen knie-en heupartroplastieken. *Ned Tijdschr Geneeskunde*, 154:A1534, 2010.
- [39] Steven Kurtz, Kevin Ong, Edmund Lau, Fionna Mowat, and Michael Halpern. Projections of primary and revision hip and knee arthroplasty in the united states from 2005 to 2030. *The Journal of Bone & Joint Surgery*, 89(4):780–785, 2007.

- [40] VS Pai. A comparison of three lateral approaches in primary total hip replacement. *International orthopaedics*, 21(6):393–398, 1998.
- [41] Kim C Bertin and Heinz Röttinger. Anterolateral mini-incision hip replacement surgery: a modified watson-jones approach. *Clinical orthopaedics and related research*, 429:248–255, 2004.
- [42] MN Smith-Petersen. Arthroplasty of the hip. *The Journal of Bone & Joint Surgery*, 21(2):269–288, 1939.
- [43] JG Kennedy, WB Rogers, KE Soffe, RJ Sullivan, DG Griffen, and LJ Sheehan. Effect of acetabular component orientation on recurrent dislocation, pelvic osteolysis, polyethylene wear, and component migration. *The Journal of arthroplasty*, 13(5):530–534, 1998.
- [44] Alejandro Gonzalez Della Valle, Gastón Shullitel, Francisco Piccaluga, and Eduardo A Salvati. The precision and usefulness of preoperative planning for cemented and hybrid primary total hip arthroplasty. *The Journal of arthroplasty*, 20(1):51–58, 2005.
- [45] M Viceconti, R Lattanzi, B Antonietti, S Paderni, R Olmi, A Sudanese, and A Toni. Ct-based surgical planning software improves the accuracy of total hip replacement preoperative planning. *Medical engineering & physics*, 25(5):371–377, 2003.
- [46] Alejandro González Della Valle, Douglas E Padgett, and Eduardo A Salvati. Preoperative planning for primary total hip arthroplasty. *Journal of the American Academy of Orthopaedic Surgeons*, 13(7):455–462, 2005.
- [47] Thierry Scheerlinck. Primary hip arthroplasty templating on standard radiographs: a stepwise approach. *Acta Orthop Belg*, 76(4):432–442, 2010.
- [48] Monika Michalíková, Lucia Bednarčíková, Martin Petřík, Jozef Živčák, and Richard Raši. The digital pre-operative planning of total hip arthroplasty. *Acta Polytechnica Hungarica*, 7(3):2, 2010.
- [49] Yona Kosashvili, Nadav Shasha, Eli Olschewski, Oleg Safir, Larry White, Allan Gross, and David Backstein. Digital versus conventional templating techniques in preoperative planning for total hip arthroplasty. *Canadian Journal of Surgery*, 52(1):6, 2009.
- [50] Riccardo Lattanzi, Marco Viceconti, Cinzia Zannoni, Paolo Quadrani, and Aldo Toni. Hip-op: an innovative software to plan total hip replacement surgery. *Informatics for Health and Social Care*, 27(2):71–83, 2002.
- [51] Masahiko Nakamoto, Yoshinobu Sato, Nobuhiko Sugano, Toshihiko Sasama, Takashi Nishii, Pyong Sik Pak, Kenzo Akazawa, Yukio Tada, Hideki Yoshikawa, and Shinichi Tamura. Automated ct-based 3d surgical planning for total hip replacement: a pilot study. In *International Congress Series*, volume 1256, pages 389–394. Elsevier, 2003.



- [52] Kyung In Jeong, Su Gwan Kim, Seong Yong Moon, Ji Su Oh, Ji Ho Jo, Hyoung Sup Lim, Jeong Sun Kim, Sung Chul Lim, and Mi Jeong. Experimental study of osseointegration and stability of intentionally exposed hydroxyapatite coating implants. *Journal of Korean Association of Maxillofacial Plastic and Reconstructive Surgeons*, 34(1):12–16, 2012.
- [53] Biswanath Kundu, Chidambaram Soundrapandian, Samit K Nandi, Prasenjit Mukherjee, Nandadulal Dandapat, Subhasis Roy, Bakul K Datta, Tapan K Mandal, Debabrata Basu, and Rupnarayan N Bhattacharya. Development of new localized drug delivery system based on ceftriaxone-sulbactam composite drug impregnated porous hydroxyapatite: a systematic approach for in vitro and in vivo animal trial. *Pharmaceutical research*, 27(8):1659–1676, 2010.
- [54] Biswanath Kundu, A Lemos, C Soundrapandian, PS Sen, Someswar Datta, JMF Ferreira, and Debabrata Basu. Development of porous hap and  $\beta$ -tcp scaffolds by starch consolidation with foaming method and drug-chitosan bilayered scaffold based drug delivery system. *Journal of Materials Science: Materials in Medicine*, 21(11):2955–2969, 2010.
- [55] Fabrizio Matassi, Alessandra Botti, Luigi Sirleo, Christian Carulli, and Massimo Innocenti. Porous metal for orthopedics implants. *Clinical Cases in Mineral and Bone Metabolism*, 10(2):111, 2013.
- [56] Joon Park and Roderic S Lakes. *Biomaterials: an introduction*. Springer Science & Business Media, 2007.
- [57] Mitsuo Niinomi. Recent metallic materials for biomedical applications. *Metallurgical and materials transactions A*, 33(3):477–486, 2002.
- [58] David W Manning, PP Chiang, JM Martell, JO Galante, and WH Harris. In vivo comparative wear study of traditional and highly cross-linked polyethylene in total hip arthroplasty. *The Journal of arthroplasty*, 20(7):880–886, 2005.
- [59] Ebru Oral, Steven D Christensen, Arnaz S Malhi, Keith K Wannomae, and Orhun K Muratoglu. Wear resistance and mechanical properties of highly cross-linked, ultrahigh-molecular weight polyethylene doped with vitamin e. *The Journal of arthroplasty*, 21(4):580–591, 2006.
- [60] Carmen Zietz, Daniel Kluess, Philipp Bergschmidt, Maximilian Haenle, Wolfram Mittelmeier, and Rainer Bader. Tribological aspects of ceramics in total hip and knee arthroplasty. In *Seminars in Arthroplasty*, volume 22, pages 258–263. Elsevier, 2011.
- [61] Guillaume Demey, Camdon Fary, Sébastien Lustig, Philippe Neyret, and Tarik Aït si Selmi. Does a collar improve the immediate stability of uncemented femoral hip stems in total hip arthroplasty? a bilateral comparative cadaver study. *The Journal of arthroplasty*, 26(8):1549–1555, 2011.
- [62] Michael A Kopec, Aaron Pemberton, Joseph C Milbrandt, and Gordon Allan. Component version in modular total hip revision. *The Iowa orthopaedic journal*, 29:5, 2009.

- [63] Alberto Cigada, Giulio Cotogno, and Roberto Chiesa. The ceramic-on-metal coupling in total hip replacements for young patients: a review study. *Journal of applied biomaterials & biomechanics: JABB*, 9(1):2–10, 2010.
- [64] Daniel J Berry, Marius Von Knoch, Cathy D Schleck, and William S Harmsen. Effect of femoral head diameter and operative approach on risk of dislocation after primary total hip arthroplasty. *The Journal of Bone & Joint Surgery*, 87(11):2456–2463, 2005.
- [65] M Marinelli, A Soccetti, N Panfoli, and L de Palma. Cost-effectiveness of cemented versus cementless total hip arthroplasty. a markov decision analysis based on implant cost. *Journal of Orthopaedics and Traumatology*, 9(1):23–28, 2008.
- [66] Rik Huiskes, Harrie Weinans, and Michel Dalstra. Adaptive bone remodeling and biomechanical design considerations. *Orthopedics*, 12:1255–1267, 1989.
- [67] S Affatato, M Spinelli, M Zavalloni, C Mazzega-Fabbro, and M Viceconti. Tribology and total hip joint replacement: current concepts in mechanical simulation. *Medical Engineering & Physics*, 30(10):1305–1317, 2008.
- [68] I Kempf and M Semlitsch. Massive wear of a steel ball head by ceramic fragments in the polyethylene acetabular cup after revision of a total hip prosthesis with fractured ceramic ball. *Archives of orthopaedic and trauma surgery*, 109(5):284–287, 1990.
- [69] Y Yan, A Neville, D Dowson, S Williams, and J Fisher. Tribo-corrosion analysis of wear and metal ion release interactions from metal-on-metal and ceramic-on-metal contacts for the application in artificial hip prostheses. *Proceedings of the Institution of Mechanical Engineers, Part J: Journal of Engineering Tribology*, 222(3):483–492, 2008.
- [70] Daniel J Berry, W Scott Harmsen, Miguel E Cabanela, and Bernard F Morrey. Twenty-five-year survivorship of two thousand consecutive primary charnley total hip replacements. *The Journal of Bone & Joint Surgery*, 84(2):171–177, 2002.
- [71] Slif D Ulrich, Thorsten M Seyler, Derek Bennett, Ronald E Delanois, Khaled J Saleh, Issada Thongtrangan, Michael Kuskowski, Edward Y Cheng, Peter F Sharkey, Javad Parvizi, et al. Total hip arthroplasties: what are the reasons for revision? *International orthopaedics*, 32(5):597–604, 2008.
- [72] Alejandro González DellaValle, Patricio Salonia Ruzo, Stephen Li, Paul Pellicci, Thomas P Sculco, and Eduardo A Salvati. Dislodgment of polyethylene liners in first and second-generation harris-galante acetabular components. *JBJS Case Connector*, (4):553–553, 2001.
- [73] Alejandro González Della Valle, Adriana Zoppi, Margaret GE Peterson, and Eduardo A Salvati. A rough surface finish adversely affects the survivorship of a cemented femoral stem. *Clinical orthopaedics and related research*, 436:158–163, 2005.

- [74] Alejandro González Della Valle, Adriana Zoppi, Margaret GE Peterson, and Eduardo A Salvati. Clinical and radiographic results associated with a modern, cementless modular cup design in total hip arthroplasty. *The Journal of Bone & Joint Surgery*, 86(9):1998–2003, 2004.
- [75] Yousef Abu-Amer, Isra Darwech, and John C Clohisy. Aseptic loosening of total joint replacements: mechanisms underlying osteolysis and potential therapies. *Arthritis Research and Therapy*, 9(1):S6, 2007.
- [76] Harry Krishnan, Kapil Sugand, Ibrahim Ali, and Jay Smith. ‘pseudo-tumour’invading the proximal femur with normal metal ions following metal on metal hip resurfacing. *BMJ case reports*, 2015:bcr2014206368, 2015.
- [77] Thorsten M Buzug. *Computed tomography: from photon statistics to modern cone-beam CT*. Springer Science & Business Media, 2008.
- [78] Stanley R Deans. *The Radon transform and some of its applications*. Courier Corporation, 2007.
- [79] Pedro Daniel Dinis Teodoro. *Robust Surface Reconstruction and US Bone Registration for Hip Resurfacing Surgery*. PhD thesis, Instituto Superior Técnico)–Universidade Técnica de Lisboa, 2015.
- [80] William E Lorensen and Harvey E Cline. Marching cubes: A high resolution 3d surface construction algorithm. In *ACM siggraph computer graphics*, volume 21, pages 163–169. ACM, 1987.
- [81] Matthew C Clark, Lawrence O Hall, Dmitry B Goldgof, Robert Velthuizen, F Reed Murtagh, and Martin S Silbiger. Automatic tumor segmentation using knowledge-based techniques. *Medical Imaging, IEEE Transactions on*, 17(2):187–201, 1998.
- [82] Nathan Moon, Elizabeth Bullitt, Koen Van Leemput, and Guido Gerig. Automatic brain and tumor segmentation. In *Medical Image Computing and Computer-Assisted Intervention—MICCAI 2002*, pages 372–379. Springer, 2002.
- [83] Lang Xu, Marcel Jackowski, A Goshtasby, D Roseman, S Bines, C Yu, Akshaya Dhawan, and A Huntley. Segmentation of skin cancer images. *Image and Vision Computing*, 17(1):65–74, 1999.
- [84] Ludwig Adams, Werner Krybus, Dietrich Meyer-Ebrecht, Rainer Rueger, Joachim M Gilsbach, Ralph Moesges, and Georg Schloendorff. Computer-assisted surgery. *Computer Graphics and Applications, IEEE*, 10(3):43–51, 1990.
- [85] H Bätthis, L Perlick, M Tingart, C Lüring, D Zurakowski, and J Grifka. Alignment in total knee arthroplasty a comparison of computer-assisted surgery with the conventional technique. *Journal of Bone & Joint Surgery, British Volume*, 86(5):682–687, 2004.

- [86] Tobias Heimann, Bram Van Ginneken, Martin Styner, Yulia Arzhaeva, Volker Aurich, Christian Bauer, Andreas Beck, Christoph Becker, Reinhard Beichel, György Bekes, et al. Comparison and evaluation of methods for liver segmentation from ct datasets. *Medical Imaging, IEEE Transactions on*, 28(8):1251–1265, 2009.
- [87] Akinobu Shimizu, Tatsuya Kimoto, Hidefumi Kobatake, Shigeru Nawano, and Kenji Shinozaki. Automated pancreas segmentation from three-dimensional contrast-enhanced computed tomography. *International journal of computer assisted radiology and surgery*, 5(1):85–98, 2010.
- [88] Tobias Klinder, Jörn Ostermann, Matthias Ehm, Astrid Franz, Reinhard Kneser, and Cristian Lorenz. Automated model-based vertebra detection, identification, and segmentation in ct images. *Medical image analysis*, 13(3):471–482, 2009.
- [89] Muhammad Waseem Khan. A survey: Image segmentation techniques. *International Journal of Future Computer and Communication*, 3(2):89, 2014.
- [90] Nobuyuki Otsu. A threshold selection method from gray-level histograms. *Automatica*, 11(285-296):23–27, 1975.
- [91] Michael Kass, Andrew Witkin, and Demetri Terzopoulos. Snakes: Active contour models. *International journal of computer vision*, 1(4):321–331, 1988.
- [92] Demetri Terzopoulos, Andrew Witkin, and Michael Kass. Constraints on deformable models: Recovering 3d shape and nonrigid motion. *Artificial intelligence*, 36(1):91–123, 1988.
- [93] Hervé Delingette. Simplex meshes: a general representation for 3d shape reconstruction. In *Computer Vision and Pattern Recognition, 1994. Proceedings CVPR'94., 1994 IEEE Computer Society Conference on*, pages 856–859. IEEE, 1994.
- [94] Stanley Osher and James A Sethian. Fronts propagating with curvature-dependent speed: algorithms based on hamilton-jacobi formulations. *Journal of computational physics*, 79(1):12–49, 1988.
- [95] Ravikanth Malladi, James Sethian, Baba C Vemuri, et al. Shape modeling with front propagation: A level set approach. *Pattern Analysis and Machine Intelligence, IEEE Transactions on*, 17(2):158–175, 1995.
- [96] Tony F Chan, Luminita Vese, et al. Active contours without edges. *Image processing, IEEE transactions on*, 10(2):266–277, 2001.
- [97] Michael E Leventon, W Eric L Grimson, and Olivier Faugeras. Statistical shape influence in geodesic active contours. In *Computer Vision and Pattern Recognition, 2000. Proceedings. IEEE Conference on*, volume 1, pages 316–323. IEEE, 2000.

- [98] Daniel Cremers, Timo Kohlberger, and Christoph Schnörr. Shape statistics in kernel space for variational image segmentation. *Pattern Recognition*, 36(9):1929–1943, 2003.
- [99] Timothy F Cootes, Christopher J Taylor, David H Cooper, and Jim Graham. Active shape models-their training and application. *Computer vision and image understanding*, 61(1):38–59, 1995.
- [100] Ju Zhang. *Development of an Automated System for Building a Large Population-based Statistical Model of Femur Morphology*. PhD thesis, Auckland Bioengineering Institute, University of Auckland, 2013.
- [101] Harry Blum. Biological shape and visual science (part i). *Journal of theoretical Biology*, 38(2):205–287, 1973.
- [102] Daniel Fritsch, Stephen Pizer, Liyun Yu, Valen Johnson, and Edward Chaney. Segmentation of medical image objects using deformable shape loci. In *Information Processing in Medical Imaging*, pages 127–140. Springer, 1997.
- [103] Stephen M Pizer, Daniel S Fritsch, Paul Yushkevich, Valen E Johnson, Edward L Chaney, et al. Segmentation, registration, and measurement of shape variation via image object shape. *Medical Imaging, IEEE Transactions on*, 18(10):851–865, 1999.
- [104] Stephen M Pizer, P Thomas Fletcher, Sarang Joshi, Andrew Thall, James Z Chen, Yonatan Fridman, Daniel S Fritsch, A Graham Gash, John M Glotzer, Michael R Jiroutek, et al. Deformable m-reps for 3d medical image segmentation. *International Journal of Computer Vision*, 55(2-3):85–106, 2003.
- [105] Paul Yushkevich, Hui Zhang, James C Gee, et al. Continuous medial representation for anatomical structures. *Medical Imaging, IEEE Transactions on*, 25(12):1547–1564, 2006.
- [106] Sourabh Niyogi, Edward H Adelson, et al. Analyzing and recognizing walking figures in xyt. In *Computer Vision and Pattern Recognition, 1994. Proceedings CVPR'94., 1994 IEEE Computer Society Conference on*, pages 469–474. IEEE, 1994.
- [107] AM Baumberg and DC Hogg. An efficient method for contour tracking using active shape models. In *Motion of Non-Rigid and Articulated Objects, 1994., Proceedings of the 1994 IEEE Workshop on*, pages 194–199. IEEE, 1994.
- [108] BJ Hafner, SG Zachariah, and JE Sanders. Characterisation of three-dimensional anatomic shapes using principal components: application to the proximal tibia. *Medical and Biological Engineering and Computing*, 38(1):9–16, 2000.
- [109] Paramate Horkaew and Guang-Zhong Yang. Optimal deformable surface models for 3d medical image analysis. In *Information Processing in Medical Imaging*, pages 13–24. Springer, 2003.

- [110] Baigalmaa Tsagaan, Akinobu Shimizu, Hidefumi Kobatake, and Kunihisa Miyakawa. An automated segmentation method of kidney using statistical information. In *Medical Image Computing and Computer-Assisted Intervention—MICCAI 2002*, pages 556–563. Springer, 2002.
- [111] Ju Zhang, Duane Malcolm, Jacqui Hislop-Jambrich, C David L Thomas, and Poul Nielsen. Automatic meshing of femur cortical surfaces from clinical ct images. In *Mesh Processing in Medical Image Analysis 2012*, pages 40–48. Springer, 2012.
- [112] Lawrence H Staib and James S Duncan. Model-based deformable surface finding for medical images. *Medical Imaging, IEEE Transactions on*, 15(5):720–731, 1996.
- [113] Art Matheny and Dmitry B Goldgof. The use of three-and four-dimensional surface harmonics for rigid and nonrigid shape recovery and representation. *Pattern Analysis and Machine Intelligence, IEEE Transactions on*, 17(10):967–981, 1995.
- [114] Christos Davatzikos, Xiaodong Tao, and Dinggang Shen. Hierarchical active shape models, using the wavelet transform. *Medical Imaging, IEEE Transactions on*, 22(3):414–423, 2003.
- [115] John C Gower. Generalized procrustes analysis. *Psychometrika*, 40(1):33–51, 1975.
- [116] Colin Goodall. Procrustes methods in the statistical analysis of shape. *Journal of the Royal Statistical Society. Series B (Methodological)*, pages 285–339, 1991.
- [117] Paul J Besl and Neil D McKay. Method for registration of 3-d shapes. In *Robotics-DL tentative*, pages 586–606. International Society for Optics and Photonics, 1992.
- [118] Ian Jolliffe. *Principal component analysis*. Wiley Online Library, 2002.
- [119] Fernando De La Torre and Michael J Black. A framework for robust subspace learning. *International Journal of Computer Vision*, 54(1-3):117–142, 2003.
- [120] Danijel Skocaj and Aleš Leonardis. Weighted and robust incremental method for subspace learning. In *Computer Vision, 2003. Proceedings. Ninth IEEE International Conference on*, pages 1494–1501. IEEE, 2003.
- [121] Aapo Hyvärinen and Erkki Oja. Independent component analysis: algorithms and applications. *Neural networks*, 13(4):411–430, 2000.
- [122] Mikkel B Stegmann, Karl Sjöstrand, and Rasmus Larsen. Sparse modeling of landmark and texture variability using the orthomax criterion. In *Medical Imaging*, pages 61441G–61441G. International Society for Optics and Photonics, 2006.

- [123] Karl Sjöstrand, Mikkel B Stegmann, and Rasmus Larsen. Sparse principal component analysis in medical shape modeling. In *Medical Imaging*, pages 61444X–61444X. International Society for Optics and Photonics, 2006.
- [124] Hans Lamecker, Thomas Lange, and Martin Seebass. *Segmentation of the liver using a 3D statistical shape model*. Citeseer, 2004.
- [125] Timothy F Cootes and Christopher J Taylor. Combining point distribution models with shape models based on finite element analysis. *Image and Vision Computing*, 13(5):403–409, 1995.
- [126] Marleen de Bruijne, Bram van Ginneken, Max A Viergever, and Wiro J Niessen. Adapting active shape models for 3d segmentation of tubular structures in medical images. In *Information Processing in Medical Imaging*, pages 136–147. Springer, 2003.
- [127] Anand Rangarajan, Haili Chui, and Fred L Bookstein. The softassign procrustes matching algorithm. In *Information Processing in Medical Imaging*, pages 29–42. Springer, 1997.
- [128] Gérard Subsol, Jean-Philippe Thirion, and Nicholas Ayache. A scheme for automatically building three-dimensional morphometric anatomical atlases: application to a skull atlas. *Medical Image Analysis*, 2(1):37–60, 1998.
- [129] Dinggang Shen, Edward H Herskovits, and Christos Davatzikos. An adaptive-focus statistical shape model for segmentation and shape modeling of 3-d brain structures. *Medical Imaging, IEEE Transactions on*, 20(4):257–270, 2001.
- [130] Yongmei Wang, Bradley S Peterson, and Lawrence H Staib. Shape-based 3d surface correspondence using geodesics and local geometry. In *Computer Vision and Pattern Recognition, 2000. Proceedings. IEEE Conference on*, volume 2, pages 644–651. IEEE, 2000.
- [131] Angela Counce and Christopher J Taylor. Building 3d sulcal models using local geometry. *Medical Image Analysis*, 5(1):69–80, 2001.
- [132] Markus Fleute, Stéphane Lavallée, and Laurent Desbat. Integrated approach for matching statistical shape models with intra-operative 2d and 3d data. In *Medical Image Computing and Computer-Assisted Intervention—MICCAI 2002*, pages 364–372. Springer, 2002.
- [133] Alejandro F Frangi, Daniel Rueckert, Julia Schnabel, Wiro J Niessen, et al. Automatic construction of multiple-object three-dimensional statistical shape models: Application to cardiac modeling. *Medical Imaging, IEEE Transactions on*, 21(9):1151–1166, 2002.
- [134] András Kelemen, Gábor Székely, and Guido Gerig. Elastic model-based segmentation of 3-d neuroradiological data sets. *Medical Imaging, IEEE Transactions on*, 18(10):828–839, 1999.

- [135] AD Brett and CJ Taylor. Automated construction of 3d shape models using harmonic maps. In *Medical Image Understanding and Analysis*, pages 175–78. London, 2000.
- [136] Brett Allen, Brian Curless, and Zoran Popović. The space of human body shapes: reconstruction and parameterization from range scans. In *ACM Transactions on Graphics (TOG)*, volume 22, pages 587–594. ACM, 2003.
- [137] Rebecca Bryan, Prasanth B Nair, and Mark Taylor. Use of a statistical model of the whole femur in a large scale, multi-model study of femoral neck fracture risk. *Journal of biomechanics*, 42(13):2171–2176, 2009.
- [138] Hans Lamecker, Thomas Lange, and Martin Seebass. A statistical shape model for the liver. In *Medical Image Computing and Computer-Assisted Intervention—MICCAI 2002*, pages 421–427. Springer, 2002.
- [139] Aaron CW Kotcheff and Chris J Taylor. Automatic construction of eigen-shape models by direct optimization. *Medical Image Analysis*, 2(4):303–314, 1998.
- [140] Rhodri H Davies, Carole J Twining, Tim F Cootes, John C Waterton, and Camillo J Taylor. A minimum description length approach to statistical shape modeling. *Medical Imaging, IEEE Transactions on*, 21(5):525–537, 2002.
- [141] Hans Henrik Thodberg and Hildur Olafsdottir. Adding curvature to minimum description length shape models. In *British Machine Vision Conference, BMVC*, 2003.
- [142] Andrew Hill, Chris J Taylor, and Alan D Brett. A framework for automatic landmark identification using a new method of nonrigid correspondence. *Pattern Analysis and Machine Intelligence, IEEE Transactions on*, 22(3):241–251, 2000.
- [143] Sharmishta Seshamani, Gouthami Chintalapani, and Russell Taylor. Iterative refinement of point correspondences for 3d statistical shape models. In *Medical Image Computing and Computer-Assisted Intervention—MICCAI 2011*, pages 417–425. Springer, 2011.
- [144] Martin A Styner, Kumar T Rajamani, Lutz-Peter Nolte, Gabriel Zsemlye, Gábor Székely, Christopher J Taylor, and Rhodri H Davies. Evaluation of 3d correspondence methods for model building. In *Information processing in medical imaging*, pages 63–75. Springer, 2003.
- [145] Martin Styner, Shun Xu, Mohammed El-Sayed, and Guido Gerig. Correspondence evaluation in local shape analysis and structural subdivision. In *Biomedical Imaging: From Nano to Macro, 2007. ISBI 2007. 4th IEEE International Symposium on*, pages 1192–1195. IEEE, 2007.
- [146] Anders Ericsson and Johan Karlsson. Benchmarking of algorithms for automatic correspondence localisation. In *BMVC*, pages 759–768, 2006.
- [147] Timothy F Cootes and Christopher J Taylor. Constrained active appearance models. In *Computer Vision, 2001. ICCV 2001. Proceedings. Eighth IEEE International Conference on*, volume 1, pages 748–754. IEEE, 2001.



- [148] Marek Brejl and Milan Sonka. Object localization and border detection criteria design in edge-based image segmentation: automated learning from examples. *Medical Imaging, IEEE Transactions on*, 19(10):973–985, 2000.
- [149] Luc Soler, Hervé Delingette, Grégoire Malandain, Johan Montagnat, Nicholas Ayache, Christophe Koehl, Olivier Dourthe, Benoit Malassagne, Michelle Smith, Didier Mutter, et al. Fully automatic anatomical, pathological, and functional segmentation from ct scans for hepatic surgery. *Computer Aided Surgery*, 6(3):131–142, 2001.
- [150] Lassad Ben Younes, Yoshikazu Nakaajima, and Toki Saito. Fully automatic segmentation of the femur from 3d-ct images using primitive shape recognition and statistical shape models. *International journal of computer assisted radiology and surgery*, 9(2):189–196, 2014.
- [151] Andrew Hill and Christopher J Taylor. Model-based image interpretation using genetic algorithms. In *BMVC91*, pages 266–274. Springer, 1991.
- [152] Michael Isard and Andrew Blake. Condensation—conditional density propagation for visual tracking. *International journal of computer vision*, 29(1):5–28, 1998.
- [153] Nicolae Duta and Milan Sonka. Segmentation and interpretation of mr brain images. an improved active shape model. *Medical Imaging, IEEE Transactions on*, 17(6):1049–1062, 1998.
- [154] Karim Lekadir, Robert Merrifield, and Guang-Zhong Yang. Outlier detection and handling for robust 3-d active shape models search. *Medical Imaging, IEEE Transactions on*, 26(2):212–222, 2007.
- [155] Mike Rogers and Jim Graham. Robust active shape model search. In *Computer Vision—ECCV 2002*, pages 517–530. Springer, 2002.
- [156] Huiqi Li and Opas Chutatape. Automated feature extraction in color retinal images by a model based approach. *Biomedical Engineering, IEEE Transactions on*, 51(2):246–254, 2004.
- [157] Timothy F Cootes, Gareth J Edwards, and Christopher J Taylor. Active appearance models. *IEEE Transactions on Pattern Analysis & Machine Intelligence*, (6):681–685, 2001.
- [158] P Furnstahl, T Fuchs, Andreas Schweizer, Ladislav Nagy, Gábor Székely, and Matthias Harders. Automatic and robust forearm segmentation using graph cuts. In *Biomedical Imaging: From Nano to Macro, 2008. ISBI 2008. 5th IEEE International Symposium on*, pages 77–80. IEEE, 2008.
- [159] Marcel Krčah, Gábor Székely, and Rémi Blanc. Fully automatic and fast segmentation of the femur bone from 3d-ct images with no shape prior. In *Biomedical Imaging: From Nano to Macro, 2011 IEEE International Symposium on*, pages 2087–2090. IEEE, 2011.
- [160] DM Greig, BT Porteous, and Allan H Seheult. Exact maximum a posteriori estimation for binary images. *Journal of the Royal Statistical Society. Series B (Methodological)*, pages 271–279, 1989.

- [161] Yuri Boykov and Gareth Funka-Lea. Graph cuts and efficient nd image segmentation. *International journal of computer vision*, 70(2):109–131, 2006.
- [162] Leo Grady and Christopher V Alvino. The piecewise smooth mumford–shah functional on an arbitrary graph. *Image Processing, IEEE Transactions on*, 18(11):2547–2561, 2009.
- [163] Anil K Jain, M Narasimha Murty, and Patrick J Flynn. Data clustering: a review. *ACM computing surveys (CSUR)*, 31(3):264–323, 1999.
- [164] Bruce J Schachter, Larry S Davis, and Azriel Rosenfeld. Some experiments in image segmentation by clustering of local feature values. *Pattern Recognition*, 11(1):19–28, 1979.
- [165] James C Bezdek, Robert Ehrlich, and William Full. Fcm: The fuzzy c-means clustering algorithm. *Computers & Geosciences*, 10(2):191–203, 1984.
- [166] GE Friedlaender. Bone grafts. the basic science rationale for clinical applications. *The Journal of Bone & Joint Surgery*, 69(5):786–790, 1987.
- [167] M Farrington, I Matthews, J Foreman, KM Richardson, and E Caffrey. Microbiological monitoring of bone grafts: two years’ experience at a tissue bank. *Journal of Hospital Infection*, 38(4):261–271, 1998.
- [168] Tobias Topp, Thorben Müller, Sebastian Huss, Peter Herbert Kann, Eberhard Weihe, Steffen Ruchholtz, and Ralph Peter Zettl. Embalmed and fresh frozen human bones in orthopedic cadaveric studies: which bone is authentic and feasible? a mechanical study. *Acta orthopaedica*, 83(5):543–547, 2012.
- [169] Richard O Duda and Peter E Hart. Use of the hough transformation to detect lines and curves in pictures. *Communications of the ACM*, 15(1):11–15, 1972.
- [170] Dana H Ballard. Generalizing the hough transform to detect arbitrary shapes. *Pattern recognition*, 13(2):111–122, 1981.
- [171] Peter E Hart. How the hough transform was invented [dsp history]. *Signal Processing Magazine, IEEE*, 26(6):18–22, 2009.
- [172] MY Cao, CH Ye, O Doessel, and C Liu. Spherical parameter detection based on hierarchical hough transform. *Pattern recognition letters*, 27(9):980–986, 2006.
- [173] Kishore Mosaliganti, Arnaud Gelas, Paul Cowgill, and Sean Megason. An optimized n-dimensional hough filter for detecting spherical image objects. *The Insight Journal*, 2009.
- [174] Banchong Mahaisavariya, Kriskrai Sitthiseripratip, Trongtum Tongdee, Erik LJ Bohez, Jos Vander Sloten, and Philip Oris. Morphological study of the proximal femur: a new method of geometrical assessment using 3-dimensional reverse engineering. *Medical engineering & physics*, 24(9):617–622, 2002.

- [175] Philip C Noble, Jerry W Alexander, Laura J Lindhal, David T Yew, William M Granberry, and Hugh S Tullos. The anatomic basis of femoral component design. *Clinical orthopaedics and related research*, 235:148–165, 1988.
- [176] Peter Lindstrom and Greg Turk. Fast and memory efficient polygonal simplification. In *Visualization'98. Proceedings*, pages 279–286. IEEE, 1998.
- [177] Gabriel Taubin. A signal processing approach to fair surface design. In *Proceedings of the 22nd annual conference on Computer graphics and interactive techniques*, pages 351–358. ACM, 1995.
- [178] JW Fernandez, P Mithraratne, SF Thrupp, MH Tawhai, and PJ Hunter. Anatomically based geometric modelling of the musculo-skeletal system and other organs. *Biomechanics and modeling in mechanobiology*, 2(3):139–155, 2004.
- [179] Ying He and Hong Qin. Surface reconstruction with triangular b-splines. In *Geometric Modeling and Processing, 2004. Proceedings*, pages 279–287. IEEE, 2004.
- [180] Demetri Terzopoulos. Regularization of inverse visual problems involving discontinuities. *Pattern Analysis and Machine Intelligence, IEEE Transactions on*, (4):413–424, 1986.
- [181] CP Bradley, AJ Pullan, and PJ Hunter. Geometric modeling of the human torso using cubic hermite elements. *Annals of biomedical engineering*, 25(1):96–111, 1997.
- [182] Thomas W Sederberg and Scott R Parry. Free-form deformation of solid geometric models. In *ACM SIGGRAPH computer graphics*, volume 20, pages 151–160. ACM, 1986.
- [183] Gene H Golub and Christian Reinsch. Singular value decomposition and least squares solutions. *Numerische mathematik*, 14(5):403–420, 1970.
- [184] Lin Mei, Michael Figl, Daniel Rueckert, Ara Darzi, and Philip Edwards. Sample sufficiency and number of modes to retain in statistical shape modelling. In *Medical Image Computing and Computer-Assisted Intervention–MICCAI 2008*, pages 425–433. Springer, 2008.
- [185] Timothy F Cootes, Cristopher J Taylor, et al. Statistical models of appearance for computer vision, 2004.
- [186] Prasanta Chandra Mahalanobis. On the generalized distance in statistics. *Proceedings of the National Institute of Sciences (Calcutta)*, 2:49–55, 1936.
- [187] Michael S Floater. Parametrization and smooth approximation of surface triangulations. *Computer aided geometric design*, 14(3):231–250, 1997.
- [188] Malte Zöckler, Detlev Stalling, and Hans-Christian Hege. Fast and intuitive generation of geometric shape transitions. *The Visual Computer*, 16(5):241–253, 2000.

- [189] Yan-Bin Jia, Liangchuan Mi, and Jiang Tian. Surface patch reconstruction via curve sampling. In *Robotics and Automation, 2006. ICRA 2006. Proceedings 2006 IEEE International Conference on*, pages 1371–1377. IEEE, 2006.
- [190] Hyun Soo Kim, Han Kyun Choi, and Kwan H Lee. Feature detection of triangular meshes based on tensor voting theory. *Computer-Aided Design*, 41(1):47–58, 2009.
- [191] M Peacock, KA Buckwalter, S Persohn, Thomas N Hangartner, MJ Econs, and S Hui. Race and sex differences in bone mineral density and geometry at the femur. *Bone*, 45(2):218–225, 2009.
- [192] Gerold Holzer, Gobert von Skrbensky, Lukas A Holzer, and Wolfgang Pichl. Hip fractures and the contribution of cortical versus trabecular bone to femoral neck strength. *Journal of Bone and Mineral Research*, 24(3):468–474, 2009.
- [193] Susan B Broy, Jane A Cauley, Michael E Lewiecki, John T Schousboe, John A Shepherd, and William D Leslie. Fracture risk prediction by non-bmd dxa measures: the 2015 iscd official positions part 1: Hip geometry. *Journal of Clinical Densitometry*, 18(3):287–308, 2015.
- [194] Sasan Mahmoodi, Bayan S Sharif, and E Graeme Chester. Contour detection using multi-scale active shape models. In *Image Processing, 1997. Proceedings., International Conference on*, volume 2, pages 708–711. IEEE, 1997.
- [195] Zhengyou Zhang. Iterative point matching for registration of free-form curves and surfaces. *International journal of computer vision*, 13(2):119–152, 1994.
- [196] Jon Louis Bentley. Multidimensional binary search trees used for associative searching. *Communications of the ACM*, 18(9):509–517, 1975.
- [197] Michael W Walker, Lejun Shao, and Richard A Volz. Estimating 3-d location parameters using dual number quaternions. *CVGIP: image understanding*, 54(3):358–367, 1991.
- [198] Arild Aamodt, Kjell A Kvistad, Eivind Andersen, Jon Lund-Larsen, Jan Eine, Pål Benum, and Otto S Husby. Determination of the hounsfield value for ct-based design of custom femoral stems. *Journal of Bone & Joint Surgery, British Volume*, 81(1):143–147, 1999.
- [199] L Giovannelli, O Marco, JM Navarro, E Giner, and JJ Ródenas. Direct creation of finite element models from medical images using cartesian grids. *Computational Vision and Medical Image Processing IV: VIPIM-AGE 2013*, page 167, 2013.
- [200] Daniel P Huttenlocher, Gregory Klanderma, William J Rucklidge, et al. Comparing images using the hausdorff distance. *Pattern Analysis and Machine Intelligence, IEEE Transactions on*, 15(9):850–863, 1993.

- [201] S Eggli, M Pisan, and ME Müller. The value of preoperative planning for total hip arthroplasty. *Journal of Bone & Joint Surgery, British Volume*, 80(3):382–390, 1998.
- [202] Masaaki Maruyama, Judy R Feinberg, William N Capello, and James A D’Antonio. Morphologic features of the acetabulum and femur: Anteversion angle and implant positioning. *Clinical Orthopaedics and Related Research*, 393:52–65, 2001.
- [203] Nitin Goyal and S David Stulberg. Evaluating the precision of preoperative planning in patient specific instrumentation: Can a single mri yield different preoperative plans? *The Journal of arthroplasty*, 2015.
- [204] Riccardo Lattanzi, Fabio Baruffaldi, Cinzia Zannoni, and Marco Viceconti. Specialised ct scan protocols for 3-d pre-operative planning of total hip replacement. *Medical engineering & physics*, 26(3):237–245, 2004.
- [205] Serge Van Sint Jan, Stéphane Sobzack, Pierre-Michel Dugailly, Véronique Feipel, Philippe Lefèvre, Jean-Louis Lufimpadio, Patrick Salvia, Marco Viceconti, and Marcel Rooze. Low-dose computed tomography: a solution for in vivo medical imaging and accurate patient-specific 3d bone modeling? *Clinical Biomechanics*, 21(9):992–998, 2006.
- [206] Hyun Woo Goo. Ct radiation dose optimization and estimation: an update for radiologists. *Korean journal of radiology*, 13(1):1–11, 2012.
- [207] Philip C Noble, Nobuhiko Sugano, James D Johnston, Matthew T Thompson, Michael A Conditt, Charles A Engh Sr, and Kenneth B Mathis. Computer simulation: how can it help the surgeon optimize implant position? *Clinical orthopaedics and related research*, 417:242–252, 2003.
- [208] Erkang Cheng, Jinwu Chen, Jie Yang, Huiyang Deng, Yi Wu, Vasileios Megalooikonomou, Bryce Gable, and Haibin Ling. Automatic dentlandmark detection in 3-d cbct dental volumes. In *Engineering in Medicine and Biology Society, EMBC, 2011 Annual International Conference of the IEEE*, pages 6204–6207. IEEE, 2011.
- [209] Sandro Moos, Federica Marcolin, Stefano Tornincasa, Enrico Vezzetti, Maria Grazia Violante, Giulia Fracastoro, Domenico Speranza, and Francesco Padula. Cleft lip pathology diagnosis and foetal landmark extraction via 3d geometrical analysis. *International Journal on Interactive Design and Manufacturing (IJIDeM)*, pages 1–18, 2014.
- [210] Maarten A Röling, Monique I Visser, Edwin HG Oei, Peter Pilot, Gert-Jan Kleinrensink, and Rolf M Bloem. A quantitative non-invasive assessment of femoroacetabular impingement with ct-based dynamic simulation-cadaveric validation study. *BMC musculoskeletal disorders*, 16(1):50, 2015.
- [211] Sofie Van Cauter, Matthieu De Beule, Annemieke Van Haver, Peter Verdonk, and Benedict Verheghe. Automated extraction of the femoral anatomical axis for determining the intramedullary rod parameters in

- total knee arthroplasty. *International journal for numerical methods in biomedical engineering*, 28(1):158–169, 2012.
- [212] Ji-Sup Yun, Yong Sang Lee, Jeong Joo Jung, Kee Hyun Nam, Woong Youn Chung, Hang Seok Chang, and Cheong Soo Park. The zuckermandl’s tubercle: a useful anatomical landmark for detecting both the recurrent laryngeal nerve and the superior parathyroid during thyroid surgery. *Endocrine journal*, 55(5):925–930, 2008.
- [213] Mohammad Y Hajeer, Ashraf F Ayoub, Declan T Millett, M Bock, and JP Siebert. Three-dimensional imaging in orthognathic surgery: the clinical application of a new method. *The International journal of adult orthodontics and orthognathic surgery*, 17(4):318–330, 2001.
- [214] Krzysztof Wrobel, Susanna R Stevens, Robert H Jones, Craig H Selzman, Andre Lamy, Thomas M Beaver, Ljubomir T Djokovic, Nan Wang, Eric J Velazquez, George Sopko, et al. A landmark analysis of 30-day mortality after coronary artery bypass surgery in patients with ischemic heart failure: Results of the surgical treatment for ischemic heart failure (stich) trial. *Circulation*, 130(Suppl 2):A19392–A19392, 2014.
- [215] Nicola Mondanelli, Francesco Giron, Michele Losco, Roberto Buzzi, and Paolo Aglietti. Opening wedge high tibial osteotomy using a monoaxial dynamic external fixator. *Knee Surgery, Sports Traumatology, Arthroscopy*, pages 1–8, 2015.
- [216] Wolfgang Beil, Karl Rohr, and H Siegfried Stiehl. Investigation of approaches for the localization of anatomical landmarks in 3d medical images. *Proc. Computer Assisted Radiology and Surgery CAR*, 97:25–28, 1997.
- [217] Seung-Yeob Baek, Joon-Ho Wang, Insub Song, Kunwoo Lee, Jehee Lee, and Seungbum Koo. Automated bone landmarks prediction on the femur using anatomical deformation technique. *Computer-Aided Design*, 45(2):505–510, 2013.
- [218] Jan Ehrhardt, Heinz Handels, Bernd Strathmann, Thomas Malina, Werner Plötz, and Siegfried J Pöpl. Atlas-based recognition of anatomical structures and landmarks to support the virtual three-dimensional planning of hip operations. In *Medical Image Computing and Computer-Assisted Intervention-MICCAI 2003*, pages 17–24. Springer, 2003.
- [219] K Subburaj, Bhallamudi Ravi, and Manish Agarwal. Automated identification of anatomical landmarks on 3d bone models reconstructed from ct scan images. *Computerized Medical Imaging and Graphics*, 33(5):359–368, 2009.
- [220] Anthony Viste, Franck Trouillet, Rodolphe Testa, Laurence Chèze, Romain Desmarchelier, and Michel-Henri Fessy. An evaluation of ct-scan to locate the femoral head centre and its implication for hip surgeons. *Surgical and Radiologic Anatomy*, 36(3):259–263, 2014.

- [221] G Lecerf, MH Fessy, R Philippot, P Massin, F Giraud, X Flecher, J Girard, P Mertl, E Marchetti, and E Stindel. Femoral offset: anatomical concept, definition, assessment, implications for preoperative templating and hip arthroplasty. *Orthopaedics & Traumatology: Surgery & Research*, 95(3):210–219, 2009.
- [222] Jan Bartoníček. Pauwels’ classification of femoral neck fractures: correct interpretation of the original. *Journal of orthopaedic trauma*, 15(5):358–360, 2001.
- [223] Scott S Kelley, Robert H Fitzgerald Jr, James A Rand, and Duane M Ilstrup. A prospective randomized study of a collar versus a collarless femoral prosthesis. *Clinical orthopaedics and related research*, 294:114–122, 1993.
- [224] SM Röhrli, Ming G Li, E Pedersen, G Ullmark, and B Nivbrant. Migration pattern of a short femoral neck preserving stem. *Clinical orthopaedics and related research*, 448:73–78, 2006.
- [225] Stephen A Yoder, Richard A Brand, Douglas R Pederson, and Thomas W O’Gorman. Total hip acetabular component position affects component loosening rates. *Clinical orthopaedics and related research*, 228:79–87, 1988.
- [226] K Herrlin, H Pettersson, and G Selvik. Comparison of two-and three-dimensional methods for assessment of orientation of the total hip prosthesis. *Acta Radiologica*, 29(3):357–361, 1988.
- [227] Christian Merle, George Grammatopoulos, Wenzel Waldstein, Elise Pegg, Hemant Pandit, Peter R Aldinger, Harinderjit S Gill, and David W Murray. Comparison of native anatomy with recommended safe component orientation in total hip arthroplasty for primary osteoarthritis. *The Journal of Bone & Joint Surgery*, 95(22):e172, 2013.
- [228] Robert Schneiders. A grid-based algorithm for the generation of hexahedral element meshes. *Engineering with computers*, 12(3-4):168–177, 1996.
- [229] Pascal Frey and Paul-Louis George. *Mesh generation*, volume 32.
- [230] Eloi Ruiz-Gironés, Xevi Roca, and Josep Sarrate. The receding front method applied to hexahedral mesh generation of exterior domains. *Engineering with Computers*, 28(4):391–408, 2012.
- [231] Y Kagiya, M Takao, N Sugano, Yasunori Tada, N Tomiyama, and Yuuki Sato. Optimization of surgical planning of total hip arthroplasty based on computational anatomy. In *Engineering in Medicine and Biology Society (EMBC), 2013 35th Annual International Conference of the IEEE*, pages 2980–2983. IEEE, 2013.
- [232] Paul Viola and Michael Jones. Rapid object detection using a boosted cascade of simple features. In *Computer Vision and Pattern Recognition, 2001. CVPR 2001. Proceedings of the 2001 IEEE Computer Society Conference on*, volume 1, pages I–511. IEEE, 2001.





